Tank designs for combined high-pressure gas and solid-state hydrogen storage

PhD Thesis

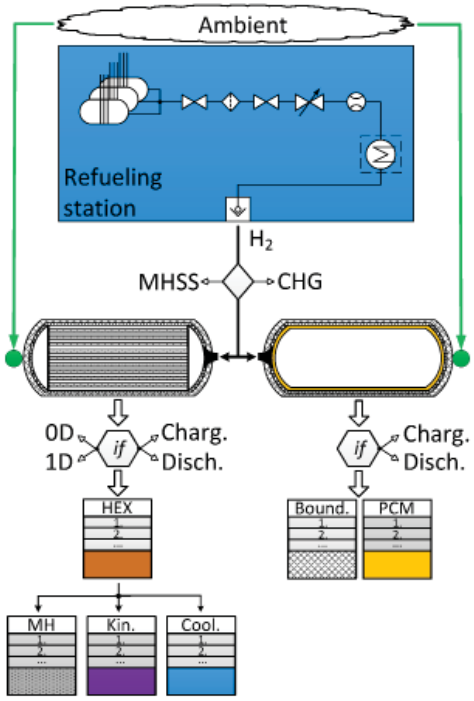

Andrea Mazzucco
DCAMM Special Report No. S197
January 2016

DTU Mechanical Engineering
Department of Mechanical Engineering

Tank designs for combined high pressure gas and solid state hydrogen storage

PhD Thesis
submitted the 31st January 2016
and defended the 11th April 2016
at the
TECHNICAL UNIVERSITY OF DENMARK

for the degree of Doctor of Philosophy

by
Andrea Mazzucco

under suggestion of:
Associate Professor Masoud Rokni (DTU), main supervisor
Associate Professor Brian Elmegaard (DTU), co-supervisor

and under recommendation of:
Professor Qingfeng Li (DTU), examiner
Professor Volodymyr Yartys (NTNU), examiner
Research scientist José M. Bellosta von Colbe (HZG), examiner

Tank designs for combined high pressure gas and solid state hydrogen storage

PhD Thesis
DCAMM Special Report no. S197
Printed by Rosendahls – Schultz Grafisk A/S
Font: Utopia typeset with LaTeX 2ε

DTU Mechanical Engineering
Section of Thermal Energy
Technical University of Denmark

Nils Koppels Allé, Bld. 403
DK-2800 Kongens Lyngby
Denmark
Phone: (+45) 45 25 41 31
Fax: (+45) 45 25 43 25
www.mek.dtu.dk
ISBN: 978-87-7475-443-5

to my family that has always been there for me
and to my friends with whom I shared happiness and sorrow

Two roads diverged in a wood, and I – I took the one less traveled by,
and that has made all the difference.

— R. Frost, *The road not taken*

Preface

The present thesis is submitted as a partial fulfillment of the requirements for the degree of Philosophiae Doctor (Ph.D.) at the Technical University of Denmark (DTU).

The thesis was completed at the Section of Thermal Energy, Department of Mechanical Engineering. This work was carried out from the 1st of November 2012 to the 31st of January 2016 under the supervision of Associate Professor Masoud Rokni and the co-supervision of Associate Professor Brian Elmegaard.

An external research stay was undertaken from April 2014 to September 2014 at the Hydrogen Systems Laboratory, an interdisciplinary facility of the Maurice J. Zucrow Laboratories at Purdue University in West Lafayette, Indiana, United States, under the supervision of Associate Professor Timothée L. Pourpoint.

The Ph.D. study was funded by the Technical University of Denmark and the Danish Energy Agency through the Hyfill-Fast International Research Project in collaboration H2Logic as the inductrial partner. Financial support was also received from the Otto Mønsted A/S Fond in the frame of the WHEC 2014 and IGEC-X 2015 conferences and of the external research stay at Purdue University.

The thesis is written in the form of a monograph and includes all the relevant publications produced in the time frame of the present research study.

Copenhagen, January 31st 2016

Andrea Mazzucco

Acknowledgments

It is hard to put into meaningful words my deep feeling of gratitude for all the people that have walked with me to the end of this journey.
My attempt might result poor to most of the people that will read these pages, but at least, I will always have the profound awareness that these simple words are nothing but true.

At first, I would like to thank the people at the university that have directly contributed to the work presented in this thesis. In particular, I would like to express my deepest gratitude to my supervisor, Professor Masoud Rokni, for his guidance and the numerous discussions we had in the past three years. I also thank him for giving me the opportunity to share a relationship of mutual confidence and respect. I am also very grateful to my co-supervisor Professor Brian Elmegaard for both the productive conversations and the friendly working environment he managed to build at the section.

It is hard not to thank all the members of the Hyfill-Fast International Research Project, including Michael Sloth from H2Logic for the many useful meetings and especially Jens-Erick Jørgensen and Torben Jensen at Aarhus University for their interesting inputs on novel research topics.

My stay at Purdue University would not have been possible without Professor Timothée Pourpoint who accepted me in his laboratory and introduced me to his research team. I am also grateful to Tyler Voskuilen whose help was fundamental to the success of the work carried out during my external stay of research.

A special thanks goes to all my friends in Denmark and abroad who supported me and with whom I shared moments of happiness and hard work. Lorenzo, for being the first who accepted me as a friend at the section and for cheering me up with jokes that will always leave a mark in my mind. Danilo, for his inspiring “joie de vivre” and his many attempts to teach me that being young is just a state of mind. Erasmus, for his warm friendship and for the help he was always ready to give me. Tuong-Van, whose name I will never be able to pronounce correctly, for proving himself a true friend over

the years and for the many dinners shared at the office and downtown. Jorrit, for his cheerful spirit in the office and the nice moments spent together beyond the doors of the university. Torben, for the many beers and jokes. Leonardo for the convivial working environment.

To Carlotta goes my profound gratitude for what is, without any doubt, the happiest time I had in Denmark. I wish you could have the same thorough confidence that I have on your success in any goals you will set for yourself and in any challenges you will brave in your future.

At last, but not least I want to thank my family. My father Guido, my mother Cristina, my brother Luca and my beloved grandmother Pierina for being a reference point in my entire life and for all the support they gave me through these many years.

Abstract

Many challenges have still to be overcome in order to establish a solid ground for significant market penetration of fuel cell hydrogen vehicles. The development of an effective solution for on-board hydrogen storage is one of the main technical tasks that need to be tackled.

The present thesis deals with the development of a simulation tool to design and compare different vehicular storage options with respect to targets based upon storage and fueling efficiencies. The set targets represent performance improvements with regard to the state-of-the-art technology and are separately defined for each storage solution investigated in this work. Attention is given to solutions that involve high-pressure solid-state and gas hydrogen storage with an integrated passive cooling system. A set of libraries is implemented in the modeling platform to select among different material compositions, kinetic equations, heat exchanger configurations and to enable the tailoring of the analysis according to the user needs.

Reliable computational models are developed to describe hydriding and dehydriding reactions as well as melting and solidification processes that occur in the metal hydride tank and novel compressed-hydrogen vessel respectively. For the former, these models are used to quantify the main design parameter, being the critical metal hydride thickness, for the tank/heat-exchanger system.

For the metal hydride tank, the tubular layout in a shell and tube configuration with 2 mm inner diameter tubes is found to achieve the desired refueling time of 3 min and store a maximum of 3.1 kg of hydrogen in a 126 L tank. The dehydriding ability of this solution is proven to withstand intense discharging conditions.

For the hydrogen gas tank, a novel design that includes a phase change material in its inner volume. Heat transfer augmentation techniques (e.g. encapsulation) are found to be the reward strategy to achieve the same stored mass and fueling time of the standard technology, while enabling ambient temperature fueling and save the energy cooling demand (4.2 MJ per fueling) at the refueling station.

Resumé

For at skabe en solid base for et markedsgennembrud af brændselscellebiler er der stadigvæk en del udfordringer der skal overkommes. Udviklingen af en tank der effektivt kan lagre brinten i køretøjet er en af de primære tekniske udfordringer som skal løses.

Denne afhandling beskæftiger sig med udviklingen af et simuleringsværktøj der kan bruges til at sammenligne forskellige brintlagringsteknologier indenfor målene for lagring- og fyldningseffektivitet. De fastsatte mål repræsenterer forbedring i ydelse i forhold til den nyeste teknologi og de er forskelligt defineret for hver lagringsteknologi. Fokus er lagt på løsninger der indebærer brint lagret som højtryksgas og brint bundet i fast stof, begge med et passivt kølesystem. I simuleringsværktøjet er der implementeret flere biblioteker der gør det muligt at vælge materiale sammensætning, varmeveksler konfiguration og design af analysen efter brugerens behov.

Pålidelige beregningsmodeller er udviklet for at beskrive absorptive og desorptive reaktioner samt smeltning- og størkningsprocesserne der forekommer i metalhydridtanke samt i højtryks brint tanke. Disse modeller er benyttet til at kvantificere det primære design, metalhydridens tykkelse i forhold til tanken og varmeveksler systemet.

For tanken indeholdende metalhydrider kan det rørformede layout i en ”shell and tube” konfiguration med 2 mm indvendig diameter af rørende opnå den ønskede påfyldningstid på 3 min mens den maksimalt kan lagre 3.1 kg i en 126 L tank. Desorptionen af denne løsning har vist sig at kunne modstå krævende afladningsforhold.

For tanke indeholdende brint ved højttryk er et nyt design med 5-mm faseskiftende materiale i tankvæggen til passiv køling af brinten foreslået. Derved opnår tanken samme mængde lagret gas som ved andre typer tanke og påfyldningstiden er indenfor standarden. Ved at bruge et faseskiftende materiale i væggen kan for-kølingen af brinten der normalt foregår på selve tankstationen elimineres. Derved spares 4.2 MJ per påfyldning mod tankene der bruges i dag.

List of publications

Part of the work performed during the Ph.D. project resulted in peer-reviewed publications, which are listed hereafter by category, order of acceptance and relevance. Some of them refer to studies that are not directly related to the work presented in this thesis. However, they were carried out in the last three years and for this reason they are listed under *Other publications* to give the reader a full view of the publications produced in the time frame of the Ph.D. project.

Journal papers

1. **Mazzucco A.**, Dornheim M., Sloth M., Jensen T. R., Jensen J. O. and Rokni M. Bed geometries, fueling strategies and optimization of heat exchanger designs in metal hydride storage systems for automotive applications: A review. International Journal of Hydrogen Energy 39(30), 17054-17074, 2014. DOI: 10.1016/j.ijhydene.2014.08.047.

2. **Mazzucco A.** and Rokni M. Generalized computational model for high pressure metal hydrides with variable thermal properties. International Journal of Hydrogen Energy 40(35), 11470-77. DOI: 10.1016/j.ijhydene.2015.03.032.

3. **Mazzucco A.**, Rothuizen E., Jørgensen J-E., Jensen T. R. and Rokni M. Integration of phase change materials in compressed hydrogen gas systems: modelling and parametric analysis. International Journal of Hydrogen Energy, 41(2), 1060-1073, 2015. DOI: 10.1016/j.ijhydene.2015.09.034.

4. **Mazzucco A.**, Voskuilen T. G., Waters E. L., Pourpoint T. L. and Rokni M. Heat exchanger selection and design analyses for metal hydride heat pump systems. International Journal of Hydrogen Energy, 41(7), 4198-4213, 2016. DOI: 10.1016/j.ijhydene.2016.01.016.

Peer-reviewed Conference papers

1. **Mazzucco A.** and Rokni M. Effect of variable thermal conductivity and specific heat capacity on the calculation of the critical metal hydride thickness

for Ti1.1CrMn. Proceedings of the 20th World Hydrogen Energy Conference (WHEC). Gwangju (Korea), June 2014.

2. **Mazzucco A.**, Rothuizen E., Jørgensen J-E., Jensen T. R. and Rokni M. A compressed hydrogen gas storage system with an integrated phase change material. Proceedings of the 10th International Green Energy Conference (IGEC-X). Taichung (Taiwan), May 2015.

Other publications

Journal papers

1. **Mazzucco A.** and Rokni M. Thermo-economic analysis of a solid oxide fuel cell and steam injected gas turbine plant integrated with woodchips gasification. Energy, 76, 114–129, 2014. DOI: 10.1016/j.energy.2014.04.035.

2. Pierobon L., Nguyen T-V., **Mazzucco A.**, Larsen U. and Haglind F. Part-Load Performance of a Wet Indirectly Fired Gas Turbine Integrated with an Organic Rankine Cycle Turbogenerator. Energies (7), p. 8294-8316, 2014. DOI: 10.3390/en7128294.

Peer-reviewed Conference papers

1. **Mazzucco A.** and Rokni M. Thermoeconomic Analysis Of a Gasification Plant Fed By Woodchips And Integrated With SOFC And STIG Cycles. Proceedings of the 8th Conference on Sustainable Development of Energy, Water and Environment Systems (SDEWES). Dubrovnik (Croatia), September 2013.

Contents

Nomenclature

Abbreviations

$\bar{h}_f$	Mean convection coefficient of heat transfer, $W \cdot m^{-2} \cdot K^{-1}$
$\bar{h}_f$	Mean convective heat transfer coefficient, $W \cdot m^{-2} \cdot K^{-1}$
$\bar{U}$	Mean global heat transfer coefficient, $W \cdot m^{-2} \cdot K^{-1}$
$\dot{m}$	Mass flow rate, $m \cdot s^{-1}$
$\dot{q}$	Heat transfer rate, $W \cdot m^2$
$\dot{q}_{MH}$	Heat generated during hydrogen absorption, W
a	Aspect ratio, -
A_{cross}	Cross flow area, m^2
A_{hex}	Area of heat transfer, m^2
A_{in}	Area at the interface between the phase change material and hydrogen volume, m^2
B	Baffle space, % of shell diameter
c	Specific heat capacity, $J \cdot kg^{-1} \cdot K^{-1}$
C_a	Activation rate, s^{-1}
C_l	Tube clearance, m or mm
c_{MH}	Effective specific heat capacity, $J \cdot kg^{-1} \cdot K^{-1}$
C_t	Tube layout constant
D	Diameter, m
D_h	Hydraulic diameter, m

D_i	Inner diameter of the inner tube, m or mm
D_o	Inner diameter of the outer tube, m or mm
D_s	Shell diameter, m
dl	Discretization step along the longitudinal dimension, m or mm
dx	Discretization step along the x-axis or the radial dimension, m or mm
E_a	Activation energy, $J \cdot mol_{H2}^{-1}$
E_c	Cooling demand, J
F	Index of performance, %
F_t	Temperature factor, -
F_{rc}	Fraction of reaction completion, $kg_{H2} \cdot kg_{H2,max}$ or %
H	Enthalpy, J
h	Specific enthalpy, $J \cdot kg^{-1}$
h_w	Specific enthalpy of the hydrogen absorbed phase, $J \cdot kg^{-1}$
k	Thermal conductivity, $W \cdot m^{-1} \cdot K^{-1}$
k_m	Linearly interpolated thermal conductivity of phase change, $W \cdot m^{-1} \cdot K^{-1}$
k_{MH}	Effective thermal conductivity, $W \cdot m^{-1} \cdot K^{-1}$
k_r	ratio between the effective conductivity that accounts for natural convection and the thermal conductivity of the liquid, -
L	Length of tube or tank, m
N	Total number of discretized metal hdyride volumes
N_t	Number of tubes
OD	Outer diameter of the inner tube, m or mm
p	Pressure, bar or Pa
p^{eq}	Equilibrium pressure, bar or Pa
p_0	Initial tank pressure, bar or Pa

p_{ramp}	Pressure ramp of refueling, bar·min^{-1} or Pa·min^{-1}
p_{ref}	Refueling or charging pressure, bar or Pa
p_{start}	Internal tank pressure before fueling takes place
P_t	Tube pitch, m or mm
PR	Pitch to tube diameter ratio
Q	Heat of reaction, W·mol^{-1}
q'''	Heat flux, W·m^3
$R_{th,cont}$	Thermal resistance of contact, m^2·K·W^{-1} or mm^2·K·W^{-1}
R_{th}	Thermal resistance, m^2·K·W^{-1} or mm^2·K·W^{-1}
S	Total number of discretized coolant volumes
T_m	Melting temperature, K or °C
t_{rc}	Time of reaction completion, s or min
t_{ref}	Refueling time, s or min
V	Volume, m^3
v	Velocity, m·s^{-1}
$v_{o,m}$	Mean value in the optimum velocity range, m·s^{-1}
V_{ratio}	Ratio between metal hydride volume and inner tank volume
w	Weight fraction of absorbed hydrogen in the hydride, kg_{H2}·kg_{MH}^{-1} or %
w_{max}	Maximum H_2 storage capacity (at saturation conditions), $kg_{H2,\,max}$·kg_{MH}^{-1}
Bound.	Boundary
CAGR	Compound annual growth rate
CFRP	carbon fiber reinforced polymer
CHG	Compressed hydrogen gas
Cool.	Coolant
CTP	Tube count calculation constant for one tube pass

Nomenclature

DOE	Department of Energy of U.S.A.
FCEV	Fuel cell electric vehicle
FVM	Finite volume method
GHG	Greenhouse gas
GUI	Graphical user interface
HEX	Heat exchanger
HPMH	High pressure metal hydride
HPMHSS	high-pressure metal hydride storage system
HTF	Heat transfer fluid
HySDeP	Hydrogen Storage Design Platform
j	Positional index of discretized volumes
Kin.	Kinetics
Lam	Laminar
LHS	Left hand side of an equation
MH	Metal hydride
MHHP	Metal hydride heat pump
MHSS	Metal hydride storage system
MW	Molecular weight, $kg \cdot mol^{-1}$
n.a.	Not applicable or not available
PC	Phase change
PCM	Phase change material
R	Universal gas constant, $J \cdot mol_{H2}^{-1} \cdot K^{-1}$
RHS	Right hand side of an equation
SMR	Steam methane reforming
Tran	Transition

Turb	Turbulent

Greek letters

α_g	Coefficient of thermal expansion, K^{-1}
ΔH	Enthalpy of reaction, $J \cdot mol_{H2}^{-1}$
ΔS	Entropy of reaction, $J \cdot mol_{H2}^{-1} \cdot K^{-1}$
δ	Critical metal hydride thickness, m or mm
ϵ	Thermal effectiveness of heat transfer, %
γ_1	Coefficient involved in the effective specific heat capacity calculation during phase change, $J \cdot kg^{-1} \cdot K^{-1}$
γ_2	Coefficient involved in the effective specific heat capacity calculation during phase change, $J \cdot kg^{-1} \cdot K^{-2}$
γ_3	Coefficient involved in the effective specific heat capacity calculation during phase change, $J \cdot kg^{-1} \cdot K^{-1}$
γ_4	Coefficient involved in the effective specific heat capacity calculation during phase change, $J \cdot kg^{-1} \cdot K^{-2}$
Λ	Coefficient of pressure derivative over time, m^3
λ	Latent heat, $J \cdot kg^{-1}$
ν	Kinematic viscosity, $m^2 \cdot s^{-1}$
ω_1	value of the asymmetric phase-change function below the melting temperature, K or °C
ω_2	value of the asymmetric phase-change function above the melting temperature, K or °C
ϕ	Porosity of the hydride bed, $m_{H2}^3 \cdot m_{MH}^{-3}$ or %
Ψ	Coefficient of weight fraction derivative over time, J
ρ	Density, $kg \cdot m^{-3}$
σ_u	Ultimate tensile strength, MPa
σ_y	Yield tensile strength, MPa

Υ	Coefficient of metal hydride temperature derivative over time, $J \cdot K^{-1}$
I	Free term dependent upon hydrogen mass flow rate and transferred heat, W

Subscripts

a	Activation
ab	Absorption process
adiab	Adiabatic conditions
c	Coolant
cont	Contact. It refers to the contact resistance
des	Desorption process
ext	External
f	Fluid of heat transfer
g	Gas
i	Inlet
in	Internal
m	Mean or average, refers to an interval, a surface or a volume
max	Maximum value (e.g. saturation conditions)
o	Outlet
s	Solid phase or crystalline
syst	System
tot	Total

1 Introduction

1.1 Outlook

Hydrogen worldwide production is not monitored, but was estimated to exceed 55 million metric tons in 2014 (11 millions metric tons only in the United States), including both captive and merchant markets. The former represents 88% of the overall produced volumes and consists in on-site production and utilization, whereas the latter refers to the actual sale from the producer to the client, which occurs either by establishing a local production plant at the customer site, or by delivering centrally produced H_2 through a dedicate infrastructure or in packs as cylinders [1].

Nowadays, 96% of the global production is derived from fossil fuels and principally through steam methane reforming (SMR) of natural gas, which is the cheapest and most common technology in use, whereas electrolysis and other renewable production methods only represent a modest share [2–5].

More than 80% of the global demand is related to the refinery and chemical industries, where H_2 is produced for captive use and employed in cracking and de-sulphurization processes of heavy hydrocarbons, as well as in the production of ammonia for fertilizers [6]. The other main uses of hydrogen include hydrogenation and iron reduction in the food and steel industries. In the future, H_2 could be used for a large variety of applications ranging from power generation and combustion engines to fuel cells.

More stringent regulations on sulphur levels for refined fuels, together with a reduction of light and sweet crude oils reservoirs, represent the key factors responsible for a growing hydrogen demand in the recent years [7]. Market studies forecast captive production to grow at a compound annual growth rate (CAGR) of 5.4%, whereas merchant production is expected to increase at a CAGR of 9.6% for the period 2014-2019. This would result in a value of $138.2 billion in 2019 for the global hydrogen

generation market [8].

A significant boost in the growth of the hydrogen market is expected to occur after 2020, in view of its role in the forthcoming renewable transport sector. Assuming a fast ramp-up of fuel cell electric vehicle (FCEV) sales, predictions envisage that after the introduction of the first 10000 FCEVs, a self-sustaining market can arise within 15 to 20 years [7]. This would result in a considerable expansion in H_2 production volumes to meet the increasing demand of the automotive industry, which has a predicted potential share of 30% of the projected global fleet in 2050 (700 millions of vehicles) [9].

Recent history has taught that most long-term market studies are based on the prediction of a continuous technological progress that often has not found confirmation in reality. Many challenges still have to be overcome to establish a solid pathway towards a reliable hydrogen economy [10]. These involve inter-dependent economic, political, social and technical aspects that can be summarized as cost reduction of processes and components from production to utilization, public acceptance and the development of effective solutions that achieve comparable performance with the present technology. Technical challenges include mainly the production and storage sectors, whereas for H_2 distribution, the main barriers are related to the high investment costs of a widespread infrastructure and the establishment of a profound cooperation between car manufacturers, oil&gas companies and government [11–13].

The development of an effective on-board storage solution is often considered as one of the most difficult tasks to tackle, in order to realize a fuel cell vehicle with a driving range comparable with the current technology based on fossil fuels [14]. Indeed, H_2 storage is made extremely challenging because of the low energy density by volume, while, on the contrary, its high energy content by weight (nearly three times gasoline) gives hope for automotive applications [15, 16].

Hydrogen storage technologies primarily differ in the form in which H_2 is stored: liquid, gas or solid-state form. The two latter offer more room for potential improvements and are the matter of interest in the present thesis.

1.2 Motivation

Interest on FCEVs has raised sharply at the end of the 20th century as fossil fuel depletion, pollution and climate change became matters of increasing concerns in the eyes of the public. The today's transport sector principally relies on fossil fuels which represents more than 95% of its global energy supply. This sector is responsible for an increase in the greenhouse gas (GHG) emissions from 23% to 27.6% in the period 2004-2011. Approximately 75% of this share is from road transportation [17–19]. In this context, FCEVs have gained attention as a potential renewable solution to the mobility service of today's conventional cars at very low carbon emissions. With a 25% share of fuel cell electric vehicles on the road by 2050 all cumulative transport-related carbon emissions can decrease by up to 10% [7].

In the perspective of establishing a solid ground for a significant market penetration of FCEVs, the on-board storage technology plays a key role. Hydrogen storage poses major challenges as it implies the reduction of significant gas volumes (11 m^3 per kg at ambient conditions). The main methods available to enhance the storage capacity are: (1) gas compression at high-pressure (in the order of 700 bar), (2) liquefaction at cryogenic temperatures (around 21 K), (3) adsorption on high-surface materials (below 100 K), (4) chemical bonding in ionic and covalent compounds (at ambient pressure), (5) oxidation of reactive metals (e.g. Zn, Mg, Na, Li, Al) in contact with water and (6) absorption in a host metallic structure. In this work only the technologies that can enable charging/discharging characteristics and storage performance potentially competitive within the current automotive industry are taken into account [20–22].

Hydrogen absorption in advance metal hydrides (MH) with reduced weight and high equilibrium pressures was found to be of particular interest by the US Department of Energy (DOE). The main reason was their capability to reversibly store hydrogen in large quantities with increased safety and higher volumetric densities than other storage options in gaseous and liquid phases [23–29]. Metal hydrides with high equilibrium pressures or high-pressure metal hydrides (HPMHs) present cold start capability (even below 0°C) and fast kinetics for both absorption and desorption reactions [30–32]. The other technology that is here investigated is compressed hydrogen gas (CHG) storage systems. The relatively low filling times (approximately three minutes) and weight, along with the simplicity of the tank construction and refueling process have made this option the straightforward candidate for the first generation of commercial FCEVs. An example of this is the Toyota Mirai [33]. CHG systems' storage performance has already been topic of extensive industrial optimization, and the main focus of this research is therefore on designs that can improve the energy efficiency of the refueling process.

1.3 Literature review

The state-of-the-art research for HPMH and CHG tanks is addressed in the following sections with respect to the relevant aspects for this work. For the former, these include tank and embedded heat management system design. For the latter, thermodynamics and energy efficiency of the refueling process.

1.3.1 Hydrogen storage in metal hydrides: tank and heat exchanger design

Hydrogen storage in metal hydrides is particularly attractive for the reversible charge and discharge characteristics of the reactions and the large density per unit volume. This can be seen in figure 1.1 which gives an immediate overview of the state-of-the-art of storage technologies and the gap from the desired target. Solid-state hydrogen absorption is capable to provide volume densities that are larger than liquid systems, but at the expenses of low gravimetric densities (stored hydrogen mass per unit weight of storage system). In the present work advanced hydrogen-absorbing alloys, in the form of high-pressure metal hydrides, are investigated for their potential to reduce the gap between actual storage performance and gasoline targets. Metal hydride storage

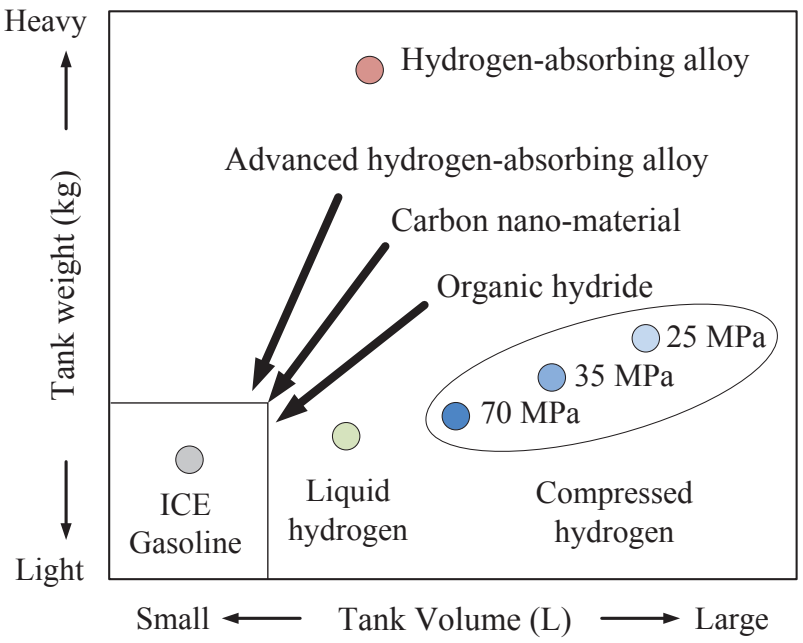

Figure 1.1: Engineering phase of current storage technologies and targets. Adapted from [15].

systems (MHSS) present two main physical components. These are the heat management system for alternative cooling/heating of the hydride bed and the pressure vessel, in which the absorbing alloy is contained. The rate at which the gas is absorbed can easily be controlled by simultaneously lowering the system's temperature and increasing the pressure, whereas the opposite is valid for the desorption process. Therefore, the heat management system is the key component in a MHSS and its design is crucial to effectively perform alternate cooling and heating of the hydride bed in order to achieve reaction times of practical interest.

The selection of the solid-bed shape is the first step in the vessel/heat-exchanger design process as discussed in Ref. [34]. Different on-board MH tanks have been manufactured in the past years, but the basic configurations fall into the following categories: planar and cylindrical solid beds. Traditional bed geometries for low pressure MHSSs correspond to those typically considered in various studies concerning MH reactors for applications other than hydrogen storage [35–40]. For vessels subjected to a significant internal pressure only shapes that allow a uniform distribution of the stresses can be considered and therefore, the planar solution is not taken into account in the current work.

Cylindrically shaped storage tanks have been widely studied and employed from automobile companies since the beginning of the 20th Century. This is also a well-known design for MH tanks as it enables high operating pressures and eases both the insertion in the vehicle and radial heat and mass transfers in the solid bed, promoting a uniform reaction pattern within the solid bed. Cylindrical vessels are divided in chamber and tubular configurations. The former has been investigated for a large variety of applications ranging from MHSSs to metal hydride heat pump (MHHP) and compressor systems, whereas the latter has mainly been mainly topic of study for hydrogen storage. The selection of the hydride bed geometry defines the actual heat transfer configuration and therefore, the approach to the management system design.

In chamber tanks, the hydrogen-absorbing alloy is hosted in a cylindrical container of considerable size and the heat exchanger module is conveniently integrated within the solid bed. Porous metallic filters in a symmetric arrangement are typically used to distribute the hydrogen gas evenly within the solid bed. This concept is shown in Fig. 1.2.
Different heat-transfer integrated units have been investigated in the literature, ranging from tube bundles [41–44] and spiral coils [45–48] to heat pipes [49–51]. The latter solution has the advantage of sparing the external pumps for the circulation of the heat transfer fluid .
Micro-channels have also been studied with the final aim to achieve relevant fueling

times in compact systems [52].

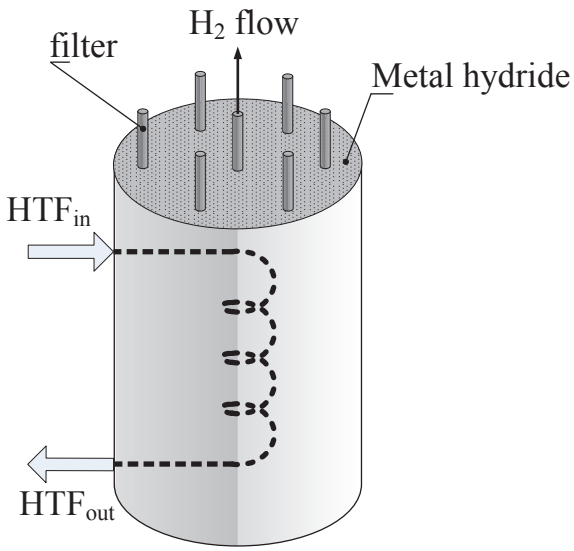

Figure 1.2: Chamber tank concept with integrated heat exchanger.

Mori et al. from Toyota [53] designed a high-pressure metal hydride storage system (HPMHSS) based on a Type III container, which is typically employed for hydrogen storage at 350 bar in CHG systems. The standard structure was modified to allow for the integration of the MH and the U-tube bundle, as the heat exchanger, in the tank. Tests were performed on 45 L vessels, with different hydrogen-absorbing alloys. A storage capacity of 80% of the saturation value was achieved in 5 min with $Ti_{1.1}CrMn$ (H_2 maximum capacity of 1.9% in mass base).
Garrison et al. [140] studied the effect of fin geometries on the storage performance of a $NaAlH_4$ tank. The comparison between transverse circular and longitudinal fins showed that the latter should be preferred as they ease the compaction of the MH and structurally support the tubes. Depending on the distribution of the cooling tubes, the use of fins can significantly improve the heat transfer within the solid bed. Similar conclusions have been drawn by Askri et al. [54].
Visaria et al. used the maximum MH thickness criterion (see Ref. [55]) to design a tank with an integrated U-tube and optimize the fin layout [56–58]. In a following study they compared this configuration with coiled-tube design [59, 60] with respect to the storage and heat-transfer performance [61]. Lower fueling times were achieved for the former solution, whereas the later improved the storage capacity.
Souahlia et al. [62] compared the performance between a finned centered tube over a finned coiled heat exchanger. The latter provided higher absorption rates at any time of the fueling process.
Mellouli et al. [63] developed a finned double-coiled tube with an external cooling

jacket. This layout reduced the cooling time (referring to 90wt% of the maximum hydrogen storage capacity) by 70% with respect to a bare single-coiled configuration. Wang et al. [64] presented a 3D computational model to investigate the performance of a $LaNi_5$ tank with embedded helical-coil cooling tube coupled with aluminum foam. They suggested a compromise between heat transfer enhancement and MH volume reduction due to the insertion of Al foam.
Kikkinides et al. investigated the effect of coupled annular rings and internal cylindrical tube for a $LaNi_5$ tank [65]. This layout provided a decrease by 60% in the refueling time with respect to 99% of the maximum hydrogen storage capacity. An extra reduction by 10% in the hydriding time was achieved by adding an external cooling jacket in Ref. [66].
At the end, it appears that for the chamber tank configuration, it is not possible to design a heat exchanger that provides sufficiently large heat transfer rates to realize a uniform pattern of reaction and at the same time occupies a volume that does not penalize much the storage capacity.

In tubular tanks the hydrogen-absorbing alloy is contained in the annular region comprised between the central artery and the vessel wall. A porous sintered filter is inserted in the center to radially distribute the hydrogen gas over the entire length of the hydride bed. The heat transfer fluid (HTF) is typically circulated externally and the heat is transferred through the wall thickness. This concept is shown in Fig. 1.3.

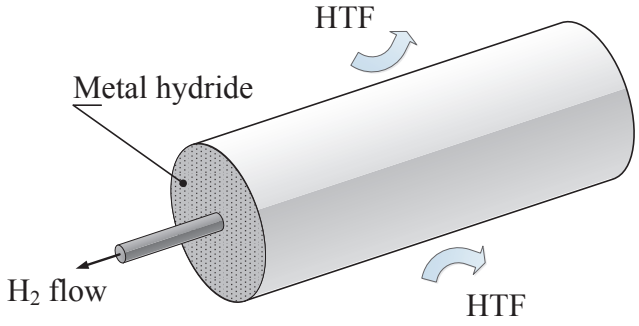

Figure 1.3: Single module for tubular-shaped metal hydride tanks. External cooling.

Depending on the bed diameter, the integration of a heat exchanger can also be realized. However, this solution generally presents lower storage and thermal performance and has been less investigated [67].
The main advantage tubular designs is the possibility to achieve a desired MH capacity by arranging the modules in a tube bundle. In Ref. [68] Johnson et al. tested a full-scale multi-tubular tank with $NaAlH_4$ and demonstrated that this solution can be succesfully designed to follow the automotive demand cycles. Historically, the first

data available refers to the studies carried out in the late 1970s and early 1980s by Billings Corp. and Daimler-Benz AG. In Ref. [69] tests on a hybrid gasoline/hydrogen vehicle were performed with respect of a multi-tubular MHSS that coupled low and high temperature hydrides, namely TiFe and $MgNi_2$ respectively. That work proved the potential of the technology and laid the foundations for future studies on MHSS for vehicular applications. In more recent years, the research on MHHS has mainly focused on the tube arrangement optimization to maximize the stored hydrogen mass and enhance the reaction kinetics by realizing effective heat transfer [70–75].
Krokos et al. [71] employed a 3-D Cartesian model to explore the effect of several uniform MH ($LaNi_5$) tube arrangements and different fluid velocities on the hydriding reaction. The tank was designed to allow 25 km driving range for a FCHV based on Honda's FCX Clarity. Main outcomes are that at constant MH total content, solutions with a large number of small MH tubes are always preferable. This is due to a higher external surface/volume ratio, which enhances the heat transfer as the more tubes are added to the system and to the shorter heat transfer path through the solid bed.
Bhouri et al. [74] drew similar conclusions after developing the concept presented in [34] as a finned three-module $NaAlH_4$ tubular tank.
Raju and Kumar [143] studied another multi-tubular MHSS, where the hydrogen absorbing alloy is hosted in 81 bare tubes in a 9x9 rectangular arrangement with three equally spaced baffles for mechanical support and HTF guidance. They pinpointed that larger tube numbers and smaller clearances provide an enhanced absorption rate, at the expense of a greater pressure drop.
Lozano et al. [47] carried out a total system weight minimization for a tubular tank of specified volume with $NaAlH_4$. Results showed that hydride compaction is the factor that affects hydrogen capacity the most, and that an extended research on light MHs is needed to meet the DOE targets on the gravimetric density.
Veerraju et al. have investigated MH tubes with elliptical cross sections. This solution resulted in a more compact system with reduced pressure losses and non-uniform hydrogen absorption within the solid bed [76, 77].
Finally, car manufacturers as Toyota, have recently investigated multi-tubular tanks with high-pressure metal hydrides to enhance the kinetics and storage performance. In Ref. [78] Komiya et al. moved from a previously adopted chamber layout [53] to a multi-tubular configuration. The hydrogen-absorbing alloy ($Ti_{1.1}CrMn$) was inserted in a tube bundle of 10 to 40 finned aluminum cylinders that were filled with hydrogen at 100-200 bar during tests. This design was capable to reduce the tank weight (from 225 kg to 207 kg) and external volume (from 95 to 83 L) while maintaining similar performance (filling time of 5 min and storage capacity of 4.2-5 kg).

For a more comprehensive literature review on this argument the reader should refer to the manuscript by Mazzucco et al. [79].

1.3.2 Hydrogen storage in compressed tanks: heat transfer and fueling analyses

Compressed hydrogen gas systems consist in the most widely adopted option for the first engineering phase of FCEVs. In this regard, an important step was taken in the 90's when strategic alliances were born within the automotive industry to push forward the research on practical on-board storage solutions [80].

Research concerning on-board CHG systems is mainly limited to analyses on the vessel's mechanical strength and life time [81–84], as well as on the thermodynamics [81, 85–87] and heat transfer of the fueling process [88–92].

Dicken et al. [93] measured a maximum temperature difference of 6 °C in a Type III tank during fueling at 350 bar by inserting 63 thermocouples in a distributed pattern. The major role in the heat development was found to be due to the gas compression rather than the Joule-Thompson effect.
Kim et al. [94] identified in the buoyancy effect the main reason for this non-uniform vertical temperature distribution.
Zhao et al. [87, 95] investigated the temperature increase during charging via validated numerical simulations and provided an empirical formula to estimate the peak temperature that was observed at the opposite end of the hydrogen inlet. The maximum temperature increase during refueling depends exponentially upon mass fueling rate, whereas is inversely proportional to the initial tank pressure. The effect of the ambient temperature was found to be modest.
Woodfield and Monde extensively investigated CHG storage systems through both experimental and computational analyses. They provided and validated analytical and numerical models to calculate the thermodynamics and heat transfer through the walls of type III and IV tanks [89, 91, 96, 97]. The averaged local convection heat transfer coefficient was found to vary locally between 150-500 $W \cdot m^{-2} \cdot K^{-1}$ during hydrogen charging depending upon the nozzle type (e.g. advanced or straight design) [90, 92]. The experimental data was used to develop a heat transfer correlation for turbulent flow that was expanded in further studies to account for the laminar refueling case [98]. The latter was characterized by combined natural and forced convection and resulted in a deeper temperature stratification along the vertical axis with consequently higher peak temperatures. For discharging the Daney's equation was proven to be valid for a wide range of several Rayleigh numbers [92].

A less explored field of research considered energy optimization analyses of the refueling process.
Hosseini et al. [99] employed exergy analyses method to determine the efficiency of

CHG storage systems. They demonstrated that higher initial pressures inside the tank increase the exergy efficiency of the fueling process, but also result in lower dispensed mass flow rates. At the end, no practical strategies were suggested for improving the efficiency of the fueling process.
Ozsaban et al. [86] performed a parametric study on exergy analyses for a multi-stage CHG storage system. Results showed the enhancement in the exergy efficiency when multi-stage compression and storage systems are used in place of single-stage solutions. Other outcomes were very similar to those presented in Ref. [99].
Rothuizen et al. developed a component modeling library for hydrogen refueling stations and extensively investigated the optimization of cascade refueling through energy and exergy analyses. They implemented the SAE fueling protocol [100, 101] to model the refueling process, as it was first done by Maus et al. [102]. Cascade refueling systems can reduce the the time required to complete a whole storage cycle at the refueling station by 5% and the compression and cooling demands by 17% and 12% respectively [103]. In further studies they provided details on strategies to maximize the energy efficiency of the refueling process. The pressure losses of each specific refueling station considerably influence the optimal pressures and volumes in the cascade system. [104].

Finally, industrial research has recently mainly focused on the cost and size reduction of standard Type IV tanks.
In Ref. [105] Yamashita et al. proposed a novel tank design to minimize weight and size of the vessel. Cheaper composite carbon fiber reinforced polymer (CFRP) was used to lower the cost of the storage system. This technology was integrated in the Toyota Mirai FCEV (see Fig. 1.4), that was openly commercialized in California in October 2015.

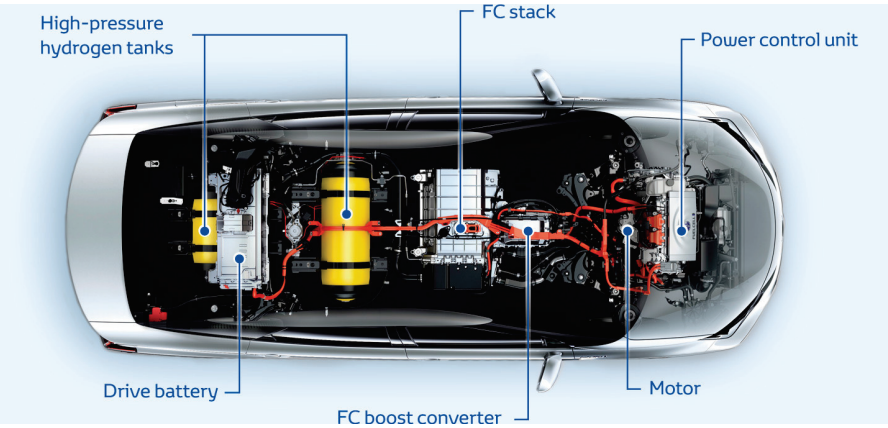

Figure 1.4: View of the high-pressure tanks. Toyota Mirai [106].

1.4 Statement

The overall objective of this work is to develop a modeling platform in order to provide a tool with which explore on-board H_2 storage solutions that have the potential to improve the state-of-the-art technology for immediate commercialisation purposes rather than modeling a storage system that can reach the DOE targets [107]. The impossibility of a MHSS to fulfill the DOE requirements was proven in Ref. [27] for any material currently available. However, the recent commercialisation of FCEVs has made clear that it is not necessary to achieve all the DOE targets to provide a product that is attractive in the eyes of the public. In this regard, it is here assumed that any relevant advancements in the present storage technology would ease the market penetration of FCEVs in this first phase of commercialisation. The fields of improvement that are here considered concern aspects that range from storage capacity to refueling time and energy efficiency.

More precisely, the research aims to:

- Describe the physical behavior of the selected storage systems with respect to thermodynamics, heat transfer, flow dynamics and chemical kinetics. The computational model that describes the reactions in the solid bed should be capable to integrate experimental data in real-time to account for the effect of the instantaneous hydrogen content on the metal hydride thermal properties.
- Evaluate the performance of the storage system in terms of refueling time, gravimetric and volumetric densities.
- Determine criteria and design strategies to solve present technology's bottlenecks.
- Investigate the effect of passive cooling via thermal phase transitions in compartments located within the tank and provide guidelines for further improvements.
- Develop a modeling platform for solid-state and gaseous H_2 storage systems for on-board applications. This platform must be user friendly, flexible and easily extendable. In particular, it should be possible to select different H_2-absorbing alloys and heat exchanger configurations from an integrated library. The heat exchangers must respect the design strategies previously identified.

1.5 Outline

The thesis contains seven chapters and four appendixes:

Chapter 1 explains the background and motivation of this study and contains the literature review, thesis statement and outline.

Chapter 2 presents the methodology and approach to the present research and sets the performance targets as well as the design requirements for the relevant on-board storage systems.

Chapter 3 investigates the physical phenomena that occur within the solid bed during fueling via the results obtained with the developed numerical model. It presents the criterion for the effective design of the tank system in respect of the set targets for storage capacity and refueling time. The effect of the refueling conditions and material properties on the design parameters is also discussed.

Chapter 4 contains the selection analysis for the heat exchanger system to be integrated in the metal hydride bed and identifies the design configuration that provides the greatest cooling performance.

Chapter 5 focuses on the proposed novel design for the CHG storage system with an integrated phase change material and outlines the practical advantages with respect to the state-of-the-art technology. Charging analyses are performed to evaluate the system's behavior under practical operating conditions. A parametric study is performed to determine the areas of improvements.

Chapter 6 describes the general layout and the details of the developed HySDeP (Hydrogen Storage Design Platform) that comprises both the MH and CHG storage tanks. Charging and discharging analyses for the tank/heat-exchanger system are presented with attention to their limitations and benefits.

Chapter 7 pinpoints the main outcomes presented in this work along with the strategies to follow for further improvements within the field.

Appendix A. Numerical model for hydrogen absorption/desorption in metal hydrides and its validation.

Appendix B. Heat exchanger design: thermal models.

Appendix C. Computational model for heat transfer in phase-change-material tanks.

Appendix D. User library implemented in the developed modeling platform.

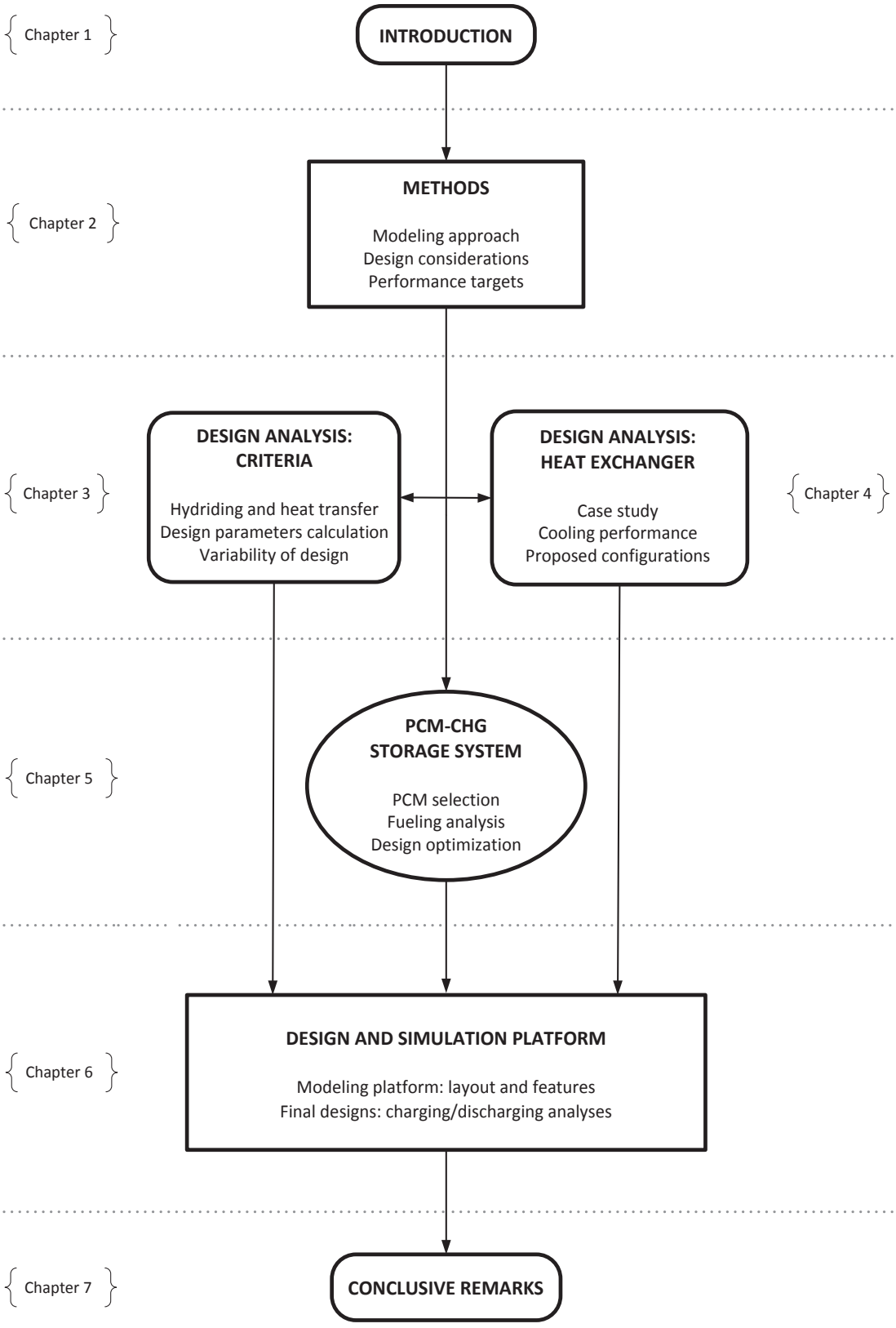
Chapter 1
INTRODUCTION
Chapter 2
METHODS
Modeling approach
Design considerations
Performance targets
Chapter 3
DESIGN ANALYSIS:
CRITERIA
Hydriding and heat transfer
Design parameters calculation
Variability of design
DESIGN ANALYSIS:
HEAT EXCHANGER
Case study
Cooling performance
Proposed configurations
Chapter 4
Chapter 5
PCM-CHG
STORAGE SYSTEM
PCM selection
Fueling analysis
Design optimization
Chapter 6
DESIGN AND SIMULATION PLATFORM
Modeling platform: layout and features
Final designs: charging/discharging analyses
Chapter 7
CONCLUSIVE REMARKS

2 Methods

2.1 Approach

This work deals with the development of a computational platform to design and simulate on-board hydrogen storage systems. These are limited to: metal hydride tanks and compressed hydrogen gas vessels. The present study is exclusively numeric and does not include any experimental work. However, it is based on real data measurements and the numerical models that describe the physics of hydrogen charging and discharging are verified with the data available in the literature.

The design of the two storage systems aims to achieve some set targets that belong to two different areas of performance.
For the metal hydride tank is of interest to build a storage system that can realize the targets in terms of storage performance. These encompass aspects that are limited to: hydrogen capacity, refueling time, compactness and weight.
For the CHG storage system, it is more meaningful to focus on the energy performance of the refueling process as, due to to the nature of the storage mechanism, the only practical way to increase the storage efficiency is compressing the gas to greater pressures. The economic and fueling-reliability aspects that derive from an increased energy performance are also taken into account. However, a detailed discussion on such aspects is not possible because of the lack of relevant information available for real systems.

This thesis is intended to be a compact and exhaustive summary of the work carried out during the development of the present Ph.D. project. Therefore, only the employed research procedure and main obtained findings are here discussed extensively, whereas for details on the auxiliary topics involved in the analyses the Reader is referred to the relevant cited literature.

2.2 Modeling tools

The analyses are carried out by means of two commercial software: Dymola™ and Matlab®.

Dymola™ is a front-end user-interface to Modelica®, which is a unified equation-based object-oriented language for physical system modeling [108]. The language is based upon true ordinary algebraic and differential equations that are solved on the basis of a non-predefined causality approach (i.e. *acasual* relation). It can be conveniently employed to simulate the dynamics of industrial multi-domain systems as it maintains the physical structure of the real problem and enables graphical editing. The component models can thus be represented graphically and used to build complex system models. The hierarchical structure and inheritance constructs ease the reuse of modeling knowledge which makes this language particularly helpful to build robust exchangeable component libraries.
It is therefore selected as the main modeling tool and employed to design on-board storage tank models that can be integrated in the compatible refueling station system library presented in Ref. [109]. Details of the modeling procedure and features are given in Ref. [110].

MATLAB® is a well-developed multi-paradigm numerical modeling environment and a high-level programming language in which the equations are solved on the basis of a pre-defined causality relation [111]. It enables graphical editing via the Simulink® interface. The modeling approach is not topological [112], as it occurs in Dymola™, but represents generic data-flow that make it a suitable tool for modeling dynamic controls. While other programming languages mostly work with numbers one at a time, MATLAB® is designed to operate primarily on whole matrices and arrays. All its variables, including strings, are defined in the form of multidimensional arrays. It is mainly intended for numerical computation of steady-state systems and it is therefore used in the present work to analyze the thermo-hydraulic performance of different heat exchangers to select the most appropriate configuration for the present application. In addition, it can be easily coupled with external algorithms and other commercial software, makes available several plotting tools, mathematical functions as well as optimization routines as built-in features.

The specific features of these software with respect to the analyses conducted here are discussed in the relevant sections of this thesis.

2.3 Methodology

The methodology applied in this work follows these steps:

1. Define the requirements for the materials that are employed in the storage system. This phase consists in determining the relevant conditions that should be satisfied by the H_2-absorbing alloy and the phase change material in order to be effectively employed in the MH tank and CHG system respectively.

2. Determine the hydrogen and heat-transfer-fluid supply strategies.

3. Set the requirements and targets for the two technologies under analysis. The targets must represent performance enhancements for the state-of-the-art technologies. The compliance with the requirements is here intended as a broad concept that includes manufacturers guidelines to ease the industrial production, mechanical constraints that must be respected to build a practical system and the compliance with the available refueling standards.

4. Determine relevant design criteria to realize a tank that achieves the targets and meets the requirements.

5. Develop numerical models that describe the phenomena that occur inside the tanks during charging and discharging and that can be employed to calculate the relevant design parameters identified in step 4.

6. Build a thermal model to evaluate relevant heat exchanger configurations for the MH tank and select the most appropriate layout according to cooling performance and mechanical considerations.

7. Integrate the models in a structured modeling platform where it is possible to simulate different layouts by selecting the main geometric parameters, materials, heat exchanger configurations, media and modeling approaches via an user-friendly interface. Such platform should be designed to be easily extendable in the future and combined with the relevant existing libraries.

8. Simulate the proposed technologies and perform parametric studies to optimize the performance of the two tank technologies during hydrogen charging and discharging and propose strategies for further improvements.

Points 1 to 4 are discussed in Sections 2.4-2.7, whereas the further steps are examined in detail in the pertinent chapters of the thesis.

2.4 Material selection criteria

This section presents the selection criteria for the H_2-absorbing alloy and the phase change material.

2.4.1 Materials for hydrogen storage

In principle the ideal candidates to be employed as H_2-absorbing alloy should possess the following characteristics [113]:

i fast absorption and desorption kinetics (i.e. provide adequate mass flow rates to realize relevant fueling times and proper operation of the fuel cell during driving).

ii Capacity of releasing hydrogen at temperatures of practical interest (i.e. between 50-100°C) for an improved thermal match with the off-gases from the fuel cell.

iii Cold start capability.

iv Stable hydriding/dehydriding performance over repeated hydrogen charging/discharging cycles.

v Small enthalpy of formation. This would result in a small heat generation per unit mass during hydriding and low heating demand to desorb hydrogen.

vi No health, flammability and physical hazards. This includes spontaneous ignition in contact with air or any oxydizers (i.e. pyrophoric nature).

vii Non aggressive toward the tank's construction materials.

viii Reduced expansion during hydriding to reduce mechanical stresses.

ix Ability to absorb hydrogen at ambient temperature and pressures.

x Large thermal conductivity.

xi High storage capacity.

xii Low density.

xiii Low cost.

At present, no material can satisfy all the desirable requirements and therefore, in this work, the fulfillment of requisites i-iv is chosen as the selection criterion for suitable candidates.

2.4.2 Phase change materials in CHG storage systems

In this study, we are primarily interested in selecting phase change materials whose properties are suitable for absorbing the compression heat that occurs inside the tank during hydrogen fueling in light-duty vehicles. The desired PCM's characteristics for such an application include [114]:

i Low cost.

ii High latent heat.

iii No health, flammability and physical hazards.

iv Large thermal conductivity for both liquid and solid phase.

v Chemical stability and congruent phase change within the material.

vi Non-reactivity with the tank materials (e.g. corrosion) and with the air/H_2 mixture.

vii Phase change must occur in the practical range of operation. This results in the melting temperature range between 50-65°C to avoid spontaneous melting in hot climates in absence of hydrogen refueling.

viii Low density (in order to limit the the extra weight added to the storage system) and large specific heat capacity.

An essential aspect that is worth taking in consideration concerns point viii in the list above. The PCM density directly affects the thermal capacity and the extra weight inserted in the tank. A compromise exists between the desire to operate with very dense materials that can store large quantities of heat and at the same time limit the extra mass added to the storage system. The use of a low density material with large specific heat capacity seems to provide an apparently simple solution to this challenge. This aspect is typically of secondary importance for applications where there exist less stringent requirements on the system weight, as for stationary storage, whereas it is critical for on-board storage systems in light duty vehicles. Therefore, in Chapter 5 a parametric analysis is carried out to assess the effect of the PCM density and specific heat capacity on the storage performance of the CHG vessel.

A small review on phase change materials reveals that although it is difficult to identify a single material that possesses all the desired characteristics, some material categories are more attractive than others for the application of interest.

Hydrated salts seem to be promising candidates for absorbing the compression heat in H_2 vessels because of the large thermal capacities and relatively high thermal conductivities (0.5 $W \cdot m^{-1} \cdot K^{-1}$). They are also generally cheaper when compared to paraffin waxes. However, the negative aspects concerning phase segregation and sub-cooling make these materials not suitable for applications where the PCM must undergo multiple phase-change cycles in a closed volume, as in the system of present interest.. The addition of thickening and nucleating agents as well as the extra water principle are under investigation as possible solutions for these issues [115]. Unfortunately, all these options have the drawback of reducing the conductivity and/or the energy storage density of the compound [116]. In addition, their corrosive nature with metals poses major challenges of compatibility with the tank materials and adequate containment measures as encapsulation are needed to prevent direct contact with the vessel components.
Several studies that aimed at characterizing the thermal properties of fatty acids have reported that these materials generally show low thermal conductivities and modest latent heats, despite the wide range of melting temperatures [117–121]. Their poor thermal properties have prevented their use in commercial systems and limited their applications to property measurements in laboratories.
Among all the PCMs, paraffin waxes appear to be the most attractive materials to be used in hydrogen storage tanks because of their suitable melting temperatures and moderately high latent heats. They are also stable, chemically inert, non-toxic and they experience congruent phase of change. However, pure paraffin waxes are very expensive and it is only advisable to use commercial grade paraffins, which are mixtures of different hydrocarbons obtained from petroleum distillation. It follows that as they are not pure substances, it is more appropriate to refer to a melting temperature range rather than a single melting point to describe the phase change process. The major drawback of these materials is their poor thermal conductivities (approximately 0.2 $W \cdot m^{-1} \cdot K^{-1}$), which limit their applications. Different technologies including the addition of metallic fillers, finned tubes, metal and graphite matrix-structures have been investigated with the final aim of augmenting the effective thermal conductivity [122]. The latter solution was proven to be very promising providing an increase in the effective thermal conductivity from 0.24 $W \cdot m^{-1} \cdot K^{-1}$ up to 4-70 $W \cdot m^{-1} \cdot K^{-1}$ for a high porous graphite matrix with 95wt% of paraffin [123].

At the end, for what above discussed, a paraffin wax is here selected as the most promising candidate to be employed in the simulations.

2.5 Tank fueling

All the refueling strategies considered in the literature and in practice stem from two different approaches. The standard fueling procedure considers a stationary station that provides hydrogen to the vehicle similarly to what occurs nowadays for gasoline cars. The alternative approach consists in fueling the vehicle by replacing entirely or partly (for multi-tubular configurations) the storage system with a full tank element. The latter is a less explored concept that has been recently proposed in the literature [124] and that provides the main benefits of very fast refuelings (in the magnitude of tens of seconds for well automated systems), maximum charging capacity, recovery of the absorption-reaction heat at the fueling station. The challenges include the development of a well automated vehicle/filling-station interface and a profound standardization of the vessel system among car manufacturers, as discussed in Ref. [79]. The concept is shown in Fig. 2.1.

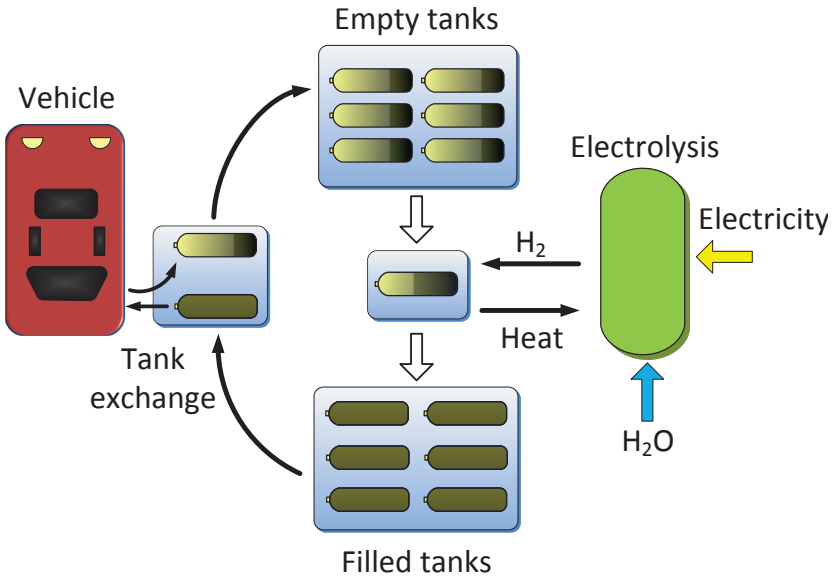

Figure 2.1: Off-board charging of tank modules. Adapted from Ref. [124].

In this study, the off-board charging procedure is not taken into account and the analysis is based on the standard fueling approach, whose strategies for the heat transfer fluid supply are discussed below.

2.5.1 Heat transfer fluid supply strategy

In a MH storage system, the heat transfer takes place between a heat transfer fluid in liquid or gaseous form and a solid medium, i.e. the metal hydride. Heating and

cooling can be performed by either using the same fluid in alternate operation, or by employing two different fluids and heat management systems. More compact designs can be realized when liquid HTFs are preferred over gaseous media, as liquid cooled/heated tanks show greater reaction rates per unit size during both hydrogen absorption/desorption [125]. For this reason, research has mostly focused on liquid cooling/heating of vehicular MHSSs and less attention has been given to gaseous media in forced convection [76, 77, 126–131]. As in this work, we are interested in exploring MHSS solutions that can compete with the current technology in terms of storage performance and thus, only the use of liquid media is considered. The heating operation of the solid bed is only required for hydrogen desorption purposes and hence occurs during driving. This means that the heating medium cannot be provided by an external facility and must be available in the vehicle at any time during operation. On the contrary, the cooling mode is performed during tank charging, when there exists a physical connection between the refueling station and the vehicle. The coolant can therefore be provided directly from the fueling facility, rather than being stored on-board and circulated in a closed loop (as it is done in a gasoline car to cool the engine). In the later case, a single heat management system switches to alternatively perform cooling and heating. The heat absorbed from the tank is dissipated to the ambient in a radiator system with an integrated fan, see Fig. 2.2.

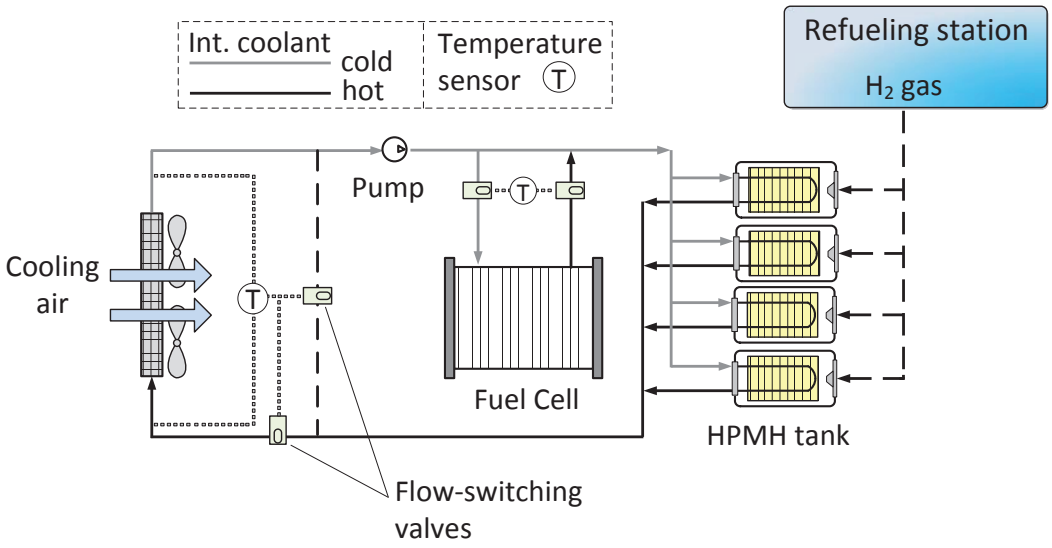

Figure 2.2: Concept of on-board coolant supply. Adapted from Ref. [15]

Volume and weigh savings can be achieved when the coolant is provided from an external facility as the components that are required to dissipate the heat of reaction can be located at the refueling station. Additional advantages are the ease of the standardization of the cooling conditions at the tank inlet (i.e. by controlling mass flow

rate and temperature) and the possibility to recover the heat of reaction for processes that take place at the refueling facility. For these reasons, the external supply strategy is adopted in this work. Its concept is presented in Fig. 2.3.

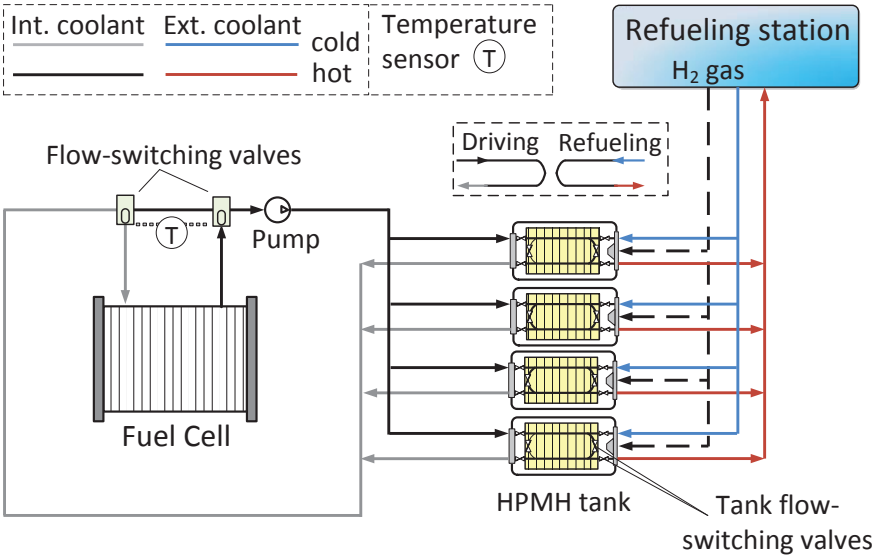

Figure 2.3: Concept of off-board coolant supply.

The heat management system embedded in the solid bed is operated with the external coolant (e.g. water or car antifreeze liquid) during hydrogen charging and then switches to the heating function in driving mode.

2.6 Design requirements and targets

This section presents the design considerations and performance targets considered in the development of this work to compare the results of the modeling platform.

2.6.1 Design requirements and targets for the MH storage tank

For all on-board storage systems, essential aspects involve compactness and weight. These are especially important for light-duty applications, that stand apart from heavy-duty vehicles for their stringent requirements on reduced volumes and masses. Under these constraints, the design of an adequate vehicular MHSS is particularly challenging because of the low gravimetric density and the required integration of a heat management system which increases the inactive volume in the tank that is not dedicated to hydrogen storage. Therefore, most research has focused on volume or weight minimization of the tank system and often overlooked other essential aspects

of the design process. A complete list of design requirements includes a variety of aspects ranging from mechanical constraints and safety concerns to economic considerations and the ease of manufacture. For the latter, it is worth considering the car manufacturers practical guidelines [57]:

- Aluminum construction.
- 2D shape that enables cost-effective fabrications methods (e.g. extrusion).
- Well-known simple designs should be preferred (e.g single coolant U-tube).

Other than these design recommendations, the practical requirements are:

- The mechanical constraints must be respected at any moment of the design process for all the components. This ensures that the designed system can be effectively and continuously operated with limited practical issues (e.g. mechanical resistance, proper fluid circulation).
- Cylindrical design for the MH container. This enables the use of high-pressure materials and eases the tank insertion in the vehicle.
- System design that ensures a uniform distribution of hydrogen during refueling and a uniform pattern of absorption.
- Appropriate operational parameters (e.g. maximum fluid velocities to avoid corrosion of the components).
- Reasonable pressure drops for the heat exchanger.
- Reduced overall weight.

Safety and cost-reduction analyses and a reliable evaluation of these issues are out of the scope of the present thesis. However, the design process has been carried also by taking into account these aspects. As discussed in Section 1.4, in this study we consider performance objectives that represent an improvement of the present state-of-the-art hydrogen storage technology [105, 132] for immediate market penetration, rather than focusing on the achievement of the DOE targets [107]. In this perspective, the performance goals for the MHSS are:

- Storage of at least 5 kg of hydrogen in 126 L (inner tank volume).

- Fast charging of maximum 3 min.

No targets are set with respect to the system's mass as, in absence of proper light hydrogen-absorbing alloys, MHSSs cannot compete with the reduced weight of CHG systems. However, as shown in the list of requirements, the system is designed with attention to weigh minimization.

2.6.2 Design requirements and targets for the CHG storage tank

In principle, similar requirements to those identified for the MHSS must be respected by the CHG tank. The present layout of commercialized hydrogen vessels is the result of an extensive industrial research that has coped with safety, economic and mechanical concerns. Therefore, as the analyses consider models of real storage vessels, it is here assumed that the practical requirements for the CHG tank are automatically satisfied and only the design considerations that concern the integration of the PCM need to be addressed. The latter consist in:

- Convenient confinement of the phase change material to prevent any displacements that might occur during phase change.
- Reduced volume of the PCM element.
- Limited weight addition to the tank due to the PCM insertion.

For the PCM-CHG system the performance targets, here considered, refer to the efficiency of the fueling process, as discussed in Section 1.4.

- Absorb a significant portion of the heat of compression that develops inside the tank during charging to maintain the wall temperature below 85°C. Realize at least the same stored mass and as the state-of-the-art technology
- Realize hydrogen fueling at higher temperatures than what is done in practice while achieving at least the same storage performance in terms of stored mass and refueling time. Ideally, the system should be designed to realize hydrogen charging at ambient conditions.

The above targets can be directly be translated in efficiency and economic benefits after noticing that in actual systems the gas is cooled to -40°C prior to tank filling. The possibility of passively absorbing large amounts of heat inside the tank can, in principle, reduce the cooling demand at the refueling station, as well as the size and cost of the heat transfer component.

2.7 Design criteria for the on-board storage system

2.7.1 Design criteria for the MH storage tank

For most metal hydrides, the reaction rates of hydrogen absorption and desorption are typically of comparable magnitude in terms of energy demand. It is therefore assumed that a design that can satisfy the cooling demand during hydriding can as well satisfy the heating demand during dehydriding. For this reason, the design of the tank/heat-exchanger is based upon the critical MH thickness concept (i.e. δ) presented in Ref. [55] for the hydriding process and shown in Fig. 2.4.

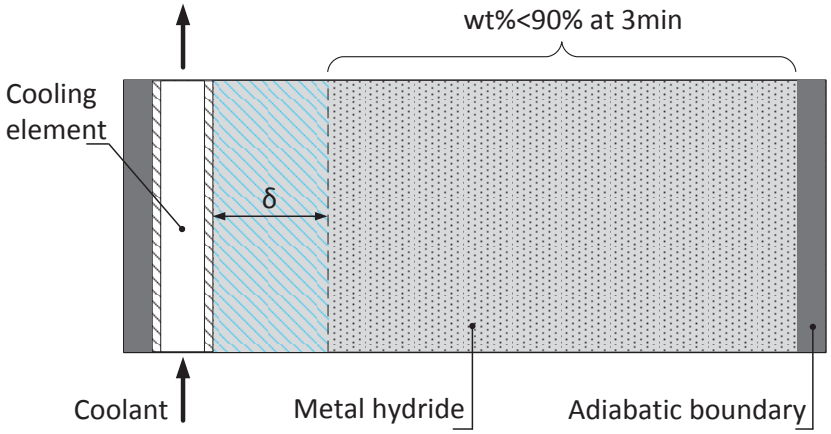

Figure 2.4: Critical metal hydride thickness principle.

It is defined as the maximum distance from the cooling surface at which the reaction is completed below the desired filling time. The fulfillment of such criterion ensures that a uniform pattern of absorption is achieved within the solid bed and that the entire hydride mass completes the absorption process within the target fueling time. In this study, a complete absorption is considered to be achieved at 90% of the MH saturation value under a refueling time of 3 min. The value of δ depends on the cooling rate and therefore, on the actual thermal resistances involved in the heat transfer process within the solid bed.
Details of the procedure used to design tank/heat-exchanger systems are provided in Chapter 3. In the same chapter the effect on the design of cooling conditions other than the design point are taken into account by studying the variation of the maximum MH thickness with respect to coolant mass flow rate and temperature. The effect of packing density and material thermal properties that vary with the hydrogen content and pressure will also be addressed.

2.7.2 Design criteria for the CHG storage tank

The design of the CHG system is carried out in respect of the actual dimensions of standard high-pressure hydrogen vessels. The thickness of the tank walls, subjected to the internal pressure, is obtained from experimental data. Therefore, this work considers the modeling of practical CHG systems as the starting point for modification.
In the novel tank design a layer of phase change material is inserted at the hydrogen/wall interface to absorb the heat of compression that develops during fueling.
A sensitivity study involving the main geometric parameters and material properties is used to improve the thermal performance while minimizing the extra volume and weight added to the standard CHG system.
Details of the novel tank design are given in Chapter 5.

3 Dynamic analysis toward the heat exchanger design

3.1 Introduction

An essential requisite for any practical metal hydride storage tanks is the accomplishment of a complete charging in a short time. As mentioned in Section 2.7.1 the fueling is considered to be complete when the material absorbs a hydrogen quantity equal to 90% of its saturation value (wt_{max}). This particular value is chosen because of the hydriding characteristics of the selected hydride. In the first part of the reaction the thermal resistance plays a key role in preventing high absorption rates, whereas when the process approaches the saturation value the hydriding is dominated by the molecular-diffusion resistance. For most hydrides, this turning point occurs at around 80%-90% of wt_{max} [78] and the reaction tends to the saturation value asymptotically. As a result, very large times are requested to complete the last portion of the process. This means that for the application we are considering, the cooling function is completed before the achievement of the equilibrium conditions.

The design of the heat management system needs to take into account this aspect in order to perform effectively. This leads to a significant difference in the design approach of the heat exchanger when compared to other heat transfer applications: the system must be designed to be operated in transitory and not in steady-state conditions. Therefore, it is not possible to identify an actual *design point* in the typical meaning of the term. In this context, the design analysis is based on the dynamic behavior of the storage system.

Sections 3.2 to 3.4 refer to a review of the main issues that are encountered, while Section 3.5 presents the methodology. The results are discusses in Section 3.8.

As mentioned in the first chapter of this thesis, the results here reported refer to high-pressure metal hydrides, but they are readily extendable to any other metal hydride

system with caution, with a focus on the differences in pressure conditions. The main operational difference is the high pressures that the MH container need to bear.

3.2 Heat transfer issues

Absorption in metal hydrides is an exothermic process which causes the solid bed temperature to rise. The increase in temperature reduces the hydriding rate and might lead to a thermally-limited reaction, in which the full potential of absorption is not used. On the other hand, desorption is an endothermic process that requires heat (and lowering the internal pressure) to take place. The thermal management system integrated in the tank should thus realize two different functions: cooling during hydriding and heating during dehydriding. Besides the technical challenge of designing a heat exchanger for such a twofold objective, different heat transfer issues can be identified. Their understanding is essential to properly model the thermodynamics and kinetics of the reaction toward the effective design of the heat exchanger. In the literature several studies have focused on the different aspects of this topic [21, 133, 134] and a comprehensive review of such argument is out of the scope of the present study. However, the main aspects that are related to the present design effort are here reported to provide the Reader the necessary tools to fully comprehend the challenge that is intended to be tackled.

The total heat transfer resistance from the bed to the heat transfer fluid can be typically divided into three parts in series (when the radiation term is neglected): conduction in the solid bed and in the tube wall, and convection in the heat transfer fluid. The two latter are typically smaller by some orders of magnitude than the conduction in the hydrogen-absorbing alloy. This is valid especially for the resistance of the tube wall, which is often neglected in calculations [126]. When small hydrogen velocities and low temperatures occur in the packed bed, the heat transfer is dominated by thermal conduction, as in this case, both radiative and convective contributions can be ignored [135–137]. An additional thermal resistance occurs at the interface between the tube wall and the hydride as the irregular shape of the solid particles reduces the contact surface available for heat transfer.
In order to improve the heat transfer in the bed, three possibilities can be identified with respect to Fourier's law of conduction: introducing a large temperature difference, reducing the metal hydride thickness or enhancing the lowest thermal conductivity. The first option consists in reducing the coolant temperature, which is easily achievable when an external HTF-supply strategy is adopted (see for example Refs. [55, 138]). The second has found large attention by a number of computational studies that showed the validity of numerical simulations that combine reaction kinetics, heat

transfer and thermodynamics to estimate the optimal bed size and configuration (e.g. Refs. [37, 139–143]). Finally, the third option results in enhancing the effective thermal conductivity of the hydride bed (k_{MH}), which is typically in the neighborhood of 1 $W \cdot m^{-1} \cdot K^{-1}$ [144, 145].
To enhance the effective thermal properties of the H_2-absorbing alloy, two methods can be applied: inserting solid matrices or creating MH compacts. The former comprises transversal or longitudinal fins [41, 146, 147] or more complex configurations including wire-matrixes [148], multi-waved sheets [149] or corrugated helical bands [150]. The insertion of metallic or carbon-fiber foams is another well-studied technique [151–154]. Such foams are characterized by a large surface in reduced volumes, low density (porosity above 90–95%), and favorable thermal properties. Carbon-fiber was suggested to be used in foams as a substitute for common materials as aluminum and copper [155]. They were found to provide less parasitic mass and still adequate heat transfer enhancement [133]. The effect of aluminum foam's amount in the MH bed on hydrogen storage efficiency was investigated via parametric study in Ref. [64]. It was shown that coupling forced convection with aluminum foam (10% of bed volume) maximizes hydrogen storage for $LaNi_5$, with a filling time of around 3 min which is a charging time of interest for vehicle application.
For a more comprehensive list of solid matrixes, the Reader is referred to the work presented in Ref. [156].
The method of enhancing the heat transfer in the solid bed by compacting it with a highly conductive material consists in firstly mixing the H_2-absorbing alloy with a binder material, as Al, Sn or with natural expanded graphite and then compacting the obtained mixture by cold-pressing or sintering [157–160]. In some cases, a thin film of copper clads the hydride particles before mixing [133]. Good structure stability of metal hydride compacts was observed over thousands of hydriding/dehydriding cycles in Refs. [64, 161] and allows achieving a considerable enhancement of the heat exchange performance. At the end, it should be considered that the use of solid matrixes or additives is a compromise between lowering the charging time and decreasing the amount of MH in the vessel, which results in a smaller hydrogen storage capacity.

Other heat transfer issues that negatively affect heat transfer performance between the solid bed and the HTF consists in heat losses by sensible heating (i.e. parasitic masses in the tank components) and through the tank wall to the environment. However, their influence is mainly limited to the heating process that is requested during dehydriding and are often of small importance.

3.3 Effect of pressure and hydrogen concentration on the effective thermal properties

A major challenge is to predict the variation of the main MH thermal properties, i.e. conductivity and specific heat capacity, during hydriding in order to build accurate computational models. Research efforts have mostly focused on the first parameter as the main thermal property that influences the heat transfer and the reaction rates. The effective thermal conductivity depends on parameters such as packing density, bed porosity and particle size, whose variation with hydrogen charging pressure and absorption concentration is challenging to measure.
Many authors observed that similarly to what happens in conventional packed beds, k_{MH} is positively influenced by increasing pressures until its value flattens for large pressure values [134, 162–166]. However, for many alloys the influence of pressure on k_MH is significant in the plateau region of hydrogen absorption and desorption. It is thus not possible to decouple the influence of pressure from the effect of concentration in practical MHSSs. In order to differentiate these two effects, high-pressure He is often used in place of H_2, as it cannot be absorbed and presents a similar thermal conductivity (approximately 0.8 times).
The effect of concentration is more complicated to assess and its significance varies with the hydride composition. The contradictory results that can be found in the literature are probably due to the different phenomena involved in the hydriding/dehydriding processes which have different importance according to the material considered. In Ref. [167] experiments on Mg hydride (with 2 wt% Ni) showed a decrease in the k_{MH} value as the hydrogen concentration increases, whereas in another experiment on Mg hydrides, k_{MH} was found to experience a maximum value at a defined concentration. In Ref. [162] experiments suggested a linear relation between k_{MH} and hydrogen concentration for $Ti_{1.5}Mn$, whereas no influence on the effective conductivity of $TiFe_{0.85}Mn_{0.15}$ could be attributed to the hydrogen concentration in Ref [168].

The analyses discussed in Section 3.8.5 refer to the experimental data of activated $Ti_{1.1}CrMn$ powder presented by Flueckiger et al. in Ref. [169]. They measured k_{MH} to vary between 0.31 and 0.69 $W{\cdot}m^{-1}{\cdot}K^{-1}$ as a function of hydrogen pressure from 2.9 to 253 bar, whereas no significant dependency on hydrogen concentration was observed. On the other hand, the effective specific capacity was found to be function solely of the hydrogen concentration. For the latter, it was correlated to the fraction of reaction completion ($F_{rc} = w/w_{max}$) and shown to vary between 500 and 1050 $J{\cdot}kg^{-1}{\cdot}K^{-1}$ from 0% to 90% with respect to w_{max}. More details on variable k_{MH} and c_{MH} are given in Subsection 3.8.5 where the interpolated experimental data are presented.

3.4 High-pressure metal hydride

High-pressure metal hydrides require repeated cycles of high-pressure cooling and vacuum heating to reduce their particle size from about 100 μm to 10 μm and to become able to absorb hydrogen. Such an activation process makes the material ignite when in contact with an oxidizer (pyrophoric nature).

The analyses conducted in this study consider $Ti_{1.1}CrMn$ as the hydrogen-absorbing alloy. Increasing attention has been given to this material for hydrogen storage applications because of its high capacity per unit volume (ca. 50 g/L) and cold start capability. The dehydriding characteristics of this material have been investigated in Ref. [61] and its ability to realize desorption rates of practical interest was demonstrated in Ref. [170] where real driving cycle tests were successfully performed. Stability of storage performance at repeated hydriding/dehydriding cycles and adequate desorption rates even at -30°C were shown in Ref. [15].
The main drawbacks include its high density (crystalline density of 6200 $kg{\cdot}m^{-3}$) and low gravimetric capacity (<2 wt%), which cause the system to be considerably heavier than the majority of the other on-board storage options, especially CHG systems [30]. Furthermore, its low effective thermal conductivity limits the cooling performance of the heat exchanger, reducing the absorption rates during hydrogen charging. However, k_{MH} values up to 10 $W{\cdot}m^{-1}{\cdot}K^{-1}$ have been obtained in compacts with Al [170].
The measured nominal thermal and kinetic properties of $Ti_{1.1}CrMn$ as well as the packing density here considered are given in Table 3.1 for hydriding [55] and in Appendix D for dehydriding [61].

Table 3.1: Thermal, kinetic properties and packing characteristic of $Ti_{1.1}CrMn$ bed.

	Property	Value	Unit	Symbol
Thermal	Effective conductivity	1	$W{\cdot}m^{-1}{\cdot}K^{-1}$	k_{MH}
	Effective specific heat capacity	500	$J{\cdot}kg^{-1}{\cdot}K^{-1}$	c_{MH}
	Crystalline density	6200	$kg{\cdot}m^{-3}$	ρ_s
	Packing density (ϕ=0.6)	2500	$kg{\cdot}m^{-3}$	ρ_{MH}
Kinetic	Enthalpy of absorption	-14390	$J{\cdot}mol_{H2}^{-1}$	ΔH_{ab}
	Entropy of absorption	-91.3	$J{\cdot}mol_{H2}^{-1}{\cdot}K^{-1}$	ΔS_{ab}
	Activation energy (absorption)	20700	$J{\cdot}mol_{H2}^{-1}$	E_a
	Activation rate (absorption)	150	s^{-1}	C_a
	Maximum H_2 storage capacity	1.5	$kg_{H2}{\cdot}kg_{MH}^{-1}$	w_{max}

3.5 Methodology

This study uses a generalized transient 1D model written in Modelica® language to calculate the main heat exchanger design parameter under different cooling and fueling conditions. The input parameters of the design process consist in the set of cooling and refueling conditions, material properties and packing characteristic described in this chapter. Energy and mass balances are combined with reaction kinetics equations to build the mathematical framework, while Coolprop is used to retrieve the hydrogen thermophysical properties during simulations [171, 172]. The model allows the user to select different hydrogen-absorbing alloys (and respective kinetic equations) in order to accurately describe the physics of absorption/desorption reactions in any metal hydride system. However, in this chapter we only present the results that refer to $Ti_{1.1}CrMn$ as it was found to be a suitable material for our purpose according to the selection criteria and performance targets discussed in Subsections 2.4.1 and 2.6.1 respectively. In addition, only the reaction and results that are relevant to the heat exchanger design process are shown in the current chapter. It follows that only the physics of the absorption reaction are discussed, whereas the ability of the model to describe the hydrogen desorption is examined in Appendix A, where the model details and its validation are reported.
The temperature profile and reaction rate at different locations are the main thermal results and highlight the importance of the critical metal hydride thickness concept, as the maximum distance from the cooling surface at which the reaction is completed below the desired filling time (see Subsection 2.7.1). In this work, the reaction is considered complete when the hydride bed achieves a hydrogen content equal to 90% of the saturation value under a refueling time of 3 min.
The tank structure refers to a standard composite Type IV vessel that consists of two layers: thermoplastic liner and CFRP layer. Simulations have shown that for the short times of interest in this analysis, the tank walls approximately behave as a an adiabatic surface. The effect of the tank walls can be related to that of an adiabatic surface due to the poor thermal conductivities of the liner and CFRP, which lie in the neighborhood of 0.66-1.17 $W \cdot m^{-1} \cdot K^{-1}$ [92].
The critical MH thickness for the $Ti_{1.1}CrMn$ bed is at first calculated with constant thermal properties and then the influence of variable MH parameters is assessed by including interpolated measured data of effective conductivity and specific heat capacity with respect to hydrogen pressure and absorbed content. This analysis provides valuable information on the degree of accuracy with which a constant-parameter model can be used to evaluate the maximum MH thickness, which consists in the main design parameter for the metal hydride storage tank.

3.6 Cooling conditions

In this analysis the liquid coolant is assumed to be supplied from the refueling station according to the HTF-supply strategy discussed in Subsection 2.5.1. Part of the cooling system is implemented off-board, which results in smaller weight and volume additions in the vehicle. In addition, this strategy enables to realize standard cooling conditions by controlling coolant mass flow rate and temperature at the heat exchanger inlet. Moreover, it eases the recovery of the absorption heat, which increases in turn the overall efficiency of the refueling facility.

The selection of the coolant properties has only a modest effect on the thermal performance of the system, as the heat transfer is dominated by the conduction resistance in the solid bed. For this reason, although the model allows choosing among different coolant compositions, here only the results that refer to Dexcool®, which is a car anti-freeze fluid, are presented.

At the mass flow rates of practical interest, required to achieve adequate cooling rates, it is reasonable to assume that the increase in the coolant's temperature between inlet and outlet is small, as also shown further in Chapter 6 of the thesis. Simulations have demonstrated that modest mass flow rates are sufficient to neglect the temperature variation in the coolant during heat absorption. The results obtained with a constant temperature model are consistent with the experimental data and the maximum coolant temperature difference was found to vary between 0.5 and 1.5 °C between inlet and outlet according to the test conditions [56, 57]. Therefore, the properties of the coolant are not varied during the simulation and refer to the chosen cooling temperature of 0°C.
These properties are reported in Table 3.2.

Table 3.2: Thermophysical properties of Dexcool™ at 0°C [170].

Property	**Value**	**Unit**	**Symbol**
Thermal conductivity	0.415	$W \cdot m^{-1} \cdot K^{-1}$	k_c
Specific heat capacity	3460	$J \cdot kg^{-1} \cdot K^{-1}$	c_c
Kinematic viscosity	$6.80 \cdot 10^{-6}$	$m^2 \cdot s^{-1}$	ν_c
Density	1060	$kg \cdot m^{-3}$	ρ_c

The effect of coolant conditions, other than those presented in this section, on the hydriding reaction and system's design is presented in Subsection 3.8.4.

3.7 System set-up and model nominal input data

For comparison purposes, the domain under study consists in the tank section shown in Fig. 3.1. The heat exchanger is assumed to be a U-tube configuration or a tube bank arrangement embedded in the solid bed. The coolant temperature is assumed to be constant along the tube (see Section 3.6), and thus, only half of the domain can be considered, as the center-line corresponds to an adiabatic boundary.

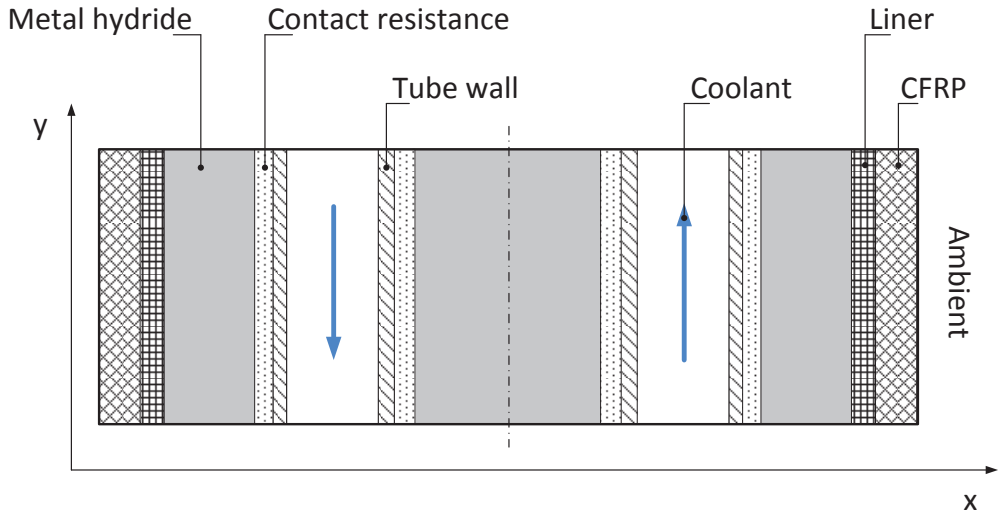

Figure 3.1: 1D domain of the metal hydride bed.

Each location in the solid bed enters into contact with the hydrogen at the same time. Such an assumption is not far from reality when the sintered filters for hydrogen distribution are uniformly placed within the solid bed. Heat transfer is only permitted along the x-axis, and the heat generated from the absorption reaction is removed by the coolant that flows in the embedded tubes. The heat is transferred from the solid bed to the coolant through the tube thickness and an additional thermal resistance that is modeled to account for the non-perfect contact between the tubes and the absorbing alloy.

The finite volume method (FVM) is used to discretize the domain along the x-axis with a central-differential scheme and a discretization step of 1 mm. The discretization concept is presented in Fig. 3.2 according to the thermal resistance-capacitance approach and with respect to the center-line of the bed domain. The temperature and hydriding conditions are calculated at different locations from the cooling tube to determine the effect of the metal hydride thickness on the reaction completion.

The volumetric form of the model is parameterized to allow for comparisons with the

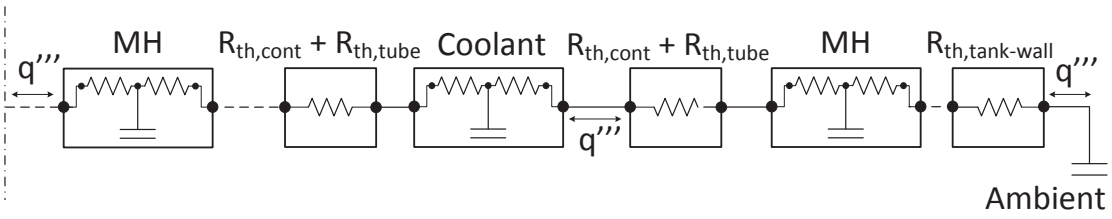

Figure 3.2: Discretization scheme.

results presented in Ref. [55]. However, the parameterization is limited to the information available. For instance, a value of 2000 $mm^2 \cdot K \cdot W^{-1}$ for the contact resistance between the aluminum tubes and the MH is considered. The coolant mass flow rate is adjusted in order to achieve the nominal average convection coefficient of 2500 $W \cdot m^{-2} \cdot K^{-1}$ according to the Nu correlations presented in Appendix A. In the present study, a value of 45 $L \cdot min^{-1}$ per tube for the coolant flow rate is needed to provide the target nominal convection coefficient. Such a value also allows to neglect the temperature variation inside the cooling tubes [170].

A large porosity value (60%) that corresponds to a packing density of 2500 $kg \cdot m^{-3}$ for $Ti_{1.1}CrMn$ (see, Table 3.1) results from powder activation, which leads to small particles sizes with sharp edges. This value ensures a moderate compaction that diminishes the risk of further particle deformation during hydrogen absorption, but increases the contact resistance. In addition, such a high porosity value allows for hydride expansion with respect to an expected maximum volume increase of 23% during hydriding and therefore, the strain effects that result from MH swelling are assumed to be compensated [173]. For this reason, the mechanical stresses that tube can experience during hydriding/dehydriding cycles are neglected in the model.

At time 0 of the refueling process, the hydride bed is assumed to be completely dehydrided and in equilibrium with the ambient conditions. The tank is filled from 1.013 bar to the target refueling pressure (p_{ref}) of 300 bar in 1 min. A well-distributed system of embedded sintered filters is assumed, resulting in a uniform distribution within the reacting bed. Under such an assumption, the only resistances that limit the hydrogen absorption are due to the thermal masses, whereas the diffusion resistances can be neglected. This hypothesis has been proven to well-describe the physical behavior for the system of interest [56], as large porosity values and pressures result in a negligible diffusion resistance through the particles.

The complete set of nominal input data for the constant parameter model is listed in Table 3.3.

Table 3.3: Set of nominal input data.

	Domain	Parameter	Component/Value
Physical	Solid bed	Material	$Ti_{1.1}CrMn$
		Porosity	60%
	Tube	Material	Aluminum alloy
		Inner/outer diameters	20/22 mm
Conditions	Fueling	Refueling pressure	300 bar
		Pressure ramp	300 bar/min
	Cooling	Coolant type	Dexcool®
		Flow rate	45 L/min
	Initial/Ambient	Temperature	293 K
		Pressure	1.013 bar

The pressure ramp and target refueling pressure p_{ref} are shown in Fig. 3.3.

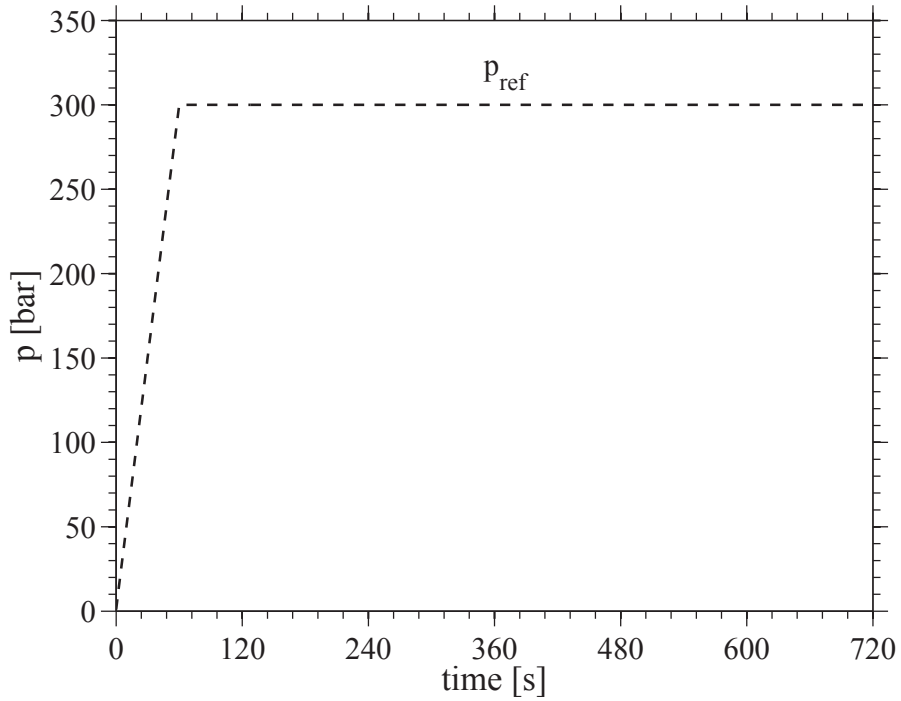

Figure 3.3: Pressure ramp and refueling pressure p_{ref}.

3.8 Results

3.8.1 Physics of absorption

The hydriding/dehydriding reactions that take place in a metal hydride can be expressed by the following reversible relation:

$$\mathrm{M} + \frac{X}{2}\mathrm{H_2} \longleftrightarrow \mathrm{MH_x} + \mathrm{Q} \tag{3.1}$$

where M represents the metal, MH_x its hydrided form and Q the heat of reaction. The direction in which the reaction occurs depend upon temperature and pressure conditions.
The overall hydriding process is often divided into two steps, which correspond to the formation of two hydride states: α-phase and β-phase, the later being the fully-formed hydride. During charging, hydrogen diffuses from the particle surface trough the β-phase to the phase-transition interface and forms additional β-phase hydride. The opposite occurs during discharging and hydrogen recombines at the particle surface to form H_2 (i.e. hydrogen molecular form).
Hydrogen absorption is a complex phenomenon that requires appropriate thermodynamic conditions and the accomplishment of a number of kinetic steps to be achieved. For details the Reader is referred to the relevant literature (e.g. Refs. [20, 174]. Several factors, of which the temperature and pressure are the essential ones, impact the reaction kinetics and prevent reaching a thermodynamic equilibrium within a reasonable time.
The difference between the equilibrium pressure of the hydride and the gas filling pressure consists in the driving force of the hydriding reaction. By means of the Van't Hoff equation, it is possible to relate the equilibrium pressure p_{eq} with the exponential form of reciprocal temperature:

$$p^{eq} = p_{amb} \cdot e^{\frac{\Delta H_{ab}}{RT_{MH}} - \frac{\Delta S_{ab}}{R}} \tag{3.2}$$

where p_{amb}, T_{MH}, R represent the ambient pressure, hydride temperature and universal gas constant respectively. According to Eq. 3.2, small variations in the hydride temperature can significantly affect the equilibrium pressure and thus, the reaction rates. As generally, the hydriding reaction is an exothermic process, heat is released during hydrogen absorption, which results in a temperature increase and a consequent reduction of the driving potential. The reaction reaches the equilibrium state before the hydriding is completed. This condition refers to a thermally-limited reaction and is reached when the cooling performance is not adequate.

In Fig. 3.4 the temperature and the equilibrium pressure of the hydride at four equidistant locations, that are representative of small and large bed thicknesses, are plotted with respect to a maximum simulation time of 12 min, which leaves room for observing the relevant mechanisms for the analysis of interest.
Before the refueling takes place, the bed temperature is at 293 K and the tank pressure is at 1.1013 bar. At these conditions the equilibrium pressure is 160 bar and there is no driving force for the reaction to start. From the moment the refueling starts, the coolant is provided from the external facility and the vessel pressure begins to rise.
The solid in contact with the tube is the first to experience the cooling effect and after 24 s its temperature decreases to nearly 280 K (Fig. 3.4a) and the equilibrium pressure meets the charging pressure at approximately 125 bar (Fig. 3.4b). As the fueling proceeds, the filling pressure exceeds the equilibrium pressure triggering the absorption reaction. A large amount of heat is released and only a part of it is dissipated by the cooling fluid. As a consequence the solid temperature rises and so does its equilibrium pressure, until the peak temperature of 302 K is reached. This condition corresponds to the end of the pressurization. The heat generated is no longer sufficient to increase the temperature of the hydride, which is rapidly cooled down, reaching 280 K at 720 s. Simulations show that, for the Mh at 0 mm, steady-state thermal conditions are reached at around 2000 s, when the hydride approaches the coolant temperature.
Similar observations can be done for the solid that is located further from the cooling surface. However, the larger is the distance from the tube and the longer it takes for the solid to start reacting.
At 4 mm the reaction is triggered at 30 s, while at 8 and 12 mm the absorption process does not start before 33 s and 35 s respectively. For the latter location, the thermal resistance is too large to enable reasonable cooling rates in the first phase of pressurization and, as a result, a small increase in temperature is observed due to the heat of compression developed during tank filling. In general, the farther is the hydride from the tube and the smaller is the realized heat removal, causing the solid to rapidly heat up, reaching a maximum temperature of 322 and 326 K at 4 and 8 mm. At 12 mm it is not possible to identify a well-pronounced peak and the temperature profile tends to flatten in proximity of the system's adiabatic (or equilibrium) temperature T_{adiab}, as the reaction becomes thermally-limited. At this location, more than 5 min are required to observe a significant temperature drop from the equilibrium conditions.
At the present refueling pressure, T_{adiab} is around 328 K (i.e. 55 °C) for $Ti_{1.1}CrMn$.
At the end, it should be noted that the temperature cannot increase above T_{adiab}, as this temperature represents the thermal equilibrium condition at which the MH pressure reaches p_{eq}. Therefore, no driving potential exists for hydriding, which causes the reaction and, hence, heat generation to stop.

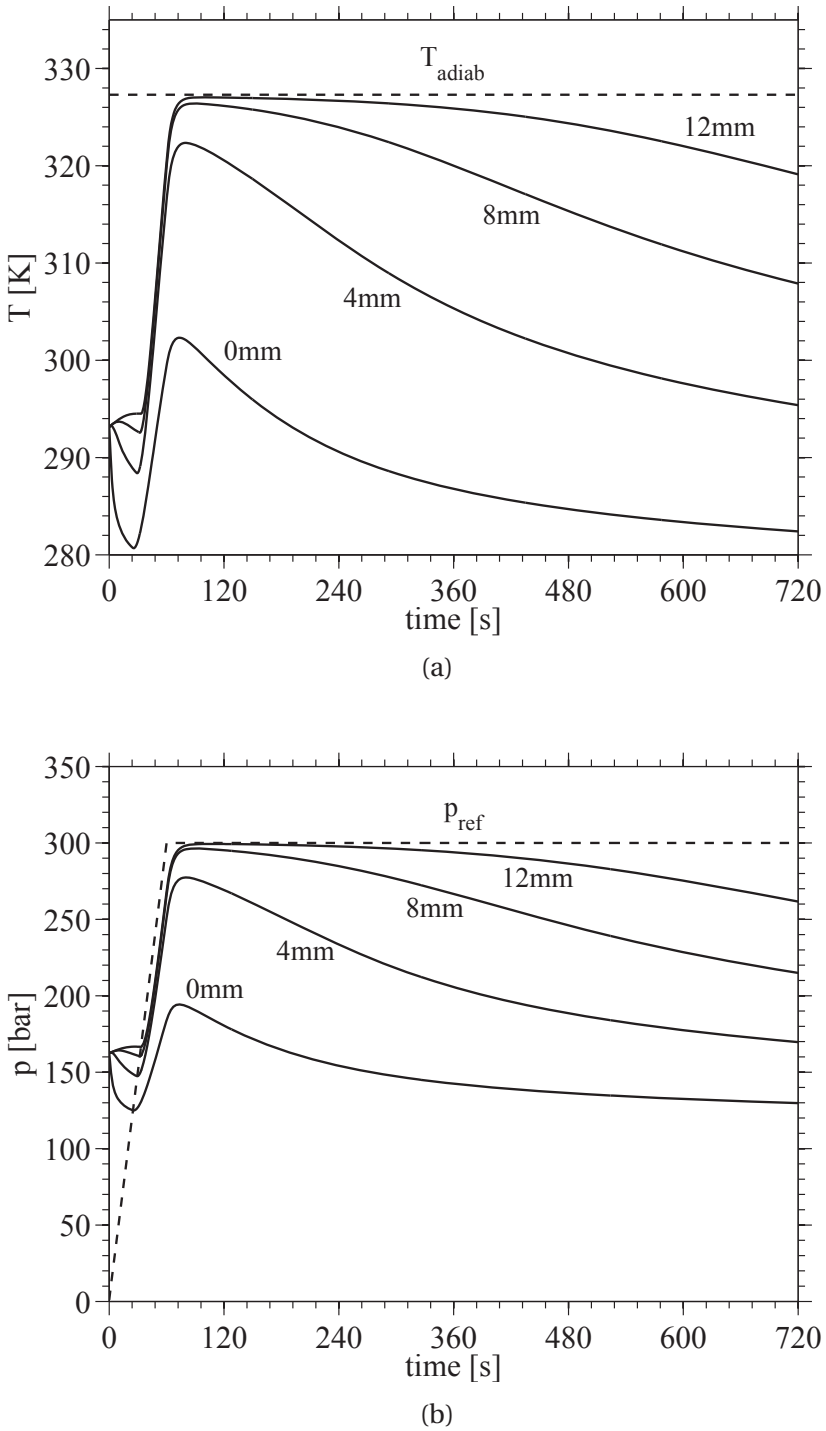

Figure 3.4: Thermodynamic conditions at different locations from the cooling surface: temperature (a); equilibrium pressure (b).

In Fig. 3.5 the hydriding characteristic and the volumetric heat generation rate within the MH bed complete the description of the phenomena that occur during tank filling. In Fig. 3.5a the volumetric heat generation rate is presented. This takes into account both the heat of pressurization and the reaction heat in the solid bed (see Appendix A). The reaction heat is a function of the absorption rate while the heat of pressurization is only function of the pressure ramp (and porosity), which is steady until the 300 bar condition is reached. For this reason, the heat of generation starts at a value different from zero and remains constant until the hydriding takes place.
It is possible to observe two maxima: an absolute and a local value. The former occurs at the end of the pressurization regardless of the hydride distance from the cooling surface. The highest value is around 3.73 $MW \cdot m^{-3}$ and corresponds to the solid in contact with the tube. At this location, the hydride experiences significant cooling, which rapidly decreases its temperature enabling fast hydriding and thus, large heat generation rates. The peak decreases with the hydride thickness and remains nearly constant for the solid at a distance beyond 8 mm, as at this location the reaction approaches the thermally-limited conditions (see Fig. 3.4). The large thermal resistance prevents an effective heat removal and the temperature rises up to its adiabatic value hindering the absorption reaction and therefore, the heat generation. At 12 mm the peak is 1.88 $MW \cdot m^{-3}$, which corresponds to half of the heat generated at 0 mm.
The local maximum occurs whenever the hydride experiences a drop in temperature that enables a larger driving force and thus, an increase in the reaction rate. It follows that, the time at which this occurs increases with the thickness and thus, with the bed's thermal resistance. It can be observed that such a maximum is not present for the solid at 0 mm, as the cooling rates are large enough to realize a rapid reaction that achieves the saturation condition with no further possibility for heat generation.
Fig. 3.5b shows the variation of the hydrogen content in the metal hydride at the four MH locations considered until now. The hydrogen content is expressed in its relative form with respect to the hydride mass. According to Table 3.1 the maximum weigh fraction of hydrogen that can be absorbed is 1.5 wt%. Fig. 3.5b should be read in the light of what discussed above for the temperature profile, equilibrium pressure and generated heat. From this figure it is immediate to notice that greater hydride thicknesses correspond to larger times for the reaction to start and complete.
The solid at 0 mm undergoes significant heat removal and the reaction proceeds rapidly until it reaches the saturation condition. No noticeable slowdown can be attributed to neither the cooling performance nor the end of pressurization and the reaction is kinetically-limited. A considerable reduction in the hydriding rates occurs for thicknesses beyond 8 mm when the absorption process reaches the equilibrium condition fast, as it was previously discussed.

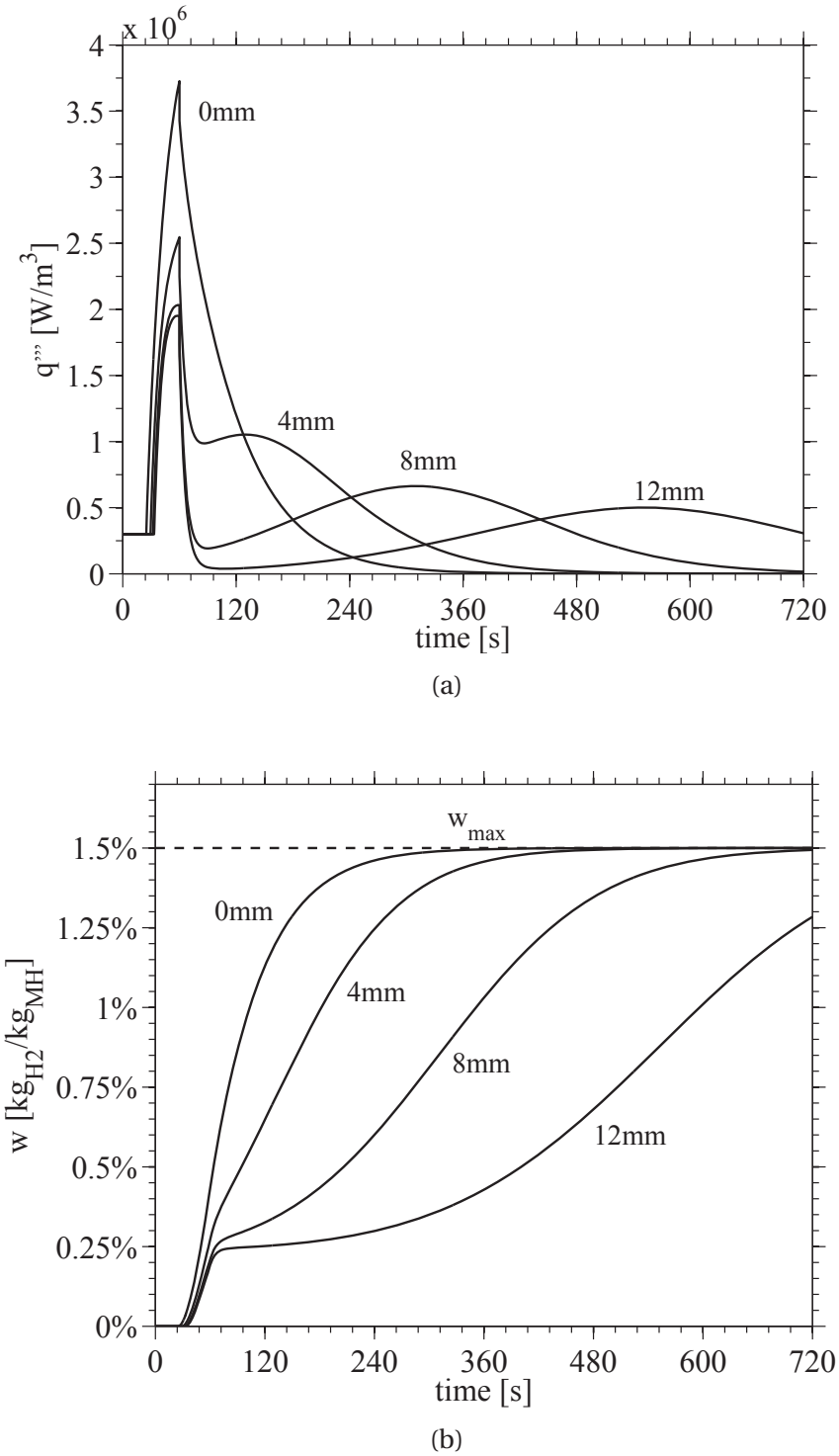

Figure 3.5: Thermo-kinetic conditions at different locations from the cooling surface: heat generation rate (a); reaction rate (b).

3.8.2 Calculation of the critical metal hydride thickness

With respect to the targets presented in Subsection 2.6.1, we aim at designing a tank/heat-exchanger system that realizes 90% of the hydriding process in 3 min. In order to do so, it is of interest to calculate the critical metal hydride thickness δ, as the maximum distance from the cooling tube that achieves the target fraction of reaction completion (F_{rc}) within the desired time. Such a parameter is highlighted in Fig. 3.6.

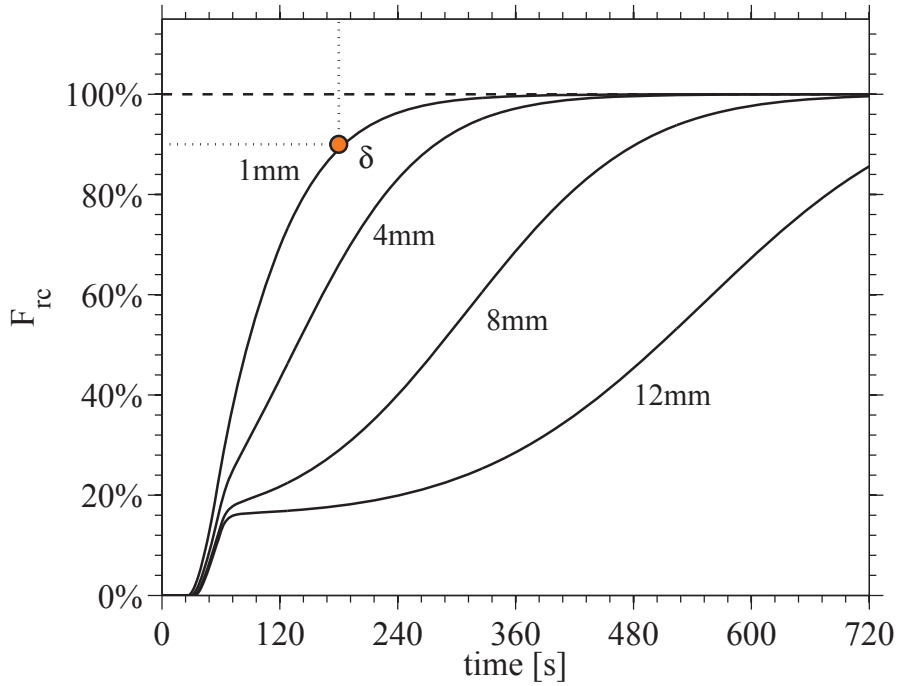

Figure 3.6: Maximum metal hydride thickness for $Ti_{1.1}CrMn$; constant parameter model.

In Fig. 3.6 it can be noticed that the storage system must be designed in the respect of a critical MH thickness value of 1 mm to achieve the desired goals. For symmetry, such a value corresponds to half of the thickness of the material between the cooling elements between two cooling elements.
The figure is useful to understand the reason for the choice of the F_{rc} target value to achieve fast refueling times, while ensuring a large stored hydrogen mass. A noticeable delay occurs after 90% of the hydriding reaction, which takes more than 4 min to reach the saturation condition. Such a relatively large time is due to the asymptotic approach to the concentration limit. Therefore, the design of a MH storage system that realizes 100% of the hydriding reaction would be unrealistic under practical filling time requirements.

The thickness values required to reach 80-90% of the reaction completion, at reasonable fueling times, are reported in Fig. 3.7. This figure illustrates the relation between the MH thickness and filling time, underlining the importance of this parameter when designing practical storage systems. This figure helps further the understanding of the importance of the MH thickness in the design of practical storage systems.

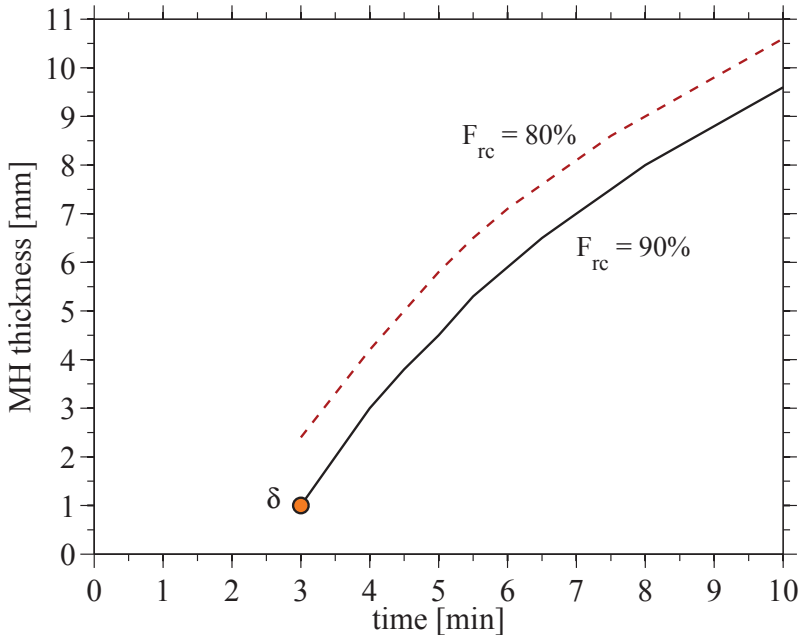

Figure 3.7: Variation of MH thickness with refueling time for 90% or 80% of reaction completion.

For the target F_{rc} of 90% the MH thickness varies between 1 and nearly 10 mm with respect to fueling times of 3 and 10 min.
Larger thicknesses are allowed when the desired fraction of reaction completion is reduced to 80%. More precisely the relative increment in the MH thickness varies between 150% and approximately 10% in the considered time range and at 5 min assumes a value of 30%.
Fig. 3.7 can also be used to estimate the variation in the fueling time for a given MH thickness when F_{rc} values other than the target one are contemplated. The average filling time decreases by approximately 1 min if the 80% condition is considered. However, this implies that for a fixed tank size the amount of stored hydrogen is reduced. Such a reduction accounts for 1.5 $g_{H2} \cdot kg^{-1}_{MH}$ or 7.5 $kg_{H2} \cdot m^{-3}_{MH}$ at the current packing density and target F_{rc} value.

3.8.3 Effect of fueling conditions

The effect of hydrogen charging pressure and pressure ramp on the hydriding rates is known from the literature, e.g. Ref. [128].
As the absorption rate depends on the difference between supply pressure and equilibrium pressure corresponding to the bed temperature, the hydriding process is positively influenced by an increase of the maximum operating pressure. However, for $Ti_{1.1}CrMn$ a large increase in the charging pressure is needed to significantly influence the hydriding process, because of the logarithmic nature of the dependency between absorption rates and pressure (see Appendix A).
Increased pressure ramps anticipate the time at which the reaction starts, as the positive pressure difference that consists in the process driving force occurs earlier.
The combined effect of p_{ref} and p_{ramp} is shown in Fig 3.8. In such figure the x-axis represents both the refueling pressure and the pressure ramp.

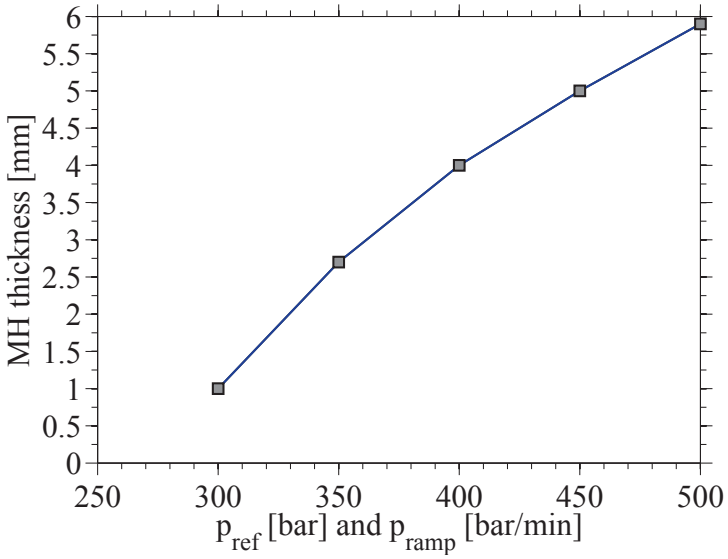

Figure 3.8: Effect of pressure on the metal hydride thickness.

Fig 3.8 presents the combined effect of increased supply pressure and pressure ramp on the critical metal hydride thickness. It can be observed that a considerable increase in the charging pressure and pressure ramp is required to achieve a relevant augmentation of δ when compared to the nominal fueling conditions. For instance, when the refueling pressure and pressure ramp are increased by 200 bar and 200 bar·min^{-1} respectively, with regards to the nominal fueling conditions, the hydride thickness is enlarged by 5 mm.
At the end, the choice of the operating pressure falls outside simple considerations

upon absorption rates and other aspects must be considered. These include mechanical limitations of the tank components (e.g. valves) and walls, as well as system's weight and cost.

3.8.4 Effect of cooling conditions, material properties and packing characteristic

The influence of different fueling conditions and MH properties on the hydriding reaction has been investigated for $Ti_{1.1}CrMn$ by Visaria et al. [55]. They found that the filling time, and thus the MH thickness, are mostly dependent on the effective thermal conductivity and coolant's temperature, followed by the contact resistance. A minimum threshold exists for the coolant's flow rate to obtain adequate convection coefficients, however, increases above this limit do not provide relevant benefits, as the hydriding reaction is dominated by the thermal conduction resistance.

The effect of the packing density on the MH thickness is negligible and therefore, its influence on the heat transfer is not accounted for in the present model (see Appendix A). The effective MH conductivity is set to its constant nominal value, which is independent of the porosity. In this context, the packing density only affects the distribution of the storage volume between the solid material and hydrogen gas, whereas its effect on the hydriding rate is not considered.
Higher packing densities provide greater masses of H_2-absorbing alloy in a fixed volume and thus, larger amounts of hydrogen are absorbed in the tank at a set time. This is discussed in Chapter 6 where the proposed storage tank design is simulated under different operating conditions. However, it is worth mentioning from now that the choice of the optimal packing density is not trivial in practice, as several aspects other than the augmentation of the theoretical stored mass of hydrogen should be taken into account. In a practical system the goal is to achieve moderate hydride compaction that reduces contact resistance and avoid particle deformation. On the other hand, considerable compaction does not allow for adequate compensation of the expansion/contraction forces that derive from hydrogen absorption/desorption reactions and might result in significant mechanical stresses for the tank components.

3.8.5 Effect of variable thermal properties

The effect of material's variable thermal properties on the MH critical thickness is here addressed with respect to the values measured in Ref. [169], as discussed in Section 3.3.
For the activated $Ti_{1.1}CrMn$ powder, k_{MH} was measured to be 0.31 to 0.69 $W \cdot m^{-1} \cdot K^{-1}$

as a function of hydrogen pressure from 2.9 to 253 bar, whereas no significant dependency on hydrogen concentration was noticed. For this reason, the thermal conductivity data are here interpolated as a function of the hydrogen charging pressure, as presented in Fig. 3.9a.
The thermal conductivity increases with the pressure, probably due to the conduction pathways in the gas phase, and a variation was observed in proximity of 170 bar, where k_{MH} reached its maximum value in the measured interval. Such a variation falls within the measurement uncertainty and is accounted for in the interpolated data, as its influence in the overall model results is negligible. At the end, it should be mentioned that the measurements were carried out at constant temperature and at lower packing densities than what is considered in this study. Despite these observations, only the effect on δ that can be addressed to the variable parameters, which have been experimentally measured, is investigated and k_{MH} is assumed not to be influenced by temperature and bed porosity in the current analysis.

The measured specific heat capacity experienced a dramatic increase, up to 1050 $J \cdot kg^{-1} \cdot K^{-1}$, at a charging pressure of approximately 170 bar, as a result of the transition to the β–phase structure and resulting phonon transport at the hydrogen occupied interstitials of the MH lattice. By relating the charging pressure and temperature to the hydrogen absorption, it was observed that such an abrupt increase is a function of the fraction of reaction completion. For this reason, c_{MH} data are interpolated as a function of the F_{rc} variable, as shown in Fig. 3.9b.
Measurements for k_{MH} and c_{MH} generally showed lower and greater values, respectively, than in the nominal case. As a result, the temperature in the solid bed increases for the combination of larger thermal resistances and inertia, which are attributed to the reduction in the conductivity and increase in the heat capacity respectively. This is discussed in detail in Ref. [175] where the effect of the thermal properties on the heat transfer and hydriding condition is addressed.

In Fig. 3.10 the influence of variable thermal properties on the fraction of reaction completion is compared with the result obtained with the constant-parameter model. When variable parameters are considered, higher temperatures occur before and after pressurization. In the light of Figs. 3.9a and 3.9b, a lower thermal conductivity is experienced in the solid bed at the beginning of the hydrogen charging, when the absorption reaction has yet to start and the heat capacity is constant and equal to its nominal value.
The influence of temperature on the reaction rate depends on the total thermal resistance between the solid powder and the coolant. At locations near the cooling surface, the reaction is kinetically-limited and an increase of a few degrees in temperature does not considerably affect the reaction rate, as the total thermal resistance is low

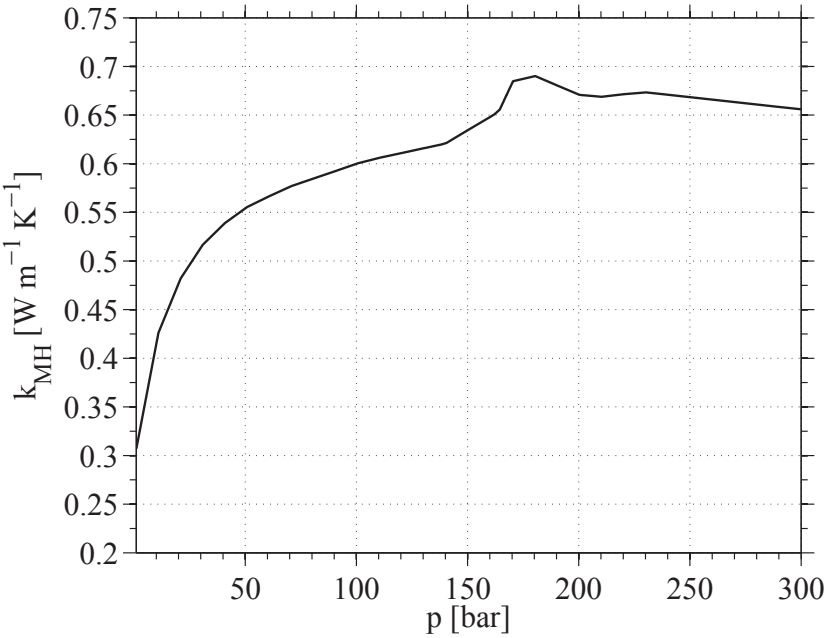

(a)

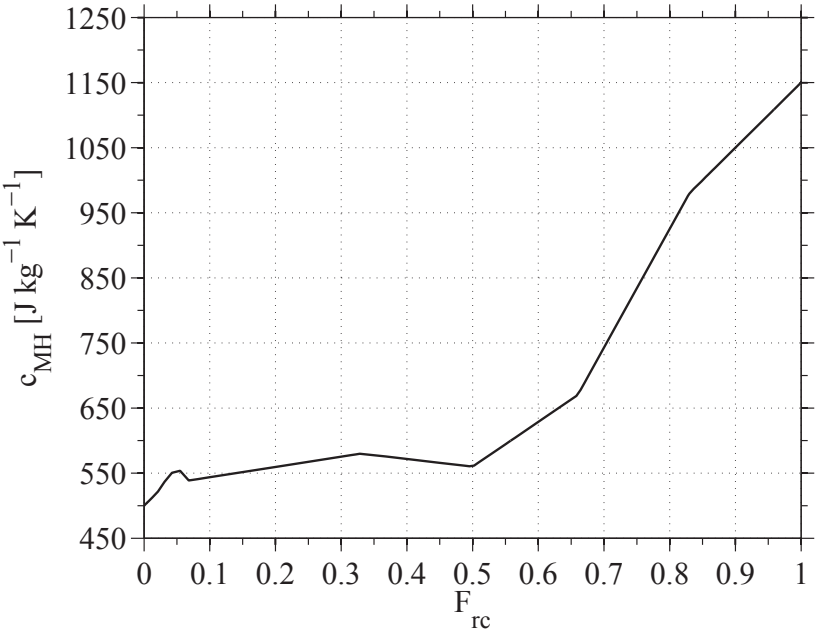

(b)

Figure 3.9: Interpolated experimental data: MH effective thermal conductivity (a); MH effective specific heat capacity (b).

enough to enable large cooling rates. As a result, the value of the previously-calculated δ remains unchanged. On the contrary, at distances further from the cooling surface the reaction is thermally-limited and the increase in both the thermal inertia and resistance delays the absorption process. As a consequence, the new F_{rc} curves shift toward longer filling times.

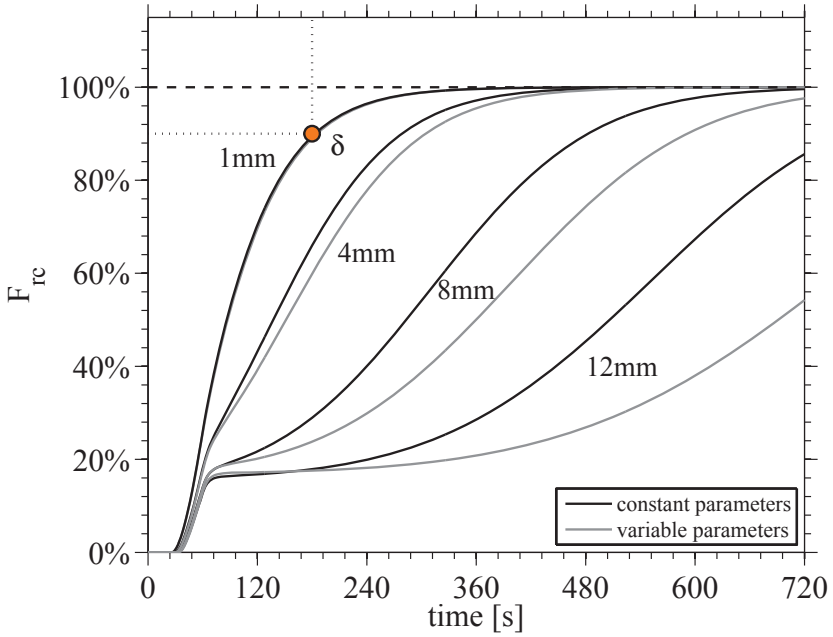

Figure 3.10: Effect of variable thermal properties on the hydriding rates and MH critical thickness.

The delay in the absorption process when variable thermal properties are considered has to be attributed mainly to the lower values of thermal conductivity. This was demonstrated in Ref. [175]. The main reason is that c_{MH} varies with F_{rc} more rapidly at locations near the cooling surface, where the metal hydride experiences intensive cooling rates and is dominated by kinetics. Indeed, the significant variation in the heat capacity that occurs between 50% and 100% of absorption process (see Fig. 3.9b) is realized at shorter times for the powder in proximity to the cooling tube, where the temperature drops at a faster rate despite the increase in thermal inertia. As a result, its effect on the reaction rate is negligible. On the contrary, at larger distances, the large total thermal resistance strongly reduces the cooling rates, preventing the solid from achieving reaction rates sufficiently high to trigger a significant variation in the c_{MH} value.

3.9 Conclusion

The results of the developed model are used to describe the physics of the absorption reaction in a MH bed. The findings confirm that an effective removal is essential to achieve hydriding rates and fueling times of practical interest.

The model can be employed to calculate the critical metal hydride thickness δ, which is the key parameter involved in the effective design of the hydrogen storage system. A value of 1 mm for δ is found to achieve the target fraction of reaction completion (i.e. 90% of the saturation value) at the desired fueling time of 3 min. This value corresponds to half of the distance between two cooling elements.

The influence of various material parameters and operating conditions is addressed with respect to the critical MH hydride thickness. Among these the coolant temperature and MH effective thermal conductivity affect the most the design of the system. When it is possible, increasing the supply pressure can be another reward strategy to increase the hydriding rates and thus, operate at larger hydride thicknesses.

The implementation of measured data for k_{MH} and c_{MH} dependencies upon supply pressure and hydrogen content shows that the use of a constant parameter model is sufficiently accurate to predict the critical metal hydride thickness for the performance of interest. Their effect on the hydriding rates is negligible for the solid in proximity of the cooling surface. It cannot be neglected for further distances, when the reaction is thermally-limited, and a reduction in the thermal conductivity from the nominal value significantly delays the absorption process.

4 Selection and design of the heat exchanger configuration

4.1 Introduction

In this chapter, the outcomes of a study on the heat exchanger selection for a metal hydride heat pump (MHHP) [176] are generalized and applied to a hydrogen MHSS. The study employs the calculation of the heat transfer effectiveness and pressure drops as the performance tool to realize a first evaluation of the three tank/heat-exchanger candidates. The capacity of each candidate to effectively perform the desired function is addressed by estimating the physical dimensions that provide reaction times of practical interest for the heat pump absorption stage. The final selection of the system is done by accounting for both the thermal performance and the reaction time with the final goal to fulfill the desired targets in respect of the mechanical and operating requirements identified in Section 4.3.

In this chapter, our only interest is to present the results of the MHHP study relevant to hydrogen storage systems. Therefore, the outcomes that solely refer to MH thermal systems and the description of the related computational models are reported in Appendix B. These include comparisons among different heat transfer correlations and their effect on the thermal performance, sensitivity analysis on the realized heat transfer effectiveness with respect to fluid properties and system geometry, and optimization of the selected design for the MHHP.

In Section 4.2 we describe the design approach applied to obtain the results presented in this chapter, whereas the limitations of the study are reported in Appendix B.

The investigated system layouts are detailed in Section 4.3, while the relevant results of the study are given in Section 4.4. The conclusions that are pertinent to MHSSs are then generalized to select the most promising heat exchanger for a hydrogen storage application.

4.2 Methodology

A general approach is established for application to systems regardless of the properties of the particular hydrides chosen. The heat transfer effectiveness is investigated according to the following assumptions:

- The heat transfer process is carried out under steady-state conditions.
- The hydrogen absorbing process is modeled as ideal.
- The thermo-physical properties of the heat transfer fluid are kept constant during the simulation.

The design assumes time-independent conditions and the heat exchanger system is modeled in steady-state conditions. This assumption is reasonable as the present study focuses on thermally limited hydride reactions for long-cycle metal hydride heat pumps, and thus, the majority of the operation is, in practice, in a quasi-steady condition. For such an application, it is desirable to maintain the HTF at an elevated temperature during each stage of the cycle and realize sustained HTF heating during hydriding rather than rapid hydride cooling as requested for vehicular storage applications. Therefore, the rapid reaction kinetics that occurs between cycle changes and the design aspects related to it are neglected in the MHHP study. As discussed in the conclusions of the present chapter, the difference in the operation objective between MHHPs and MHSSs leads to the selection of different suitable designs.
In the MHHP considered here, the pressure is held constant during hydrogen absorption and the cooling rates are sufficiently high to sustain the thermally-limited reaction, but not large enough to rapidly cool the MH. Therefore, the MH temperature rises at the beginning of hydriding when the solid bed experiences fast kinetics and then remains approximately constant (around the equilibrium temperature) for a long time, as the absorption reaction proceeds slowly. Only the nearly isothermal portion of the hydriding characteristic is considered for the heat exchanger design.
With respect to an entire heat pump cycle, the heat management system must be designed to fulfill the energy demand at any stage, including the cooling and heating of the solid bed during hydriding and dehydriding, respectively.
For most metal hydrides, the hydrogen absorption and desorption reaction rates are usually of comparable magnitude in terms of energy demand. It is therefore assumed that the heat exchanger solution that can fulfill the cooling demand during hydriding can easily satisfy the energy demand of dehydriding. For this reason, the present analysis is focused on the hydrogen absorption process.
For thermal design, assuming an idealized hydriding reaction, the absorption process

can be seen as a pure-substance-condensation problem in which the heat source evolves isothermally. This means that, for any metal hydride, it is possible to identify a constant temperature at which to consider the absorption reaction. This assumption better approximates the behavior of rapidly reacting hydrides, for which the majority of the reaction occurs at the thermodynamic equilibrium temperature. On the opposite, for slowly reacting hydrides the disparity between the assumed constant absorption temperature and its actual value at any moment of the hydriding reaction would be more marked. As this study focuses on long-cycle MHHPs, fast reacting materials are to be preferred and therefore, this assumption well describes the practical operation of the system [130].
The general design approach employed in the present work is based on the effectiveness expression defined in Appendix B. Such an approach is independent from the specific hydride used. It follows that the inlet and outlet HTF temperature can thus not be precisely determined, and the thermo-physical properties are then estimated at ambient temperature. This assumption is realistic for the end application of heating water, as the minimum temperature at which the liquid is fed to the heat exchanger is generally close to the ambient temperature (20 °C in the current analysis). To avoid steam generation inside the tubes the maximum outlet temperature is limited by the boiling point of water. For this reason, it can be assumed that the outlet temperature will not exceed 90 °C at atmospheric pressure. As a result, the mean thermo-physical properties used herein are evaluated at an average temperature of 55 °C.
The effect of thermo-physical properties on the results is addressed in the sensitivity analysis section presented in Appendix B; they are varied over a wide range of values encompassing the cases of average temperatures other than 20 °C and the case of alternative heat transfer mediums.

4.3 Configurations

The vessel containing the absorbing alloy is here considered cylindrical to allow for a uniform distribution of the mechanical stresses that result from hydrogen pressurization. Under such a constraint, the vessel/heat-exchanger designs chosen for the analysis are based on a shell-and-tube layout, a common heat exchanger configuration.
Three shell-and-tube configurations are considered in this work, named as HEX1, HEX2, and HEX3. In configuration HEX1, the coolant flows inside tubes which are surrounded by metal hydride. In HEX2, the metal hydride is packed inside the inner tubes and the coolant flows parallel to the tube. This represents a tube-in-tube configuration where the hydrogen-absorbing alloy occupies the volume in the inner tubes and the coolant flows in the annular region comprised between inner and outer

tubes. Finally, in HEX3, the metal hydride is packed inside the tube and the coolant circulates in the shell in a combined cross-parallel flow over the tube bank. These arrangements are shown in Fig. 4.1 .

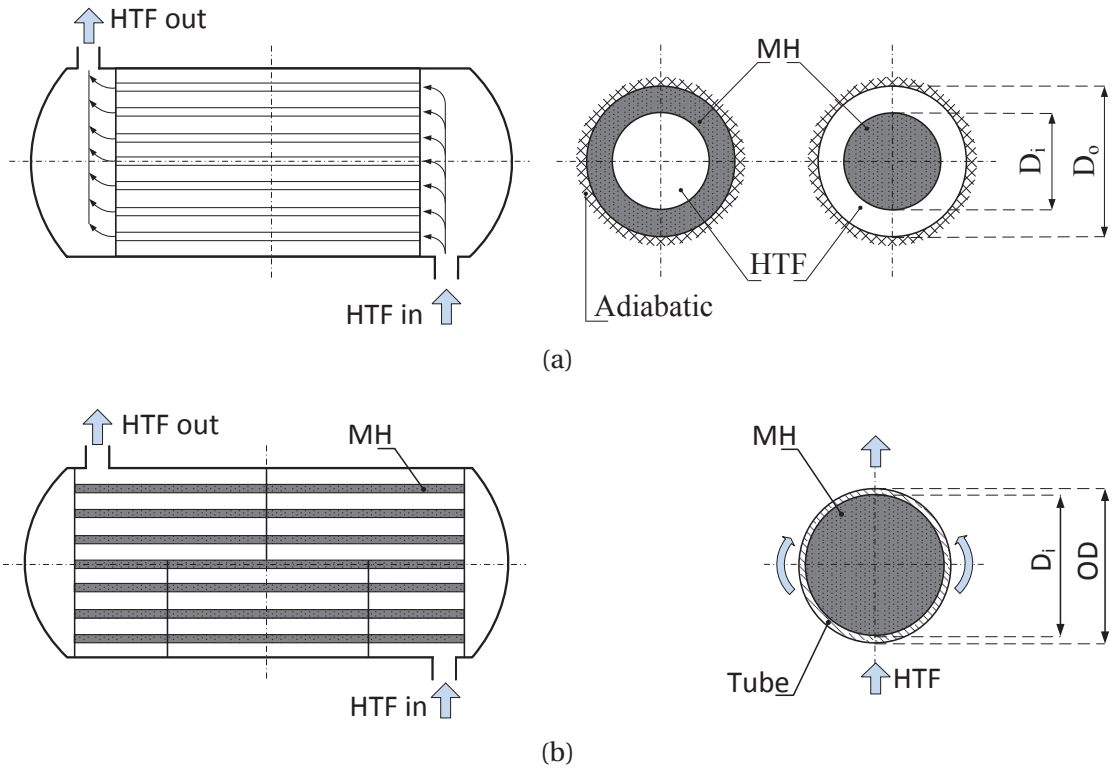

Figure 4.1: Longitudinal system's section and tubes' transversal sections for: HEX1, HEX2 with external adiabatic boundary (a) and HEX3 (b)

When compared to HEX1 and HEX2, HEX3 configuration presents a mirror arrangement of the solid and fluid domains as shown in Fig. 4.1c, where its longitudinal section and tubes' transversal section are presented. The MH bed consists of single modules and the heat is transferred through the tube thickness to the HTF that flows over the tube bank in a combined cross-parallel flow. The flow-path depends upon the geometry of the tube bank, e.g. inclination angle and baffle arrangement. On the other hand, for HEX1 and HEX2, it is assumed that each tube represents a stand-alone heat transfer module and that the number of tubes only affects the overall heat transferred and not the flow conditions or heat transfer characteristics.
Under the assumption of employing water as the HTF, the velocity interval identified in Table 4.1 (i.e. $1 \leqslant v \leqslant 2.5$ m/s) is used as the optimum velocity range, since water velocities below 1 m/s can lead to deposit formation, while velocities above 2.5 m/s increase corrosion for most common aluminum/copper alloys and contribute to tube

vibrations [177]. However, it should be noted that lower minimum velocities are practicable when de-mineralized water is used and velocities around 0.8 m/s are often used in practice.

Table 4.1: List of performance, design and operative requirements for the MHHP system.

Performance, design and operative requirements
• HTF heating realized at the target effectiveness: ϵ = 0.95. • Fulfill the MH cooling demand. • Modest pumping power (i.e. pressure drops). • Practical sizes (smallest tube diameter 2 mm). • Safe and continuous operation (i.e. avoid issues as corrosion; limit deposits and vibrations): $1 \leqslant v \leqslant 2.5$ m/s; B = (20–60)%·Ds and PR=1.25-1.5 [177].

In Table 4.1, v is the HTF velocity, B is the relative baffle space expressed as percentage of the inner shell diameter D_s and PR is the pitch to tube-diameter ratio. It can be noticed that the lower limit of the range defined for practical tube sizes corresponds to the inner tube diameter estimated in Section 3.8.2 according to the δ-criterion.

4.4 Results

4.4.1 Thermal efficiency and pressure drops

The thermal model presented in Appendix B is used to compute the heat exchanger effectiveness and pressure drops for each layout. The two main variables considered for each design are the tube diameter and coolant flow rate. For HEX1 and HEX2 we consider diameters up to 10 mm; for larger tube sizes the performance assumes very low values that are not of interest for this design. For the same reason, the maximum tube size considered for HEX3 is 40 mm. For all the heat exchangers, the flow velocity is limited to 5 m/s. In Figs. 4.2-4.4 the effectiveness ϵ and pressure drop over such a range of values are presented.
For HEX1 and HEX2 the diameter considered is the tube hydraulic diameter, D_h, while for HEX3, the outer tube diameter OD is considered as the characteristic length. The dashed lines in the figures show the boundaries between laminar, transitional, and turbulent flow.

Fig. 4.2a shows the different regions for the three flow regimes the system is operat-

ing in. The highest effectiveness, above 0.9, are where the small hydraulic diameter ensures high heat transfer coefficients regardless of the flow velocity; for this layout the hydraulic diameter is the cooling tube inner diameter. As expected, the combination of low velocities and small diameters provides the greatest ϵ-values, requiring the system to be designed for the size typical of mini-tube heat exchangers. With the limitation that the coolant velocity remains between 1 m/s and 2.5 m/s to avoid deposits and prevent corrosion in the aluminum tubes, it is not possible to achieve an effectiveness of 0.9 for diameters greater than 2 mm. For velocities in this range, the transition regime, shown between the black dashed lines, provides the highest practical efficiencies (excluding the region where $D_h \rightarrow 0$). However, it is generally not recommended to operate the system in the transition regime because the sudden fluctuations from laminar to turbulent flow cause the thermal performance to be discontinuous.

A maximum effectiveness of 0.8 can be obtained in the turbulent regime at velocities of around 4.5-5 m/s, while lower ϵ-values, i.e. 0.25-0.6, can be achieved in the optimum velocity range and for diameters greater than 4 mm.

The pressure drop shown in Fig. 4.2b indicates regions where pumping power may become too large to be practical. At 1.75 m/s, the maximum loss is approximately 2 bar for practical diameters and the minimum loss is approximately 0.04 bar for D_h = 10 mm. It is important to note that these values refer to the overall system and are independent of the total number of tubes as these are connected in a parallel arrangement (see Fig. 4.1a). The diagonal red lines represent a region where the calculated pressure drop exceeds 15 bar, value selected for ease of reading. For velocities below the optimal range considered in this study, pressure drops measurements are available for HEX1 for an inner tube diameter of 4.57 mm in Ref. [178].

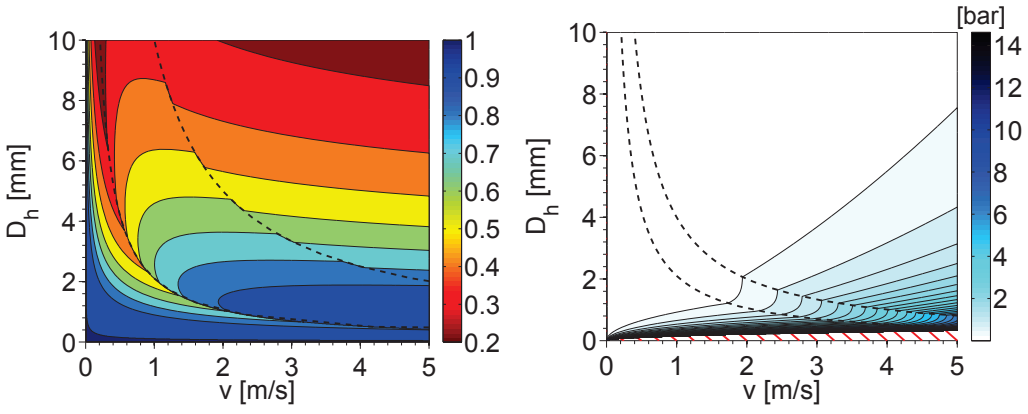

Figure 4.2: Effectiveness map (a); distributed pressure drops (b) for L_{tot} = 1 m -HEX1

Fig. 4.3 shows the results of the performance analysis for HEX2. This layout provides generally lower performance than HEX1 for all regimes, and effectiveness values above 0.8 are only possible at significantly small hydraulic diameters (<1 mm) and/or velocities (<0.2 m/s). For any given velocity, the effectiveness of heat transfer decreases from laminar to turbulent regions; in the latter it is not possible to achieve ϵ-values above 0.45. In the optimum velocity range, the transition to turbulent flow conditions occurs for a hydraulic diameter between 4 mm and 10 mm. With respect to the pressure drop analysis, conclusions similar to those discussed for HEX1 can be drawn for HEX2 and the main outcomes identified from Fig. 4.2b are also valid for Fig. 4.3b. For HEX2, operation in the laminar region is generally not advisable; the ϵ-regions are much narrower than for the other regimes, making it difficult to operate the system continuously at a selected effectiveness value.

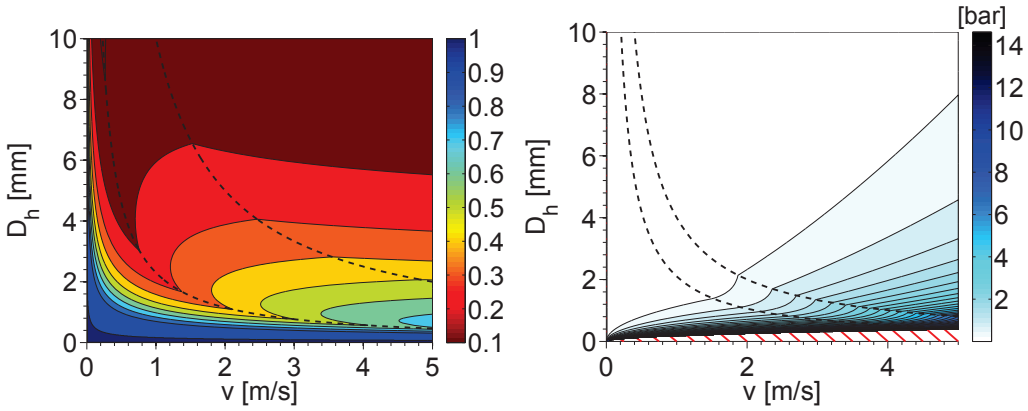

Figure 4.3: Effectiveness map (a); distributed pressure drops (b) for L_{tot} = 1 m -HEX2

From Fig. 4.4a, it is apparent that HEX3 provides the greatest performance of the three candidates. Unlike the two other designs, the effectiveness varies significantly for tube diameters larger than 10 mm and for this reason, the analysis is extended beyond such a value and up to tube sizes that correspond to poor performance.
No noticeable change in shapes of the ϵ-regions is observed since the transition from laminar to turbulent flow conditions is smooth due to the use of a modified version of the Bell-Delaware method [179].
Effectiveness values close to or above 0.9 can be obtained for a wide range of tube diameters and fluid velocities.
Considering the requirements listed in Table 4.1 for the optimum velocity range and practical tube diameters (i.e. >2 mm), the system can operate in the turbulent regime where the accuracy of the heat transfer correlations is higher and the fluid flow conditions are stable. For a given velocity the pressure drops in HEX3 are greater than in

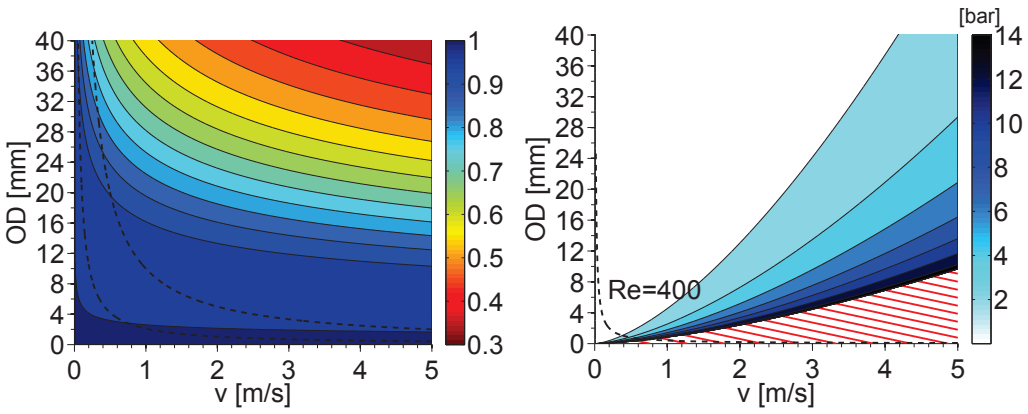

Figure 4.4: Effectiveness map (a); distributed pressure drops (b) for L_{tot} = 1 m -HEX3

HEX1 and HEX2 for any values of the characteristic length. As the equation employed (i.e. Kern method) is only valid for 400<Re<10^6 [179], the results under the dashed line in Fig. 4.4b are not shown. However, such a limitation does not affect the main conclusions that can be drawn for HEX3, as it refers to a region with non-practical tube sizes and/or very small velocities.
Reasonable values can be obtained for outer diameters above 9 mm where the effectiveness reaches values around 0.9. For instance, a loss of 0.7 bar can be achieved at $v_{o,m}$ for D_i=10 mm.
As mentioned before, the use of de-mineralized water can allow the operation at low velocities with reduced risks of deposit formation, moving the operational point towards lower pressure drops. However, unlike the other heat exchangers, high performance values and reasonable pressure losses for HEX3 can be achieved in the turbulent regime within the optimum velocity range. Therefore, there is no need to operate with demineralized water and low velocities to gain a modest performance enhancement.

As the sensitivity analysis presented in Appendix B shows, a reliable way to enhance the effectiveness for any configuration is to increase the heat transfer area by increasing the total length of the tubes from the base case reported here (L_{tot}=1 m).

4.4.2 Heat demand analysis and hydrogen-absorption time

The calculation of the time of reaction completion for each heat exchanger is used to identify the operational regions that provide practical reaction times and heat exchanger designs which fulfill the hydride cooling demand and ensure a continuous exothermic reaction. Although the description reported below refers to the MH heat pump, the main outcomes of the analysis are used at the end of this chapter to select the most promising heat exchanger configuration for a vehicular hydrogen storage application.

Even when high pressure systems are considered, the heat of compression developed in the tank is typically modest (c.a. 10%) when compared to the heat generated in the solid bed (see Section 3.8, Fig. 3.5a) and therefore is neglected in the present analysis. Under this assumption, the total heat that must be removed from the solid bed coincides with the heat of reaction.
The time of absorption reaction completion t_{rc} is calculated according to the equations presented in Appendix B and is shown in Figs. 4.5a, 4.5b and 4.5c for HEX1, HEX2 and HEX3 respectively. For a MHHP t_{rc} represents the time of the heat pump cycle stage in which the desired effect is generated, whereas for a hydrogen storage system it refers to the refueling time t_{ref}.
The diameter range in Fig.4.5 is between 0 mm and 40 mm to investigate the cooling time at relatively large tube sizes. It is worth mentioning that although the results below refer to a metal hydride thickness of 5 mm, which is large enough to well appreciate the differences in the cooling performance of the three configurations, the main conclusions that can be drawn are not affected by the chosen value of the bed thickness. They can be generalized and applied to the hydrogen storage system of interest in this work.

The diagonal red lines represent regions where t_{rc} exceeds a prescribed limit value set differently for each heat exchanger to ease the reading of the relevant results. The limits are defined as 2000 s, 200 s, and 60 s for HEX1, HEX2, and HEX3, respectively. The highest t_{rc} values correspond to the region where the ratio between generated energy and transferred heat is larger. These areas refer to relatively low cooling rates and thus to small diameter and velocity values for HEX1, where the coolant flows inside the tubes, and to large diameters and low velocities for HEX2 and HEX3, where the MH is inserted in the tubes. The plots show that t_{rc} reaches its maximum in the laminar regime and decreases towards the turbulent regime. As discussed in the Section 4.2, for long-cycle MHHPs the steady state assumption better describes the portions of heat pump stage between stage cycles where the operation is actually in a quasi-steady condition. Therefore, Fig.4.5 does not intend to be predictive on the low

time-end, but rather to show what heat exchanger design space would be required for a long-operation cycle and which cooling rates and reaction times are attributable to the operation of each heat exchanger.

HEX1 presents the largest reaction times, greater by a factor two to three orders of magnitude with respect to the other layouts. For a hydride bed thickness of 5 mm, times greater than 300 s are obtained for different diameters below 2 mm for a wide range of velocities. Practical times of approximately 5 min can occur at a diameter of 2 mm with realistic velocities in the neighborhood of 1 m/s.

In Fig.4.5b the reaction time for HEX2 is presented. For a fixed aspect ratio a, increasing the hydraulic diameter results in relatively larger inner tube volumes, where the MH is located, and decreased coolant rates. However, for $a = 0.5$, the HTF cross flow area is much larger than for HEX1 for the same hydraulic diameter and the ratio between generated energy and transferred heat is lower. In other words, the large cooling rates enable the transfer of all the generated heat in short times and at extremely low velocities. It can be observed that diameters of approximately 10 mm are needed to achieve reaction times of 1 min. At practical sizes and fluid velocities (e.g. $D_h = 3$ mm and $v = 0.8 m/s$), the reaction is completed in less than 10 s; this suggests that such a layout is not suitable for a heat pump application.

From Fig.4.5c, showing the results for HEX3, similar conclusions can be drawn as for HEX2, but with the distinction that shorter reaction times occur. The coolant that flows in the shell and over the tube bank provides very large cooling rates that can transfer the heat generated inside the tubes in even less than 60 s for a wide range of diameters and velocities. No practical reaction times are achieved for a realistically-sized design in a reasonable velocity range and the only way to extend further the reaction is to employ longer tubes. Since the hydride volume is linearly dependent upon the tube length while the coolant velocity remains constant, the reaction time increases linearly with the length. Indeed, although increasing the tube length also leads to higher heat transfer efficiencies and thus larger temperature differences (see Appendix B), their effect on the removed heat is modest at large effectiveness values and the main result consists in augmenting the hydride volume. For instance, at 20 mm and 1 m/s the reaction time goes from approximately 30 s to 300 s when the tube length is increased from 1 m to 10 m. It follows that the large HTF flow rates prevent the system from achieving adequate cooling times with realistically-sized tubes for a MHHP system. These results suggest that HEX3 could be of greater interest for applications where the final goal is to dissipate the reaction heat in a short time rather than maintaining a desired temperature lift in the HTF for a long period.

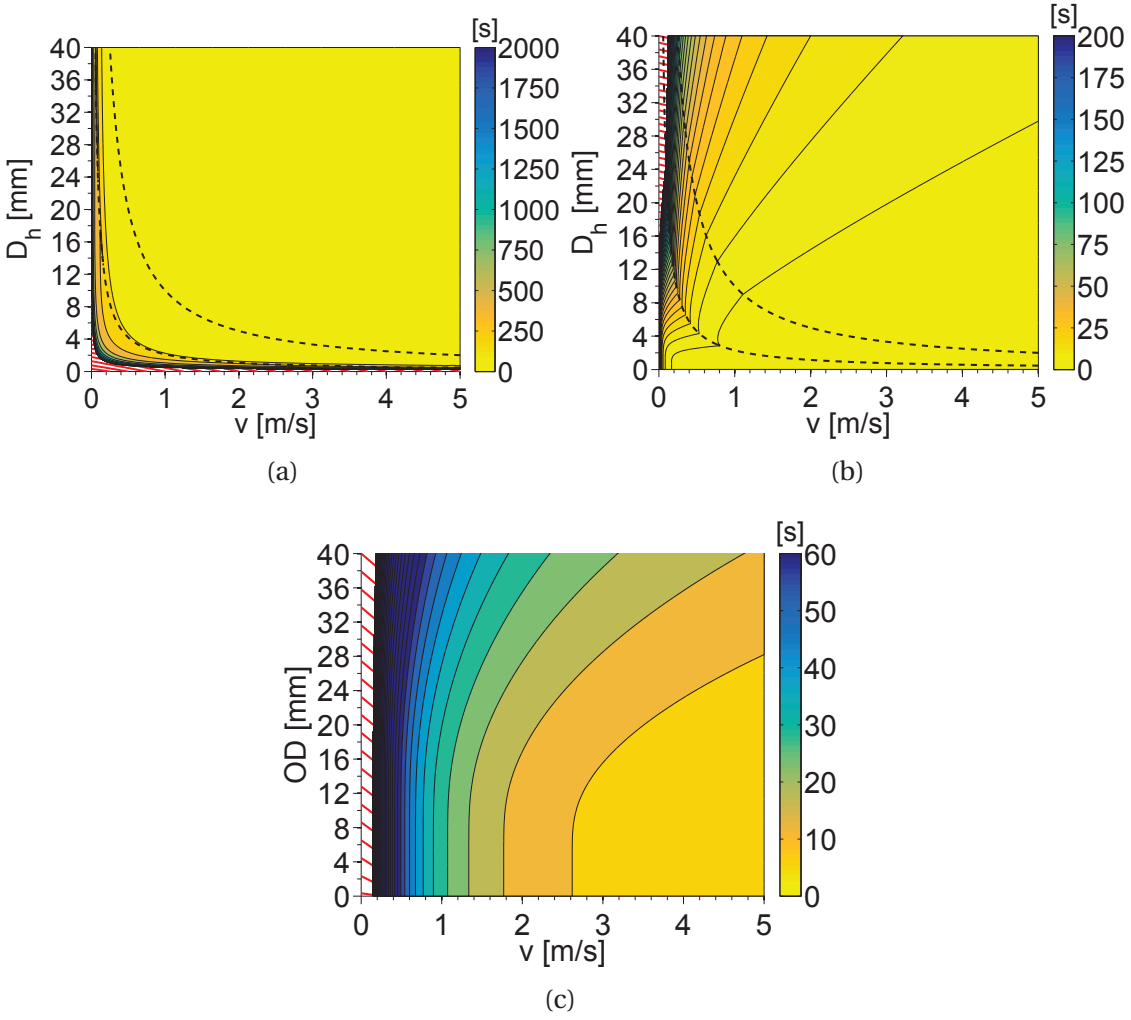

Figure 4.5: Time of reaction completion for HEX1 with a MH thickness of 5 mm (a), HEX2 with a=0.5 (b), HEX3 (c). L_{tot}=1m.

4.5 Conclusion

The results of a heat exchanger selection analysis for a metal hydride heat pump system are used to identify the most promising layout for a MH hydrogen storage application.

A thermal model was developed for performing an analysis of three layouts of shell-and-tube heat exchangers. It is applicable to any type of absorbing alloy and takes into account mechanical and operational constraints.
In HEX1, the coolant flows inside tubes surrounded by metal hydride. In HEX2, the metal hydride is packed in the tubes and the coolant flows parallel to the tube in a standard tube-in-tube layout.
In HEX3, the metal hydride is also packed in the tube, but the coolant circulates in combined cross-parallel flow over the tube bank.
While the former is found to be most suitable for MHHP applications (see Appendix B for more details), the latter provides modest pressure drops and greater cooling performance and thus, shorter reaction times for hydrogen absorption which is in turn of interest for MHSSs. This advantage adds to the convenience of using a tubular tank in place of a chamber tank design for vehicular hydrogen storage purposes.
Firstly, holding the metal hydride in tubes, rather than in a large-diameter vessel, eases the confinement and compaction of the hydrogen-absorbing alloy, which is hard to handle especially in the powder form.
Additional advantages of such a configuration that are particularly important for high-pressure MHSSs, include: reduced tank weight and maintenance cost, increased heat transfer performance and uniformity of reaction in the solid bed.
As the mechanical component that is dedicated to bear the high-pressure hydride is a small-diameter tube, and not a large-diameter vessel, it can be designed with a smaller thickness for any given pressure. This results in lower tank weight as the vessel has the only function to provide the volume for the circulation of the low-pressure HTF and therefore, it can be constructed with a light plastic material. On the other hand, smaller thicknesses also imply smaller thermal resistance and reduced parasitic mass during heating/cooling.
The confinement of the active alloy in small tubes promotes the realization of a uniform pattern of absorption/desorption, because it is easier to design the system according to the critical MH thickness principle.
The tubular tank design with MH tubes is also attractive for its modularity which enables, in principle, to ease the maintenance of the system by replacing only the storage module that presents malfunctioning. A consequent reduction in the maintenance cost of the system is therefore expected.
At the end, the storage tank can be a cheap plastic vessel with integrated thin metallic

tubes that are easily obtainable in the market, that serve the function of independent hydrogen-storage modules.
For all these reasons, the tubular tank design with the HEX3 configuration is chosen as the most promising candidate to fulfill the targets and requirements defined in Subsection 2.6.1. Such a layout is investigated in detail in Chapter 6, where the modeling platform is described, to address the advantages and drawbacks of the system with respect to a refueling analysis.

5 Integration of phase change materials in compressed hydrogen gas storage systems

5.1 Introduction

In this chapter, the advantages and drawbacks of the integration of a phase change material in a CHG tank are addressed with respect to the targets presented in Section 2.6.2. The results here reported mainly refer to the research published in Ref. [114].
As discussed in Chapter 2 the main objective of this study is improving the state of the art technology by enhancing the energy efficiency of the refueling process and at the same time reducing the cost. In order to do so, fueling analyses are performed to investigate the novel system's behavior under practical operating conditions. In Subsection 5.3.2 the energy benefits of the proposed technology and the effect of the phase change on the stored hydrogen mass are presented. The influence of different material properties and design parameters are investigated in Subsection 5.3.3.
Finally, strategies that can further improve the novel proposed tank are suggested in the conclusive section of the chapter.

The integration of a PCM is investigated as a valuable solution to passively absorb the heat developed in the tank during fueling and reduce the cooling demand and component cost at the refueling station. The hydrogen temperature rises sharply in the tank during fueling because of the compression heat, whereas the inverse Joule-Thomson effect only plays a modest role. The materials that are used in the walls of standard tanks must be kept below 85 °C in order to ensure the mechanical integrity of the vessel. As the maximum temperature for hydrogen compressed up to 700 bar well exceeds the maximum allowed value, a significant cooling is requested at the refueling station before tank filling. The gas is cooled from the ambient temperature down to -40 °C to prevent the hydrogen maximum temperature inside the tank to reach 85 °C during pressurization and preserve the mechanical integrity of the storage system even in presence of non-uniform temperature distribution at the tank wall

and local effects as hot spots. However, the resulting system is costly in terms of both energy and capital investment due to the low operation temperatures and the non-conventional technology employed in the hydrogen cooling. Another drawback of the present fueling procedure concerns the lack of reliability that occurs whenever active cooling systems are used. Indeed, even in presence of redundant heat exchangers, possible malfunctioning or failures can threaten the normal operation of the fueling station and hence, the fueling of the vehicle.

Phase change materials have been widely investigated as options to store the thermal energy coming from intermittent sources and enable a continuous availability of the stored heat. Their use provides considerable advantages when compared to technologies that are based on sensible cooling/heating processes. Indeed, great convenience arises from the possibility of using their high energy storage densities to store large amounts of heat in a reduced space, as well as the capability of absorbing and releasing the heat via isothermal heat transfer. These aspects have made PCMs promising candidates for a large variety of applications, including solar energy storage, air conditioning of buildings and spacecrafts, passive cooling of electronics, textiles and fabrics [116, 180–187].
A considerably less explored area of study is hydrogen storage. In such a field, research has mainly focused on employing PCMs to absorb the heat of reaction that is generated during hydrogen absorption in metal hydride tanks for stationary applications [188, 189].
To the best of the Author's knowledge no studies are available in the literature on the application of interest in this chapter.

The use of integrated passive cooling solutions in the tank is here investigated with the final aim to reduce the cooling demand at the refueling station by absorbing a significant amount of the heat of compression inside the tank and, at the same time, keeping the walls below the critical temperature.

5.2 Methodology

A computational model that enables to calculate the PCM temperature and provides information on the position of the moving melting layer is developed by means of the effective capacity method, as presented in Appendix C. Then, such a model is integrated in a larger simulation system that comprises the hydrogen storage tank and a fictitious refueling station.
The phase change model is applied to a 10-mm-thick layer placed at the inner wall of a storage tank, which is filled with high pressure hydrogen. Such a thickness value is

the result of an optimization analysis discussed in Subsection 5.3.1.
The gas is delivered at practical fueling conditions that are function of the tank type and ambient temperature according to the fueling protocol implemented in the refueling station model, as explained in detail in Subsection 5.2.2. The results are used to evaluate the effect of the PCM on the stored hydrogen mass and temperature at the walls for the novel vessel design in comparison with the standard tank solution currently available on the market.
The developed model allows for both charging and discharging analyses. However, only the results that refer to the former are presented in this chapter, as the phenomena that occur during discharging can easily be understood based on the outcomes of the charging process.

5.2.1 Phase change material

The results presented in this chapter are obtained with a paraffin wax as the phase change material. This PCM was selected according to the criteria identified for hydrogen storage applications in Section 2.4.2. Its properties are reported in Table 5.1.

Table 5.1: Thermo-physical properties of the selected phase change material at 55 °C, Ref. [190].

	Property	Value	Unit	Symbol
Solid	Conductivity	0.24	$W \cdot m^{-1} \cdot K^{-1}$	$k_{PCM,s}$
	Specific heat capacity	2905	$J \cdot kg^{-1} \cdot K^{-1}$	c_{PCM}
	Density	785.3	$kg \cdot m^{-3}$	$\rho_{PCM,s}$
	Latent heat of phase change	224360	$J \cdot kg^{-1}$	λ
Liquid	Conductivity	0.18	$W \cdot m^{-1} \cdot K^{-1}$	$k_{PCM,l}$
	Specific heat capacity	2905	$J \cdot kg^{-1} \cdot K^{-1}$	c_{PCM}
	Density	769.2	$kg \cdot m^{-3}$	$\rho_{PCM,l}$
	Kinematic viscosity	6.5×10^{6}	$m^2 \cdot s^{-1}$	$\nu_{PCM,l}$
	Thermal expansion coefficient	8×10^{3}	K^{-1}	$\beta_{PCM,l}$

As the selected paraffin wax is not a pure substance, it is more correct to refer to a range for the melting temperature, rather than to a single value. For the PCM of interest here, such a range is comprised between 52 °C and 56 °C. Therefore, the value of 55 °C to which the properties listed in Table 5.1 refer, lies within the melting range of the considered material. From the table, it can be noticed that the material presents poor thermal conductivities, which are well below 1 $W \cdot m^{-1} \cdot K^{-1}$ for both

the solid and liquid phase. The specific heat capacity value is constant and thus, is represented with the notation c_{PCM} for both phases. The kinematic viscosity and thermal expansion coefficient, defined for the liquid phase, are used to compute the parameters involved in the heat transfer by natural convection according to the model reported in Appendix C.

Although, the results here reported refer to the paraffin wax whose properties are listed above, other materials compositions can be selected by the user in the simulation platform. This is discussed in detail in Chapter 6.

5.2.2 Fueling model

The concept of the fictitious refueling station model and its operation principle are here presented along with some main results of the charging process. A simplified sketch representing the dynamic fueling model implemented in Dymola^{TM} is presented in Fig. 5.1.

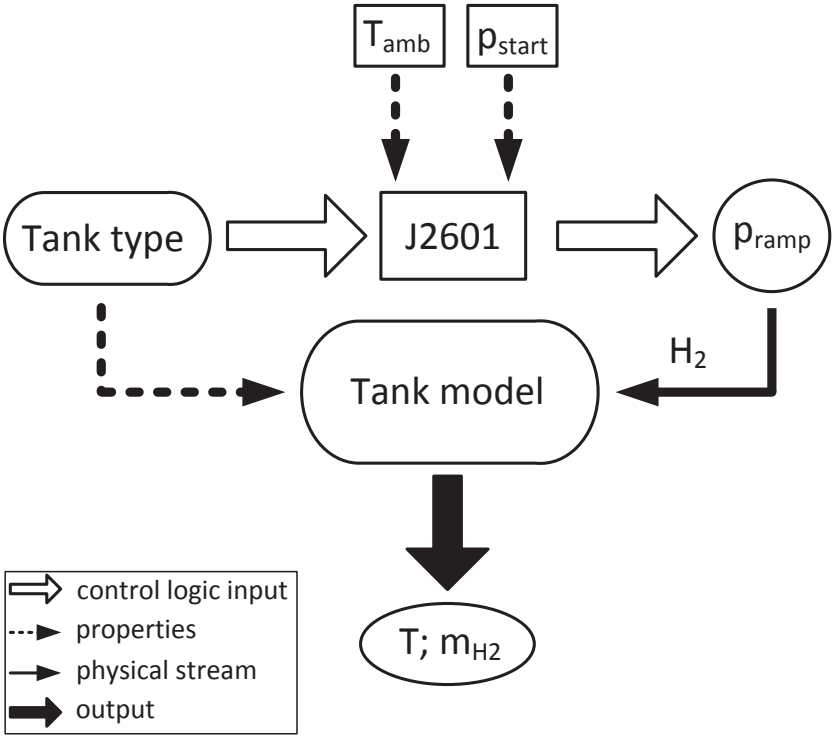

Figure 5.1: Sketch of the computational fueling model structure.

From such a figure, it can be observed that the tank type (e.g. Type III, Type IV) with its

physical properties and initial internal pressure (p_{start}), and the ambient temperature (T_{amb}) constitute the main inputs that are passed to the J2601 model component that selects the hydrogen charging pressure (350 or 700 bar) and its pressure ramp according to the refueling protocol SAE J2601 [100]. For instance for a Type IV tank with an initial tank pressure of 20 bar and an ambient temperature of 20 °C, the pressure ramp is 282 bar and the pressure evolution in the tank is shown in Fig. 5.2.

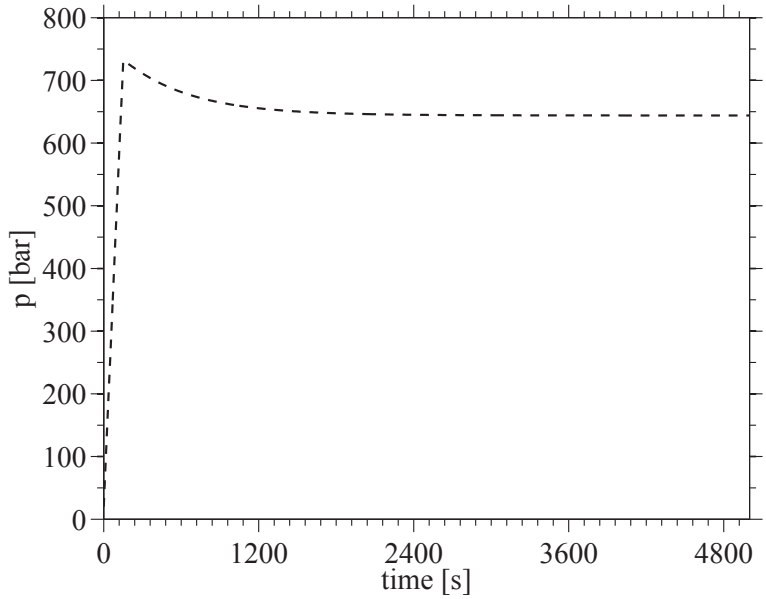

Figure 5.2: Pressure profile in a Type IV tank. T_{amb} = 20 °C; p_{start} = 20 bar.

From the figure one can notice that the fueling process is terminated at a final pressure larger than the reference value of 700 bar. This occurs because the storage target the density of hydrogen at 700 bar and 15 °C. As in the considered case the gas is warmer than the reference value, an over-pressurization of 32 bar is required to reach the target density.

With respect to Fig. 5.1, the stored hydrogen mass, its temperature and the heat that is transferred to the surrounding walls (and PCM thickness) is calculated in the tank model.
The main outputs of the model include the hydrogen temperature, the temperature profile in the PCM layer and in the walls at different locations, as well as the stored hydrogen mass (i.e. m_{H2}).
In the model, it is possible to select the boundary condition for the outer surface of the tank as adiabatic or alternatively calculate the heat losses due to the natural convection in the ambient air. The hydrogen temperature profiles that correspond to these cases are presented in Fig. 5.3a for a standard Type IV tank (i.e. no PCM is

integrated) with a refueling temperature of 20 °C (i.e. absence of pre-cooling at the refueling facility). The gas temperature increases until the pressurization phase is completed and then decreases for the heat transferred to the tank and the ambient. As one could expect, larger temperatures occur in absence of external cooling. The effect of the heat transfer with the ambient provides noticeable temperature reductions at very large times compared to the pressurization phase. This can be better appreciated in Fig. 5.3b where the results for the non-adiabatic case are presented for an extended simulation time. With a heat transfer coefficient of for natural convection, the system requires more than 13 hr to reach the thermal equilibrium with the ambient.

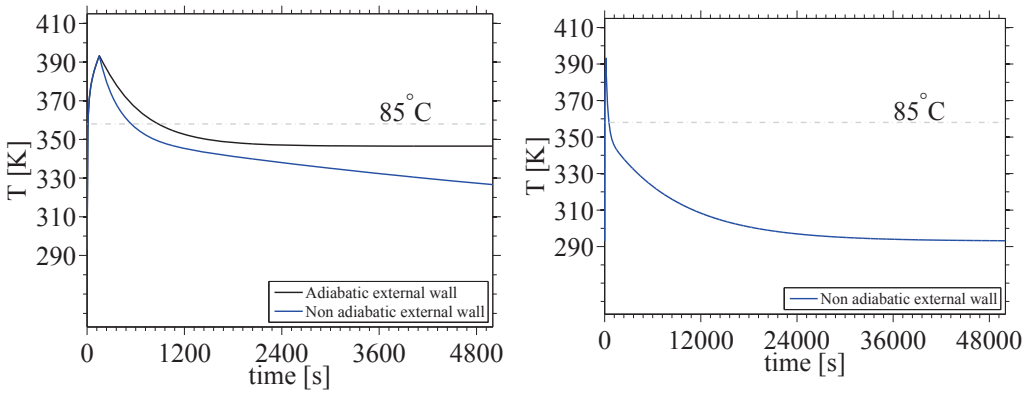

Figure 5.3: Hydrogen temperature profiles in a standard Type IV tank for: adiabatic external wall and non-adiabatic case (a), non-adiabatic case with extended time of simulation (b). No hydrogen cooling at the station.

For the scope of this study, the adiabatic case provides a more conservative approach and it is therefore used to obtain the results presented in the result section. However, the non-adiabatic case is useful to assess the ability of the developed model to predict the complete thermal cycle of the PCM layer (i.e. solid-liquid-solid) and therefore is investigated for the novel tank design in Appendix C.

5.2.3 Novel tank design

In Fig. 5.4 the dimensions of the novel tank proposed in this study are shown, while the properties of the thermo-plastic liner and carbon fiber are given in Ref. [92] with respect to a Type IV vessel. The inner volume is approximately 126 L, which is a realistic size for a practical storage system to be used in a FCEV.

In practice, a thin aluminum layer can be used to keep the phase change material in

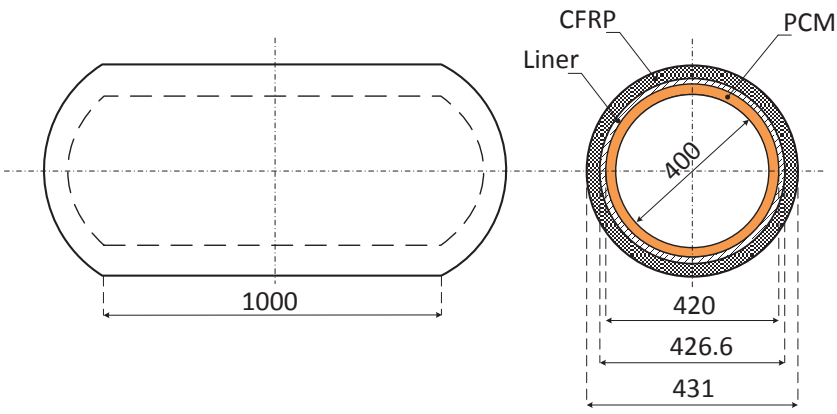

Figure 5.4: Longitudinal and transversal sections of the proposed novel Type IV tank design. All dimensions are in mm.

place and prevent it to flow to the bottom of the tank during melting. The thickness of the confinement layer is hereby assumed to be small enough to have a negligible influence on the total tank's volume and weight as well as on the heat transfer process. Further studies should focus on the selection of the most adequate technology to confine the PCM and the analysis of its mechanical stresses during periodical fueling. These aspects are out of the scope of the present work which aims at addressing the potential convenience of the proposed technology from an energy-saving perspective. In Table 5.2, an immediate comparison between the overall size and weight of the two tanks is given. The two tanks are compared with respect to the same inner volume.

Table 5.2: Type IV tank and novel design: size and weight.

Case	$\mathbf{V_{tot}}$ [L]	$\mathbf{m_{tank}}$ [kg]	$\mathbf{m_{PCM}}$ [kg]
Standard Type IV	160	45.6	/
Type IV with PCM	174 (+9%)	57.75 (+27%)	10

When a 10-mm-thick layer is inserted on the inner wall, the overall tank volume increases by 9%, and it's mass by 27%. Such a mass increase is mainly due to the PCM, which accounts for 10 kg of the extra 12 kg added to the tank. The rest is due to the larger masses of the liner and carbon fiber reinforced polymer that result from keeping the same thickness at larger radii. At the end, while the difference in volume is modest, the mass increase appears quite significant. However, the extra weight added to the system is relatively negligible when the comparison is made with respect to the overall FCEV mass.

5.3 Results

5.3.1 Thickness analysis

The discretization of the PCM layer enables to identify the solid/liquid front as it moves toward the tank wall, making possible to determine whether exists a portion of the PCM material that does not undergo the phase change and hence provides mainly an insulation effect rather than heat absorption. In case this occurs, it should be investigated whether it is possible to decrease the PCM thickness, reducing the extra mass and volume added to the vessel, while maintaining the same thermal performance.
Different thicknesses are here investigated, ranging from 2.5 mm to 50 mm. Such a range also includes the nominal condition presented in Fig. 5.4, which considers a 10-mm-thick layer.
Three different cases can be identified by investigating the adiabatic temperature T_{adiab}:

1) $T_{adiab} > T_m + \omega_2$

2) $T_m - \omega_1 < T_{adiab} < T_m + \omega_2$

3) $T_{adiab} < T_m - \omega_1$

where $T_m - \omega_1$ and $T_m + \omega_2$ represent the lower and upper limits of the melting range respectively (see Appendix C for details).
For case 1) all the PCM melts and in stationary conditions the material is in the liquid form. This is in principle the most favorable scenario, as it implies that the entire mass of PCM has experienced the phase change and absorbed the energy that corresponds to its latent heat.
Case 2) implies that the material is partially melted; hence its latent heat has not been entirely exploited.
Case 3) considers equilibrium temperatures below the melting range, indicating that only the sensible heat has been exchanged and hence, considering the poor thermal properties of the paraffin wax, the PCM behaves as an insulation thickness during the phase change process.

In Fig. 5.5 the melting range is represented as a gray area. The results are presented for a location *x½* that corresponds to the half-thickness of the corresponding layer. In order to give the reader direct information of the total thickness' value, *x½* is expressed as the entire thickness divided by two in the figure's legend. As expected, for thicker

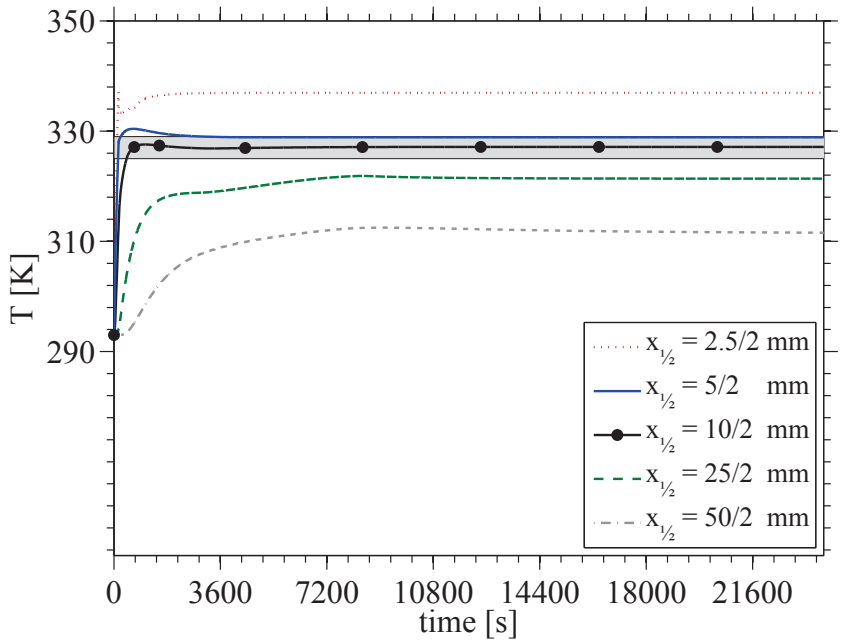

Figure 5.5: Temperature profiles at the half of the PCM layer for different thicknesses.

layers the adiabatic temperature decreases and the system reaches the stationary conditions at larger times. For a thickness of 5 mm T_{adiab} lies on the upper value of the melting range and therefore, this condition belongs to case 1). It follows that layers below or equal to 5 mm ensure a complete melting of the PCM thickness, whereas above such a value, T_{adiab} belong to case 2) or case 3).
It can be observed that for the nominal thickness of 10 mm, the temperature at stationary conditions assumes the value of 326 K which lies within the melting range. As a result, case 2) occurs and the actual cooling does not take advantage of the entire latent heat available. For layers of 25 and 50 mm, T_{adiab} settles at approximately 317 and 301 K respectively and the material only exchanges sensible heat. The large thermal capacity of the PCM is unused.
As only the adiabatic temperatures have been discussed here, the comparison among different thicknesses has been made with respect to large times, when the system reaches stationary conditions. However, in order to further investigate the effect of the thickness on the system's cooling performance, a dynamic refueling analysis for different layer thicknesses is presented in Subsection 5.3.3).

5.3.2 Refueling analysis and energy savings

A comparison in results between a standard Type IV tank and the design with integrated PCM is here provided. The temperatures in the plots refer to the location corresponding to half of the thickness of each wall layer.

In Fig. 5.6 the results obtained under the assumptions of adiabatic outer wall and absence of hydrogen cooling at the fueling station are shown. The gas is filled at the ambient temperature of 20 °C, which is the system's equilibrium temperature before the fueling takes place, and rapidly heats up due to the compression into the tank. With a pressure ramp of 282 bar/min, the fueling is completed in approximately 150 s, and the gas reaches its peak temperature around 390 K. Being the outer tank wall adiabatic, the heat can only be transferred from the gas to the surrounding walls and the system tends to thermal equilibrium.

In Fig. 5.6a, where the results for a standard Type IV tank are presented, the adiabatic temperature is around 74 °C and the thermal equilibrium is reached at 3300 s. During fueling, the gas thermal convection coefficient is set to 150 $W \cdot m^{-2} \cdot K^{-1}$ (see Ref. [92]) and the plastic liner experiences higher heat rates, whereas, when the filling process is completed, the convection coefficient drops to 50 $W \cdot m^{-2} \cdot K^{-1}$ and the liner undergoes an abrupt decrease in temperature, because more heat is transferred outward to the wall, and then it heats up again. Under these conditions, the adiabatic temperature is below the critical value for both the liner and CFRP. However, the presence of hot spots where the local temperature might be greater than 85 °C should not be excluded, with the result that the mechanical integrity of the tank might be damaged.

In Fig. 5.6b the temperature results that refer to the novel Type IV tank with PCM material are presented. The system reaches the thermal equilibrium at a temperature around 54 °C, which is approximately 20 °C lower than for the standard tank case. It follows that, the phase change material succeeds in absorbing a significant amount of the heat of compression, keeping the walls considerably below the critical temperature at any time. However, as in the previous case, the hydrogen temperature seems affected by the heat transfer to the walls only after the filling process is completed and large times are required to reduce the gas temperature below 85 °C and later reach the thermal equilibrium. By comparing Fig. 5.6b with Fig. 5.6a, it can be observed that the peak temperature is reduced by only 2 K when the phase change material is inserted, meaning that the heat transfer rates are not high enough to effectively exchange the heat of compression during fueling. Indeed, the high thermal resistances at the hydrogen/gas interface, as well as the poor thermal properties of the paraffin wax, limit the gas cooling and slow down the heat transfer process.

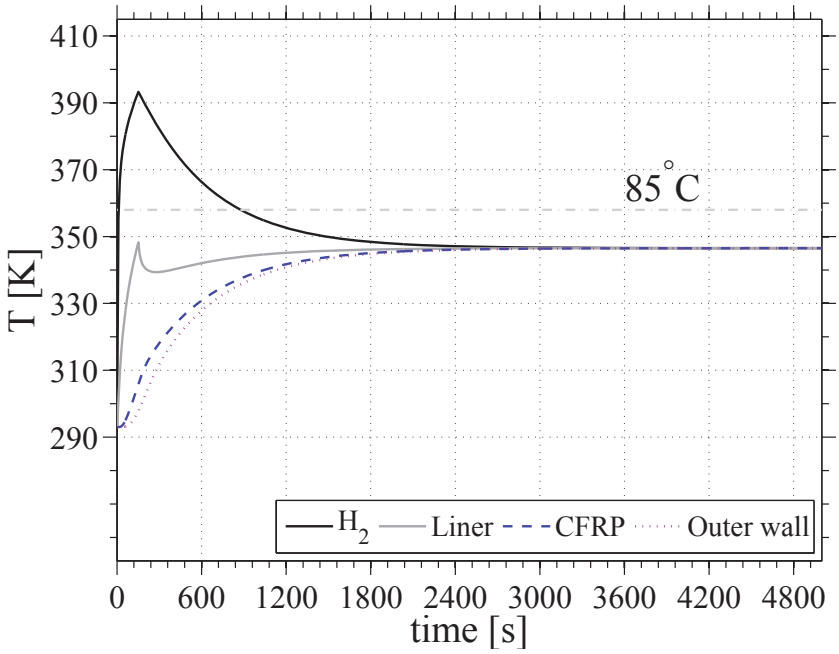

(a)

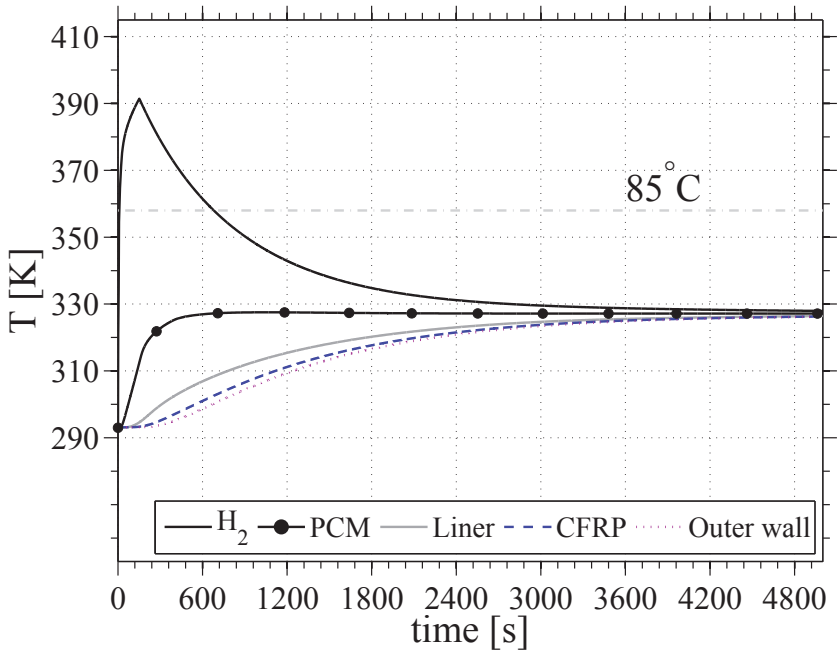

(b)

Figure 5.6: Temperature profiles for a standard Type IV tank (a) and for a Type IV tank with integrated PCM at the inner wall (b). No hydrogen cooling at the station.

At the end, two main conclusions can be drawn. First, the presence of hot spots at the walls cannot be entirely excluded, although the insertion of the PCM layer makes such a situation quite unlikely; second, the gas density during fueling is the same for the two tanks, resulting in the same overall mass that is fueled into the storage system. With respect to the latter assertion and even if it is assumed that no hot spots would result in practice, the present novel design cannot provide the same storage performances of a regular CHG system, where the hydrogen is cooled prior to filling.

This can be observed in Fig. 5.7a where the hydrogen mass inside the tank is presented at different gas inlet temperatures. At time zero, the gas inside the tank is at the initial conditions of 20 bar and 20 °C and the resulting initial hydrogen mass is 0.2 kg. When refueling starts, the gas mass increases until the target charging pressure is reached at 150 s. Then, the inlet valve closes and the stored mass remains constant. For the same storage volume, the overall fueled mass is reduced from 4.67 kg, when hydrogen is filled at -40 °C, to 4.17 kg in absence of gas cooling. This corresponds to a decrease by 12% in the storage capacity of the system.

Ideally, the novel tank design should guarantee the mechanical integrity even in absence of gas cooling and store the same amount of hydrogen as a regular gas-cooled system. If this could be realized, the only drawbacks would be the larger weight and volume, whereas the benefits would include the energy saving and the heat exchanger size-reduction/removal at the refueling station, as well as the increase in the filling process reliability.

In Fig. 5.7b the cooling energy per refueling that is needed at the refueling station is presented for different temperatures at the tank inlet along with the energy saving calculated with respect to the standard cooling case (i.e. TH2 = -40 °C). The reduction in cooling demand is nearly linear with the charging temperature, ranging approximately from 16.6% to 66.6% when the inlet gas temperature is increased from -40 °C to -30 °C and 0 °C respectively. As in the present study the COP and its dependency upon temperature are unknown for the actual refrigeration system in use at the refueling station, it is hereby assumed that the energy savings coincide with the reduction in cooling demand. This corresponds to having a refrigeration system with a unitary COP and thus the obtained energy savings in Fig. 5.7b are to be intended as maximum values. Such an assumption seems not to be far from reality, if we consider that a COP of approximately 1.1 was recently estimated for a refrigeration system operating at the same ambient temperature considered in this work (i.e. 20 °C) and for a final hydrogen temperature of -40 °C [191]. In practice, when detailed information on the cooling performance is available, it is possible to calculate the real energy savings by dividing their maximum values by the actual COP.

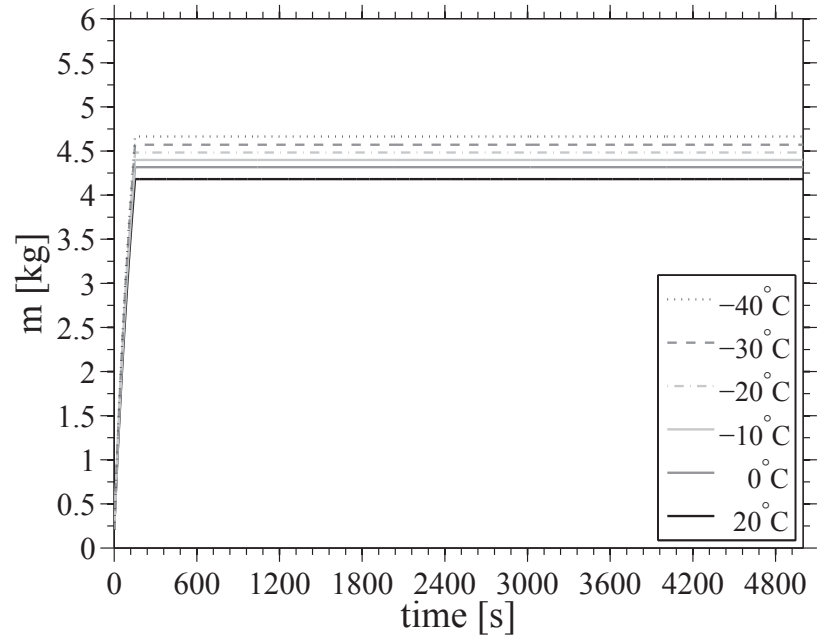

(a)

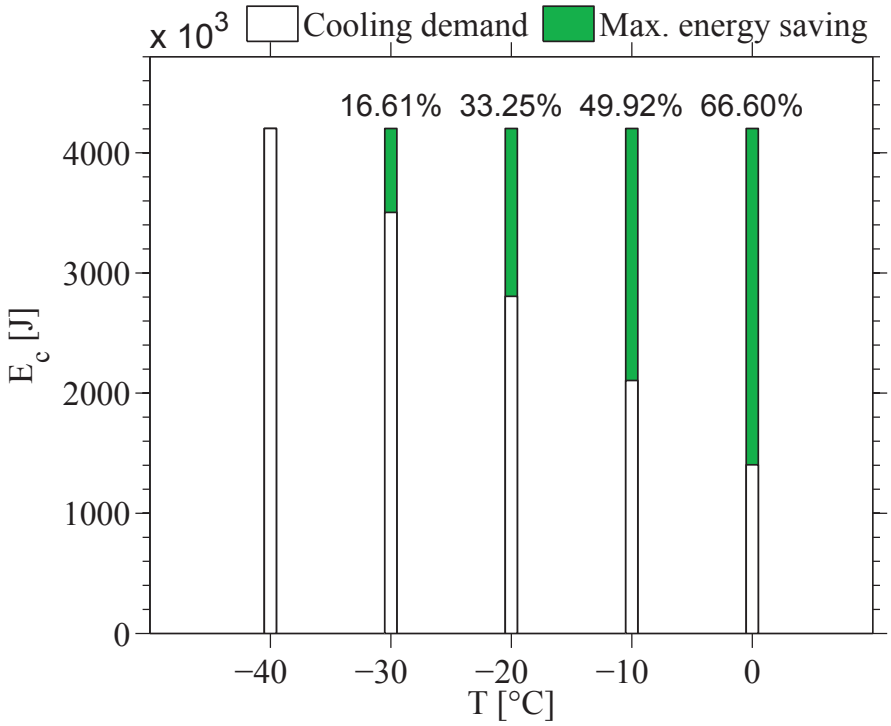

(b)

Figure 5.7: Hydrogen mass fueled into the tank for different inlet temperatures (a); Cooling demand per refueling at the refueling station and relative maximum energy saving with respect to an inlet gas temperature of -40 °C (b).

Although from an economic perspective the most favorable case occurs in absence of gas cooling, temperatures around -10 °C allow the use of heat exchangers normally employed in the refrigeration industry, resulting in a considerable cost reduction when compared to non-conventional cooling systems. However, in order to exploit the complete potential of this solution and realize a storage system that is attractive on the market, the tank should enable the same storage performance as the current technology at inlet gas temperatures greater than -40 °C. In order to achieve such an objective, the heat transfer from the gas to the phase change material must be enhanced and, at the same time, the PCM physical properties should be carefully tailored.

5.3.3 Parametric analysis

Different parameters that are expected to control the heat transfer process are varied to investigate their influence on the hydrogen temperature evolution. These parameters include the main PCM's thermal properties, thickness and the heat transfer area.
The hydrogen convection coefficient is not varied in the present analysis as the thermal resistance is low compared to the PCM resistance and therefore, no considerable effects on the gas temperature are expected to occur by its augmentation. In addition, the hydrogen convection coefficient is determined by the refueling conditions and the resulting turbulence inside the tank and hence is fixed for a given design.

PCM properties

In this section, the effect that the main physical properties have on the hydrogen peak temperature is investigated. The main goal is to determine whether it is possible to reduce the gas temperature at the end of refueling by individually improving the thermal properties of the PCM.

The comparison on the gas temperature during filling is presented in Fig. 5.8 for different values of thermal conductivity, specific heat capacity, density and latent heat of phase change. It must be noticed that the variation ranges for such properties comprise upper values that are non-practical for conventional materials. This choice has been made to obtain a broad view on the extent to which the gas temperature is dependent upon a large variation in the main thermal properties of the PCM.
In Fig. 5.8a the thermal conductivities for solid and liquid phases are increased from the nominal conditions by a factor up to 10^3. Different strategies can be employed to enhance the thermal conductivity, as the use of a PCM with favorable thermal properties, enhancing the heat transfer by forming PCM stable composites with a highly

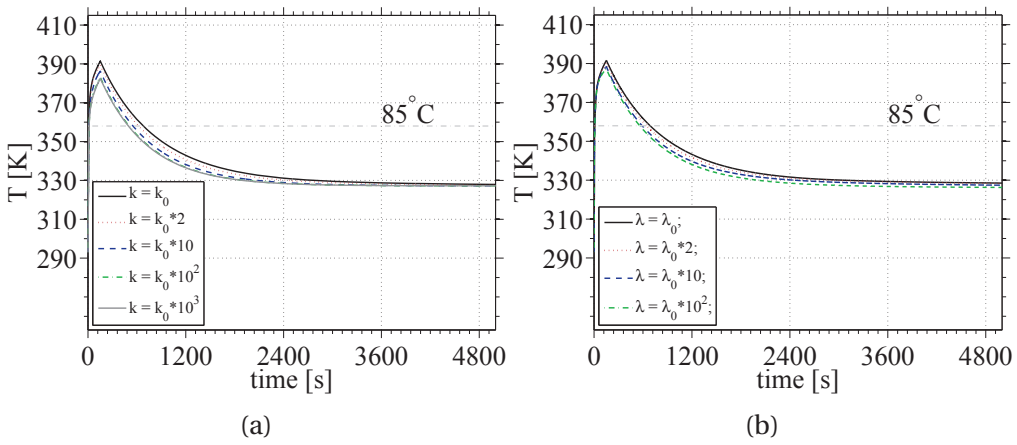

Figure 5.8: Hydrogen temperature evolution during fueling for different values of PCM's thermal conductivity (a) and latent heat (b).

conductive material, as well as inserting the PCM in a metallic structure [192, 193]. Results show that only modest reductions in the peak temperature occur for such a wide variation range. The maximum hydrogen temperature decreases by only 2 K when the conductivity is doubled and by 4 K when it is augmented by a factor of 10. A more significant reduction can be observed when the conductivities are of the same magnitude as the hydrogen convection coefficient. The gas temperature at the end of fueling reaches a maximum value of 382 K, which is approximately 10 K less than the value obtained at nominal conditions. Further increases in conductivity only have a negligible effect and the gas temperature curves differ by less than 1 K when the multiplying factor for k_0 increases from 10^2 to 10^3. As the dominating thermal resistance has now become the convection one on the hydrogen side in order to additionally augment the heat transfer, the thermal resistances must be reduced together.
Fig. 5.8b shows a negligible dependency of the gas temperature upon the latent heat at any time of the filling process as well as after the refueling is completed. In particular, the peak temperature experiences a negligible reduction between the nominal conditions and the maximum latent heat value in the range. This occurs because, although greater latent heats increase the thermal capacity of the system during phase change, the poor thermal properties limit the heat transfer rates preventing the entire PCM mass to undergo the phase change in the short time of the filling process. As a result, the effect of larger latent heats is more important after the refueling is completed, where the divergence of the temperature curves is more evident, leading to lower temperatures at thermal equilibrium. However, the adiabatic temperature remains approximately constant and a negligible reduction of nearly 2 K occurs for an increase in λ by 10^2 from the nominal conditions. The reason is that at present conditions and

for the current design, the lowest adiabatic temperature that the system can reach corresponds to the lowest value in the melting range (i.e. 52 °C) at which the temperature curve for the PCM tends to flatten until the phase change is completed. As for λ_0 the temperature at equilibrium already lies in the melting range and corresponds to 54 °C, it is not possible to decrease T_{adiab} further than 2 K even at large λ. Smaller thicknesses that would lead to higher equilibrium temperatures would leave more room for T_{adiab} reduction at large latent heats.

In Fig. 5.9 the effect of the specific heat capacity and density on the gas temperature during fueling is investigated within a range that goes from the nominal conditions, to ten times the nominal case and a value corresponding to an increase by a factor of 10^2 from the nominal case. In Fig. 5.9a the gas temperature during fueling is shown

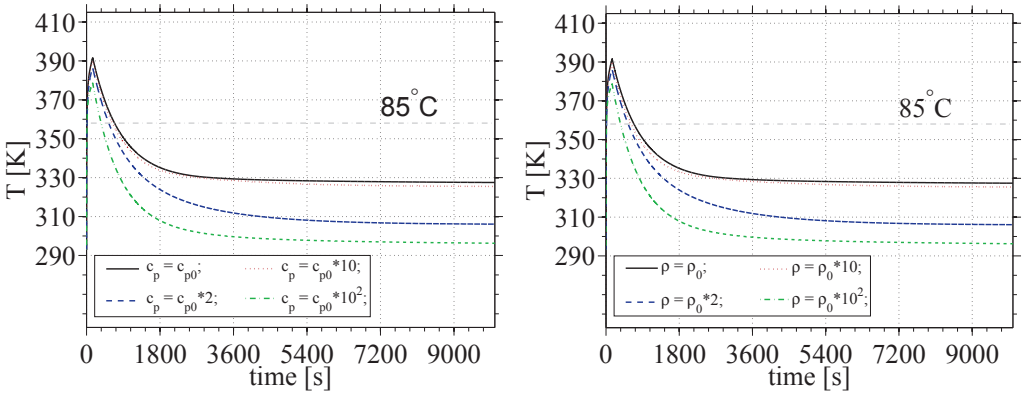

(a) (b)

Figure 5.9: Hydrogen temperature evolution during fueling for different values of PCM's specific heat capacity (a) and density (b).

for different specific heat capacity values, ranging from the nominal conditions to a value increased by a factor of 10^2. As it was found in the conductivity analysis, the peak temperature only presents a poor dependency upon c_p. Indeed, the main effect of using a PCM with greater thermal capacities consists in increasing the overall heat that can be absorbed within the phase change material. This can be observed by comparing the adiabatic temperatures obtained for the different c_p values. Doubling the heat capacity only reduces T_{adiab} by 2 K, while for specific heat capacities augmented by a factor of 10 and 10^2, the adiabatic temperature drops by 21 K and 31 K respectively. On the other hand, the maximum gas temperature reduces by only 1.5 K, 5 K and 13 K respectively, in the same range of variation for c_p. From Fig. 5.9b, it is possible to draw similar conclusions, as the dependency of gas temperature upon the PCM density replicates the trend observed in Fig. 5.9a. This is valid for both the gas

maximum and adiabatic temperatures. As for the c_p augmentation, an increase in the PCM density provides a greater thermal capacity for the heat-absorbing system and hence, a lower temperature at equilibrium, but does not affect much the rate at which the heat transfer occurs.
It should be remembered that the upper limit in the density range is non-practical and that the modest benefit in peak temperature reduction that is gained at such density value is overcompensated by the corresponding increase in the system's mass, which would increase by 10^2 kg.

At the end, it appears that it is not possible to identify a significant dependency of the peak temperature upon a single thermal property of the PCM. For a given design, this result suggests that a combination of different properties values and other parameters should be investigated.

PCM thickness

In Fig. 5.10 the evolution of the hydrogen temperature over time is shown for different PCM thicknesses.
In Fig. 5.10a it can be observed that the main effect of operating at thicker layers is the reduction of T_{adiab}, whereas the peak temperature appears unvaried. The former outcome has been already pointed out in Fig. 5.5 with respect to the PCM temperature at a location corresponding to half thickness of each layer. Stationary conditions occur at larger times as the thickness increases, ranging approximately from 3600 s to 23760 s for a layer of 2.5 mm and 50 mm respectively. In addition, it can be noticed that for the first 9360 s the temperature profiles are nearly overlapping for thicknesses of 5 mm and above. In such a time span, the stationary conditions are not reached for the PCM located at more than 10 mm which starts melting at 9360 s, participating significantly to the heat absorption and producing a further decrease in temperature. Figs. 5.10b and 5.10c present a zoomed-in view of the previous figure at the end of refueling, for a better comparison among the peak temperatures. Such figures point out the negligible effect of larger thicknesses on the maximum gas temperature. This is due to the poor heat transfer rate at the hydrogen/gas interface, resulting in a decrease by 7 K when the thickness is increased from 2.5 mm to 50 mm. This temperature reduction is more important for layers up to 25 mm, whereas is negligible at larger thicknesses.

At the end, when comparing the tanks with 10 and 5 mm layers, the difference between adiabatic and peak temperatures is modest and hence, the cooling performance can be considered nearly the same. Similar conclusions can be drawn for the amount of hydrogen when considering the two different thicknesses of the layer. The only actual

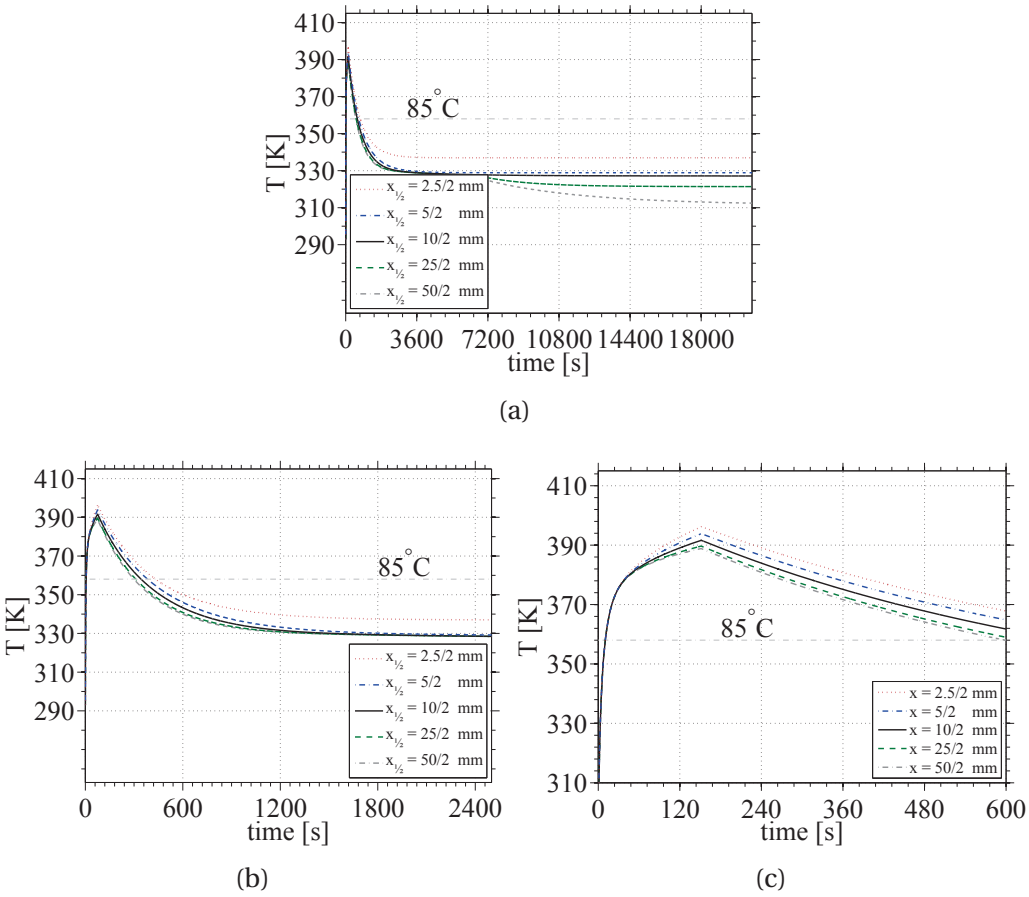

Figure 5.10: Hydrogen temperature evolution during fueling for different values of PCM's thickness: extended simulation time (a); regular simulation time (b); zoomed-in view of the peak-temperatures (c)

benefit that arises from operating with a 5 mm thick layer is the decrease in the overall system's volume and mass from 174 L and 57.75 kg to 166 L and 51.6 kg respectively. The latter values correspond to an increase by 3.6% in volume and 13.2% in mass with respect to the standard tank case presented in Table 5.2.

Heat transfer area enhancement

Solutions to augment the heat transfer area include extended surfaces and PCM encapsulation in the liner lattice [122]. The former method only influences the heat transfer area at the hydrogen/PCM interface (A_{in}), whereas the latter affects the entire PCM mass. In the present analysis the computational model is modified to account for both cases by allowing a manual entry of the inner surface area or the heat transfer area (A_{in} and/or A_{hex}) values, without changing the PCM volume and mass. The tank dimensions are kept the same, whereas the heat transfer area is redefined as an input to establish whether it is a limiting parameter for the heat transfer process in the present design. This simplified procedure is based on the assumption that, for the purposes of the heat transfer process, the main effect of extended surfaces and encapsulation lies in the heat transfer area augmentation.

In Fig. 5.11 the effect of A_{in} and A_{hex} on the hydrogen temperature is shown. The adiabatic temperature remains obviously unchanged as the heat transfer area affects the heat rate and not the heat capacity of the PCM, but larger heat transfer areas make the stationary conditions occur at shorter times.

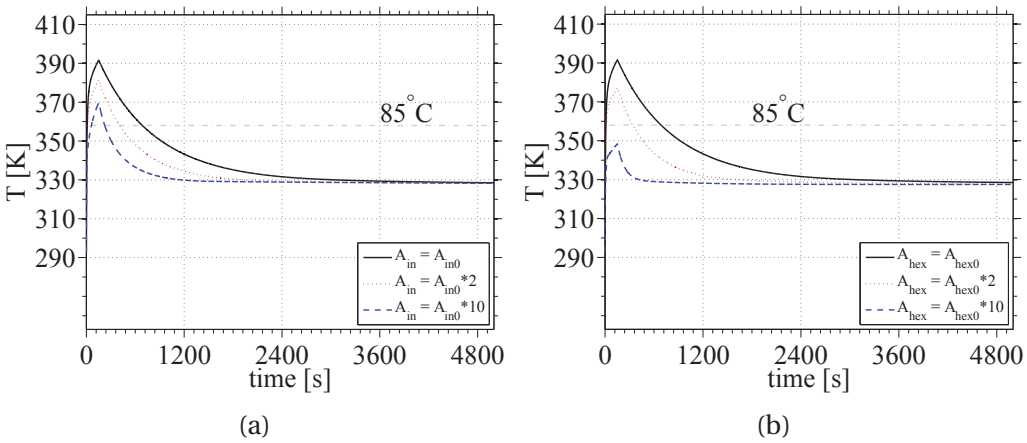

Figure 5.11: Hydrogen temperature evolution during fueling for different values of the heat transfer area: at the hydrogen/PCM interface only (a) and for both the hydrogen/PCM interface and the entire PCM layer (b)

In Fig. 5.11a, it can be observed that modest variations in A_{in} provide considerable reductions in the peak temperature. When this area is doubled from the nominal conditions, the maximum hydrogen temperature decreases by 10 K, providing a cooling effect more important than any other parameters investigated above in the same variation range. This suggests that the limiting factor for the heat transfer process in the current design is the reduced area at the hydrogen/PCM interface. The influence on the gas temperature is decreased for larger values of A_{in}, as the poor thermal properties of the heat-absorbing material delay the heat transfer, preventing significant heat absorptions to take place at the end of refueling. As a result, the maximum temperature reduces by only 21 K when A_{in} increases tenfold. Solutions for this involve the enhancement of the heat transfer rate in the PCM, which can be achieved by enlarging the heat transfer area via encapsulation and/or improving the thermal conductivity. The former option is presented in Fig. 5.11b, where both the heat transfer area at the hydrogen/PCM interface and of the PCM are augmented at constant volume and mass. The benefit of encapsulation is modest for relatively small increases in the heat transfer area, accounting for a further reduction by approximately 4 K at doubled A_{hex} values. On the other hand, when A_{hex} is increased tenfold, the PCM's thermal resistance is reduced by the same magnitude, enabling significant heat transfer rates and resulting in a considerable decrease in the hydrogen temperature at the end of refueling. Such a reduction accounts for 44 K with respect to the nominal conditions, pointing out the notable effect of operating at lower PCM's thermal resistances for augmented heat transfer areas at the gas interface. What is more important is that the peak temperature is now reduced below the critical value for the mechanical integrity of the tank walls. This excludes the presence of hot spots at the walls and provides higher gas densities at the end of the filling process, resulting in larger hydrogen masses stored in the tank. The overall fueled mass is now 4.52 kg, which accounts for a reduction by 3.3% with respect to the target value obtained for the standard tank case, where the gas is cooled to -40 °C to tank fueling.

At the end, it should be stressed that similar results can be achieved by augmenting the thermal conductivity, as mentioned above. This can be seen in Fig. 5.12 where a comparison between encapsulation and conductivity enhancement at large A_{in} values is proposed. The temperature trend is nearly the same, differing only in correspondence of the end of refueling, where the curves diverge, leading to a difference in the peak values by approximately 3 K. Such a difference is due to the non-linear influence that the effective thermal conductivity has on the thermal resistance in presence of natural convection.

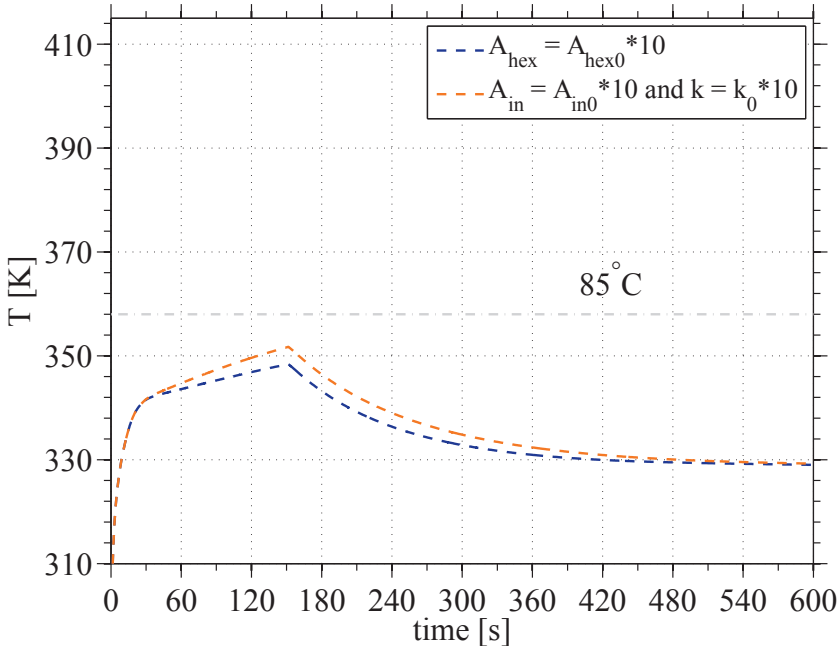

Figure 5.12: Comparison between encapsulation strategy and thermal conductivity enhancement for large heat transfer areas at the hydrogen/PCM interface. Zoomed-in view, detail of the peak temperature.

5.4 Conclusion

In order to reduce the cooling demand at the refueling station, a tank with an integrated phase change material is proposed to absorb the heat of compression released during hydrogen fueling. In addition to the energy saving, the novel tank design can improve the economy and the reliability of the fueling process, due to a reduction in the investment cost of the heat exchanger at the refueling station and to the replacement of an active cooling system with a passive one.

Two tank designs are considered for comparison in absence of hydrogen-cooling at the refueling station: a standard Type IV tank and the novel tank design with a 10-mm-thick layer of PCM in the inner volume.
Results show that the integration of the PCM reduces the system's adiabatic temperature from 74 °C to 53 °C when compared to the standard case, but due to the modest heat transfer rates at the hydrogen/PCM interface and in the PCM thickness, the hydrogen peak temperature is essentially independent from the PCM insertion. The maximum temperature reaches values above the critical limit of 85 °C and thus the presence of hot spots that can damage the mechanical integrity of the walls cannot be excluded. The high gas temperatures that occur during fueling cause the fueled hydrogen mass to reduce by 12% with respect to the standard tank. In order to solve this issue a parametric analysis is carried out to separately evaluate the influence of the maximum gas temperature upon the PCM's main thermal properties, thickness and area of heat transfer. The results show that the material's thermal properties and thickness are found to only have a modest effect on the hydrogen temperature during fueling.

The reward strategy that is identified consists in a heat transfer improvement by surface augmentation or combined enhancements of the heat transfer area at the hydrogen/PCM interface and PCM's thermal conductivity.
The encapsulation technique can provide sufficiently high surface enlargements to reduce the peak temperature below the critical limit and eliminate the risk of hot spots at the tank walls wile providing proper PCM confinement during repeated melting-solidification cycles. In addition, with such a technique the hydrogen stored mass becomes comparable with the value obtained for the standard case. As an example, when the encapsulation method increases the heat transfer area tenfold, the maximum gas temperature is reduced from 118 °C to approximately 74 °C, the fueled hydrogen mass is only 3.3% less than the target value and the maximum energy saving at the refueling station accounts for 4.2 MJ per fueling. Additional benefits involve the cost reduction of the heat exchanger and increased reliability of the fueling process.

At the end, in order to maximize the hydrogen stored mass and minimize the extra volume and weight added to the tank, future research should focus on optimization studies that involve the heat transfer area and layer's thickness as the main variables. The PCM's properties can also be included in the optimization analysis to operate a comprehensive material selection in respect of the requirements identified above for the application of interest.

6 Design and simulation platform for on-board hydrogen storage systems

6.1 Introduction

This chapter presents the modeling platform (HySDeP), developed for the design of on-board storage systems for light-duty vehicles built in Dymola^{TM} environment. This platform is intended to be used as a tool for charging/discharging analyses of MH and PCM-tanks, based on the methodology and models reported in Chapters 2-5 and in Appendix A and Appendix C. It can be found in the gitHub repository of the *DTU-TES* group. The direct link to HySDeP is:
https://github.com/DTU-TES/HySDeP_Hydrogen-Storage-Design-Platform.

In Sections 6.2-6.3 the architecture and methodology followed to build the modeling platform are described along with the underlying philosophy and the implementation of the main features that the user can select to tailor the charging/discharging analyses for the chosen storage system.

In Section 6.4 the simulation platform is applied to a MH tank with shell-and-tube and tube-in-tube configurations. Charging and discharging analyses are presented with attention to the gravimetric and volumetric densities. A parametric analysis is then performed to address the effect of different geometric parameters on the total stored mass of hydrogen and on the absorption/desorption rates.

Details of the implemented user libraries that also include heat exchanger configurations, metal hydride compositions, kinetic models and phase change materials can be found in Appendix D.

In Section 6.5 the structure and philosophy of the developed platform as well as the main conclusions drawn from the modeling results are summarized with attention to the thermal and storage performance of the investigated systems.

6.2 Methodology

The platform has been designed in Dymola™ to take advantage of a robust environment for topological modeling with a non casual approach.
The object-oriented language Modelica® offers the possibility to reuse packages and modeling knowledge via the hierarchical structure and inheritance constructs. This aspects make Dymola™ a particularly convenient tool to develop robust exchangeable component libraries. The graphical user interface (GUI) allows customizing the component figures by either editing simple shapes and colors or by uploading external picture files.

The design approach of the platform is based on three criteria, such as: flexibility, user-friendliness and facility of third part development. These concepts are chosen to make the platform work as both a design/simulation tool for users and a well-structured environment for model developers. This means that the platform should be designed to adapt to the needs of different users and should be based on an efficient and clear architecture in order to ease the modification. In order to make the use of the platform as straightforward as possible for both types of end-users, its design is based on a multi-level architecture. The first level corresponds to the *macro*-models representing the main physical components. Such components correspond to containers within which multiple nested sub-models are defined to perform intermediate calculation tasks. These sub-models represent the second level of hierarchy.
The user should have direct access only to the *macro*-components. This occurs via the graphical interface, through which the domain of investigation and the values for the input parameters can be defined. To simplify the user interaction with the platform, the number of macro-models is limited to three, namely *Ambient*, *Refueling station* and the tank system.
The developer should have access to both levels in order to modify the structure and operation of the platform.
Different *if*-scenarios guide the user through the model set up, enabling the selection of various options and thus, the tailoring of the analysis based on specific needs. The first choice the user is asked to take, refers to which storage system should be investigated: MHSS or CHG-tank with or without PCM.
The component hierarchy should be implemented with preference for constructs that keep the modeling approach as simple and intuitive as possible. In Modelica® the above preference translates in the use of *inner*/*outer* and port/connector elements rather than nested *extends* constructs to exchange constant and variables between models. In addition, the code should be well commented to ease the understanding of all the implemented features. A reference list is included at the end of each component code to make transparent the source of equations, thermo-physical properties,

thermal models and assumptions.
These aspects are of fundamental importance as the platform should in principle allow for its use and modification by different users, including both company employees and researchers.

In Fig. 6.1 the platform structure is shown in view of its *macro*-components and main implemented features. This figure should be read as a black box scheme where the main components and information flows are presented. A more detailed description of the sub-models contained inside each *macro*-component is given in Section 6.3.
The ambient model serves as the environment where the user defines the ambient conditions in terms of pressure and temperature (i.e. p_{amb} and T_{amb}) that are passed to the refueling station and tank models.
In the refueling station the user selects the hydrogen temperature at the tank inlet. In addition, if the PCM-tank is selected as the investigated system, the tank type (e.g. Type III or IV) and the initial pressure should also be given as inputs. These two parameters are used together with p_{amb} and T_{amb} to determine the appropriate refueling protocol, which, in turn, defines the fueling pressure ramp for CHG storage systems according to SAEJ2601 as discussed in Section 5.2.2.
In the tank model all the equations concerning energy and mass balances, kinetics and heat transfer are solved. This occurs according to the model setup that the user defines. The user is requested to participate to the model setup by defining the values for the free variables and by selecting different options that are given through *if*-scenarios and libraries. The former concern the actual analysis that needs to be carried out (i.e. charging or discharging) and, if the MH tank is selected, the level of detail for the domain discretization (i.e. 0D or 1D). The latter refers to additional information that the user can edit to further tailor the chosen analysis. Such libraries correspond to databases implemented as records in Modelica® language.
The libraries give access to different heat exchanger configurations, metal hydride and phase change material compositions, boundary conditions, kinetic models and heat transfer media. A more detailed description of the libraries is given in Section 6.3.
If a specific choice is not taken, the nominal option for each database is selected by default (see Appendix D).

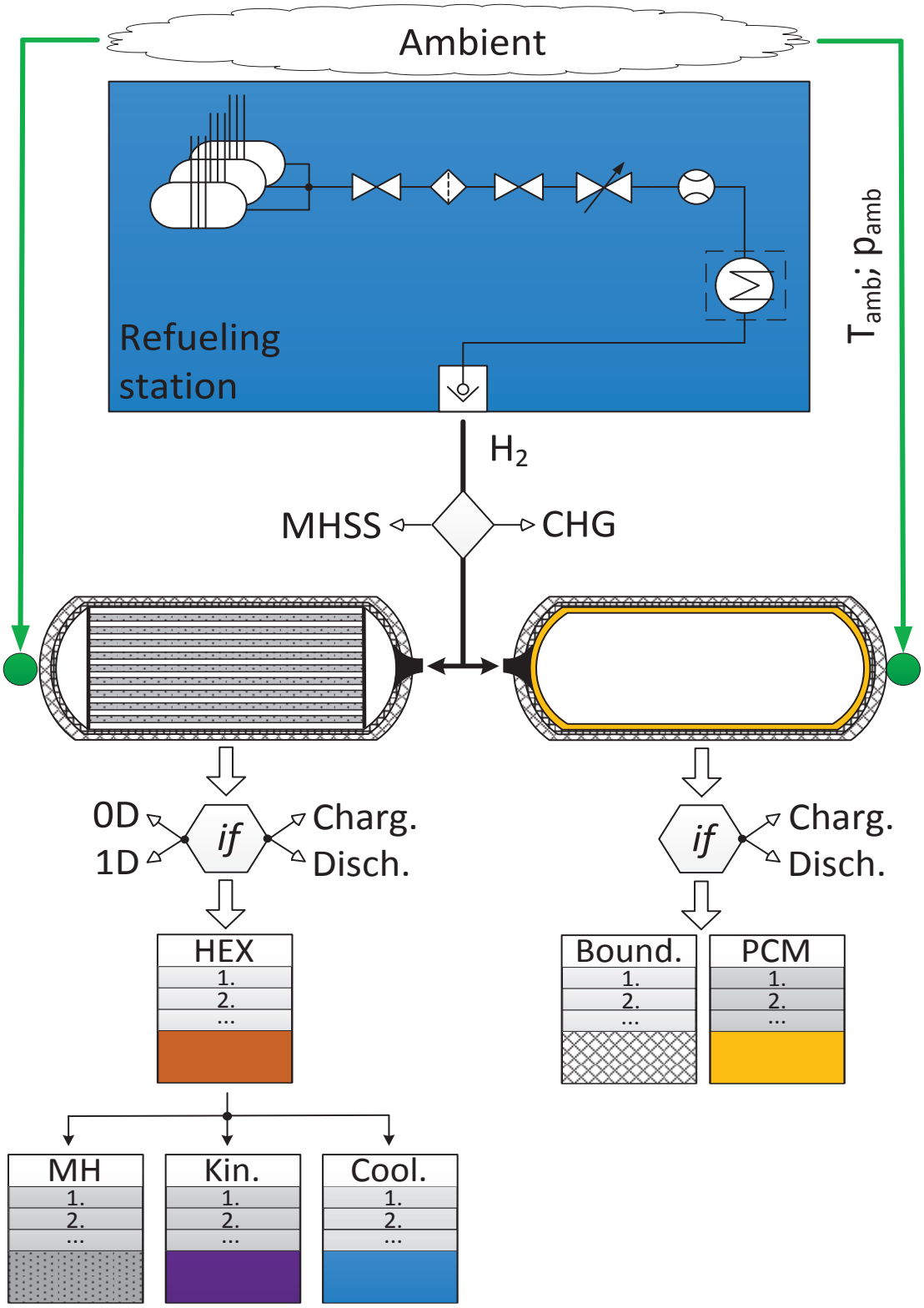

Figure 6.1: Modeling platform. Architecture concept.

6.3 Platform implementation

This section presents the implementation of the simulation platform developed in this thesis with attention to the main sub-models, whereas the list of the different features included in the user libraries is described in Appendix D.
In Fig. 6.2 a view of the modeling platform is shown. The first step in the simulation process is to select which storage system needs to be studied: MHSS or CHG tank.

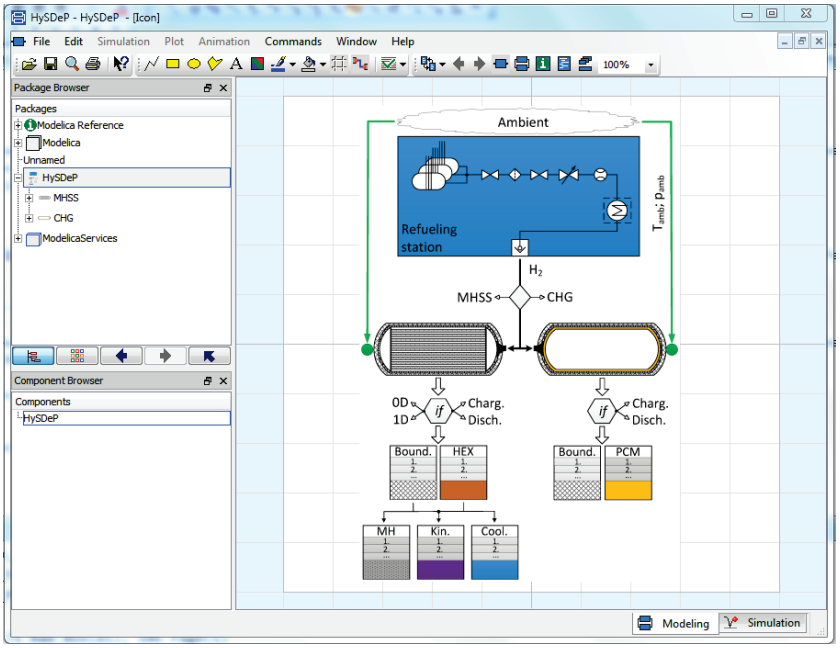

Figure 6.2: View of HySDep in Dymola^{TM} environment.

6.3.1 MHSS

In the metal hydride storage system macro-model, the sub-models are divided by category and included in one of the seven model packages, see Fig. 6.3. These are named as *Tanks_With_Hex*, *Ports*, *Sources*, *Properties*, *Heat Transfer*, *Kinetics*, *TESTS*. Among these, the user has only access to the *TESTS* package, where the main design parameters can be edited to tailor the simulation. On the other hand, the developer can edit the code of any sub-models contained in each package.
The *Tanks_With_Hex* package contains the 0D and 1D tank models, see Fig. 6.4a.
Ports includes all the interfaces between sub-models defined to dynamically exchange information (e.g. thermodynamic properties of physical streams).
Sources encloses the refueling station (i.e. the hydrogen source) model and the coolant source.

Properties contains the property libraries for the hydrogen-absorbing alloys, tube material and heat transfer fluid.
Heat Transfer incorporates the heat exchangers sub-models and their library.
Finally, *Kinetics* encloses the kinetic equations library.

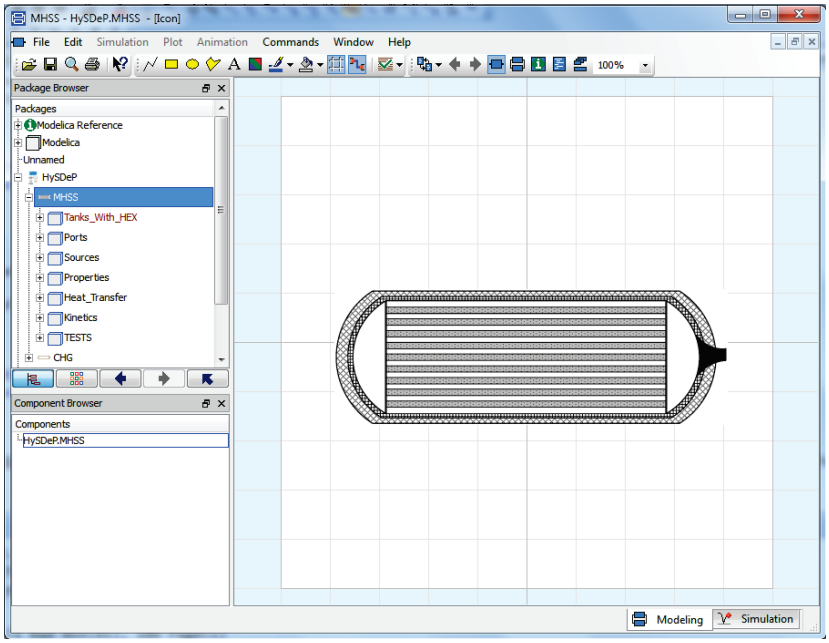

Figure 6.3: HySDeP: packages contained in the MHSS macro-model.

In Fig. 6.4 a view of both the sub-models and the complete simulation system that refer to the 1D tank are shown.

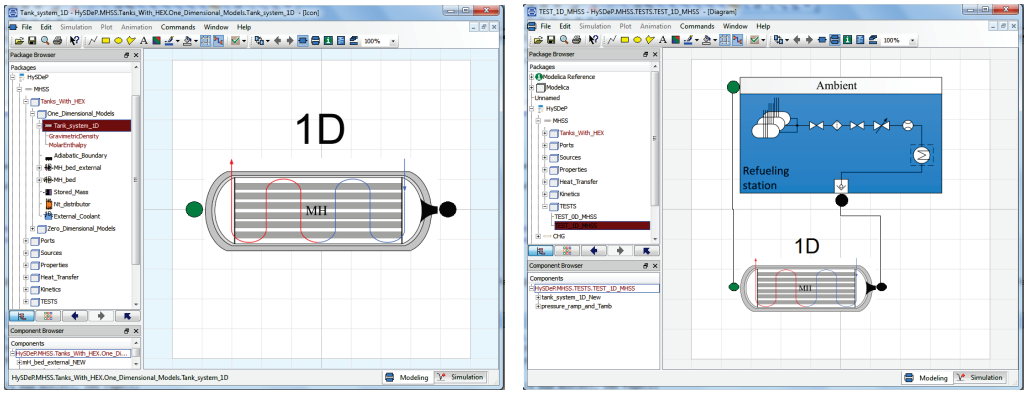

(a) (b)

Figure 6.4: HySDeP: 1D MH tank models (a); complete simulation model for the 1D analysis (b).

The user defines the values for the main inputs involved in the analysis (see Section 6.2). The list of editable parameters for the 1D analysis is shown in Fig. 6.5 for the refueling station and in Fig. 6.6 for the tank, with their symbols and a short description.

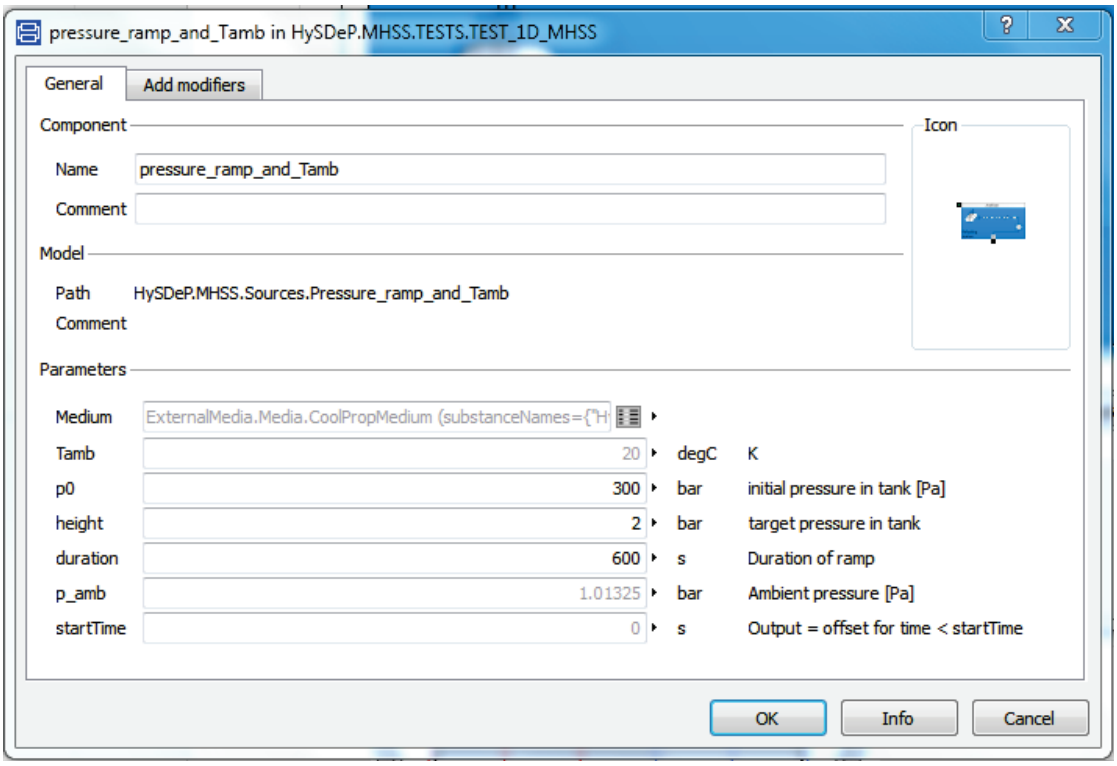

Figure 6.5: HysDeP: editable parameters for the refueling station.

The refueling-station/ambient inputs include the ambient temperature and pressure, the initial and the final tank pressure. The pressure ramp is completely defined, based on this parameters, after the user types in the values for the ramp duration and the time off-set from the start of the simulation.
These parameters are then passed to the tank model where the user is requested to first define some *if*-scenarios (i.e. *true* or *false*) such as: *Calculated_Volume, VariableProperties, Bell_Delaware_Method, Charging.*
Depending of which option is chosen for *Calculated_volume*, the tank inner volume is either calculated from diameter *d_tank* and length *L* (assuming a cylinder shape) or directly defined by typing in the desired value (*V_input*).
If *VariableProperties* is selected *true* then k_{MH} and c_{MH} are interpolated from experimental data as functions of hydrogen pressure and content. On the contrary constant parameters are used if *true* is chosen.
Bell_Delaware_Method defines which method is used to calculate the heat transfer coefficient and pressure drops in the shell and tube, as explained in Subsection 6.3.1.

Charging is set *true* for charging analyses and *true* false if discharging analyses need to be performed. The pressure ramp as well as the initial and final pressure values in the tank need to be modified accordingly.

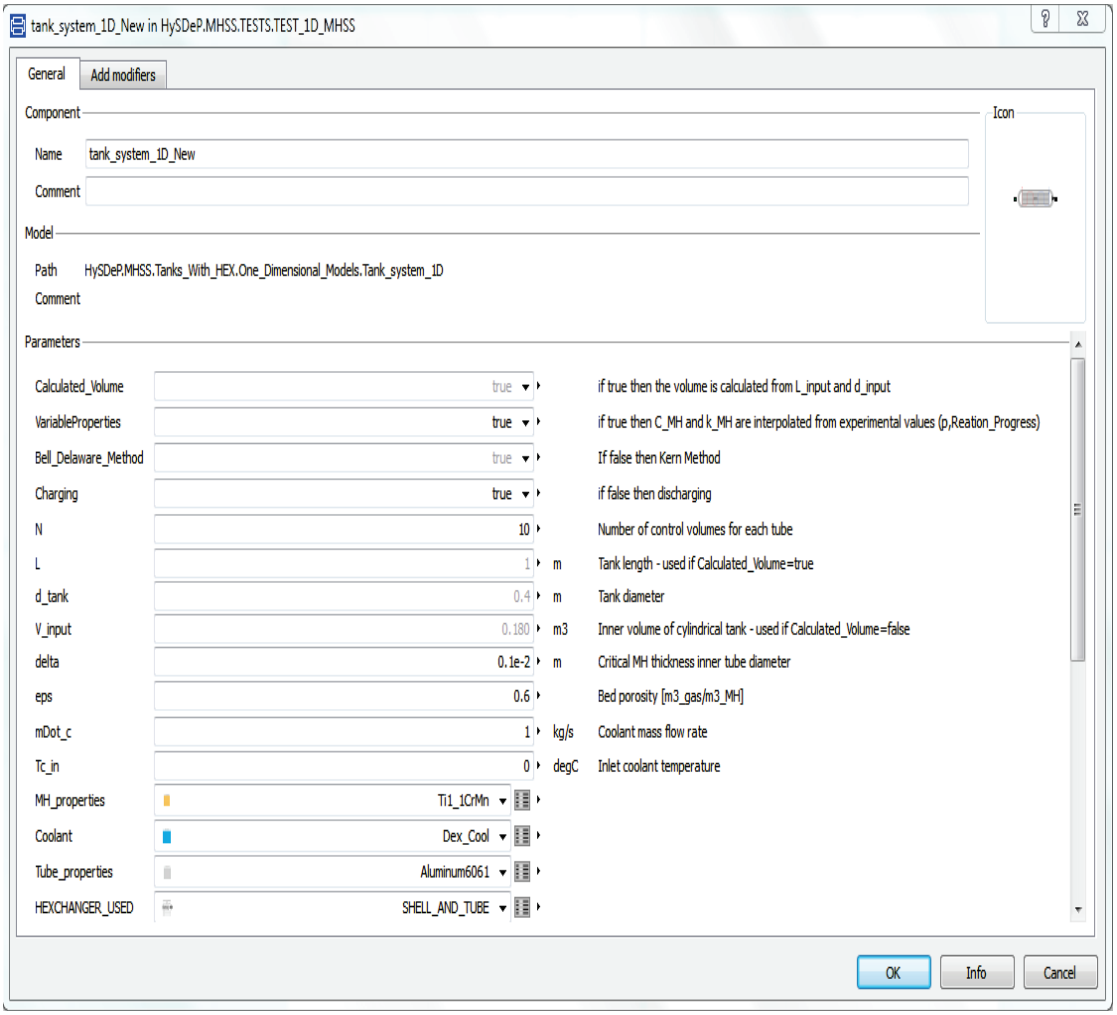

Figure 6.6: HysDeP: editable parameters for the MH tank model.

The number of control volumes per MH tube N, the metal hydride thickness δ and the porosity complete the definition of the domain geometry.
The coolant conditions are entirely defined by the mass flow rate and the inlet temperature, whereas temperature at the outlet is a result of the simulation.
Drop-down menus allow the user to access the implemented libraries to select among different MH compositions (*MH_properties*), coolant types (*Coolant*), tube materials (*Tube_properties*) and heat exchanger configurations.

Heat exchanger designs

In Chapter 4 the shell and tube design (i.e. HEX3) was selected as the most promising configuration to achieve the targets identified in Chapter 2. Such a design refers to the tubular tank design, where the MH is located in small diameter tubes and the coolant flows over the tube bank. The advantages of such a configuration are (see Section 4.5 for details):

- Modularity (ease of maintenance and thus, lower cost).
- Ease to realize a uniform pattern of reaction.
- Reduced parasitic mass.
- Reduced tank weight.

The latter is particularly important for high-pressure metal hydrides, for which the insertion of the hydrogen-absorbing alloy in small-diameter tubes rather than in large-diameter vessels enables the use of small thickness at any pressure. This can be seen in Fig. 6.7 where the calculated tube thickness is plotted over the inner tube diameter for low and high pressures values for two different materials: Al 6061-T6 in Fig. 6.7a and AISI 304 austenitic steel in Fig. 6.7b. For any given tube size and pressure, the latter provides smaller thicknesses due to its higher tensile strength [194].
It should be mentioned that both materials are used in practice for hydrogen systems, due to their resistance to embrittlement [195, 196].

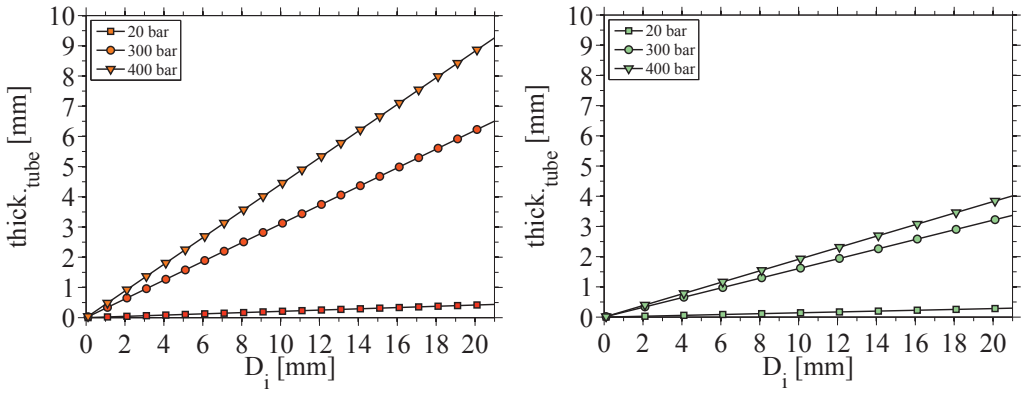

Figure 6.7: Minimum tube thickness for: Al 6061-T6 (a); AISI 304 (b). Tube temperature below 100 °C [197].

The main drawback of the tubular design is the reduced MH capacity when compared to chamber-tank designs, as discussed in Section 1.3.1.

Two heat exchanger configurations that refer to the tubular tank design have been so far implemented in HySDeP. The current status of the heat exchanger library is shown in Fig 6.8 together with the heat exchangers sub-models.

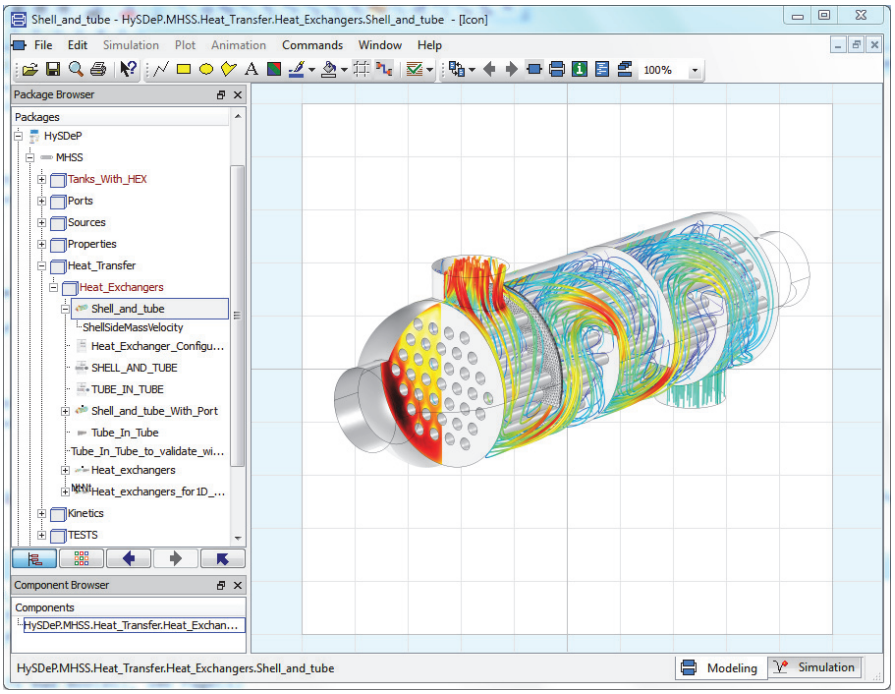

Figure 6.8: HysDeP: Heat exchangers models.

The HEX3 configuration, named *Shell_and_tube*, presents a standard shell and tube design in which the coolant flows in combined cross-parallel flow over the MH tube bank. This layout corresponds to the configuration that provided the lowest reaction times in Chapter 4.
In the HEX2 layout, named *Tube_In_Tube* the HTF is circulated parallel to the MH tube and occupies the annular region of a tube-in-tube arrangement. Although it was found that larger reaction times are associated with this configuration, it is implemented for the purpose of comparison in the context of an actual charging/discharging analysis.

Heat exchanger design model

The tubular domain under investigation and the concentric discretized MH volumes n are shown in Fig. 6.9 together with the longitudinal and radial discretization steps, i.e. dl and dx respectively. The latter parameter is calculated once the inner diameter

D_i and the number of discretized volumes N (i.e. 4 in the figure) are set by the user. On the other hand, dl is computed with respect to the tube length and a constant number for the coolant volumes S (i.e. 6). A large number of discretization volumes is not necessary for the coolant domain, as the temperature gradient between inlet and outlet is typically negligible. Each tube is treated as a separate heat transfer module

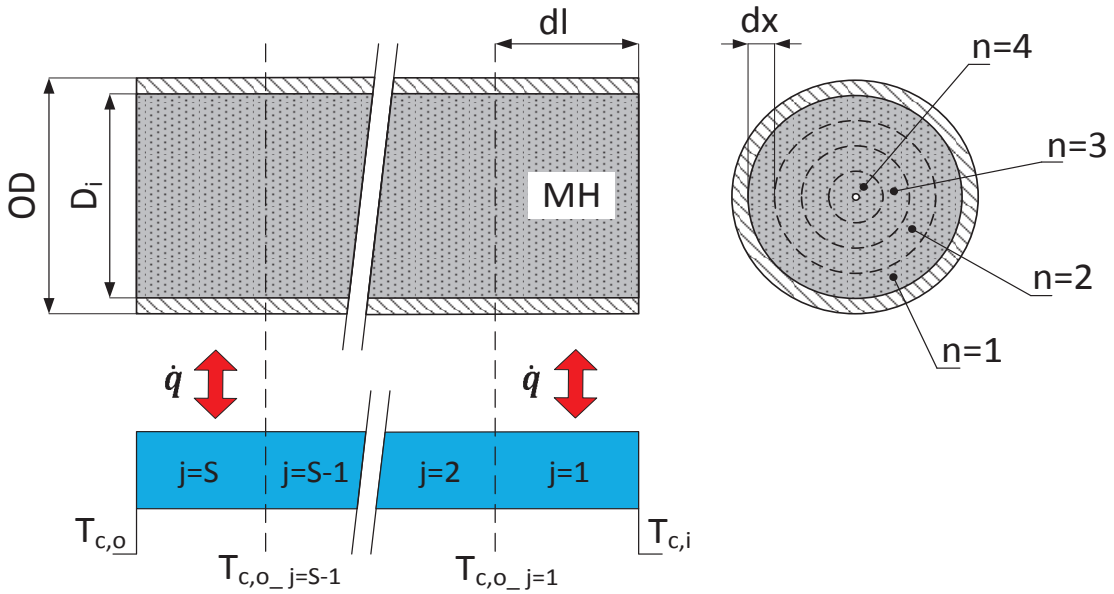

Figure 6.9: HysDeP: MH tubular domain and discretization details.

that transfers the heat to the coolant. The total transferred heat is calculated by multiplying the single contributions by the maximum number of tubes that fit in the tank volume (see Appendix B). The heat is radially exchanged between the heat transfer fluid and the MH in the bed and it is used to calculate the HTF outlet temperature for each HTF volume based on a central differential scheme. As the heat transfer takes place radially, the center of the tube is an adiabatic surface.
The mathematical framework, including the relevant boundary conditions, is presented in Appendix A.
When the shell and tube configuration is selected, it is possible to choose either the Bell-Delaware or Kern methods to calculate the convection coefficient of heat transfer and the pressure drops. Even though the former provides a higher precision in the calculation of $\bar{h}_f$, it requires the detailed definition of the heat exchanger geometry, which is not typically available in a pre-design stage. In such cases, it might be better to use the Kern method, which gives a good approximation of the value $\bar{h}_f$ in an early stage of design. In Fig. 6.10 the parameters required for applying the Bell-Delaware method are shown. These mainly include the pitch to tube diameter ratio, the baffle space and cut, the layout angle for the tube bank and the pair number of sealing strips.

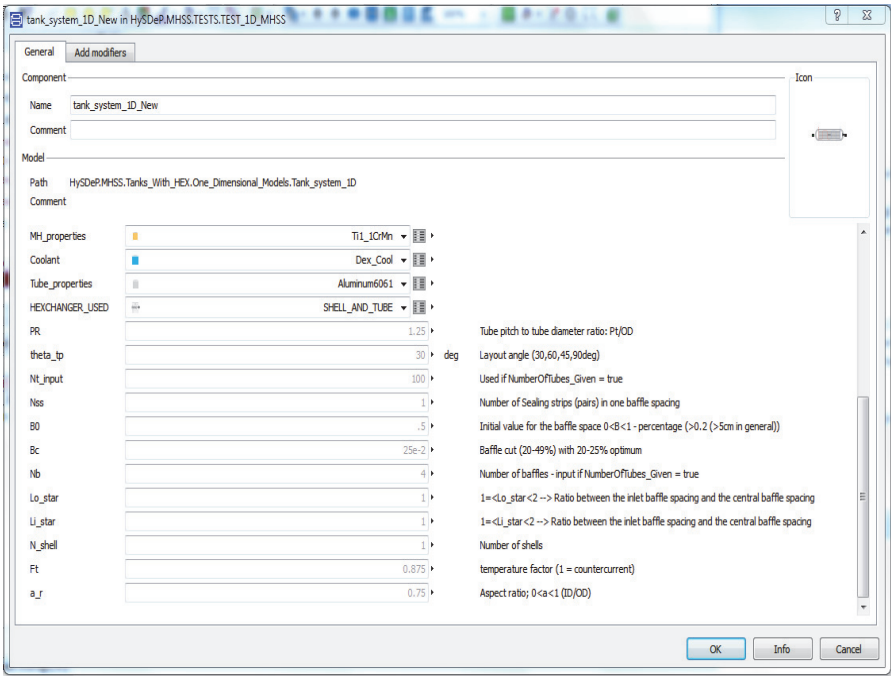

Figure 6.10: HysDeP: Shell and tube design inputs.

6.3.2 CHG tank

In the CHG macro-model, as for the MHSS, the sub-models are divided by category. There are six different packages, as shown in Fig. 6.11. These are named as *Tanks*, *Ports*, *Sources*, *Properties*, *Heat Transfer*, *TESTS*. Once again, while the devloper has access to the code of each sub-model in any package, the user can only edit some prescribed input parameters in the *TESTS* package. *Tanks* contains the tanks sub-models (standard CHG and PCM vessels).
Ports includes the port objects in Modelica® language, defined to allow information transfer between component models.
In *Sources* the refueling station model is defined.
Properties contains the PCM library. The *Heat Transfer* package includes all the component sub-models that are involved in heat transfer processes. These include the tank walls (liners and CFRP) and PCM volumes.
Finally, in *TESTS* the main input parameters can be edited to perform complete charging/discharging analyses.
The graphical layout that guides the user/developer to the definition of the input parameters to carry out the analysis of interest and to the sub-models contained in each package and for the libraries is very similar to what described in Subsection6.3.1 and therefore is not repeated here.

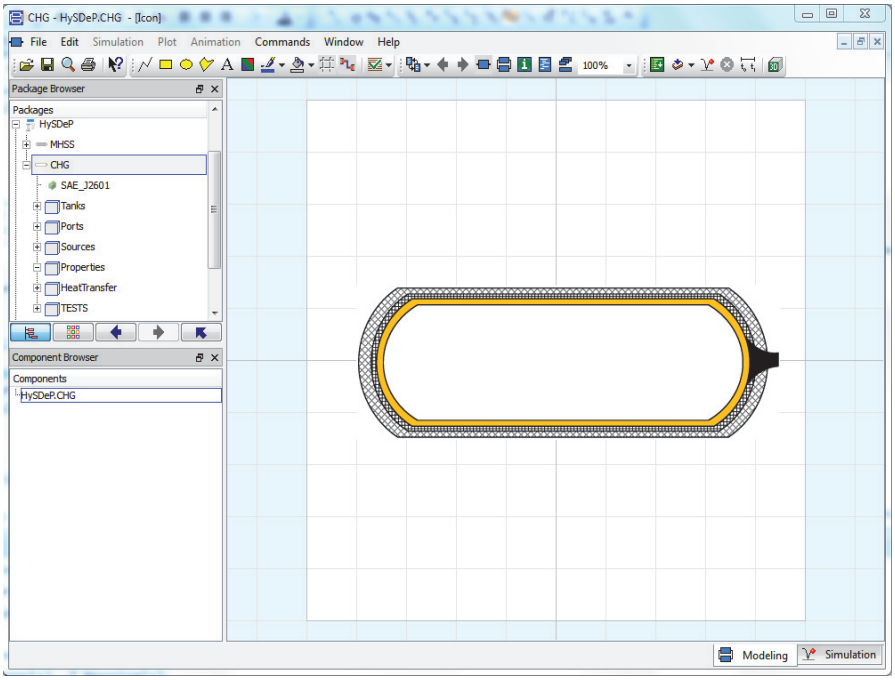

Figure 6.11: HysDeP: packages contained in the CHG macro-model.

The principle of the refueling-station/ambient model and its main parameters (e.g. pressure ramp) have already been discussed in Section 5.2.2. For these reasons, only a description of the main input parameters for the PCM tank model are here described. Such parameters are represented in Fig. 6.12.

The access to the boundary conditions library occurs via a drop-down menu where the user can choose among three options. The first option considers that no heat transfer takes place between the hydrogen gas and the tank walls. The second condition enables heat transfer from the gas to the PCM layer and tank walls only. The third condition consists in a non-adiabatic tank, for which the heat losses to the ambient are accounted for.

The tank geometry is defined through the length, inner diameter, PCM thickness and number of discretized PCM volumes.

The main *if*-scenarios include *Convection*, *Manual_area_inner* and *Manual_area_PCM*. If *Convection* is set *true* then combined conduction and natural convection phenomena participate to the heat transfer during melting (see Appendix C), otherwise conduction and convection are accounted for separately in the solid and phase-change regions and during melting respectively. The comparison between results obtained with these two options show the major role that convection plays in the heat transfer

process. If *Manual_area_inner* and *Manual_area_PCM* are set *true* then it is possible to separately account for heat transfer area augmentation at the hydrogen/PCM interface and within the PCM layer. These options can be used to approximate the effect of PCM encapsulation (see results in Chapter 5).
The *G* parameters are multiplying factors for the PCM thermo-physical properties and heat transfer area as described at the right of the editable space. These are the parameters used to perform the sensitivity analyses presented in Chapter 5.
The tank type (e.g. tank III or IV) can be selected from a drop-down menu. The information on the properties of the liner and CFRP as well as on their thickness and the adequate fueling protocol with respect to SAEJ2601, is automatically passed to the relevant model components.
If *Charging* is set *true* then refueling analysis take place otherwise discharging. The heat transfer coefficients for the hydrogen gas change accordingly as reported in the literature.
At the end, although the tank walls thickness are defined when the tank type is chosen, it is possible to manually edit the thicknesses of liner and CFRP separately.

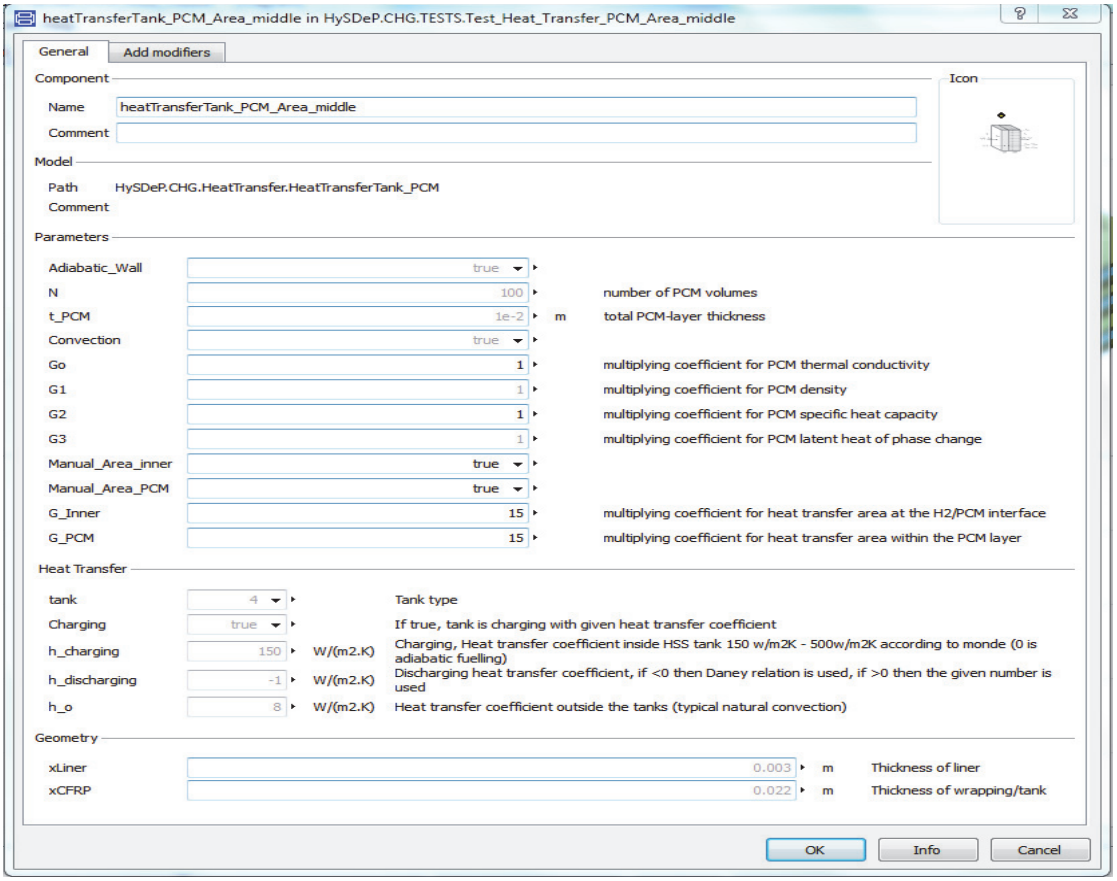

Figure 6.12: HysDeP: editable parameters for the PCM tank model.

6.4 Results

This sections focuses on the results obtained with HySDeP for charging and discharging processes in vehicular MH hydride storage tanks. The analyses are conducted for both the implemented heat exchangers and a sensitivity analysis is carried out to address the effect of the main design parameters on the storage performance. The results refer to the input parameters identified in Chapter 3, unless otherwise specified. The CHG systems have been investigated in detail in Chapter 5 and therefore, their analyses are not repeated here.

6.4.1 Charging

The results of 0D and 1D models fueling models are presented in this section for the solid bed temperature, fraction of reaction completion and stored hydrogen mass. For both models the main inputs are listed in Table 6.1 for the HEX3 configuration.

Table 6.1: Model input parameters for charging analysis (HEX3).

Domain	Parameter	Value	Unit
Amb.	p_{amb}	1.013	bar
	T_{amb}	20	°C
p_{ramp}	p_0	1.013	bar
	p_{ref}	300	bar
	duration	60	s
	time offset	0	s
Cool.	Dexcool®		
	$\dot{m}_c$	20	kg/s
	$T_{c,i}$	0	°C
Tank	L	1	m
	d_{tank}	0.4	m
MH	$Ti_{1.1}CrMn$		
	ϕ	60%	-
	δ	1	mm
Tube	Al 6061-T6		
	OD	2.5	mm
HEX	Shell and tube		
	PR	1.25	-
	Layout angle	30	deg
	Baffle cut	25%	-
	Baffle space	50% d_{tank}	m

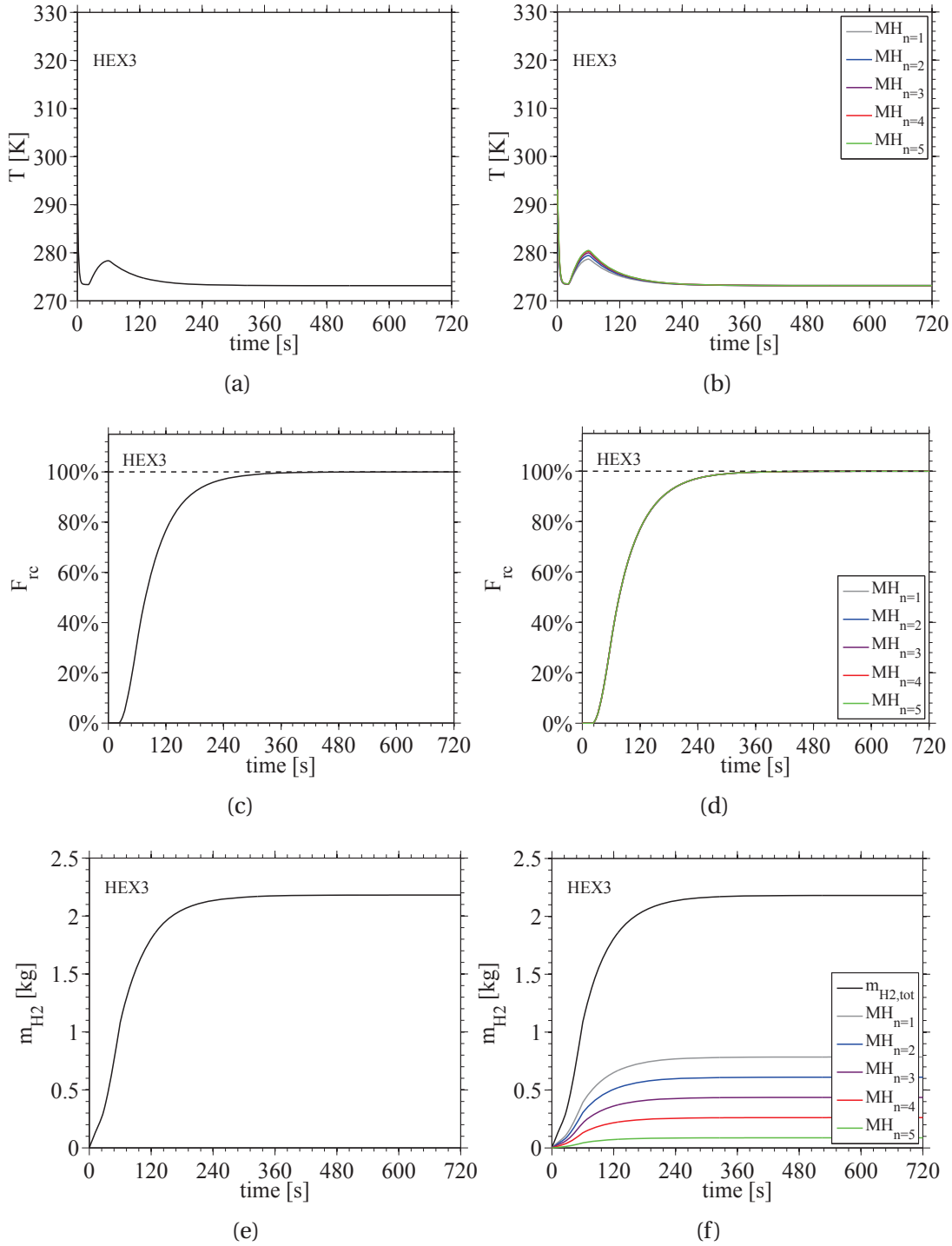

Figure 6.13: Charging analysis: bed temperature for 0D (a) and 1D (b); fraction of reaction completion for 0D (c) and 1D (d); stored mass for 0D (e) and 1D (f). HEX3 configuration

From Fig. 6.13 it is possible to observe that the difference in results between the 0D and 1D model (with 5 MH concentric volumes) is negligible. This occurs because the investigated inner diameter is small enough (i.e. 2 mm as estimated in Chapter 3) that a lumped model is adequate to accurately describe the hydriding reaction within the solid bed.
Figs. 6.13a-b show that the large cooling rates enable a rapid reduction in temperature, which drops from the initial conditions (i.e. 20 °C) to the coolant temperature before the absorption process takes place and then suddenly increases by 8 °C at the end of pressurization. Finally, the MH temperature tends to the coolant temperature reaching steady state conditions at 360 s.
Figs. 6.13c-d show the fraction of reaction completion for the 0D and 1D models. The small size of the MH tubes enable considerable bed cooling and therefore, significant hydriding rates. The small temperature differences between the concentric MH volumes have a negligible effect on the absorption rates, as the reaction is kinetically-limited. As a result the F_{rc} curves are coincident in Fig. 6.13d.
It is wort pointing out that the design achieves the desired F_{rc} of 90% within the target refueling time of 3 min.
Figs. 6.13e-f presents the total stored hydrogen mass which accounts for approximately 2.2 kg. In Fig.. 6.13f the total fueled mass is obtained by adding the contributions of each concentric volume multiplied by the calculated number of tubes. Even though the hydrogen-absorbing alloy only occupies 40% of the bed volume (i.e. ϕ= 60%), c.a. 74% of the total fueled mass is stored in the absorbed phase and only 26% is stored in the gaseous form in the pores. This can be seen in Fig. 6.14.

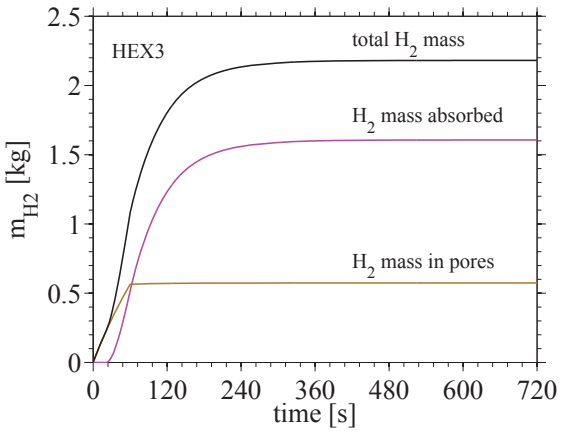

Figure 6.14: Hydrogen mass stored in the solid bed: mass in pores and in absorbed phase. HEX3 configuration.

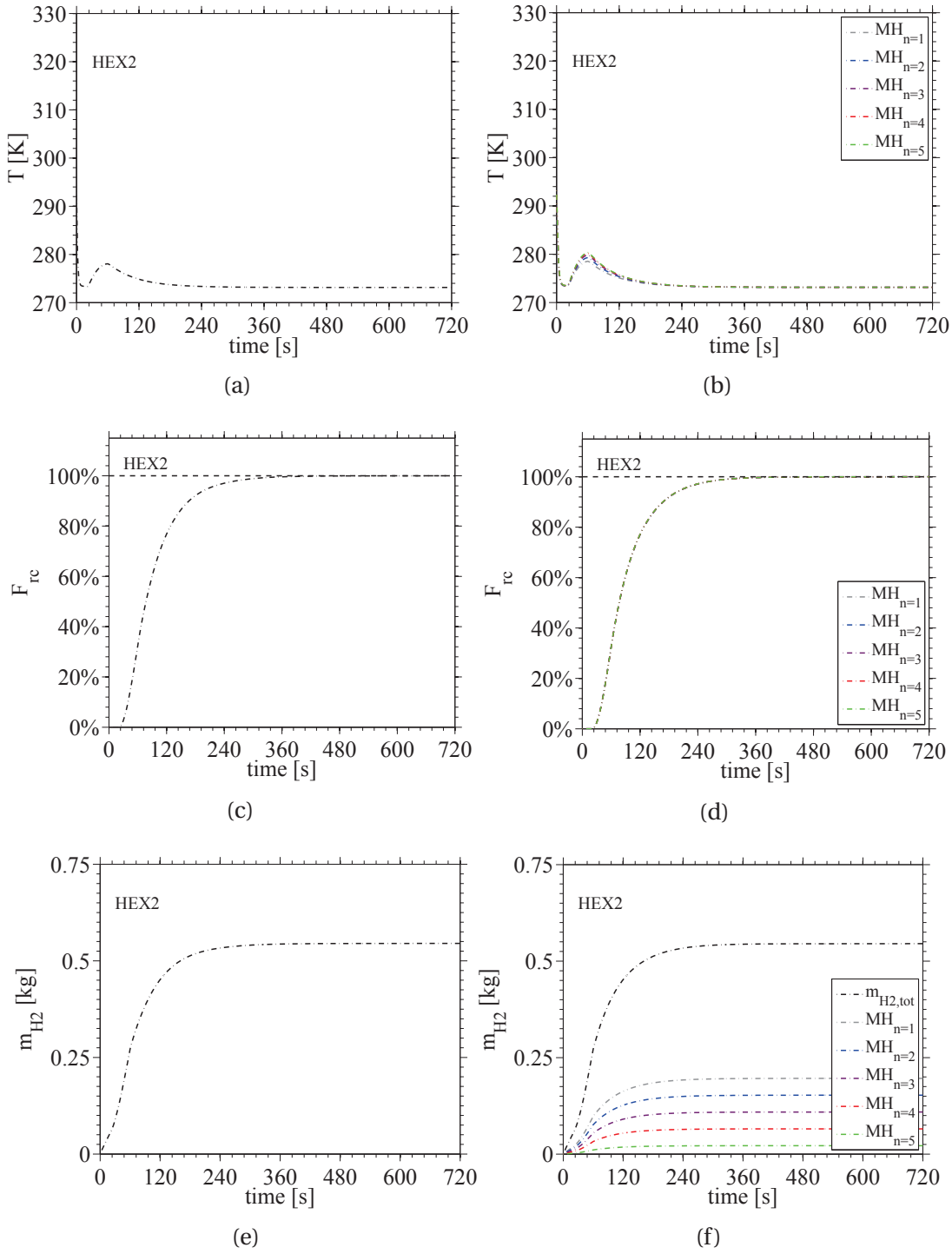

Figure 6.15: Charging analysis: bed temperature for 0D (a) and 1D (b); fraction of reaction completion for 0D (c) and 1D (d); stored mass for 0D (e) and 1D (f). HEX2 configuration

In Fig. 6.15 the 0D and 1D results for the bed temperature, fraction of reaction completion and stored mass are obtained for the HEX2 configurations with an aspect ratio of 0.5. From such a it can be observed that the difference in results between the lumped and spatially distributed models is negligible and the 0D model well describes the physical behavior of the storage system, as it was found for HEX3.
The solid bed temperature profiles and the hydriding rates shown in Figs.6.15a-b and in Figs. 6.15c-d are nearly coincident with those obtained for HEX3, even though the convection coefficient of heat transfer for HEX2 (i.e. 1500 $W \cdot m^{-2} \cdot K^{-1}$) is less than half than for HEX3 (i.e. 3420 $W \cdot m^{-2} \cdot K^{-1}$) under the same cooling conditions. This occurs because the heat transfer process is dominated by the conductive thermal resistance of the metal hydride (see Subsection 3.8.4).
Although the cooling performance and hydriding rates are comparable for HEX2 and HEX3, it is possible to notice that the former configuration stores a much lower hydrogen mass (Fig. 6.15e-f). The reason for this lies in the disparity of the MH volume, which occupies only 8.5% of the total inner tank volume for HEX2 and 34.7% for HEX3. As a result, HEX3 enables storing 4 times more stored hydrogen mass than HEX2. In order to maximize the hydrogen stored mass, its dependency upon the main geometric parameters is investigated in Subsection 6.4.3.
Results similar to those presented in Figs. 6.13 and 6.15 can be obtained for coolant rates much lower than the chosen value of 20 $kg \cdot s^{-1}$ that is here selected to operate at a shell-side velocity value (i.e. 1.17 $m \cdot s^{-1}$) within the optimum range (see Chapter 4). In addition, from Fig. 6.16 it can be noticed that such a flow rate provides a maximum difference of only 2 °C between inlet and outlet temperatures. This confirms the assumption of constant cooling conditions over the entire length of the heat exchanger (see Chapter 3) for practical MHSSs. Differently, caution in using this assumption should be taken when very low coolant rates are considered (i.e. $\leq$15 $kg \cdot s^{-1}$).

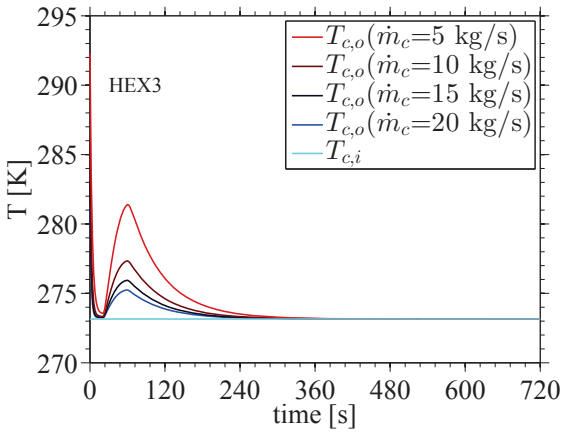

Figure 6.16: Inlet and outlet coolant temperatures. HEX3 configuration.

6.4.2 Discharging

A fast dehydriding analysis is here presented to investigate the ability of the system to fulfill intense discharging conditions. It is here assumed that any MHSS that can fulfill such conditions can also satisfy cyclic dehydriding characteristics, as it is typically required in real FCEVs operation.
Simulations show that, as it was found for hydrogen absorption, the difference in results between the 0D and 1D models is negligible for the desorption process. Therefore, the results of the discharging analysis are presented with respect to the 0D model to ease the reading of the plots.

In this analysis a complete discharging from 300 bar to atmospheric pressure is achieved in 10 min, as shown in Fig. 6.17, where the pressure ramp is presented together with the equilibrium pressure calculated with the properties reported in Appendix D for the dehydriding process.

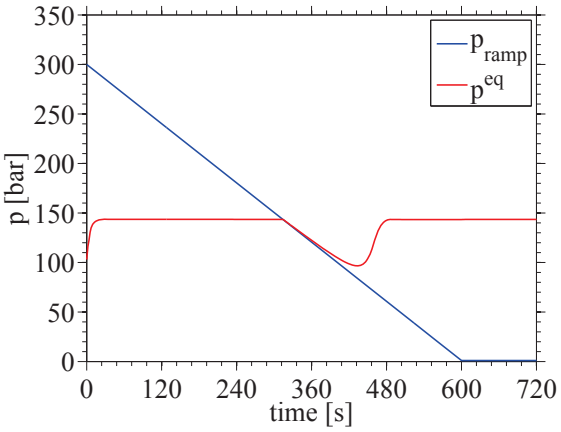

Figure 6.17: Pressure ramp and equilibrium pressure. Discharging process.

From Fig. 6.17 it can be noticed that hydrogen desorption is triggered when the pressure ramp falls below the equilibrium pressure. This corresponds to a time of 312 s. The decrease in p^{eq} that occurs after such a time is due to the endothermic nature of the desorption process, which causes a reduction of the metal hydride temperature. The equilibrium pressure then increases due to solid-bed heating and finally stabilizes when the system reaches steady-state conditions.

The list of input data is presented in Table 6.2 with respect to the HEX3 configuration. In addition to the information reported in such a table, the initial value for F_{rc} is set equal to 90%. This is consistent with the methods considered until now to carry out

the refueling analyses, as at 90% of the absorption reaction, the charging process is considered completed, the inlet hydrogen valve closes and the tank is ready for discharging.
Besides the heat exchanger geometric parameters, the input data listed in Table 6.1 are also used to study the dehydriding process for HEX2. For such a configuration, the results are obtained with an aspect ratio of 0.5.

Table 6.2: Model input parameters for discharging analysis (HEX3).

Domain	Parameter	Value	Unit
Amb.	p_{amb}	1.013	bar
	T_{amb}	20	°C
p_{ramp}	p_0	300	bar
	p_{ref}	1	bar
	duration	600	s
	time offset	0	s
Cool.	Dexcool®		
	$\dot{m}_c$	5	kg/s
	$T_{c,i}$	30	°C
Tank	L	1	m
	d_{tank}	0.4	m
MH	$Ti_{1.1}CrMn$		
	ϕ	60%	-
	δ	1	mm
Tube	Al 6061-T6		
	OD	2.5	mm
HEX	Shell and tube		
	PR	1.25	-
	Layout angle	30	deg
	Baffle cut	25%	-
	Baffle space	50% d_{tank}	m

From the table it should be observed that a much lower mass flow rate than in Table 6.1 is considered for the discharging process. This is done to take into account of the actual operation of the FCEV. In practice, the heating fluid is circulated in a closed loop inside the car and therefore, the mass flow rate is limited by the size of the heating system components (e.g. valves, tubes) and the cooling demand of the fuel cell.
The heating fluid temperature at the inlet is set to 30 °C, which is the assumed value for the HTF that returns from the fuel cell system.

Fig. 6.18 shows the results obtained for the bed temperature, fraction of reaction completion and desorbed hydrogen mass for both HEX3 and HEX2 configurations. In Fig. 6.18a it is possible to notice that the metal hydride temperature rises sharply from the initial conditions to the heating fluid inlet temperature of 30 °C and then remains constant until the tank pressure decreases below p^{eq} triggering the hydrogen desorption at approximately 312 s. The endothermic nature of the reaction causes a the solid bed to suddenly cool down, reaching similar minima for the two configurations in a specular way of what observed for the hydriding process. Finally, the heat absorbed to maintain the desorption reaction increases the metal hydride temperature back to the inlet HTF temperature

Fig. 6.18b shows that the two heat exchanger configurations provide nearly coincident profiles for the fraction of reaction completion. The reaction is kinetically-limited and the temperature decrease observed in Fig. 6.18a has only a negligible effect on the dehydriding rates.

In Fig. 6.18c the stored mass decreases at first for the effect of the decreasing pressure until the dehydriding reaction is triggered. A considerable mass leaves the tank between 312 s and 456 s when the reaction is completed. From this moment only the hydrogen mass in the pores continues to decrease until the valve closes at 600 s and the system reaches stationary conditions.

The total desorbed hydrogen mass shows significantly different values for the two configurations, because of the different storage volumes realized by the two configurations (see Subsection 6.4.1).

It can be observed that, for both configurations, the initial mass differ from the values reached at the end of the charging process in Figs. 6.15e-f and Figs. 6.13e-f. This is mainly due to the difference in the starting and final conditions set for F_{rc} in the two processes (i.e. 90% and 100% for hydriding and dehydriding respectively) and in minor part to the different temperatures, thus densities, of the hydrogen in the gas phase.

At the end, both configurations enable fast discharging under practical heating conditions. The difference in the dehydriding performance is negligible for HEX2 and HEX3 and the only considerable disparity lies in the storage volume of the two layouts and thus, in the total hydrogen mass available to operate the FCEV.

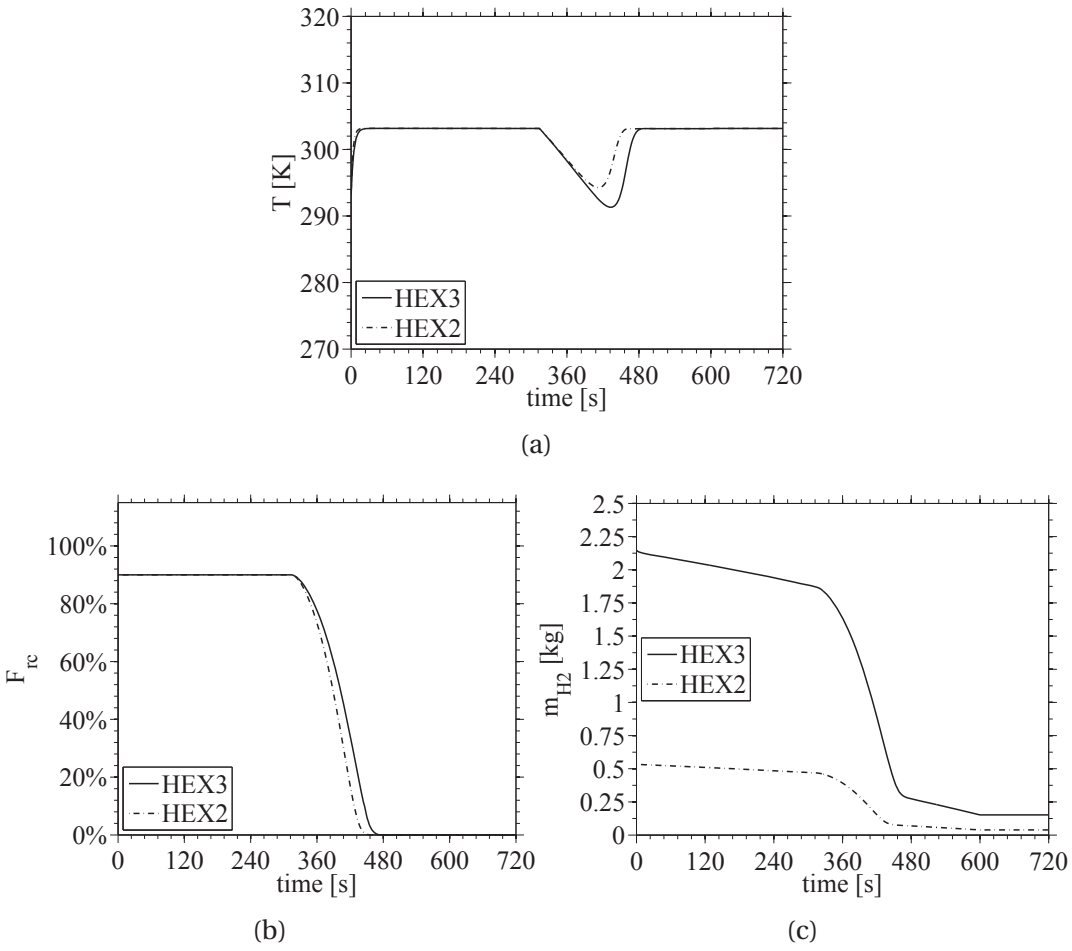

Figure 6.18: Disharging analysis: bed temperature (a); fraction of reaction completion (b); stored mass (c). HEX3 and HEX2 configurations.

6.4.3 Parametric analysis

The charging and discharging analyses presented in Subsections 6.4.1 and 6.4.2 showed that the drawback of the investigated designs is the small MH volume available for hydrogen storage. Therefore, in this section a sensitivity study on the main geometric parameters is carried out with the aim of optimizing the overall stored hydrogen mass.
The results here reported refer to the input data listed in Table 6.1.
It is worth pointing out that the inner diameter is not varied here as its value is the result of a design analysis based upon the critical MH thickness that achieves the target F_{rc} and t_{ref}. According to the thermal model described in Subsection 6.3.1 and Appendix B the only design parameters that influence the hydrogen stored mass are the pitch to tube diameter ratio PR and the aspect ratio a.

Fig. 6.19 shows the dependency of the hydrogen mass upon the pitch to tube diameter ratio PR for HEX3 on the left y-axis. The corresponding ratio between the MH volume and the inner tank volume (i.e. V_{ratio}) is plotted on the right y-axis.

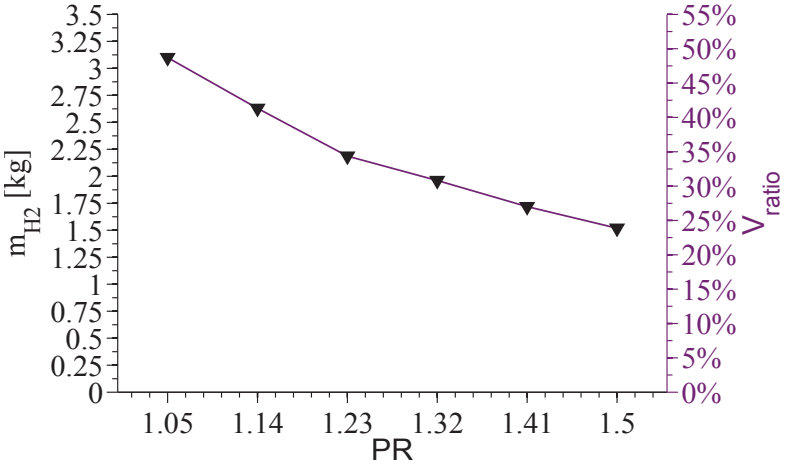

Figure 6.19: Stored hydrogen mass and volume ratio as functions of pitch to tube diameter ratio.

A decrease in the PR value corresponds to a reduced distance between the tubes and therefore to an increase number of MH tubes inside the tank. A maximum value of 3.09 kg is achieved for a pitch to tube diameter ratio of 1.05 and V_{ratio} becomes 48.7%. However, it is worth mentioning that practical PR values typically do not fall below 1.25 to avoid the weakening of the tube sheet [177]. In addition, as the storage capacity is enlarged by increasing the MH volume, the stored hydrogen mass increases with the absorbing alloy's weight resulting in a larger volumetric density and a constant

gravimetric density, which settles at 1.25%. This can be seen in Fig. 6.20 where the weight of the tank is shown for a pitch to tube diameter ratio of 1.05 and for its nominal value.

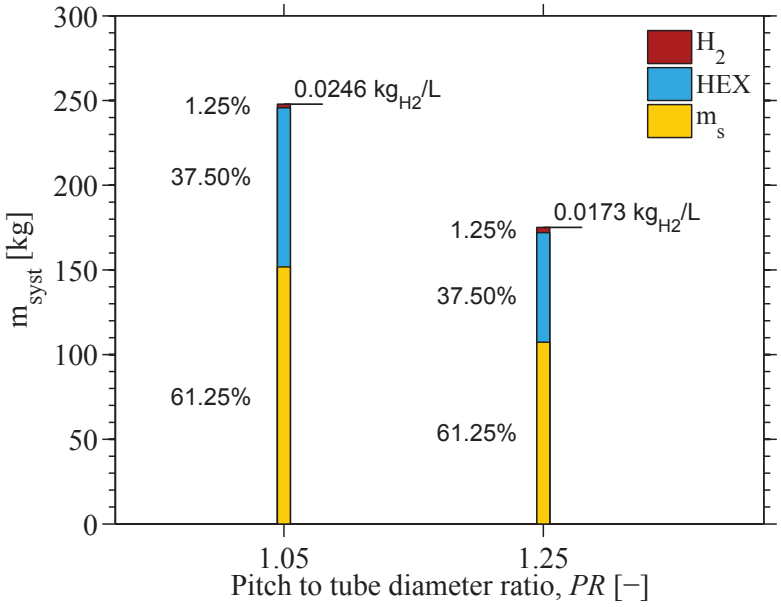

Figure 6.20: Weight of the main tank's components: hydrogen, heat exchanger and absorbing alloy.

The volumetric density increases from 0.0173 to 0.0246 kg_{H2}/L_{syst}. The increase in the volumetric density that occurs at lower pitch to tube diameter ratio values is compensated by the larger storage system's weight, which varies from 175 kg to 250 kg in the PR range of 1.25-1.05. In both cases the heaviest tank components is the absorbing alloy, which accounts for more than 61% of the total tank's weight, followed by the heat exchanger, i.e. 37.5% (Al6061-T6 tubes), and hydrogen 1.25%.

It should be considered that a stored hydrogen mass of approximately 3.1 kg can also be obtained by reducing the porosity to 0.3 at 300 bar or to 0.4 at 600 bar. As discussed in Chapter 3 reducing the void fraction and/or increasing the charging pressure are not advisable strategies, as failures in the mechanical components subjected to repeated hydriding/dehydriding cycles may occur when a considerable packing density is used, whereas larger operating pressures will require dedicated high-pressure tank components (e.g. valves) and a thicker vessel resulting in a more expensive system with effect on both volume and weight.
In Ref. [198] the effect of charging pressure and alloy quantity on the volume and weight of a hybrid high-pressure Al-CFRP vessel was estimated under some simplified assumptions. The results suggested that for a system dimensioned to store 5 kg of

hydrogen, an increase in the quantity of the absorbing alloy only enhances the volumetric density and does not affect the weight when hydrides with a w_{max} of at least 4.1% are used. This occurs because at relatively large hydrogen capacities, increasing the alloy content provides a significant reduction in the system's volume, resulting in a lighter vessel which balances the larger weight of the hydride.
Smaller system's volume and weight can also be obtained in principle by augmenting the operating pressure. However, these positive effects were found to be more important for void fractions above 70%. Below such a value, a large portion of the fueled hydrogen is stored in the metal hydride and increasing the charging pressure only benefits the volumetric density of the gas phase, which is modest compared to that of the absorbed phase. This concept can be observed in Fig. 6.21 where the amount of stored hydrogen for different charging pressures is plotted against the bed porosity ϕ. In such a figure the effect of the pressure on the MH tube thickness, and thus, on the overall volume, is neglected as for the small diameters of interest here the thickness is only modestly affected by the operating pressure (see Fig. 6.7).

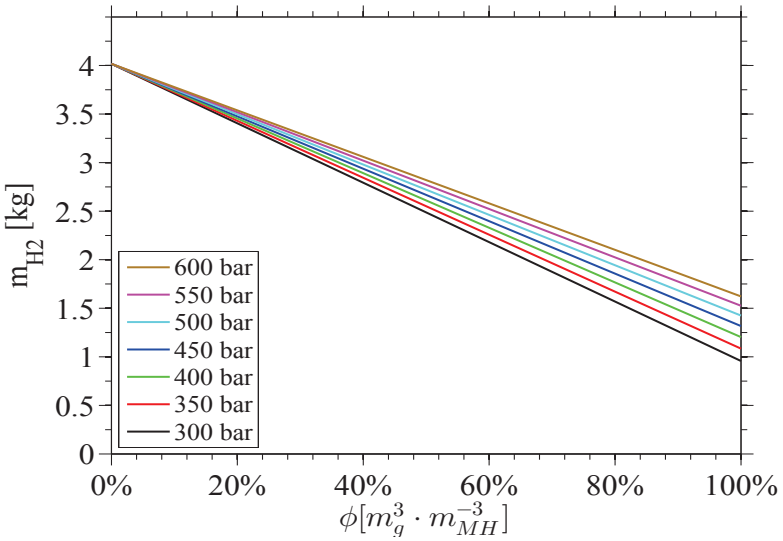

Figure 6.21: Stored hydrogen mass as a function of bed porosity and pressure.

Fig. 6.21 shows that for a fixed bed volume the amount of stored hydrogen increases linearly with the quantity of alloy and thus, with the reduction of porosity. The overall system's weight is mainly affected by the hydride mass, which varies considerably with the packing density. For a porosity variation between 0 and 1, the alloy's weight varies between 268 kg and 0 kg and becomes 107 kg at the nominal bed porosity (0.6).
The effect of pressure on the hydrogen mass becomes important only at large void fractions and thus, when a considerable quantity of hydrogen is stored in the gas phase. This is evident for the limit case of unitary porosity, for which the system

behaves as a pure CHG tank and the effect of pressure upon the hydrogen mass is maximum. In this case, the hydrogen mass augments by more than 80% when the operating pressure is raised from 300 bar to 600 bar. On the other hand, increasing the charging pressure has a positive effect on the reaction kinetics, but does not influence the storage capacity of the hydrogen-absorbing alloy. As a result, at large packing densities the hydrogen mass becomes less sensitive to the pressure and reaches the common value of 4 kg for the unrealistic case of a null void fraction.
From Fig. 6.21 it appears that for HEX3 it is not possible to achieve the target hydrogen mass of 5 kg for any combinations of alloy quantity and charging pressure. Despite the small MH volume, the main reason for this is the low gravimetric capacity of $Ti_{1.1}CrMn$ (1.5wt%), which limits the hydrogen storage. Simulations show that in order to achieve the target hydrogen mass at the nominal porosity, storage capacities of 4.2wt% and 3.7wt% are required at system's pressures of 300 bar and 600 bar respectively.
Finally, it is worth mentioning that the results reported in Ref [198] should be considered as the outcomes of a preliminary study which does not take into account the important effect that the heat exchanger has on the system's volume and weight. In addition, it is assumed that the MH will absorb hydrogen for its full capacity, which is unrealistic at practical reaction times (see 3.8.2). Detailed investigations were planned to address these issues and provide more reliable results. Unfortunately, to be best of the author's knowledge it is not possible to find any further study on this topic.

Fig. 6.19 shows the dependency of the hydrogen mass upon the aspect ratio for HEX2 on the left y-axis. The respective V_{ratio} is plotted on the right y-axis.
For HEX2, increasing the aspect ratio at constant inner diameter corresponds to reducing the outer tube inner diameter (see Appendix B) and therefore increasing the available volume for MH tubes.

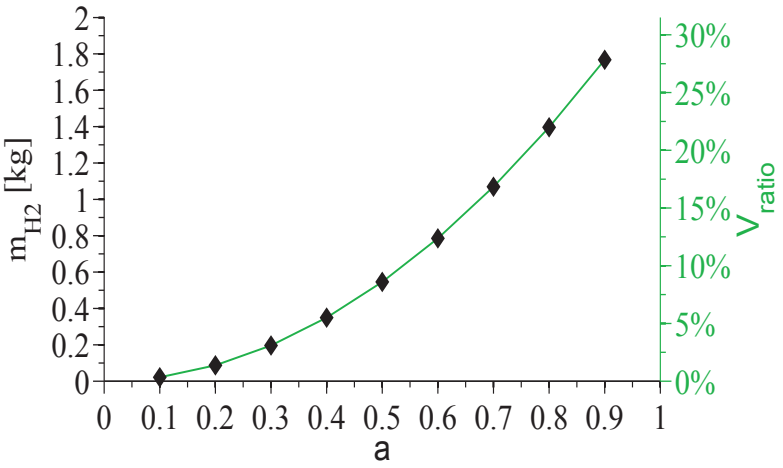

Figure 6.22: Stored hydrogen mass and volume ratio as functions of aspect ratio.

The stored hydrogen mass (and the MH volume) increase exponentially with the aspect ratio, as the number of tubes has an exponential dependency upon the outer diameter [179]. However, reducing the outer tube diameter means that the cross flow area for the heat transfer fluid decreases with a. As a result one could expect that decreasing the HTF mass flow rate would cause a reduction in the cooling performance. Simulations have shown that for an inner diameter of 2 mm and an aspect ratio of 0.9 the minimum mass flow rate that enables achieving the target F_{rc} at the desired time of 3 min is 0.5 kg $\cdot$ s^{-1}.
Finally, although the stored hydrogen mass significantly increases when the aspect ratio varies from 0.1 to 0.9, the maximum m_{H2} (i.e. 1.77 kg) is comparable with the minimum value obtained with a PR of 1.5 for HEX3 (i.e. 1.51 kg).

At the end, it is important to mention that other solutions that are based on the tubular tank design can be investigated to further enhance the hydrogen capacity of the storage system. In Ref. [199] steel tubes of approximately the same size as that considered in the present work are employed to store the metal hydride for a thermal compression application. Each tube has an outer diameter of 3 mm and is placed inside the vessel in a helical-coil arrangement. The tubes are brazed to a ring manifold located at the center of the tank and the heat transfer fluid flows over the tubes on the shell side. Results show that such a design is able to withstand pressures up to 345 bar and realize hydrogen-absorption/desorption cycles within 16 min when air is used as the HTF. In addition, it is claimed that such a configuration provides a lighter and more compact solution than a conventional shell-and-tube design with straight tubes. Therefore, it would be worth investigating the possibility to use a ring manifold design to maximize the hydride volume for a hydrogen storage application. Under the assumption that the same number of tubes as for HEX3 is achieved, the helical-coil design can provide longer tubes for the same length of the vessel. As the MH volume is directly proportional to the tube length, an increase by 2.3 times in the longitudinal dimension can lead to a hydrogen capacity of 5 kg for a 126 L tank. However, due to the complex design, detailed studies on the heat transfer performance should be carried out to ensure that the system can achieve fueling times of practical interest while maintaining a compact size.

6.5 Conclusion

A modeling platform is successfully developed in the Dymola™ environment to design and simulate on-board hydrogen storage systems. At the moment of the submission of the thesis HySDeP includes a MH storage system model based on tubular tank layout and a CHG storage system with a standard and a novel design with integrated PCM.
The computational platform is built with attention to the key design criteria of user-friendliness, flexibility and facility of third party development. The main structures (or classes in the Modelica® language) are divided in macro and sub-models, records, ports and functions. The architecture is kept simple and the models are grouped in modeling packages by category.
For the MHSS, seven packages are defined. These are: *Tanks_With_Hex*, *Ports*, *Sources*, *Properties*, *Heat Transfer*, *Kinetics*, *TESTS*. The developer has access to the modeling code contained in each package, whereas the user has only access to *TESTS* where a simulation model can be tuned with the values of choice for the main design parameters. The same occurs for the CHG system which comprises six packages: *Tanks*, *Ports*, *Sources*, *Properties*, *Heat Transfer*, *TESTS*.
Depending of which tank is selected, the user has access to a number of libraries that include different heat exchanger designs, material properties, kinetic models and heat transfer boundary conditions. Among these, the most important are the databases for the compositions of hydrogen-absorbing alloy and phase change material.
HySDeP can be used to perform both charging and discharging analyses. Examples of both are discussed in the present chapter for the MHSS and a comparison between the storage and cooling performance of two shell and tube layouts is provided. The heat exchangers refer to the HEX3 and HEX2 configurations, according to the notation used in Chapter 4. The MH is placed in tubes of 2 mm of inner diameter in order to achieve the targets for F_{rc} (i.e. 90%) and t_{ref} (i.e. 3 min) in agreement with the design analysis reported in Chapter 3. If a sintered filter is introduced in the tube to enable hydrogen distribution within the solid bed, the tube size should be enlarged in practice to account for the filter diameter. However, as the filter would be inserted at the adiabatic center-line of the tube, its mass would not affect the heat transfer and therefore, it has been neglected in this study.
For both the HEX3 and HEX2 layouts the 0D and 1D models provide equivalent results and well describe the reactions that occur within the solid bed.
The small tube size enable efficient heat transfer over the entire MH thickness and thus considerable significant hydriding rates. As a result, the reaction is kinetically-limited and the temperature increase that occurs during hydrogen absorption is not sufficient to slow down the reaction.

Although the two heat exchanger configurations realize similar cooling and kinetic performance, a great disparity occurs for the amount of stored hydrogen mass. This is due to the difference in the MH volume available for hydrogen storage. HEX3 achieves a total hydrogen mass of nearly 2.2 kg, whereas HEX2 is able to store approximately one fourth of this value. Such a mass is stored mainly in the absorbed phase (c.a. 74% of the total fueled mass), even though the hydrogen-absorbing alloy occupies only 40% of the bed volume (i.e. ϕ= 60%).
The same results can be obtained under the assumption of constant HTF temperature between inlet and outlet, as for practical flow rates the thermal gradient in the fluid flow can be neglected.
The discharging analysis reveals that both HEX3 and HEX2 enable fast dehydriding under practical heating conditions. As it was found for the charging process, the two layouts provide similar heat-transfer and kinetic performance and the only considerable difference lies in the amount of hydrogen that is available to operate the FCEV. To overcome this issue a sensitivity analysis is carried out with respect to the main geometric parameters for each configuration to optimize the hydrogen stored mass.
For HEX2 increasing the aspect ratio provides significant hydrogen mass augmentation, which varies between 0.02 kg to 1.77 kg in the range of 0.1-0.9 for a. However, even in the most favorable conditions for a, the total stored mass is slightly larger than the minimum value realized for HEX3 (1.51 kg), which occurs for a pitch to tube diameter ratio, PR, of 1.5. Decreasing PR allows packing more MH tubes in a fixed volume and thus, storing a larger hydrogen mass, which reaches 3.1 kg for a pitch to tube diameter ratio of 1.05. However, the increase in the volumetric density (from 0.0173 to 0.0246 kg_{H2}/L_{syst}) is compensated by the larger storage system's weight, which varies from 175 kg to 250 kg for a PR between 1.25 to 1.05. In both cases the heaviest tank components is the absorbing alloy, which accounts for more than 61% of the total tank's weight, followed by the heat exchanger, i.e. 37.5% (Al6061-T6 tubes), and hydrogen 1.25%. As a result the gravimetric storage capacity is found to be independent from PR with a constant value of 1.25%.
The same optimized storage capacity can be obtained for a packing density that corresponds to a porosity of 0.3 at the nominal pressure of 300 bar or of 0.4 at 600 bar.
Caution must be taken when the augmentation of the hydrogen stored mass is achieved by decreasing PR or ϕ. The former strategy may weaken the tube sheet, whereas the latter can cause failures of the mechanical components subjected to repeated hydriding/dehydriding cycles.
Finally, the hydrogen storage density can be augmented by employing configurations that provide higher hydride densities. One example is the helical-coil design reported in Ref. [199]. This configuration has the potential to provide large hydride volumes in a compact space. However, any storage solution that aims at increasing the hydrogen

capacity by enlarging the volume of the hydride will always be penalized by the weight of the absorbing alloy. Therefore, the development light-weight alloys with adequate storage capacities is fundamental to significantly improve the gravimetric density of the on-board storage system.

7 Conclusion

7.1 Concluding remarks

Nowadays, the hydrogen global production settles above 55 million metric tons, including both merchant and captive markets. The latter represents 88% of the overall produced volumes and comprises the main consumers, being the petrochemical and fertilizer industries. The hydrogen market is foreseen to considerably grow after 2020, when fuel cell electric vehicles will start playing an increasing role in the forthcoming renewable transport sector. However, in order to establish a solid ground for significant market penetration of FCEVs, several inter-dependent issues first need to be addressed. Among these, the development of an an effective on-board storage system is a major challenge to be tackled.

The present work aims at developing a modeling platform, named HySDeP, for the design and simulation of vehicular hydrogen storage systems.
The scope of the platform is to provide a starting point for a comprehensive model library that includes the main on-board storage solutions, enabling comparisons among the promising technologies. In order to achieve this goal, the platform is built according to some key criteria that allow both user and developer to take advantage of a simple architecture. The principles that guide the design of the computational structure encompass the concepts of user-friendliness, flexibility and ease of third party development.
The platform implementation is carried out in Dymola™ software, a front-end user-interface to Modelica® language, which offers a convenient environment for modeling the dynamics of industrial multi-domain systems with a topological approach. The components can be represented graphically and the hierarchical structure facilitates the reuse of the modeling knowledge, making this language particularly suitable to build robust exchangeable component libraries.

The first modeling effort is made with regard to storage solutions that show large room for potential improvement. In this work, these technologies are identified as high-pressure metal hydride and compressed hydrogen gas systems. The main materials that affect the storage and thermal performance are selected according to some prescribed requirements.
A list of targets and constraints is defined to lead the analysis towards efficient designs that can improve the storage and energy efficiency of the fueling process with respect to the state-of-the-art technology. The current state of commercial CHG systems is considered as the reference point upon which the performance objectives are defined. For the MHSS the storage targets are: 5 kg of hydrogen in 126 L and fueling time within 3 min. The main requirements are: cylindrical shape of the high-pressure vessel and uniform pattern of reaction within the MH bed to maximize the storage capacity of the available active volume.
For the novel CHG system, here proposed, the objectives are to realize the same storage performance in terms of stored mass and fueling time as the current technology and improve the efficiency of the charging process. This is intended to be achieved by inserting a phase change material that serves as a passive cooling system to absorb the heat of compression inside the tank. The main requirement is that the tank walls must be kept below the critical temperature of 85 °C at any time to ensure the mechanical integrity of the pressurized vessel.

Reliable computational models are developed to describe the physical phenomena that occur inside the tanks during periodical charging/discharging processes. The models can be adapted to the needs of the specific study by selecting the features of interest from implemented user libraries. These serves as databases for different heat exchanger designs, material compositions (for tubes, MH and PCM), heat transfer fluid properties, kinetic equations and heat transfer boundary conditions.
In this thesis the developed model is used to determine the maximum MH bed thickness at which the hydriding reaction reaches 90% of its saturation value at the target refueling time. The respect of the critical MH thickness is considered as the design criterion to meet the prescribed targets and requirements.
The application of such a to a $Ti_{1.1}CrMn$ bed provides a maximum distance from the cooling surfaces of 1 mm.
A thermal selection analysis for the tank/heat-exchanger system suggests the tubular tank design in a standard shell and tube configuration as a promising candidate to achieve the goals identified in this study.
The combination of the results from the critical MH thickness and heat-exchanger selection analyses provides a final MHSS design that consists in MH tubes of 2 mm of inner diameter and external heat transfer fluid flow over the tube bank.
The advantages of placing the hydrogen-absorbing alloy inside small-diameter tubes

encompass technical and economic aspects. The main ones include: small tube thickness and thus, reduced tank weight, ease of confinement and compaction of the MH powder, uniform reaction pattern and modularity which facilitates the access to the main tank components and helps decrease the maintenance cost. On the other hand, the main drawback of this design consists in a smaller MH capacity when compared to chamber-tank layouts.
A comparison between the shell-and-tube design and the tube-in-tube configuration is performed in HySDeP with regard to complete charging and discharging analyses. For both layouts the small tube size enables efficient heat transfer over the entire MH bed, which achieves the desired fraction of reaction completion within the target refueling time. However, a great disparity occurs when the total amount of stored hydrogen is taken into account. Approximately 2.2 kg are fueled in a 126 L tank for the shell and tube configuration whereas only 0.55 kg are stored for the tube-in-tube configuration. This is due to the difference in the MH volume, which represents 34.7% and 8.5% of the available inner tank volume for the shell-and-tube and tube-in-tube configurations respectively. With a porosity of 60% the absorbed phase corresponds to 74% of the total fueled mass, whereas the rest is stored in the gas phase in the void volume of the bed.
A fast discharging analysis reveals that both configurations enable intense dehydriding rates under practical heating conditions. Once again, the main difference for the two layouts lies in the total amount of desorbed mass, in a specular way to what observed for the charging process.
In order to maximize the total amount stored hydrogen the main geometric parameters for the two configurations have been varied within a practical range. For the shell and tube design a maximum stored mass of c.a. 3.1 kg is obtained when the pitch to tube diameter ratio is decreased to 1.05 which corresponds to the lowest value of in the variation range. However, caution should be taken when values below 1.25 are considered, as the increased density of tubes can substantially weaken the tube sheet according to the design guidelines for shell and tubes.
For the tube in tube configuration the most effective strategy for hydrogen mass maximization consists in increasing the aspect ratio to 0.9. Under this condition the annular region occupied by the heat transfer fluid becomes small when compared to the inner tube volume where the MH is placed. However, even in the most favorable conditions the stored mass assumes a modest value, i.e. 1.51 kg, which is smaller than for the other design and far from the prescribed target.

For the novel CHG tank, refueling analyses carried out for a type IV tank show that the integration of a 5 mm PCM layer enables significant hydrogen cooling at times that are too large to be of practical interest. This occurs because of the poor heat transfer at the hydrogen/PCM interface which prevents effective gas cooling within

the target refueling time. In addition, the presence of hot spots at the tank wall cannot be entirely excluded and therefore, the requirement cannot be considered satisfied. A parametric analysis for the main design parameters is carried out to solve these issues. The results show that the material's thermal properties and thickness are found to only have a modest effect on the storage performance and that the reward strategy consist in augmenting the heat transfer area.
The encapsulation technique can provide sufficiently high surface enlargements to reduce the peak temperature well below 85 °C and eliminate the risk of hot spots at the walls, while providing a proper confinement structure for the phase change material during repeated melting-solidification cycles. Furthermore, the storage performance in terms of mass becomes the same as for the standard tank case, although the fueling occurs at ambient temperature. As a result, the intense hydrogen cooling, from ambient conditions to -40 °C, that takes place at the refueling station can be avoided. This leads to a maximum energy saving of 4.2 MJ per fueling. Additional advantages, that are difficult to quantify, involve the cost reduction of the heat exchanger and increased reliability of the fueling process.

At the end, the developed computational platform proves to be a valuable tool for the design and simulation of on-board storage systems.
The results show that, while the novel PCM vessel qualifies as a potential advancement towards a more efficient hydrogen storage, the high-pressure MH tank does not provide valuable benefits when compared to the current status of commercial CHG systems for light-duty vehicles.
The proposed MHSS design succeeds in fulfilling the performance requirements as well as the fueling time target. In particular, the tubular tank design achieves the desired fraction of reaction completion within 3 min, while enabling a uniform pattern of reaction for both hydriding and dehydriding. However, the set target for the stored hydrogen mass is not satisfied. There are two complementary reasons for this. On one side, the stored mass is limited by the relatively small MH volume that this design is able to provide and on the other side, the low gravimetric capacities of the investigated material prevent adequate hydrogen storage for reasonable tank weights. As an example, it is worth pointing out that in the presented study, 2.2 kg of hydrogen are stored at the expenses of a metal hydride weight above 100 kg. The latter value not accounting for the mass of the tank and its components. This observation falls within a more general debate, that has animated the scientists for the last decades, on the feasibility of MHSSs as a solution to the storage needs of the transport sector. Although being promising candidates, at the moment no MH seems to possess all the required properties to achieve this goal.
Further research on both tank design and light-weight absorbing alloys is needed to address the issues of limited volumetric and gravimetric storage capacities of MHSSs.

7.2 Recommendations for future work

Future efforts should focus on expanding the model library to include other types of hydrogen storage that can be used for vehicular applications. The next step in this direction is to use the developed models to design MH tanks based on the chamber layout and different heat exchanger configurations that can be selected from a wide library. Among these, the helical-coil design has the potential to improve the volumetric density of the storage system and should be investigated with particular attention to the heat transfer performance in order to achieve fueling times of practical interest. In addition, the databases for material properties and kinetic models should be broadened to include other promising alloys and mass diffusion equations. Furthermore, it would be interesting to combine the developed platform with other open-source component libraries as the one presented in Ref. [200] for a complete hydrogen refueling station. Models for electrolyzers and main FCEV components can also be incorporated to build a universal hydrogen platform.
Finally, the proposed PCM tank technology should be further investigated to assess its convenience and select the optimal confinement method (e.g. encapsulation, nano-tubes, graphite composites) with respect to criteria on storage performance, fueling efficiency and cost.

Bibliography

[1] V. Subramani, A. Basile, and N. T. Veziroglu. *Compendium of hydrogen energy. Vol. 1, Hydrogen production and purification.* Woodhead Publishing Series in Energy, 2015.

[2] A. Sieminski. World energy outlook 2015 - with predictions to 2040. Technical report, International Energy Agency, 2015.

[3] D.O.E. Report of the hydrogen production expert panel: A subcommittee of the hydrogen & fuel cell technical advisory committee. Technical report, United States Department of Energy (D.O.E.), 2013.

[4] E. Miller, C. Ainscough, and A. Talapatra. Hydrogen production status 2006-2013. Technical report, United Stated Department of Energy (DOE) - Hydrogen and Fuel Cells Program Record, 2014.

[5] D.O.E. Multi-year research, development, and demonstration plan - 3.1 hydrogen production. Technical report, United States Department of Energy (D.O.E.), 2013. URL http://energy.gov/sites/prod/files/2015/06/f23/fcto_myrdd_production.pdf.

[6] D. Bessarabov, H. Wang, H. Li, and N. Zhao. *PEM electrolysis for hydrogen production: principles and applications.* CRC (Taylor and Francis Group), 2015. ISBN-10: 1482252295.

[7] A. Körner, C. Tam, S. Bennett, and J.-F. Gagné. Technology roadmap - hydrogen and fuel cells. Technical report, International Energy Agency (IEA), 2015.

[8] Markets&Markets technical team. Hydrogen generation market by geography, by mode of generation & delivery, by applications and by technology - global trends & forecasts to 2019. Technical report, Markets&Markets, 2014.

[9] G. Simbolotti. Hydrogen production & distribution. Technical report, International Energy Agency (IEA) - Energy Technology Essentials, 2007.

[10] T. Riis, E. F. Hagen, P. J. S. Vie, and Ø. Ulleberg. Hydrogen production and storage–r&d priorities and gaps. *International Energy Agency-Hydrogen Co-Ordination Group-Hydrogen Implementing Agreement*, 2006.

[11] A. Züttel, A. Borgschulte, and L. Schlapbach. *Hydrogen as a future energy carrier*. John Wiley & Sons, 2011.

[12] J. W. Kim, K. J. Boo, and Cho J. H. *Advances in Hydrogen Production Storage and Distribution - Ch. 1*. Woodhead Publishing (Series in Energy), 2015. doi: 10.1533/9780857097736.1.3.

[13] D.O.E. Multi-year research, development, and demonstration plan - 3.9 market transformation. Technical report, United States Department of Energy (D.O.E.), 2013. URL http://energy.gov/sites/prod/files/2015/05/f22/fcto_myrdd_market_transformation.pdf.

[14] R. Harris, D. Book, P. A. Anderson, and P. P. Edwards. Hydrogen storage: the grand challenge. *The Fuel Cell Review*, 1:17–23, 2004.

[15] D. Mori and K. Hirose. Recent challenges of hydrogen storage technologies for fuel cell vehicles. *International Journal of Hydrogen Energy*, 34(10):4569–4574, 2009.

[16] K. Hirose and M. Hirscher. *Handbook of hydrogen storage: new materials for future energy storage*. John Wiley & Sons, 2010.

[17] O. Edenhofer, R. Pichs-Madruga, Y. Sokona, E. Farahani, Kadner S., K. Seyboth, A. Adler, I. Baum, S. Brunner, P. Eickemeier, J. Kriemann, B. Savolainen, S. Schlömer, C. von Stechow, T. Zwickel, and J. C. (eds.) Minx. Climate change 2014: Mitigation of climate change. contribution of working group iii to the fifth assessment report of the intergovernmental panel on climate change. Technical report, Intergovernmental Panel on Climate Change (IPCC), 2014.

[18] Core Writing Team, R. K. Pachauri, and L. A. (eds.) Meyer. Climate change 2014: Synthesis report. contribution of working groups i, ii and iii to the fifth assessment report of the intergovernmental panel on climate change. Technical report, Intergovernmental Panel on Climate Change (IPCC), 2014.

[19] J. Dulac, P. Cazzola, and V. (coordinators) Aneris. Railway handbook 2014 - energy consumption and co2 emissions. Technical report, International Energy Agency (IEA) and the International Union of Railways (IUR), 2014.

[20] A. Züttel. Materials for hydrogen storage. *Materials today*, 6(9):24–33, 2003.

[21] J. Zhang, T. S. Fisher, P. V. Ramachandran, Jay P Gore, and I. Mudawar. A review of heat transfer issues in hydrogen storage technologies. *Journal of Heat Transfer*, 127(12):1391–1399, 2005.

[22] J. O. Jensen, A. P. Vestbø, Q. Li, and N.J. Bjerrum. The energy efficiency of onboard hydrogen storage. *Journal of Alloys and Compounds*, 446:723–728, 2007.

[23] K. C. Hoffman, J. J. Reilly, F. J. Salzano, C. H. Waide, R. H. Wiswall, and W. E. Winsche. Metal hydride storage for mobile and stationary applications. *International Journal of Hydrogen Energy*, 1(2):133–151, 1976.

[24] K. Lu. Hydrogen storage and materials. *Materials in Energy Conversion, Harvesting, and Storage*, pages 387–417, 2002.

[25] S. Satypal. Us department of energy hydrogen and fuel cells program 2011 annual merit review and peer evaluation report. Technical report, National Renewable Energy Laboratory (NREL), Golden, CO., 2011.

[26] H. Wu. Strategies for the improvement of the hydrogen storage properties of metal hydride materials. *ChemPhysChem*, 9(15):2157–2162, 2008.

[27] J. M. Pasini, C. Corgnale, B. A van Hassel, T. Motyka, S. Kumar, and K. L. Simmons. Metal hydride material requirements for automotive hydrogen storage systems. *International Journal of Hydrogen Energy*, 38(23):9755–9765, 2013.

[28] S. Satypal. Merit review and peer evaluation report - hydrogen storage. Technical report, US Department of Energy (DOE), 2015.

[29] D.O.E. Multi-year research, development, and demonstration plan - 3.3 hydrogen storage. Technical report, United States Department of Energy (D.O.E.), 2013. URL http://energy.gov/sites/prod/files/2015/05/f22/fcto_myrdd_storage.pdf.

[30] Y. Kojima, Y.and Kawai, S. Towata, T. Matsunaga, T. Shinozawa, and M. Kimbara. Development of metal hydride with high dissociation pressure. *Journal of alloys and compounds*, 419(1):256–261, 2006.

[31] A. W. C. van den Berg and C. O. Areán. Materials for hydrogen storage: current research trends and perspectives. *Chemical Communications*, (6):668–681, 2008.

[32] W. M. Mueller, J. P. Blackledge, and G. G. Libowitz. *Metal hydrides*. Elsevier, 2013.

[33] T. Yoshida and K. Kojima. Toyota mirai fuel cell vehicle and progress toward a future hydrogen society. *Electrochemical Society Interface*, Summer:45–49, 2015.

[34] C. Na Ranong, M. Hoehne, J. Franzen, J. Hapke, G. Fieg, M. Dornheim, N. Eigen, J. M. Bellosta von Colbe, and O. Metz. Concept, design and manufacture of a prototype hydrogen storage tank based on sodium alanate. *Chemical Engineering & Technology*, 32(8):1154–1163, 2009.

[35] H. Choi and A.F. Mills. Heat and mass transfer in metal hydride beds for heat pump applications. *International Journal of Heat and Mass Transfer*, 33(6): 1281–1288, 1990.

[36] A. Demircan, M. Demiralp, Y. Kaplan, M.D. Mat, and T.N. Veziroglu. Experimental and theoretical analysis of hydrogen absorption in lani5–h2 reactors. *International Journal of Hydrogen Energy*, 30(13):1437–1446, 2005.

[37] A. Jemni and S. Ben Nasrallah. Study of two-dimensional heat and mass transfer during desorption in a metal-hydrogen reactor. *International Journal of Hydrogen Energy*, 20(11):881–891, 1995.

[38] S. Ben Nasrallah and A. Jemni. Heat and mass transfer models in metal-hydrogen reactor. *International Journal of Hydrogen Energy*, 22(1):67–76, 1997.

[39] A. Jemni, S. Ben Nasrallah, and J. Lamloumi. Experimental and theoretical study of ametal–hydrogen reactor. *International Journal of Hydrogen Energy*, 24(7): 631–644, 1999.

[40] A. Chaise, P. Marty, P. De Rango, and D. Fruchart. A simple criterion for estimating the effect of pressure gradients during hydrogen absorption in a hydride reactor. *International Journal of Heat and Mass Transfer*, 52(19):4564–4572, 2009.

[41] Z. Dehouche, W. De Jong, E. Willers, A. Isselhorst, and M. Groll. Modelling and simulation of heating/air-conditioning systems using the multi-hydride-thermal-wave concept. *Applied thermal engineering*, 18(6):457–480, 1998.

[42] D. A. Mosher, S. Arsenault, X. Tang, and D. L. Anton. Design, fabrication and testing of naalh 4 based hydrogen storage systems. *Journal of Alloys and Compounds*, 446:707–712, 2007.

[43] M. Verga, F. Armanasco, C. Guardamagna, C. Valli, A. Bianchin, F. Agresti, S.L. Russo, A. Maddalena, and G. Principi. Scaling up effects of mg hydride in a temperature and pressure-controlled hydrogen storage device. *international journal of hydrogen energy*, 34(10):4602–4610, 2009.

[44] T. Maeda, K. Nishida, M. Tange, T. Takahashi, A. Nakano, H. Ito, Y. Hasegawa, M. Masuda, and Y. Kawakami. Numerical simulation of the hydrogen storage with reaction heat recovery using metal hydride in the totalized hydrogen energy utilization system. *international journal of hydrogen energy*, 36(17):10845–10854, 2011.

[45] B. Bogdanović, A. Ritter, B. Spliethoff, and K. Straβburger. A process steam generator based on the high temperature magnesium hydride/magnesium heat storage system. *International journal of hydrogen energy*, 20(10):811–822, 1995.

[46] S. Mellouli, F. Askri, H. Dhaou, A. Jemni, and S. Ben Nasrallah. A novel design of a heat exchanger for a metal-hydrogen reactor. *International Journal of Hydrogen Energy*, 32(15):3501–3507, 2007.

[47] H. Dhaou, A. Souahlia, S. Mellouli, F. Askri, A. Jemni, and S. Ben Nasrallah. Experimental study of a metal hydride vessel based on a finned spiral heat exchanger. *international journal of hydrogen energy*, 35(4):1674–1680, 2010.

[48] H. Dhaou, N. Ben Khedher, S. Mellouli, A. Souahlia, F. Askri, A. Jemni, and S. Ben Nasrallah. Improvement of thermal performance of spiral heat exchanger on hydrogen storage by adding copper fins. *International Journal of Thermal Sciences*, 50(12):2536–2542, 2011.

[49] I. Yonezu, K. Nasako, N. Honda, and T. Sakai. Development of thermal energy storage technology using metal hydrides. *Journal of the Less Common Metals*, 89(2):351–358, 1983.

[50] C.A. Chung, S.-W. Yang, C.-Y. Yang, C.-W. Hsu, and P.-Y. Chiu. Experimental study on the hydrogen charge and discharge rates of metal hydride tanks using heat pipes to enhance heat transfer. *Applied Energy*, 103:581–587, 2013.

[51] Y. Liu, H. Wang, A. K. Prasad, and S. G. Advani. Role of heat pipes in improving the hydrogen charging rate in a metal hydride storage tank. *International Journal of Hydrogen Energy*, 39(20):10552–10563, 2014.

[52] I. Mudawar and M. Visaria. Coiled and microchannel heat exchangers for metal hydride storage systems, July 15 2014. US Patent 8,778,063.

[53] D. Mori, N. Haraikawa, N. Kobayashi, H. Kubo, K. Toh, M. Tsuzuki, T. Shinozawa, and T. Matsunaga. High-pressure metal hydride tank for fuel cell vehicles. In *MRS Proceedings*, volume 884, pages GG6–4. Cambridge Univ Press, 2005.

[54] F. Askri, M. Ben Salah, A. Jemni, and S. Ben Nasrallah. Optimization of hydrogen storage in metal-hydride tanks. *International Journal of Hydrogen Energy*, 34(2): 897–905, 2009.

[55] M. Visaria, I. Mudawar, T. Pourpoint, and S. Kumar. Study of heat transfer and kinetics parameters influencing the design of heat exchangers for hydrogen storage in high-pressure metal hydrides. *International Journal of Heat and Mass Transfer*, 53(9):2229–2239, 2010.

[56] M. Visaria, I. Mudawar, and T. Pourpoint. Enhanced heat exchanger design for hydrogen storage using high-pressure metal hydride: Part 1. design methodology and computational results. *International Journal of Heat and Mass Transfer*, 54(1):413–423, 2011.

[57] M. Visaria, I. Mudawar, and T. Pourpoint. Enhanced heat exchanger design for hydrogen storage using high-pressure metal hydride–part 2. experimental results. *International Journal of Heat and Mass Transfer*, 54(1):424–432, 2011.

[58] I. Mudawar, M. Visaria, H. Zhang, and T. Pourpoint. Finned heat exchangers for metal hydride storage systems, January 28 2014. US Patent 8,636,836.

[59] M. Visaria and I. Mudawar. Coiled-tube heat exchanger for high-pressure metal hydride hydrogen storage systems–part 1. experimental study. *International Journal of Heat and Mass Transfer*, 55(5):1782–1795, 2012.

[60] M. Visaria and I. Mudawar. Coiled-tube heat exchanger for high-pressure metal hydride hydrogen storage systems–part 2. computational model. *International Journal of Heat and Mass Transfer*, 55(5):1796–1806, 2012.

[61] M. Visaria and I. Mudawar. Experimental investigation and theoretical modeling of dehydriding process in high-pressure metal hydride hydrogen storage systems. *international journal of hydrogen energy*, 37(7):5735–5749, 2012.

[62] A. Souahlia, H. Dhaou, F. Askri, M. Sofiene, A. Jemni, and S. Ben Nasrallah. Experimental and comparative study of metal hydride hydrogen tanks. *international journal of hydrogen energy*, 36(20):12918–12922, 2011.

[63] S. Mellouli, F. Askri, H. Dhaou, A. Jemni, and S. Ben Nasrallah. Numerical simulation of heat and mass transfer in metal hydride hydrogen storage tanks for fuel cell vehicles. *International Journal of Hydrogen Energy*, 35(4):1693–1705, 2010.

[64] H. Wang, A. K. Prasad, and S. G. Advani. Hydrogen storage systems based on hydride materials with enhanced thermal conductivity. *International Journal of Hydrogen Energy*, 37(1):290–298, 2012.

[65] E. S. Kikkinides, M. C. Georgiadis, and A. K. Stubos. Dynamic modelling and optimization of hydrogen storage in metal hydride beds. *Energy*, 31(13):2428–2446, 2006.

[66] E. S. Kikkinides, M. C. Georgiadis, and A. K. Stubos. On the optimization of hydrogen storage in metal hydride beds. *International Journal of Hydrogen Energy*, 31(6):737–751, 2006.

[67] R.K. Ahluwalia. Sodium alanate hydrogen storage system for automotive fuel cells. *International journal of hydrogen energy*, 32(9):1251–1261, 2007.

[68] T. A. Johnson, S. W. Jorgensen, and D. E. Dedrick. Performance of a full-scale hydrogen-storage tank based on complex hydrides. *Faraday discussions*, 151: 327–352, 2011.

[69] H. Buchner and R. Povel. The daimler-benz hydride vehicle project. *International Journal of Hydrogen Energy*, 7(3):259–266, 1982.

[70] G. A Lozano, C. Na. Ranong, J. M. Bellosta von Colbe, R. Bormann, G. Hapke, J.and Fieg, T. Klassen, and M. Dornheim. Optimization of hydrogen storage tubular tanks based on light weight hydrides. *International Journal of Hydrogen Energy*, 37(3):2825–2834, 2012.

[71] C. A. Krokos, D. Nikolic, E. S. Kikkinides, M. C. Georgiadis, and A. K. Stubos. Modeling and optimization of multi-tubular metal hydride beds for efficient hydrogen storage. *international journal of hydrogen energy*, 34(22):9128–9140, 2009.

[72] A. Nakano, T. Maeda, H. Ito, T. Motyka, J. M. Perez-Berrios, and S. Greenway. Experimental study on a metal hydride tank for the totalized hydrogen energy utilization system. *Energy Procedia*, 29:463–468, 2012.

[73] A. Nakano, H. Ito, T. Maeda, T. Munakata, T. Motyka, C. Corgnale, S. Greenway, and J. M. Perez-Berrios. Study on a metal hydride tank to support energy storage for renewable energy. *Journal of Alloys and Compounds*, 580:S418–S422, 2013.

[74] M. Bhouri, J. Goyette, B. J. Hardy, and D. L. Anton. Numerical modeling and performance evaluation of multi-tubular sodium alanate hydride finned reactor. *international journal of hydrogen energy*, 37(2):1551–1567, 2012.

[75] Z. Bao, Z. Wu, S. N. Nyamsi, F. Yang, and Z. Zhang. Three-dimensional modeling and sensitivity analysis of multi-tubular metal hydride reactors. *Applied Thermal Engineering*, 52(1):97–108, 2013.

[76] C. Veerraju and M. R. Gopal. Heat and mass transfer studies on elliptical metal hydride tubes and tube banks. *international journal of hydrogen energy*, 34(10): 4340–4350, 2009.

[77] C. Veerraju and M. R. Gopal. Heat and mass transfer studies on plate fin-and-elliptical tube type metal hydride reactors. *Applied Thermal Engineering*, 30(6): 673–682, 2010.

[78] K. Komiya, M. Daigoro, M. Shinpei, H. Norihiko, Y. Kousei, W. Shintaro, T. Keiji, K. Hidehito, M. Mituo, and M. et al. Seiichiro. High-pressure hydrogen-absorbing alloy tank for fuel cell vehicles. Technical report, SAE Technical Paper, 2010.

[79] A. Mazzucco, M. Dornheim, M. Sloth, T. R. Jensen, J. O. Jensen, and M. Rokni. Bed geometries, fueling strategies and optimization of heat exchanger designs in metal hydride storage systems for automotive applications: A review. *International Journal of Hydrogen Energy*, 39(30):17054–17074, 2014.

[80] K. M. Lynn and G. Boyle. Making choices about hydrogen: Transport issues for developing countries. *UNUPress*, NA:978–92, 2008.

[81] A. R. Bunsell, F. Barbier, A. Thionnet, H. Zejli, and B. Besancon. Damage accumulation and lifetime prediction of carbon fiber composite pressure vessels. In *ASME 2010 Pressure Vessels and Piping Division/K-PVP Conference*, pages 303–310. American Society of Mechanical Engineers, 2010.

[82] A. Suryan, H. D. Kim, and T. Setoguchi. Three dimensional numerical computations on the fast filling of a hydrogen tank under different conditions. *international journal of hydrogen energy*, 37(9):7600–7611, 2012.

[83] M. C. Galassi, D. Baraldi, B. A. Iborra, and P. Moretto. Cfd analysis of fast filling scenarios for 70 mpa hydrogen type iv tanks. *International Journal of Hydrogen Energy*, 37(8):6886–6892, 2012.

[84] M. Heitsch, D. Baraldi, and P. Moretto. Numerical investigations on the fast filling of hydrogen tanks. *international journal of hydrogen energy*, 36(3):2606–2612, 2011.

[85] J. C. Yang. A thermodynamic analysis of refueling of a hydrogen tank. *international journal of hydrogen energy*, 34(16):6712–6721, 2009.

[86] M. Ozsaban, A. Midilli, and I. Dincer. Exergy analysis of a high pressure multi-stage hydrogen gas storage system. *international journal of hydrogen energy*, 36 (17):11440–11450, 2011.

[87] Y. Zhao, G. Liu, Y. Liu, J. Zheng, Y. Chen, L. Zhao, J. Guo, and Y. He. Numerical study on fast filling of 70 mpa type iii cylinder for hydrogen vehicle. *International Journal of Hydrogen Energy*, 37(22):17517–17522, 2012.

[88] P. .L Woodfield, S. Moroe, J. Fukai, M. Fujii, M.i Kohno, M. Takata, and K. Shinzato. Numerical simulation for design of probe to measure hydrogen thermal conductivity at high pressure by the transient short-wire method. *Memoirs of the Faculty of Engineering, Kyushu University*, 67(4):209–220, 2007.

[89] M. Monde, Y. Mitsutake, P. L. Woodfield, and S. Maruyama. Characteristics of heat transfer and temperature rise of hydrogen during rapid hydrogen filling at high pressure. *Heat Transfer (Asian Research)*, 36(1):13–27, 2007.

[90] P. L. Woodfield, M. Monde, and Y. Mitsutake. Measurement of averaged heat transfer coefficients in high-pressure vessel during charging with hydrogen, nitrogen or argon gas. *Journal of Thermal Science and Technology*, 2(2):180–191, 2007.

[91] P. L. Woodfield, M. Monde, and T. Takano. Heat transfer characteristics for practical hydrogen pressure vessels being filled at high pressure. *Journal of Thermal Science and Technology*, 3(2):241–253, 2008.

[92] M. Monde, P. Woodfield, T. Takano, and M. Kosaka. Estimation of temperature change in practical hydrogen pressure tanks being filled at high pressures of 35 and 70 mpa. *international journal of hydrogen energy*, 37(7):5723–5734, 2012.

[93] C. J. B. Dicken and W. Merida. Measured effects of filling time and initial mass on the temperature distribution within a hydrogen cylinder during refuelling. *Journal of Power Sources*, 165(1):324–336, 2007.

[94] S. H. Kim, S. C.and Lee and K. B. Yoon. Thermal characteristics during hydrogen fueling process of type iv cylinder. *International Journal of Hydrogen Energy*, 35 (13):6830–6835, 2010.

[95] L. Zhao, Y. Liu, J. Yang, Y. Zhao, J. Zheng, H. Bie, and X. Liu. Numerical simulation of temperature rise within hydrogen vehicle cylinder during refueling. *International journal of hydrogen energy*, 35(15):8092–8100, 2010.

[96] P. L. Woodfield, T. Takano, and M. Monde. Characteristics of heat transfer for hydrogen and wall during filling hydrogen into actual tank at high pressure. In *ASME/JSME 2007 Thermal Engineering Heat Transfer Summer Conference collocated with the ASME 2007 InterPACK Conference*, pages 1069–1076. American Society of Mechanical Engineers, 2007.

[97] P. .L Woodfield and M. Monde. A thermodynamic model for a high-pressure hydrogen gas filling system comprised of carbon-fibre reinforced composite pressure vessels. In *Australasian fluid mechanics conference*, 2010.

[98] M. Heath, P. L. Woodfield, W. Hall, and M. Monde. An experimental investigation of convection heat transfer during filling of a composite-fibre pressure vessel at low reynolds number. *Experimental Thermal and Fluid Science*, 54:151–157, 2014.

[99] M. Hosseini, I. Dincer, G. F. Naterer, and M. A. Rosen. Thermodynamic analysis of filling compressed gaseous hydrogen storage tanks. *international journal of hydrogen energy*, 37(6):5063–5071, 2012.

[100] Society of Automotive Engineers (S.A.E.). Fuelling protocols for light duty gaseous hydrogen surface vehicle. Technical report, Technical Information Report J2601, 2010.

[101] J. Schneider, G. Meadows, S. .R Mathison, M. J. Veenstra, J. Shim, R. Immel, M. Wistoft-Ibsen, S. Quong, M. Greisel, and T. et al. McGuire. Validation and sensitivity studies for sae j2601, the light duty vehicle hydrogen fueling standard. *SAE International Journal of Alternative Powertrains*, 3(2014-01-1990):257–309, 2014.

[102] S. Maus, J. Hapke, C. Na Ranong, E. Wüchner, G. Friedlmeier, and D. Wenger. Filling procedure for vehicles with compressed hydrogen tanks. *International Journal of Hydrogen Energy*, 33(17):4612–4621, 2008.

[103] E. Rothuizen, W. Mérida, M. Rokni, and M. Wistoft-Ibsen. Optimization of hydrogen vehicle refueling via dynamic simulation. *International Journal of Hydrogen Energy*, 38(11):4221–4231, 2013.

[104] E. Rothuizen and M. Rokni. Optimization of the overall energy consumption in cascade fueling stations for hydrogen vehicles. *International Journal of Hydrogen Energy*, 39(1):582–592, 2014.

[105] A. Yamashita, M. Kondo, S. Goto, and N. Ogami. Development of high-pressure hydrogen storage system for the toyota mirai. Technical report, SAE Technical Paper, 2015.

[106] Toyota Motor Corp. Toyota mirai. a turning point from the inside out. https://ssl.toyota.com/mirai/fcv.html, 2016.

[107] U.S. DRIVE Partnership. Target explanation document: Onboard hydrogen storage for light-duty fuel cell vehicles. Technical report, U.S. Department of Energy (D.O.E.), 2015.

[108] P. Fritzson. *Principles of object-oriented modeling and simulation with Modelica 2.1*. John Wiley & Sons, 2010.

[109] E. D. Rothuizen. *Hydrogen Fuelling Stations - A Thermodynamic Analysis of Fuelling Hydrogen Vehicles for Personal Transportation*. PhD thesis, Technical University of Denmark, 2013.

[110] H. Elmqvist. Dymola-dynamic modeling language-user's manual. *Dynasim AB, Lund, Sweden*, 1994.

[111] M. A. Natick. Matlab user's manual. the mathworks inc. *Natick, M. A.*, 2001.

[112] The Math Works Inc. *Using simulink*, 2000.

[113] E. David. An overview of advanced materials for hydrogen storage. *Journal of materials processing technology*, 162:169–177, 2005.

[114] A. Mazzucco, E. Rothuizen, J.-E. Jørgensen, T. R. Jensen, and M. Rokni. Integration of phase change materials in compressed hydrogen gas systems: Modelling and parametric analysis. *International Journal of Hydrogen Energy*, 2015.

[115] Y. R. Tang, D. L. Gao, Y. F. Guo, S. Q. Wang, and T. L. Deng. Supercooling and phase separation of inorganic salt hydrates as pcms. In *Applied Mechanics and Materials*, volume 71, pages 2602–2605. Trans Tech Publ, 2011.

[116] M. M. FarFarid, A. M. Khudhair, S. A. K. Razack, and S. Al-Hallaj. A review on phase change energy storage: materials and applications. *Energy conversion and management*, 45(9):1597–1615, 2004.

[117] D. Feldman, M. M. Shapiro, D. Banu, and C. J. Fuks. Fatty acids and their mixtures as phase-change materials for thermal energy storage. *Solar energy materials*, 18(3):201–216, 1989.

[118] A. Hasan. Phase change material energy storage system employing palmitic acid. *Solar energy*, 52(2):143–154, 1994.

[119] M. N. R. Dimaano and A. D. Escoto. Preliminary assessment of a mixture of capric and lauric acids for low-temperature thermal energy storage. *Energy*, 23 (5):421–427, 1998.

[120] M. M. Farid, F. A. Hamad, and M. Asu-Arabi. Phase change cool storage using dimethyl-sulfoxide. *Energy conversion and management*, 39(8):819–826, 1998.

[121] S. Zuca, P. M. Pavel, and M. Constantinescu. Study of one dimensional solidification with free convection in an infinite plate geometry. *Energy conversion and management*, 40(3):261–271, 1999.

[122] S. M. Hasnain. Review on sustainable thermal energy storage technologies, part i: heat storage materials and techniques. *Energy Conversion and Management*, 39(11):1127–1138, 1998.

[123] X. Py, R. Olives, and S. Mauran. Paraffin/porous-graphite-matrix composite as a high and constant power thermal storage material. *International Journal of heat and mass transfer*, 44(14):2727–2737, 2001.

[124] O. M. Løvvik. Viable storage of hydrogen in materials with off-board recharging using high-temperature electrolysis. *international journal of hydrogen energy*, 34(6):2679–2683, 2009.

[125] P. Muthukumar, A. Singhal, and G. K. Bansal. Thermal modeling and performance analysis of industrial-scale metal hydride based hydrogen storage container. *international journal of hydrogen energy*, 37(19):14351–14364, 2012.

[126] B. D. MacDonald and A. M. Rowe. Impacts of external heat transfer enhancements on metal hydride storage tanks. *International Journal of Hydrogen Energy*, 31(12):1721–1731, 2006.

[127] B. D MacDonald and A. M. Rowe. A thermally coupled metal hydride hydrogen storage and fuel cell system. *Journal of power sources*, 161(1):346–355, 2006.

[128] G. Mohan, M. P. Maiya, and S. S. Murthy. Performance of air cooled hydrogen storage device with external fins. *International Journal of Low-Carbon Technologies*, 3(4):265–281, 2008.

[129] Y. Kaplan. Effect of design parameters on enhancement of hydrogen charging in metal hydride reactors. *International Journal of Hydrogen Energy*, 34(5): 2288–2294, 2009.

[130] P. Muthukumar and M. Groll. Metal hydride based heating and cooling systems: a review. *International journal of hydrogen energy*, 35(8):3817–3831, 2010.

[131] G. Mohan, M. P. Maiya, and S. S. Murthy. The performance simulation of air-cooled hydrogen storage device with plate fins. *International Journal of Low-Carbon Technologies*, page ctp039, 2010.

[132] N. Nakagaki. The newly developed components for the fuel cell vehicle, mirai. Technical report, SAE Technical Paper, 2015.

[133] F. S. Yang, G. X. Wang, Z. X. Zhang, X. Y. Meng, and V. Rudolph. Design of the metal hydride reactors - a review on the key technical issues. *international journal of hydrogen energy*, 35(8):3832–3840, 2010.

[134] S. S. Murthy. Heat and mass transfer in solid state hydrogen storage: a review. *Journal of Heat Transfer*, 134(3):031020, 2012.

[135] A. V. Kuznetsov and K. Vafai. Analytical comparison and criteria for heat and mass transfer models in metal hydride packed beds. *International journal of heat and mass transfer*, 38(15):2873–2884, 1995.

[136] T. Nakagawa, A. Inomata, H. Aoki, and T. Miura. Numerical analysis of heat and mass transfer characteristics in the metal hydride bed. *International Journal of Hydrogen Energy*, 25(4):339–350, 2000.

[137] A. Askri, F.and Jemni and S. Ben Nasrallah. Study of two-dimensional and dynamic heat and mass transfer in a metal–hydrogen reactor. *International Journal of Hydrogen Energy*, 28(5):537–557, 2003.

[138] D. L. Hardy, B. J.and Anton. Hierarchical methodology for modeling hydrogen storage systems. part ii: Detailed models. *International Journal of Hydrogen Energy*, 34(7):2992–3004, 2009.

[139] S. Da-Wen and D. Song-Jiu. Study of the heat and mass transfer characteristics of metal hydride beds: a two-dimensional model. *Journal of the Less Common Metals*, 155(2):271–279, 1989.

[140] K. Aldas, M. D. Mat, and Y. Kaplan. A three-dimensional mathematical model for absorption in a metal hydride bed. *International Journal of Hydrogen Energy*, 27(10):1049–1056, 2002.

[141] F. Askri, A. Jemni, and S. Ben Nasrallah. Prediction of transient heat and mass transfer in a closed metal–hydrogen reactor. *International Journal of Hydrogen Energy*, 29(2):195–208, 2004.

[142] Z. Guo and H. J. Sung. Technical note conjugate heat and mass transfer in metal hydride beds in the hydriding process. *International journal of heat and mass transfer*, 42(2):379–382, 1999.

[143] M. Y. Ha, I. K. Kim, H. D. Song, S. Sung, and D. H. Lee. A numerical study of thermo-fluid phenomena in metal hydride beds in the hydriding process. *International Journal of Heat and Mass Transfer*, 47(14):2901–2912, 2004.

[144] S. Suda, Y. Komazaki, and N. Kobayashi. Effective thermal conductivity of metal hydride beds. *Journal of the Less Common Metals*, 89(2):317–324, 1983.

[145] T. G. Voskuilen, E. L. Waters, and T. L. Pourpoint. A comprehensive approach for alloy selection in metal hydride thermal systems. *International Journal of Hydrogen Energy*, 39(25):13240–13254, 2014.

[146] H.-H. Lee, S.-G.and Lee, K.-Y. Lee, and J.-Y. Lee. Dynamic reaction characteristics of the tubular hydride bed with large mass. *Journal of alloys and compounds*, 235(1):84–92, 1996.

[147] M. Melnichuk, N. Silin, and H. A. Peretti. Optimized heat transfer fin design for a metal-hydride hydrogen storage container. *international journal of hydrogen energy*, 34(8):3417–3424, 2009.

[148] M. Nagel, Y. Komazaki, and S. Suda. Effective thermal conductivity of a metal hydride bed augmented with a copper wire matrix. *Journal of the Less Common Metals*, 120(1):35–43, 1986.

[149] S. Suda and Y. Komazaki. The effective thermal conductivity of a metalhydride bed packed in a multiple-waved sheet metal structure. *Journal of the Less Common Metals*, 172:1130–1137, 1991.

[150] A. Isselhorst and M. Groll. Two-stage metal hydride heat transformer laboratory model. *Journal of alloys and compounds*, 231(1):888–894, 1995.

[151] I. Sheft, D. M. Gruen, and G. J. Lamich. Current status and performance of the argonne hycsos chemical heat pump system. *Journal of the Less Common Metals*, 74(2):401–409, 1980.

[152] H. Bjurstrom, Y. Komazaki, and S. Suda. The dynamics of hydrogen transfer in a metal hydride heat pump. *Journal of the Less Common Metals*, 131(1):225–234, 1987.

[153] H.-P. Klein and M. Groll. Development of a two-stage metal hydride system as topping cycle in cascading sorption systems for cold generation. *Applied thermal engineering*, 22(6):631–639, 2002.

[154] F. Laurencelle, Z. Dehouche, F. Morin, and J. Goyette. Experimental study on a metal hydride based hydrogen compressor. *Journal of Alloys and Compounds*, 475(1):810–816, 2009.

[155] S.-C. Bae, T. Tanae, M. Monde, and M. Katsuta. Heat transfer enhancement of metal hydride particle bed for heat driven type refrigerator by carbon fiber. *Journal of Thermal Science and Technology*, 3(1):2–10, 2008.

[156] M. Groll. Reaction beds for dry sorption machines. *Heat Recovery Systems and CHP*, 13(4):341–346, 1993.

[157] M. Ron, D. Gruen, M. Mendelsohn, and I. Sheet. Preparation and properties of porous metal hydride compacts. *Journal of the Less Common Metals*, 74(2): 445–448, 1980.

[158] K. J. Kim, B. Montoya, A. Razani, and K.-H. Lee. Metal hydride compacts of improved thermal conductivity. *International Journal of Hydrogen Energy*, 26 (6):609–613, 2001.

[159] A. R. Sánchez, H.-P. Klein, and M. Groll. Expanded graphite as heat transfer matrix in metal hydride beds. *International Journal of Hydrogen Energy*, 28(5): 515–527, 2003.

[160] H.-P. Klein and M. Groll. Heat transfer characteristics of expanded graphite matrices in metal hydride beds. *International Journal of Hydrogen Energy*, 29 (14):1503–1511, 2004.

[161] K. J. Kim, G. Lloyd, A. Razani, and K. T. Feldman. Development of lani 5/cu/sn metal hydride powder composites. *Powder technology*, 99(1):40–45, 1998.

[162] S. Suda, N. Kobayashi, K. Yoshida, Y. Ishido, and S. Ono. Experimental measurements of thermal conductivity. *Journal of the Less Common Metals*, 74(1): 127–136, 1980.

[163] S. Suda, N. Kobayashi, and K. Yoshida. Thermal conductivity in metal hydride beds. *International Journal of Hydrogen Energy*, 6(5):521–528, 1981.

[164] Y. Ishido, M. Kawamura, and S. Ono. Thermal conductivity of magnesium-nickel hydride powder beds in a hydrogen atmosphere. *International Journal of Hydrogen Energy*, 7(2):173–182, 1982.

[165] E. Suissa, I. Jacob, and Z. Hadari. Experimental measurements and general conclusions on the effective thermal conductivity of powdered metal hydrides. *Journal of the Less Common Metals*, 104(2):287–295, 1984.

[166] S. Da-Wen and D. Song-Jiu. Theoretical descriptions and experimental measurements on the effective thermal conductivity in metal hydride powder beds. *Journal of the Less Common Metals*, 160(2):387–395, 1990.

[167] J. Kapischke and J. Hapke. Measurement of the effective thermal conductivity of a metal hydride bed with chemical reaction. *Experimental thermal and fluid science*, 9(3):337–344, 1994.

[168] A. Kempf and W. R. B. Martin. Measurement of the thermal properties of tife 0.85 mn 0.15 and its hydrides. *International journal of hydrogen energy*, 11(2): 107–116, 1986.

[169] S. Flueckiger, T. Voskuilen, T. Pourpoint, T. S. Fisher, and Y. Zheng. In situ characterization of metal hydride thermal transport properties. *international journal of hydrogen energy*, 35(2):614–621, 2010.

[170] M. Raju, J. P. Ortmann, and S. Kumar. System simulation model for high-pressure metal hydride hydrogen storage systems. *International Journal of Hydrogen Energy*, 35(16):8742–8754, 2010.

[171] I. H. Bell, S. Quoilin, J. Wronski, and V. Lemort. Coolprop: An open-source reference-quality thermophysical property library. In *ASME ORC 2nd International Seminar on ORC Power Systems*, 2013.

[172] I. H. Bell, J. Wronski, S. Quoilin, and V. Lemort. Pure and pseudo-pure fluid thermophysical property evaluation and the open-source thermophysical property library coolprop. *Industrial & engineering chemistry research*, 53(6):2498–2508, 2014.

[173] K. C. Smith and T. S. Fisher. Models for metal hydride particle shape, packing, and heat transfer. *international journal of hydrogen energy*, 37(18):13417–13428, 2012.

[174] M. Dornheim. *Thermodynamics of metal hydrides: tailoring reaction enthalpies of hydrogen storage materials*. INTECH Open Access Publisher, 2011.

[175] A. Mazzucco and M. Rokni. Generalized computational model for high-pressure metal hydrides with variable thermal properties. *International Journal of Hydrogen Energy*, Published Online, 2015.

[176] A. Mazzucco, T. G. Voskuilen, E. L. Waters, T. L. Pourpoint, and M. Rokni. Heat exchanger selection and design analyses for metal hydride heat pump systems. *International Journal of Hydrog*, Accepted, 2016.

[177] Tubular Exchanger Manufacturers Association (TEMA). *Standards of the Tubular Exchanger Manufacturers Association*, 1999.

[178] S. Anbarasu, P. Muthukumar, and Subhash C. Mishra. Tests on lmni 4.91 sn 0.15 based solid state hydrogen storage device with embedded cooling tubes–part b: Desorption process. *International Journal of Hydrogen Energy*, 39(10): 4966–4972, 2014.

[179] S. Kakac, H. Liu, and A. Pramuanjaroenkij. *Heat exchangers: selection, rating, and thermal design*. CRC press, 2012.

[180] M. Kenisarin and K. Mahkamov. Solar energy storage using phase change materials. *Renewable and Sustainable Energy Reviews*, 11(9):1913–1965, 2007.

[181] S. M. Shalaby, M. A. Bek, and A. A. El-Sebaii. Solar dryers with pcm as energy storage medium: A review. *Renewable and Sustainable Energy Reviews*, 33: 110–116, 2014.

[182] A. M. Khudhair and M. M. Farid. A review on energy conservation in building applications with thermal storage by latent heat using phase change materials. *Energy conversion and management*, 45(2):263–275, 2004.

[183] M. K. Choi. Using pre-melted phase change material to keep payload warm without power for hours in space. In *10th International Energy Conversion Engineering Conf., Atlanta, GA, Paper AIAA-2012-3894*, 2012.

[184] G. Tan and D. Zhao. Study of a thermoelectric space cooling system integrated with phase change material. *Applied Thermal Engineering*, 86:187–198, 2015.

[185] F. L. Tan, W. Shen, and S. C. et al. Fok. Thermal performance of pcm-cooled mobile phone. In *Electronics Packaging Technology Conference, 2009. EPTC'09. 11th*, pages 640–645. IEEE, 2009.

[186] S. Mondal. Phase change materials for smart textiles–an overview. *Applied Thermal Engineering*, 28(11):1536–1550, 2008.

[187] N. Sarier and E. Onder. The manufacture of microencapsulated phase change materials suitable for the design of thermally enhanced fabrics. *Thermochimica Acta*, 452(2):149–160, 2007.

[188] S. J. Hynek and W. D. Fuller. Stationary hydrogen storage using a phase change material. *HYDROGEN ENERGY PROGRESS*, 2:1197–1202, 1996.

[189] S. Garrier, B. Delhomme, P. de Rango, P. Marty, D. Fruchart, and S. Miraglia. A new mgh 2 tank concept using a phase-change material to store the heat of reaction. *International Journal of Hydrogen Energy*, 38(23):9766–9771, 2013.

[190] M. M. Farid, F. A. Hamad, and M. Asu-Arabi. Melting and solidification in multi-dimensional geometry and presence of more than one interface. *Energy conversion and management*, 39(8):809–818, 1998.

[191] A. Elgowainy and K. Reddi. Hydrogen fueling station pre-cooling analysis. Technical report, 2015 DOE Hydrogen and Fuel Cells Program. Annual Merit Review, June 2015, 2015.

[192] V. Canseco, Y. Anguy, J. J. Roa, and E. Palomo. Structural and mechanical characterization of graphite foam/phase change material composites. *Carbon*, 74:266–281, 2014.

[193] S.-T. Hong and D. R. Herling. Aluminum foam-phase change material composites as heat exchangers. Technical report, SAE Technical Paper, 2007.

[194] ASME Boiler. Pressure vessel code section xi. *Rules for inservice inspection of nuclear power plant components*, 1995.

[195] M. R. Louthan, G. R. Caskey, J. A. Donovan, and D. E. Rawl. Hydrogen embrittlement of metals. *Materials Science and Engineering*, 10:357–368, 1972.

[196] L. Klebanoff. *Hydrogen storage technology: materials and applications*. CRC Press, 2012.

[197] L. E. Brownell and E. H. Young. *Process equipment design: vessel design*. John Wiley & Sons, 1959.

[198] Nobuhiko Takeichi, Hiroshi Senoh, Tomoyuki Yokota, Hidekazu Tsuruta, Kenjiro Hamada, Hiroyuki T Takeshita, Hideaki Tanaka, Tetsu Kiyobayashi, Toshio Takano, and Nobuhiro Kuriyama. "hybrid hydrogen storage vessel", a novel high-pressure hydrogen storage vessel combined with hydrogen storage material. *International Journal of Hydrogen Energy*, 28(10):1121–1129, 2003.

[199] Mark Golben and David H DaCosta. Advanced thermal hydrogen compression. *Proceedings of the 2001 US DOE Hydrogen Program Review, Baltimore, MD: NREL/CP-570-30535*, 1999.

[200] E. D. Rothuizen, M. Rokni, and B. Elmegaard. *Hydrogen Fuelling Stations: A Thermodynamic Analysis of Fuelling Hydrogen Vehicles for Personal Transportation*. PhD thesis, Technical University of DenmarkDanmarks Tekniske Universitet, Department of Energy EngineeringInstitut for Energiteknik, 2013.

[201] R. B. Bird. Transport phenomena. *Applied Mechanics Reviews*, 55(1):R1–R4, 2002.

[202] U. Mayer, M. Groll, and W. Supper. Heat and mass transfer in metal hydride reaction beds: experimental and theoretical results. *Journal of the Less Common Metals*, 131(1):235–244, 1987.

[203] T. L. Bergman, F. P. Incropera, and A. S. Lavine. *Fundamentals of heat and mass transfer*. John Wiley & Sons, 2011.

[204] R. H. Perry, D. W. Green, and J. O. Maloney. Perry's chemical engineering handbook. *McGraw-Hill*, pages 419–420, 1997.

[205] V. Gnielinski. Berechnung des druckverlustes in glatten konzentrischen ringspalten bei ausgebildeter laminarer und turbulenter isothermer strömung. *Chemie Ingenieur Technik*, 79(1-2):91–95, 2007.

[206] VDI-Wärmeatlas Berechnungsblätter für den Wärmeübergang, editor. *VDI-Gesellschaft Verfahrenstechnik und Chemieingenieurwesen*. Auflage, 2010.

[207] S. W. Churchill. Friction-factor equation spans all fluid-flow regimes. *Chemical engineering*, 84(24):91–92, 1977.

[208] K. Thulukkanam. *Heat exchanger design handbook*. CRC Press, 2013.

[209] R. W. Serth and T. Lestina. *Process heat transfer: Principles, applications and rules of thumb*. Academic Press, 2014.

[210] P. .L Young and Satish G. Brackbill, T. P.and Kandlikar. Estimating roughness parameters resulting from various machining techniques for fluid flow applications. In *ASME 2007 5th International Conference on Nanochannels, Microchannels, and Minichannels*, pages 827–836. American Society of Mechanical Engineers, 2007.

[211] A. F. Mills. *Basic Heat Transfer*. Prentice-Hall, 1999.

[212] J. Dirker and J. P. Meyer. Convective heat transfer coefficients in concentric annuli. *Heat Transfer Engineering*, 26(2):38–44, 2005.

[213] V. Gnielinski. Heat transfer coefficients for turbulent flow in concentric annular ducts. *Heat transfer engineering*, 30(6):431–436, 2009.

[214] J. W. Palen. *Heat exchanger sourcebook*. Hemisphere Publishing, New York, NY, 1986.

[215] DowChemical. Technical data sheet. fluid properties., 1999.

[216] Paratherm Ltd. Thermal properties calculator v6.4. http://paracalc.paratherm.com., 2015.

[217] T. Voskuilen and L.E. Waters. Metal hydride toolbox. https://github.com/PurdueH2Lab/MetalHydrideToolbox, 2015.

[218] J. P. Vanhanen, M. T. Hagström, and P. D. Lund. Combined hydrogen compressing and heat transforming through metal hydrides. *International journal of hydrogen energy*, 24(5):441–448, 1999.

[219] M. T. Hagström, J. P. Vanhanen, and P. D. Lund. Ab 2 metal hydrides for high-pressure and narrow temperature interval applications. *Journal of alloys and compounds*, 269(1):288–293, 1998.

[220] F. Laurencelle and J. Goyette. Simulation of heat transfer in a metal hydride reactor with aluminium foam. *International Journal of Hydrogen Energy*, 32(14): 2957–2964, 2007.

[221] B. S. Sekhar, S. P. Pailwan, and P. Muthukumar. Studies on metal hydride based single-stage heat transformer. *International Journal of Hydrogen Energy*, 38(17): 7178–7187, 2013.

[222] V. Hovland. *Integrated cabin and fuel cell system thermal management with a metal hydride heat pump.* Citeseer, 2004.

[223] Y. Osumi, H. Suzuki, A. Kato, K. Oguro, T. Sugioka, and T. Fujita. Hydrogen storage properties of ti 1+ x cr 2- y mn y alloys. *Journal of the Less Common Metals*, 89(1):257–262, 1983.

[224] G. Sandrock. A panoramic overview of hydrogen storage alloys from a gas reaction point of view. *Journal of alloys and compounds*, 293:877–888, 1999.

[225] G. Walker. *Solid-state hydrogen storage: materials and chemistry*. Elsevier, 2008.

[226] S. Luo, J. D. Clewley, Ted B. Flanagan, R. C. Bowman, and L. A. Wade. Further studies of the isotherms of lani 5- x sn x–h for x= 0–0.5. *Journal of alloys and compounds*, 267(1):171–181, 1998.

[227] M. Peruzzini and R. Poli. *Recent advances in hydride chemistry*. Elsevier, 2002.

[228] E. L. Huston and G. D. Sandrock. Engineering properties of metal hydrides. *Journal of the less common metals*, 74(2):435–443, 1980.

[229] C. Lexcellent and G. Gondor. Analysis of hydride formation for hydrogen storage: Pressure–composition isotherm curves modeling. *Intermetallics*, 15(7):934–944, 2007.

[230] T. Førde, J. P. Maehlen, V. A. Yartys, M. V. Lototsky, and H. Uchida. Influence of intrinsic hydrogenation/dehydrogenation kinetics on the dynamic behaviour of metal hydrides: A semi-empirical model and its verification. *International journal of hydrogen energy*, 32(8):1041–1049, 2007.

[231] I. H.and the CoolProp Team Bell. http:www.coolprop.orgfluid_propertiesPure PseudoPure.html#list-of-fluids, Last access: 23 December 2015.

[232] N. Ukrainczyk, S. Kurajica, and J. Šipušić. Thermophysical comparison of five commercial paraffin waxes as latent heat storage materials. *Chemical and Biochemical Engineering Quarterly*, 24(2):129–137, 2010.

[233] National Institute of Standards and Technology (NIST). Webbook. http://webbook.nist.gov, 2015.

[234] G. A. Lane. *Solar heat storage: latent heat materials.* CRC Press, Boco Raton, FL, 1983.

[235] S. D. Sharma, H. Kitano, and K. Sagara. Phase change materials for low temperature solar thermal applications. *Res. Rep. Fac. Eng. Mie Univ*, 29(1), 2004.

A Hydrogen absorption/desorption model and validation

A.1 Hydrogen absorption/desorption model

The mathematical framework consists in energy and mass balances combined with a kinetics model to describe the time evolution of the hydriding/dehydriding rate, MH bed temperature and hydrogen mass flow rate. This general form renders it applicable to different H_2-absorbing/desorbing alloys after selecting the relevant values for the material properties and, if needed, modifying the kinetics equations.
The thermophysical properties of hydrogen gas are obtained with Coolprop [171, 172].
In a MHSS the essential thermal masses that actively participate to the reaction mechanisms are the porous medium (i.e. metal hydride) and the hydrogen gas. The latter is partly stored in its absorbed phase and partly in the gaseous phase in the pores, meaning that the MH system must be treated as a discontinuous medium. In this context, the effective thermal properties of the metal hydride are expressed according to the bed porosity as

$$k_{MH} = \phi k_g + (1-\phi) k_s \tag{A.1}$$

$$c_{MH} = \phi c_{p,g} + (1-\phi) c_{p,s} \tag{A.2}$$

where the porosity ϕ is defined as the ratio of the gas volume (in the pores) to the MH volume (i.e. V_g / V_{MH}).
A relation similar to Eq.A.2 can be written for the overall bed density ρ_{MH} as

$$\rho_{MH} = \phi \rho_g + (1-\phi) \rho_s \tag{A.3}$$

A.1.1 Continuity equation

At any moment of the hydriding/dehydriding reaction, the continuity equation reads as

$$\dot{m}_{g,i} h_i - \dot{m}_{g,o} h_o = V_g \cdot \frac{\partial \rho_g}{\partial t} + \rho_s V_s \cdot \frac{\partial w}{\partial t} \tag{A.4}$$

where the left hand side (LHS) term represents the difference between inlet and outlet hydrogen mass flow rates, respectively $\dot{m}_{g,i}$ and $\dot{m}_{g,o}$. The first and second term on the right-hand-side (RHS) refer to the rate of stored hydrogen in the gas and absorbed phases respectively. The gas and solid volumes (i.e. V_g and V_s) are linked to the overall MH bed volume via the following relation

$$V_{MH} = V_g + V_s \tag{A.5}$$

$$= \phi V_{MH} + (1-\phi) V_{MH} \tag{A.6}$$

As the system operates either in charging or discharging mode, $\dot{m}_{g,o}$ and $\dot{m}_{g,i}$ are alternatively null. The integration of Eq. A.4 over the entire fueling or driving process provides the total hydrogen mass that entered or was drawn from the tank. The hydrogen mass inside the tank at a given instant is obtained by adding or subtracting the two latter terms to the relevant initial condition (i.e. full or empty system). The absolute porosity of the metal hydride is expressed with the term ϕ, while ρ_g, ρ_s, w, and V_{MH} are the gas and solid density, the weight fraction of hydrogen absorbed in the bed and the MH volume, respectively.

A.1.2 Energy equation

In the model the energy equation is applied to the outer tank volume, consisting of the coolant, solid bed and tank walls. However, in the assumption of using a Type IV tank or an thermally insulated vessel, the effect of the tank walls on the internal reaction is negligible at the short times of interest for the present analysis. Therefore, the terms that refer to the tank walls are neglected in the following equations in order to provide a simpler model form where only the relevant terms are presented. In addition, the insertion of these non-reacting thermal masses is straightforward.
In porous packed beds, the contact area between the gas and solid phases is typically large enough to assume local thermal equilibrium, and hence, one single energy equation can be employed to describe the thermodynamics of the system. This is especially valid when a large value for the porosity is considered, as occurs in this

work. The energy balance is obtained from its general form [201] and reads as

$$\frac{\partial H_{syst}}{\partial t} = \dot{m}_{g,i} h_i - \dot{m}_{g,o} h_o + V_g \cdot \frac{dp}{dt} + \dot{q} \tag{A.7}$$

The RHS of the equation represents the inlet and outlet energy terms related to the hydrogen mass flow, the compression heat $V_g \cdot \frac{dp}{dt}$ and the heat flow exchanged from the hydride to the coolant and ambient. The latter term is neglected for the assumption of adiabatic tank walls as previously discussed. After assuming constant porosity and solid density within the hydride bed, the LHS in Eq. A.7 is expanded as

$$\frac{\partial H_{syst}}{\partial t} = \rho_s V_s \cdot \frac{\partial h_s}{\partial t} + \rho_g V_g \cdot \frac{\partial h_g}{\partial t} + h_g V_g \cdot \frac{\partial \rho_g}{\partial t} + \rho_s V_s w \cdot \frac{\partial h_w}{\partial t} + \rho_s V_s h_w \cdot \frac{\partial w}{\partial t} \tag{A.8}$$

where the derivatives involve h_s, h_g and h_w as the specific enthalpy of the absorbing alloy, hydrogen in the gas and absorbed phases, respectively. With respect to the hydriding process, the enthalpy of the absorbed phase is obtained from the definition of enthalpy of absorption:

$$h_w = h_g + \frac{\Delta H_{ab}}{MW_g} \tag{A.9}$$

Assuming a constant average heat of absorption (desorption), independent upon temperature and pressure, the $\frac{\partial h_w}{\partial t}$ term in Eq. A.9 becomes

$$\frac{\partial h_w}{\partial t} = \frac{\partial h_g}{\partial t} \tag{A.10}$$

The partial derivatives of h_g and h_s can be re-written for a real gas and solid by accounting for the dependency upon both temperature and pressure and assuming constant hydride properties

$$\frac{\partial h_g}{\partial t} = c_{p,g} \cdot \frac{\partial T_{MH}}{\partial t} + \frac{(1 - \alpha_g T_{MH})}{\rho_g} \cdot \frac{\partial p}{\partial t} \tag{A.11}$$

$$\frac{\partial h_s}{\partial t} = c_{p,s} \cdot \frac{\partial T_{MH}}{\partial t} + \frac{1}{\rho_s} \cdot \frac{\partial p}{\partial t} \tag{A.12}$$

where in Eq. A.11 α_g is the hydrogen coefficient of thermal expansion.

Under the assumption of isotropic and homogenous thermal properties in the hydride bed, the $\dot{q}$ term in Eq. A.7 is modeled as

$$\dot{q} = -k_{MH} \cdot \nabla^2 T_{MH} \tag{A.13}$$

By substituting Eqs. A.10 to A.13 and manipulating the energy balance in the light of the mass balance of Eq. A.4 it is possible to write the coefficients of T, p and w as

$$\Upsilon = [(1-\phi) \cdot \rho_s w c_{p,g} + \rho_{MH} c_{MH}] \cdot V_{MH} \tag{A.14}$$

$$\Lambda = \left[(1-\phi) + \left((1-\phi) \cdot \frac{\rho_s}{\rho_g} w + \phi \right) \cdot (1 - \alpha_g T_{MH}) - \phi \right] \cdot V_{MH} \tag{A.15}$$

$$\Psi = [(1-\phi) \cdot \rho_s \frac{\Delta H_{ab}}{MW_g}] \cdot V_{MH} \tag{A.16}$$

$$I = \dot{m}_{g,i} \cdot (h_{g,i} - h) + \dot{q} \tag{A.17}$$

where h is the specific enthalpy of hydrogen in the pores and it is calculated at the charging pressure p and temperature T_{MH} at any time of the simulation. During discharging the terms that refer to the hydrogen flow at the inlet in Eq. A.17 must be substituted with the respective form for the outlet with the proper sign.
At the end, the energy balance assumes the following expression

$$\Upsilon \frac{\partial T_{MH}}{\partial t} = -\Lambda \frac{\partial p}{\partial t} - \Psi \frac{\partial w}{\partial t} + I \tag{A.18}$$

A.1.3 Kinetics model

The nominal kinetic equation employed in this work is based on an expression for hydrogen absorption in $LaNi_5$ derived by Mayer et al. [202] that assumes first order kinetics, as it is often observed in metal hydrides. The reaction rate of hydrogen per unit mass of metal hydride is expressed as

$$\frac{\partial w}{\partial t} = C_a e^{E_a/(RT_{MH})} ln\left(\frac{p}{p^{eq}}\right) \cdot (w_{max} - w) \tag{A.19}$$

where p^{eq} is the MH equilibrium pressure defined in Subsection 3.8. All the other parameters refer to Table 3.1.
For desorption in $Ti_{1.1}CrMn$ a modified version of Eq.A.19 was suggested in Ref.[61] to better represent the experimental results. This relation is used in the modeling

platform when the discharging analysis is performed. It reads as

$$\frac{\partial F_{rc}}{\partial t} = C_{a,des} e^{E_{a,des}/(RT_{MH})} ln\left(\frac{p}{p^{eq}}\right) \cdot F_{rc} \tag{A.20}$$

The hydriding and dehydriding regions identified that refer to p^{eq} are shown in Fig. A.1 for $Ti_{1.1}CrMn$.

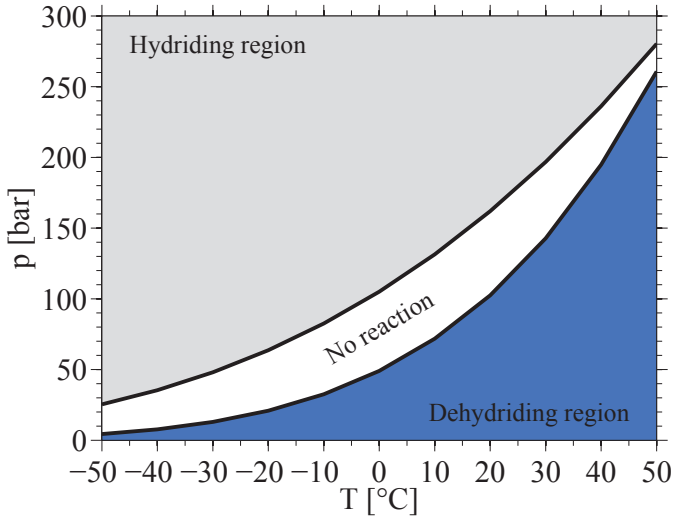

Figure A.1: Hydriding and dehydriding regions for $Ti_{1.1}CrMn$.

Relations other than those presented above for the calculation of the absorption/desorption rates are presented in Appendix D where the alternative model equation implemented in the simulation platform are described.

A.1.4 Boundary conditions

A number of boundary conditions have been defined in order to solve the set of equations presented above. Such conditions are expressed as follows For the hydride volume in contact with the coolant tube:

$$\dot{q} = \frac{1}{R_{th,tot}} * A_{hex,ext} * (T_{MH} - \bar{T}_c) \tag{A.21}$$

$$R_{th,tot} = \left(\frac{1}{A_{hex,ext}/(\bar{h}_c \cdot A_{hex,in}) + R_{th,cont} + R_{th,MH} + R_{th,tube}}\right)^{-1} \tag{A.22}$$

where $A_{hex,ext}$ and $A_{hex,in}$ are the internal and external heat transfer areas with respect to the coolant tube.

The average heat transfer coefficient on the HTF side $\bar{h}_f$ is calculated by means of the following procedure:

$$
\begin{aligned}
&if\ Re_c < 2100 \\
&Nu_{Lam} = 1.86 \cdot \left(Re_c \cdot Pr \frac{D_i}{L} \right)^{1/3} \\
&if\ 2100 \leq Re_c \leq 10^4 \\
&Nu_{Tran} = 0.116 \cdot \left[1 + \left(\frac{D_i}{L} \right)^{2/3} \right] \cdot (Re_c^{2/3} - 125) \cdot Pr^{1/3} \\
&if\ Re_c > 10^4 \\
&Nu_{Turb} = 0.023 \cdot \left[1 + \left(\frac{D_i}{L} \right)^{0.7} \right] \cdot (Re_c^{0.8} \cdot Pr^{1/3})
\end{aligned}
$$

For the hydride in contact with the tank wall:

$$\dot{q} = \frac{1}{R_{th,tot}} \cdot A_{hex,in} \cdot (T_{MH} - \bar{T}_{air}) \tag{A.23}$$

$$R_{th,tot} = \left(\frac{1}{A_{hex,int} / (\bar{h}_{air} \cdot A_{hex,ext}) + R_{th,cont} + R_{th,MH} + R_{th,wall}} \right)^{-1} \tag{A.24}$$

where the areas refer to the tank walls and $\bar{h}_{air}$ is set equal to 8 $W \cdot m^{-2} \cdot K^{-1}$ [203]. For the solid in contact to an adiabatic surface (e.g. the symmetry line in Fig. 3.1):

$$\dot{q} = 0 \tag{A.25}$$

$$T_{Bound} = T_{MH} \tag{A.26}$$

A.2 Model validation

The validation of the constant-parameter model is presented in Fig. A.2 with respect to the results presented in Ref. [55] for the hydriding process of $Ti_{1.1}CrMn$ and obtained with a simple heat-diffusion model. The comparison between the two models is carried out at three relevant distances. However, the present model employs a discretization step of 1 mm and therefore, the results presented in the literature for distance of 7.5 mm from the cooling surface are here compared with the reaction parameters calculated at a location of 7 mm, as a reasonable approximation.

The volumetric heat rate of generation is presented in Fig. A.2a. It takes into account the heat of pressurization and the reaction heat in the solid bed. The former is function of the absorption rate whereas the latter is only dependent upon the pressure ramp (and the porosity) which remains constant until p_{ref} is reached. For this reason, the heat of generation starts at a value that is different from zero and remains constant until the absorption reaction takes place.

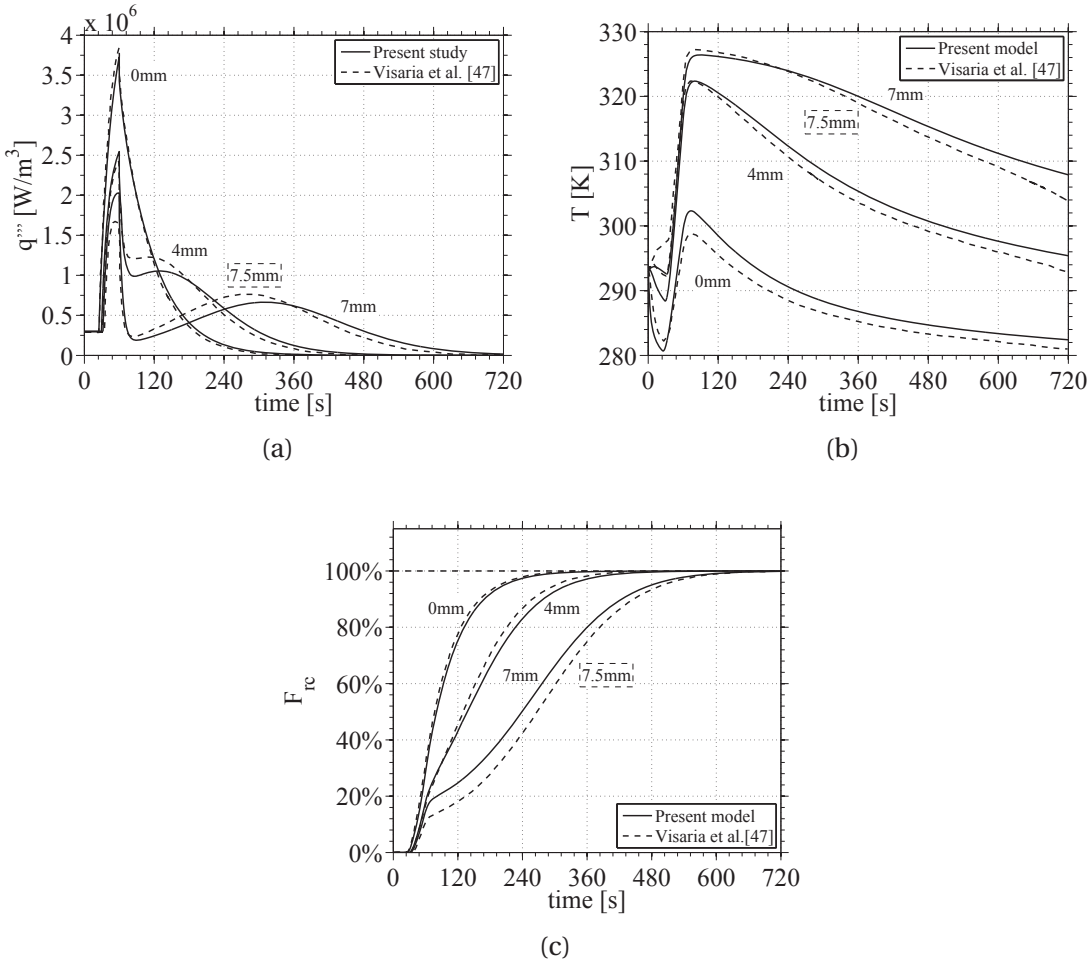

Figure A.2: Model comparison: volumetric generated heat (a); metal hydride temperature (b); fraction of reaction completion (c).

The results are consistent with what reported in the literature. However, the maximum relative difference increases with the distance from 2.6% at 0 mm to approximately 25% at around 7.5 mm.
The solid in direct contact with the cooling element experiences the greatest heat generation rate, of approximately 3.73 MW, which corresponds to the largest cooling rate. A decrease in the maximum heat value is observed as we move farther away from the cooling surface until the thermally-limited condition is reached at approximately 8 mm. Beyond such a distance poor heat removal dominates the hydriding reaction and thus, the heat generation. Similar conclusions can be drawn from Fig. A.2b, where the temperature profile in the reaction bed is shown. However, the maximum relative difference (2%) occurs at the end of pressurization for the solid at 0 mm and corresponds to a discrepancy of 6.5 K in the results.
From Fig. A.2c, it can be observed that the disparity in the fraction of reaction completion value between the present model and literature results increases with the distance from the cooling element. The maximum relative difference in the results ranges from approximately 0% for the solid in contact with the tube to 28% when the comparison id done between the F_{rc} value calculated at 7 mm and at 7.5 mm.

The fact that the agreement in the results generally decreases for locations farther from the tube indicates that the discrepancy in the models is mainly due to thermal differences, the effect of which is more significant at larger solid thicknesses. These can be attributed to the different nature of the models, gas equations (e.g. ideal gas formulation was used in Ref. [55]) and the non-perfect parameterization. The proof for this is provided in Fig. A.3 where it is possible to observe that the hydriding characteristic obtained in Ref. [55] at 7.5 mm falls within the calculated absorption profiles at 7 and 8 mm.

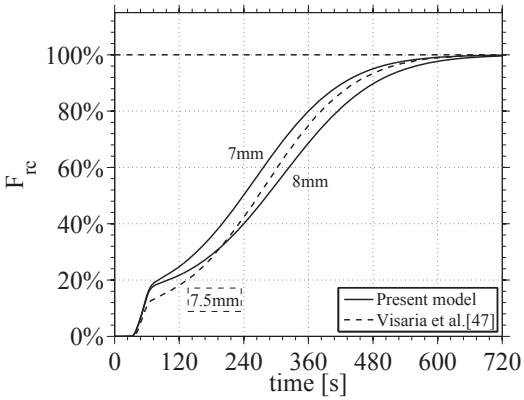

Figure A.3: Comparison between among F_{rc} values at 7, 7.5 and 8 mm.

A relatively significant discrepancy can be observed only at the end of pressurization, where the model from the literature underestimates the hydriding rate.
At the end, the current model results are in well agreement with those presented in the relevant literature. The difference in results are negligible at small distances from the cooling surface meaning that, for the desired F_{rc} and t_{ref} targets, the developed model well predicts the critical metal hydride thickness.

B Metal hydride heat pump: heat exchanger design

This appendix is meant to provide the Reader with the necessary information needed to complete the study presented in Chapter 4. It provides details on the thermal models for the investigated heat exchangers as well as additional results that complete the MHHP work presented in the main text of this thesis. Although the results, here presented, refer to a MH thermal system and are not directly applicable to a hydrogen storage application, they are reported because, at the time of the thesis submission, the manuscript that contains the details of the MHHP study has not yet been published [176]. However, as the manuscript has been accepted for publication, it is cited in the relevant sections of this appendix.

B.1 Thermal performance

Hydrogen storage systems for which the major goal is to rapidly cool the hydride during absorption aim at dissipating the heat of reaction while realizing a negligible temperature rise of the HTF across the heat exchanger and therefore, consistent cooling conditions where the coolant is in contact with the MH. In a MHHP system, however, a significant temperature increase in the cooling fluid must be provided in order to obtain useful heating for other system components. For this analysis, only the most energy-demanding process of the heat pump cycle (i.e. the absorption reaction) is considered, rather than the complete thermal cycle. To quantify the effectiveness of the system during the absorption stage, an index of performance based on the temperature change in the coolant is defined.
With respect to the entire tube length, using the assumptions reported in Section 4.2,

it is possible to write [203]:

$$ln\frac{\Delta T_{out}}{\Delta T_{in}} = -\frac{\bar{U}A_{hex}}{\dot{m}_f c_{p,f}} \tag{B.1}$$

where ΔT_{out} and ΔT_{in} represent the differences between the constant metal hydride temperature during hydrogen absorption and the mean outlet and inlet fluid temperatures, respectively. $\bar{U}$ is the average overall heat transfer coefficient, A_{hex} is the heat transfer area, $\dot{m}_f$ is the HTF mass flow rate, and $c_{p,f}$ is the specific heat capacity.
In order to define an index of performance, the previous equation is rearranged as:

$$F = \frac{T_{MH} - T_{f-m,out}}{T_{MH} - T_{f-m,in}} = exp\left(-\frac{\bar{U}A_{hex}}{\dot{m}_f c_{p,f}}\right) \tag{B.2}$$

where F is the index of performance representing the mean fluid temperature increase from the inlet conditions, $T_{f-m,in}$, to the outlet, $T_{f-m,out}$, and T_{MH} is the metal hydride temperature that evolves isothermally during hydrogen absorption. The parameter F defines the realized fraction of the total coolant temperature increase as a dimensionless ratio of temperature differences between the hot source (i.e. the metal hydride that undergoes an absorption reaction) and the hot outlet and cold inlet fluid. This metric indicates how well the heat transfer process is performed. With constant MH and fluid inlet temperatures, lower F values correspond to higher outlet temperatures and consequently, better performance. According to the assumption that the MH temperature evolves isothermally, the following relation, can be applied for condensation problems:

$$\epsilon = 1 - F \tag{B.3}$$

where the heat exchanger effectiveness, ϵ, is related to the index of performance. The index of performance is only dependent upon design variables, heat and mass transfer parameters and fluid properties. Further details on the effectiveness, F formulations, and the models used for the different heat exchangers are given in the next section.

B.1.1 Limitation of the analysis

The metal hydride heat pump system is a cyclic system in which all processes are time dependent and thus, the present steady-state analysis should be considered a pre-design study to select the most efficient configuration in terms of the heat transfer effectiveness. A more complete design analysis would require the estimation of the actual COP for an entire time-dependent cycle. In addition, variable properties should

be considered for the heat transfer medium once its inlet and outlet temperatures and the hydride pair are defined. The study relies on a single-phase HTF with the approximate properties of water at 55 °C. It follows that, if the hydride exceeds the boiling point of water, a suitable alternative HTF must be selected.
Finally, it was assumed that the process limiting the heat transfer is the convective resistance of the HTF, shown by in Eqs. B.1-B.3. In an actual design, sufficiently small metal hydride thicknesses and significant thermal enhancement are required to achieve such a condition. Simulations carried out in the present study have shown that a solid thermal resistance of 2.5x10-4 $m^2 \cdot K \cdot W^{-1}$ would be generally necessary in the diameter-velocity space considered here. This value could be obtained by employing a bed thickness of either 0.25 mm, referring to a thermal conductivity of 1 $W \cdot m^{-1} \cdot K^{-1}$, or 2.5 mm in presence of thermal enhancement up to 10 $W \cdot m^{-1} \cdot K^{-1}$ [170]. However, to optimize a configuration for a particular hydride pair, the model can be readily modified to include the actual thermal conductivity, leaving the thickness as a variable of optimization.

B.1.2 Thermal model for the heat exchanger design

The following procedure and set of equations were implemented in Matlab® to compute the performance and pressure losses for each heat exchanger. The inputs of the model consist of the HTF velocity and the flow path and heat transfer geometries. The hydraulic diameter, D_h, for HEX1, HEX2 and HEX3 is defined in Eq. B.6:

$$D_{h,HEX1} = D_i \tag{B.4}$$

$$D_{h,HEX2} = D_o - D_i \tag{B.5}$$

$$D_{h,HEX3} = OD \tag{B.6}$$

A value for the total active length of the tube is assumed for each configuration. For HEX2 and HEX3 it corresponds to the MH tube length, while for HEX1 it is defined as

$$L_{tot} = N_p \cdot L_{tube} \tag{B.7}$$

where N_p is the number of passes and L_{tube} is the single-tube length actively involved in the heat transfer process. For HEX2 and HEX3, other input parameters are required to completely define the geometry. For HEX2, only the aspect ratio a is needed and is defined as

$$a = \frac{D_i}{D_o} \tag{B.8}$$

This equation is coupled with Eq. B.6b and used to determine D_o and D_i for any given values of a and $D_{h,HEX2}$.
For HEX3, the other main geometrical inputs include the inner diameter of the shell, D_s, the segmental baffle cut (25-35%), the tube-pitch layout, and the parameters listed in Table B.1:

Table B.1: Main additional geometric parameter for HEX3

Parameter	**Symbol**	**Value**	**Ref.**
Relative baffle space (% of Ds)	*B*	20%	[177]
Pitch to tube-diameter ratio	*PR*	1.25	[177]
Temperature correction factor	*Ft*	0.875	[203]
Tube count calculation constant for one tube pass	*CTP*	0.93	[179]
Tube layout constant	*Ct*	0.87	[179]

The chosen values of B, PR and F_t and their influence on fluid flow, mechanical strength of components and heat transfer are discussed in the sensitivity analysis section. The tube count constant, CTP, accounts for the imperfect coverage of the shell diameter by the tubes due to necessary clearances between the shell and the outer tube circle and its assumed value refers to one tube pass, as it is the closest condition to the case here considered. The value for C_t applies for a tube layout inclined by 30 or 60 degrees and was chosen due to the increased tube density that it provides for any given D_s, and thus was expected to realize a greater temperature increase in the HTF. Performance results have confirmed such a prediction when the C_t value valid for a layout angle of 45 and 90 degrees was employed in the simulations. Similar conclusions can be drawn when a triangular tube pitch is used in place of a squared pitch. The cross flow areas are computed by means of the following equations for HEX1, HEX2 and HEX3 respectively:

$$A_{cross,HEX1} = \pi \frac{D_{h,HEX1}^2}{4} \tag{B.9}$$

$$A_{cross,HEX2} = \frac{\pi}{4}(D_o^2 - D_i^2) \tag{B.10}$$

$$A_{cross,HEX3} = \frac{B \cdot D_s^2 \cdot C_l}{P_t} \tag{B.11}$$

where P_t is the tube pitch (calculated with PR and D_o) and C_l is the tube clearance defined according to Ref. [203]. Next, all the parameters required to estimate Pr and Re are calculated. For HEX3, these parameters include the maximum number of tubes that fit the prescribed inner shell volume and the equivalent diameter, according to the design procedure reported in Ref. [179]. The pressure drops are calculated

by means of the friction factor for the laminar and turbulent regimes given in Ref. [204] for HEX1 and in Refs. [205, 206] for HEX2. For HEX1, the Churchill equation is used in the turbulent regime for ease of computation [207]. Due to the lack of a dedicated correlation for the friction factor in the transition region, an interpolation between the values calculated in laminar and turbulent regimes is proposed in the appendix. For HEX3, the pressure drops are estimated by means of the Kern method [179], the validity of which is addressed in the results section with respect to the Bell-Delaware method [208, 209]. In the friction factor correlations, a value of $1.118\text{x}10^{-6}$ is assumed for the roughness of the smooth aluminum tubes when applicable [210]. The effectiveness, ϵ, is calculated for each configuration by means of Eq. B.3 where the index of performance defined in Eq. B.2 can be re-written by separating the variables as

$$F = exp(-1) \cdot exp\left(\frac{A_{hex}}{A_{cross}}\right) \cdot exp\left(\frac{1}{\rho_f \cdot c_{p,f}}\right) \cdot \left(\frac{\bar{h}_f}{v}\right) \tag{B.12}$$

$$G = \left(\frac{A_{hex}}{A_{cross}}\right); P = \frac{1}{\rho_f \cdot c_{p,f}}; V = \frac{\bar{h}_f}{v} \tag{B.13}$$

It is then possible to identify the three main exponential terms dependent upon geometries of heat transfer and flow, G, HTF thermo-physical properties, P, and model variables, V. For model variables, the assumption $\bar{h}_f = \bar{U}$ is applied for HEX1 and HEX2, whereas for HEX3 such relation reads $F_t \cdot \bar{h}_f = \bar{U}$, where $\bar{h}_f$ is the mean convection coefficient of heat transfer. The parameter $\bar{h}_f$ is calculated according to the correlations described in Section B.2.
Finally, G can be made explicit by using the expressions for heat transfer area and mass flow rate for each heat exchanger to see the influence of the input terms on the performance. As a result we obtain Eqs. B.16a-B.16c for HEX1, HEX2 and HEX3, respectively:

$$G_{HEX1} = \frac{4 \cdot L_{tot}}{D_{h,HEX1}} \tag{B.14}$$

$$G_{HEX2} = \frac{4 \cdot L_{tot}}{D_{h,HEX2} \cdot \left(\frac{1}{a} + 1\right)} \tag{B.15}$$

$$G_{HEX3} = \frac{\pi \cdot L_{tube} \cdot C_1}{B \cdot PR \cdot (PR - 1)} \tag{B.16}$$

where Eq. B.16b is obtained by using Eqs. B.6b, B.8 and B.11b. In Eq. B.16c, C_1 is a constant defined as:

$$C_1 = 0.785 \cdot \frac{CTP}{C_t} \tag{B.17}$$

For HEX3, the geometric term is independent of the number of tubes, D_s, and the characteristic length under the prescribed assumptions. As a result, G is a constant for any simulations of HEX3 where the tube length does not vary. For HEX1 and HEX2, G depends on the hydraulic diameter and the aspect ratio. The dependency of ϵ upon the characteristic length is found in the $\bar{h}_f$ term according to the Bell-Delaware method. A more explicit formulation for F can be used when it is possible to express $\bar{h}_f$ as a function of Nu, fluid thermal conductivity, and characteristic length by rearranging these parameters into their respective exponential terms.

B.1.3 Thermal model for the heat demand analysis

The time-dependent heat generated during hydrogen absorption is given as

$$\dot{q}_{MH} = \frac{dF_{rc}}{dt} \cdot w_{max} \cdot m_{MH} \cdot \frac{\Delta H_{ab}}{MW_{H2}} \tag{B.18}$$

where F_{rc} is the reaction progress parameter which varies between 0 at fully dehydrided conditions and 1 at fully hydride conditions; m_{MH} is the mass of the hydride and MW_{H2} is the molecular weight of hydrogen. The total heat demand that must be fulfilled for the reaction to reach the saturation condition is the integral of Eq. B.18 from F_{rc} = 0 to 1 divided by a target value for the reaction completion time. Thus, it can be written as,

$$\dot{q}_{MH} = \frac{1}{t_{rc}} \cdot w_{max} \cdot m_{MH} \cdot \frac{\Delta H_{ab}}{MW_{H2}} \tag{B.19}$$

where t_{rc} is the absorption reaction completion time. For a MHHP this corresponds to the time of the heat pump cycle stage where the desired effect is generated, whereas for a hydrogen storage system it coincides with t_{ref}. For a heat pump application, it is preferable to operate with a reaction time in the range of 30-60 min to avoid frequent system cycling. A relevant system needs to fulfill three main constraints: the hydride cooling must be performed to allow for a complete absorption reaction, the design must be realistically sized (including the limitations on the coolant velocity identified in Table 4.1) and the design must achieve appropriate reaction times. The first constraint expresses a physical condition that must be satisfied to ensure a continuous exothermic reaction; the heat removed from the coolant must equal the heat generated in the solid bed, according to the following heat balance

$$\dot{q}_{MH} = \dot{m}_{f,tot} \cdot c_{p,f} \cdot (T_{f-m,out} - T_{f-m,in}) \tag{B.20}$$

where $\dot{m}_{f,tot}$ is the total mass flow of HTF that flows through the system and the positive temperature difference between outlet and inlet represents the desired effect for the MHHP system. The second constraint limits the results of the analysis to practical designs, as presented in Table 4.1.
Finally, in order to calculate the reaction time in Eq. B.19 it is first necessary to assume a value for the constant hydride temperature during hydrogen absorption (T_{MH}= 100°C) and the HTF temperature at the inlet ($T_{f-m,in}$ = 20°C). The outlet HTF temperature is estimated from Eq. B.3 and thus the temperature difference in Eq.B.20 is defined in the entire diameter-velocity space. The hydride volume hidden in the m_{MH} term can be easily linked to the tube diameters for HEX2 and HEX3, while for HEX1 it is necessary to define the thickness of the solid bed placed around the tubes. This is shown in Table B.2 along with the assumed reasonable values for the hydride properties and porosity. A quick comparison shows that most chosen values are similar to those of $Ti_{1.1}CrMn$ (see Table 3.1).

Table B.2: Assumed values for metal hydride properties, porosity and bed thickness for the MHHP system.

Parameter	**Value**	**Unit**
wt_{max}	5%	$kg_{\mathrm{H2,\,max}} \cdot kg^{-1}_{\mathrm{MH}}$
ΔH_{ab}	20000	$J \cdot mole^{-1}_{\mathrm{H2}}$
ρ_{MH}	6000	$kg \cdot m^{-3}$
ϕ	50%	-
MH thickness (HEX1 only)	5	mm

At the end, t_{rc} is calculated as:

$$t_{rc-HEX1} = \frac{w_{max} \cdot m_{MH,tube-HEX1}}{m_{f,tube-HEX1} \cdot c_{p,f} \Delta T_{f-HEX1}} \cdot \frac{\Delta H_{\mathrm{ab}}}{MW_{H2}} \tag{B.21}$$

$$t_{rc-HEX2} = \frac{w_{max} \cdot m_{MH,tube-HEX2}}{m_{f,tube-HEX2} \cdot c_{p,f} \Delta T_{f-HEX2}} \cdot \frac{\Delta H_{\mathrm{ab}}}{MW_{H2}} \tag{B.22}$$

$$t_{rc-HEX3} = \frac{w_{max} \cdot m_{MH,tube-HEX3}}{m_{f,tube-HEX3} \cdot c_{p,f} \Delta T_{f-HEX3}} \cdot N_t \cdot \frac{\Delta H_{\mathrm{ab}}}{MW_{H2}} \tag{B.23}$$

where N_t is the number of tubes. The equations above are used to compute the time of reaction completion for each heat exchanger and identify the operational regions that provide practical reaction times (see Section 4.4).

B.2 Nusselt correlation study

The nominal and alternative Nu correlations investigated in this work and their influence on the calculated heat transfer performance is discussed in the present section.

B.2.1 Nusselt correlations: nominal and alternative

The nominal correlations are given for each heat exchanger in Table B.3 with respect to their name, Re interval, and flow regime of validity. For additional information, the reader is referred to the listed references, as a detailed description of such correlations falls outside the objective of the present study.

Table B.3: Nominal equations for the Nu correlation analysis.

Flow regime	HEX1	HEX2	HEX3
Lam.	Sieder-Tate p. 5-15 [204] (Re<2100)	Martin pp. 702-703 Ref. [206] (Re<2300)	
Tran.	Hausen p. 5-16 Ref. [204] (2100$\leqslant$Re<10^4)	n.a. p. 702 Ref. [206] 2300<Re<10^4	Bell-Delaware pp. 317-320 [179] any Re
Turb.	Dittus-Boelter/Colburn* pp. 516-517 Ref. [203] (Re$\geqslant 10^4$)	Gnielinski p.703 Ref. [206] (Re$\geqslant 10^4$)	

*modified Dittus-Boelter with Colburn analogy.

The alternative correlations are reported in Table B.4.

Table B.4: Alternative equations for the Nu correlation analysis.

Flow regime	HEX1		HEX2	HEX3
Lam.	Mills Ref. [211] Re<2100		n.a.	
Tran.	Gnielinski Ref. [203] 3000⩽Re<5x10^6		n.a.	Kern* pp. 307 [179] 2000⩽Re⩽10^6
Turb.	Dittus-Boelter pp. 516 [203] Re⩾10^4	Gnielinski Ref. [203] 3000⩽Re<5x10^6	Dirker-Meyer Ref. [212] Re⩾10^4	

*The Kern method actually refers to a correlation found by McAdams.

B.2.2 Effect of Nusselt correlations on the heat transfer effectiveness

The results presented in Chapter 4 have been obtained by using the nominal Nu correlations. In this section, the effects on the heat transfer effectiveness that can be attributed to other Nu correlations are explored. For HEX1 and HEX2, the effect on the results is accounted for by displaying the influence on both Nu and ϵ values at the mean optimum velocity. For HEX3, since only two correlations are explored, it is more convenient to present their effect on the heat transfer effectiveness by displaying the relative difference of the performance for the entire domain of velocities and outer diameters. Nominal and other investigated correlations are reported in the appendix for each configuration.
In Fig. B.1, the lines marked with a star symbol represent the nominal correlations employed in the calculations, while the other lines indicate the alternative correlations as labeled in the legend. The solid lines refer to the Nu values reported on the left y-axis, while the dashed blue lines represent the calculated ϵ-values on the right y-axis. Finally, the vertical lines display the Reynolds number validity thresholds for the nominal correlations as reported in Subsection B.2.1 of this appendix (i.e. Re_{Lam} = 2100 or 2300 and $Re_{Turb} = 10^4$). The transitions at these lines are the reason for the abrupt changes of the ϵ-values and Nu.

Fig. B.1a shows that the greatest discrepancies in Nu occur in the turbulent regime. In this region, the maximum relative difference for Nu increases up to 9% when

employing the simple version of the Dittus-Boelter correlation and up to 16% when the Gnielinski correlation is used. However, it should be noted that their impact on the effectiveness is more modest and accounts for 7.3% and 13%, respectively. Another relatively significant discrepancy in the value occurs in the laminar region when the Mills equation is employed. In this case, a maximum relative difference for Nu of 34.6% causes a variation of only 10.7% in the effectiveness value. This apparent disparity with the trend discussed for the turbulent regime can be explained by considering that the exponential nature of the ϵ-equation makes the function less sensitive to the Nu variation for ϵ-values closer to unity.

In Fig. B.1a (i.e. HEX2), only one alternative equation has been investigated for an aspect ratio $a = D_i/D_o = 0.5$, as a detailed correlation study for concentric annuli was carried out in Ref. [212] where the Dirker-Meyer equation was proposed for the turbulent region. Such a correlation underestimates the mean Nu by 16% when compared to the Gnielinski equation, in agreement with the results presented in Ref. [213]. Although the influence on ϵ is not significant, accounting for only about 11%, it should be mentioned that, in the study by Gnielinski, doubts on the reliability of the data processing and experimental facility have been raised for the Dirker-Meyer correlation. For this reason, the Gnielinski equation has been employed as the nominal correlation in the thermal analysis.

Fig. B.2 shows the relative difference in the effectiveness calculation when the Bell-Delaware method (nominal correlation) is employed in place of the simpler Kern method. The former is universally considered to be the most accurate for the estimation of the average heat transfer coefficient on the shell side [179] with a mean error of 15% [214]. The figure shows the application of both methods in the entire domain under study; although the Kern method is only valid for the turbulent regime (i.e. above the upper dashed line that corresponds to $Re_{Turb}=10^4$), while the Bell-Delaware method provides performance values greater by up to 16%. The opposite trend can be seen in part of the transition and laminar regions, where the Bell-Delaware method results in a relative difference of about -2%.

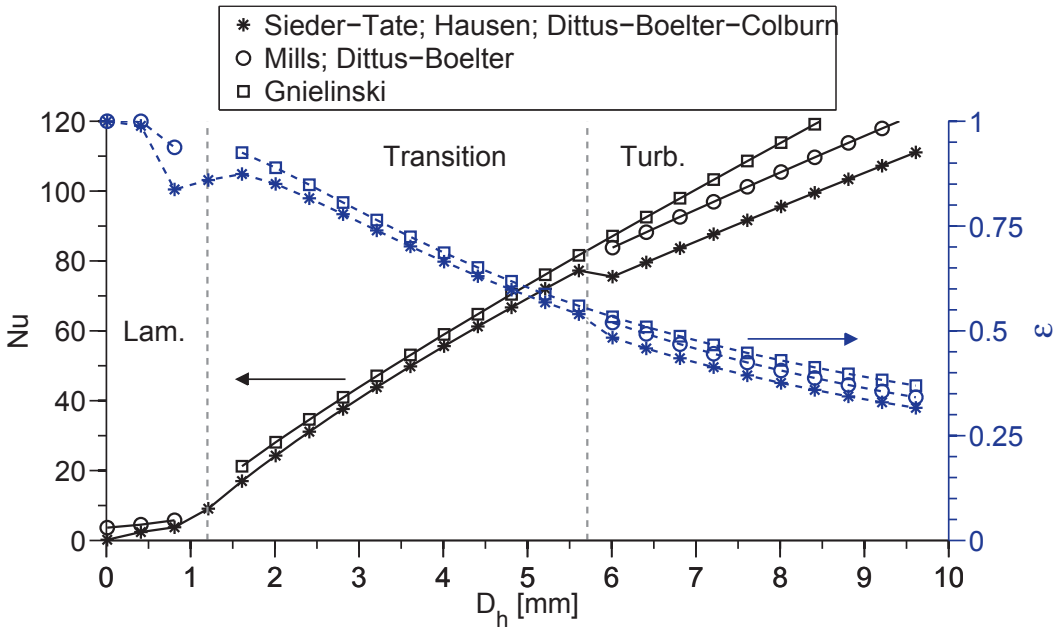

(a)

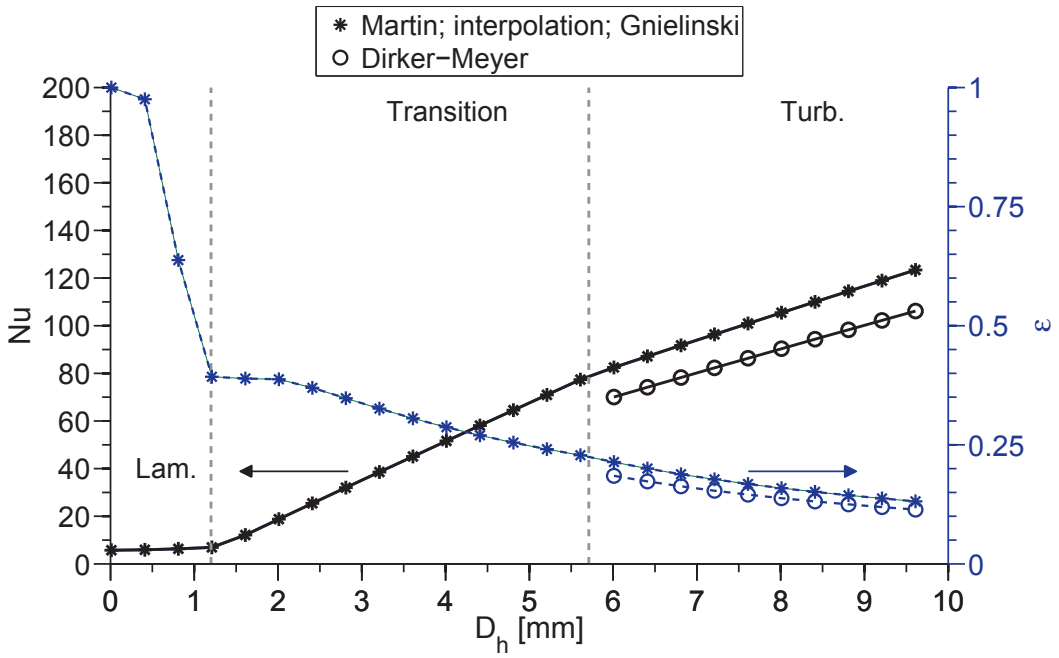

(b)

Figure B.1: Nu and ϵ-values for different correlations with v = 1.75m/s. HEX1 (a); HEX2 (b).

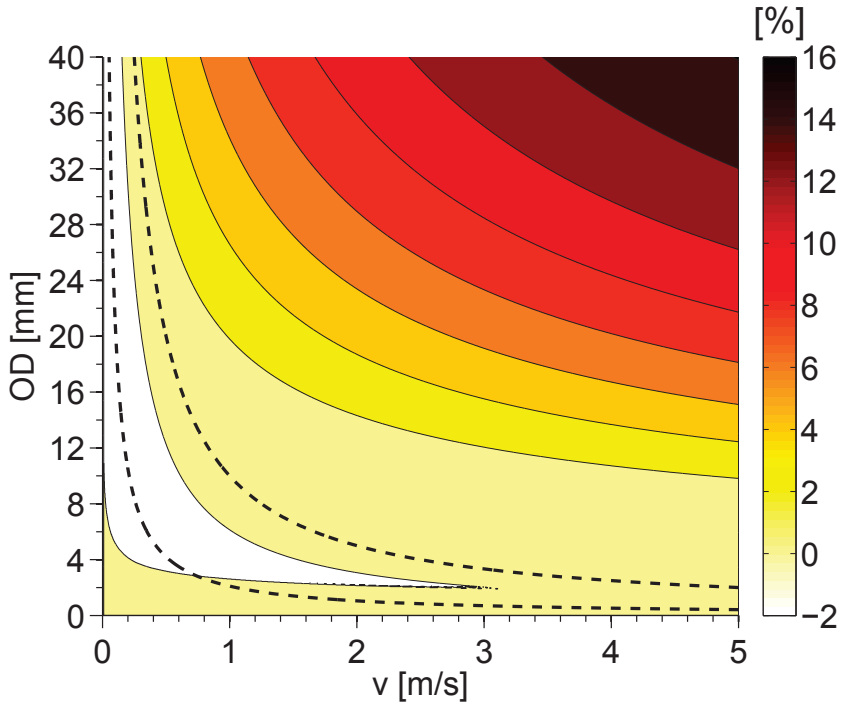

Figure B.2: Relative difference (in %) for ϵ between Bell-Delaware and Kern methods.

B.3 Sensitivity analysis on the thermal effectiveness: design parameters

A sensitivity study is carried out to evaluate the effect of both the design and HTF thermo-physical properties on the performance results using the mean optimum velocity of 1.75 m/s and the mean characteristic length defined as half of the diameter range here investigated. The mean diameter corresponds to 5 mm for the less efficient configurations, namely HEX1 and HEX2, and to 20 mm for HEX3. From the sensitivity analysis perspective, such values are selected in order to leave room for effectiveness variation while representing practical sizes. In Fig. B.3, each parameter on the left side of the box is alternatively varied, while the others are kept constant during the simulation. The effect on the effectiveness is reported on the x-axis for each parameter. The vertical red lines in each blue box represent the conditions which meet the target effectiveness of 0.95, while the values above such a line correspond to the nominal parameters' values. For the fluid properties, these values for water at 20 °C as discussed Section 4.2.

The numbers reported by the whiskers are the upper and lower limits in the parameters' variation range, while the extremities of each blue box refer to a parameter value

of 25% and 75% in the corresponding range. The variation range encompasses the properties' values of water and other common heat transfer pure-fluids between 20 °C and 100 °C [215, 216].

As one could expect, an increase in the thermal conductivity of the HTF and a decrease in its specific thermal capacity and density provides a benefit to the performance. However, it should be noted that lowering HTF's ρ and c_p causes the thermal capacity to decrease, suggesting a tradeoff between an increase in the performance and a decrease in the heat that can be removed from the MH. It follows that even if the effectiveness is augmented, lower cooling capacities occur, making it more difficult to fulfill the cooling demand of the absorbing alloy. The kinematic viscosity seems to have a significant impact on the heat transfer effectiveness. However, the minimum and maximum values in viscosity variation range vary by an order of magnitude of 3, which is much larger than for the other physical properties. It is thus more pertinent to consider the effect on the performance due to the parameters that are directly part of the design process.

A comparison between the two layouts reported in Figs. B.3a- B.3b shows that the same tube length provides much lower performance for HEX2 than HEX1, as was expected by examining Figs. 4.2a and 4.3a in Section 4.4. In order to reach the desired value of 95% for ϵ, HEX2 needs to be more than 3 times longer when nominal parameters' values are considered. This outcome suggests that HEX1 can achieve the same performance as HEX2 with a reduced size, which in turn makes it a better candidate design for applications where volume constraints are more stringent or where the size of the system needs to be modest for experimental purposes (e.g. lab-scale systems). However, in order to have a wider view of the problem, the results from the heat demand analysis discussed in the following section should also be considered. For HEX2, the aspect ratio a is varied between 0.01 and 0.99, close to the limiting conditions of a circular tube of diameter D = D_h with an "infinitesimal" thin wire at the center and the parallel plate case, respectively. The former condition provides greater ϵ-values per unit total length of active tube and is geometrically equivalent to the HEX1 solution. Alternatively, when the coaxial tube configuration approaches the parallel plate geometry, a significant drop in the performance can be seen, making the aspect ratio the most influential parameter within the ranges considered here.

The high performance per unit size of HEX3 makes this configuration apparently convenient for use in a MHHP application. Indeed, Fig. B.3c shows that a tube length of approximately 1.7 m is required to reach the target effectiveness at nominal conditions. The temperature factor, F_t, takes into account the direction of the flow over the tube

bank and has a marginal effect in the range considered. The minimum value for such a factor is limited to 0.75 as it is typically not convenient to manufacture a heat exchanger with lower values [203]. The effect of the relative baffle spacing, B, and the tube to pitch ratio, PR, is explored for values that exceed the recommended optimum range reported in Table 4.1. From a performance point of view, the lower these parameters are the greater the heat transfer effectiveness will be. Relative baffle spacings smaller than 20% of the inner shell diameter should be excluded due to the negative effect on the flow circulation and deposit and values lower than 1.25 for PR are not recommended as they embrittle the tube sheet [177]. For these reasons, the nominal values for these two parameters have been set equal to the lower limits of their respective optimal ranges, to provide the highest performance. As described earlier, the shell diameter, D_s, does not influence the performance and thus, its variation is not considered in this sensitivity analysis.

It should be noted that given the velocity and characteristic length conditions used in this sensitivity analysis, the operational point falls within the transition regime for HEX1 and HEX2 and within the turbulent regime for HEX3. However, the trend and main outcomes determined from Fig. B.3c are still valid for any velocity and characteristic length values.

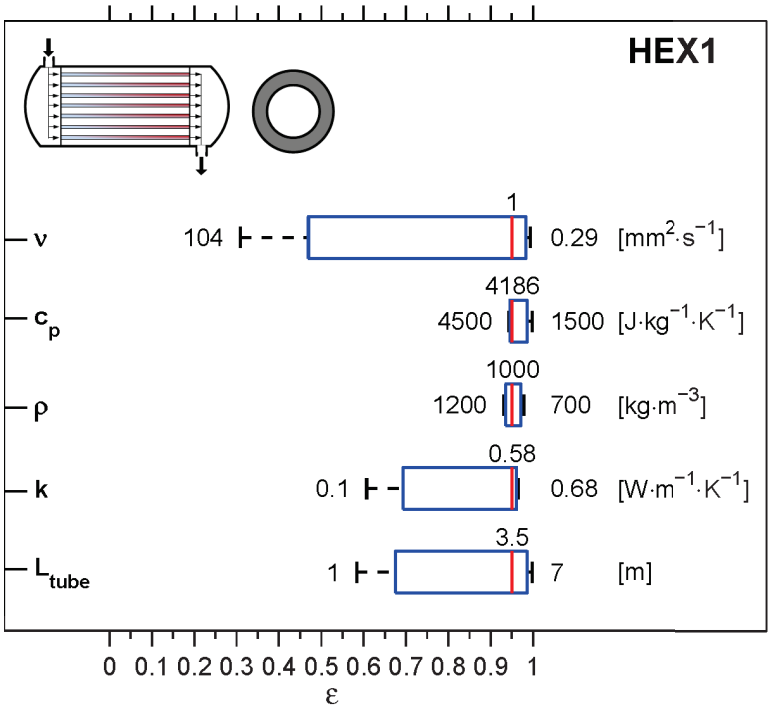

(a)

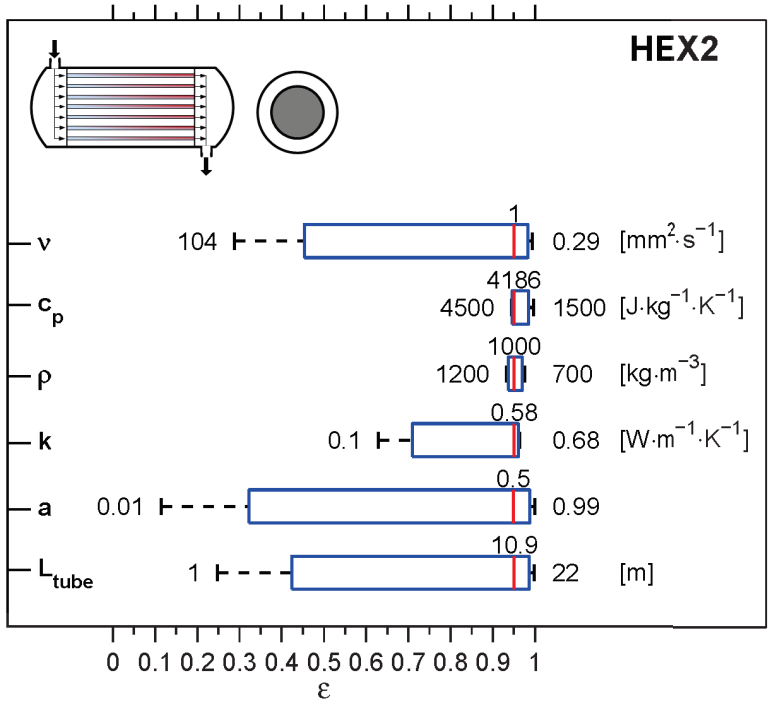

(b)

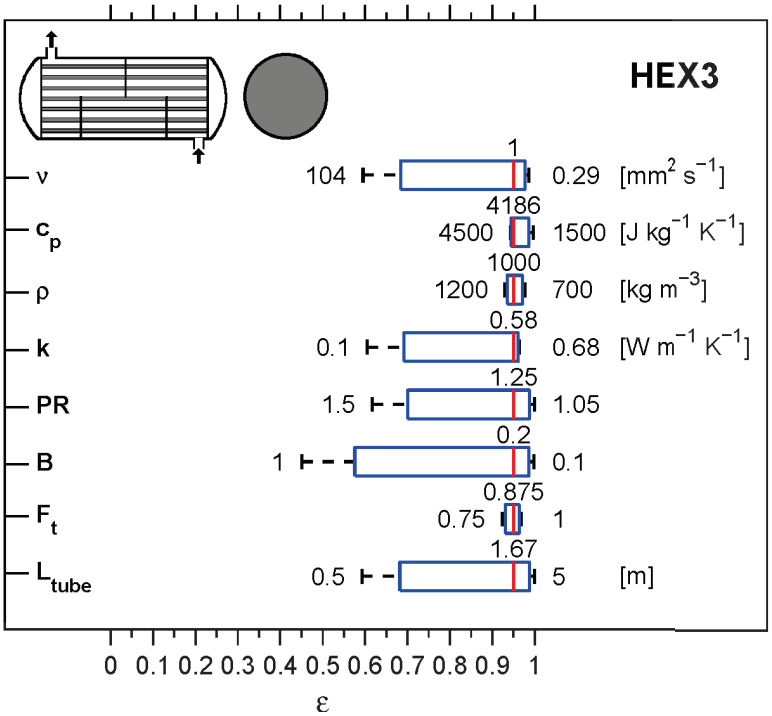

(c)

Figure B.3: Sensitivity analysis for ϵ. HEX1 (a); HEX2 (b); HEX3 (c).

B.4 Heat demand analysis: HEX1

As shown in Chapter 4 and in the previous sections of the present appendix, HEX1 configuration is the most attractive for a MHHP system since it has the potential of providing an adequate HTF temperature lift, indicator of the desired effect of the heat pump, and reasonable cycling times. For this reason, it should be further investigated with respect to some target reaction times and using the hydride bed thickness as the free variable. This investigation is shown in Fig. B.4, where three t_{rc} target values (i.e. 5, 30, 60 min) are plotted for three representative values of the hydride bed thickness, 1 mm, 2.5 mm, and 5 mm.

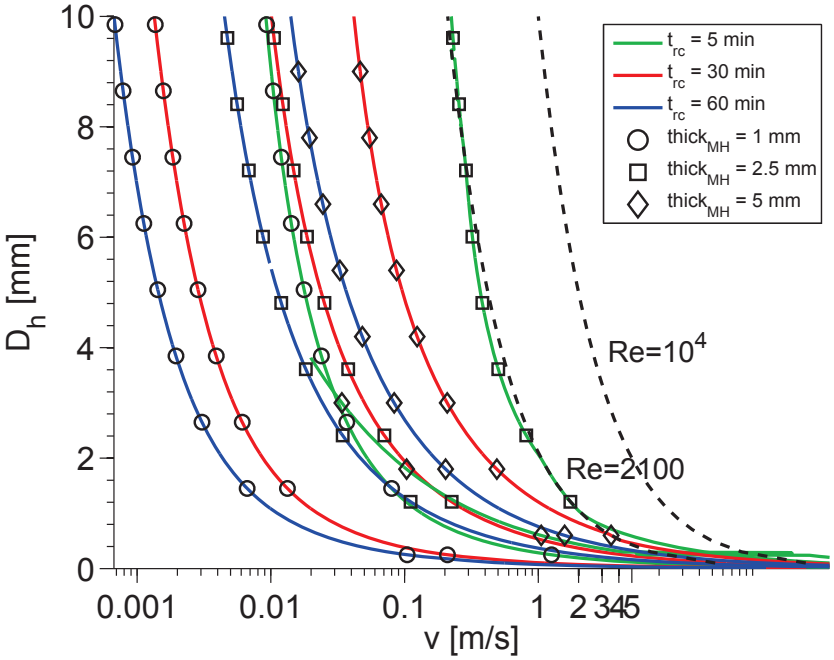

Figure B.4: Time of reaction completion for some target values and representative solid bed thicknesses for HEX1.

A semi-logarithmic plot is used to better appreciate the points that lie on the operational curves at velocities below 1 m/s. The black dashed lines correspond to the flow regime transitions and are plotted for consistency with the previous plots and to provide additional relevant information. It should be noted that all the curves essentially lie in the laminar regime. For a given thickness, the lines that refer to greater times are closer to the y-axis, which is representative of the limit condition of null mass flow rates and thus of non-practical designs. Similarly, when the lines that correspond to a certain reaction time (i.e. the same color) are compared, lower values of velocity belong to smaller thickness values.

Reaction times of 5 min can be obtained for realistically-sized designs starting from 5 mm of bed thickness and velocities around 1 m/s. However, as it is preferable to operate at relatively high t_{rc}, it is more relevant to focus on the lines that refer to target reaction times of 30 and 60 min. As shown in Fig. B.4, such lines correspond to designs characterized by unrealistic diameters and/or velocities. For example, for a 5 mm thickness and a 2 mm diameter, extremely low velocities are needed to provide reaction times of 30 and 60 min: 0.1 m/s and 0.05 m/s, respectively. Such velocity values are too small to avoid the risk of debris formation and ensure a continuous operation in absence of constant monitoring and periodical cleaning. In practice, for relevant tube sizes and fluid velocities, simulations have shown that for HEX1 is possible to achieve a reaction time of 30 min by either enlarging the metal hydride bed around the tubes or recirculating the HTF in a multi-pass configuration. If cooling tubes of 2 mm and velocities of 0.8 m/s are considered, a reaction time of 30 min can be achieved, for instance, by designing an annular bed thickness of 10 mm with a length of 2 m or by recirculating the heat transfer fluid eight times through a 5 mm bed. The former option provides a larger system, whereas the latter solution is more compact but at the expenses of a smaller total amount of heated HTF and larger pressure drops. Therefore, depending on which requirement is the most stringent (i.e. volume, pressure drops) the design can be adapted to fulfill the operating requirements listed in Table B.1.

The final selection of the design should also account for the performance values and thus the actual temperature increase than can be achieved for a target time. It must be noted that for HEX1, an increase in the tube length has a positive effect on both the effectiveness and the reaction time; the larger amount of heat is accounted for by an increase in the hydride mass. It is also possible to further increase the reaction time by employing thicker solid beds around the cooling tubes. Both options provide increased performance and reaction time at the expenses of a larger system volume, which can be the most stringent constraint in some applications.

B.5 Conclusion

Performance and pressure drop maps for reasonable tube sizes and a wide velocity range are obtained for each heat exchanger candidate; giving the reader all the information needed to select a suitable solution in a pre-design stage.

The effectiveness values seem to be modestly influenced by the particular correlation used to compute the HTF convection coefficient. It follows that any trustable Nusselt number correlations investigated in this study provide a sufficiently correct estimation of the performance, with a maximum relative difference of 13% for HEX1 in the turbulent regime.

The tube length is the design parameter that affects HEX1 performance the most due to its linear effect on the heat transfer area which influences the exponent in the index of performance formulation. It also has a significant effect on the heat transfer effectiveness values for HEX3, although the baffle space is found to be the most sensitive parameter for such a configuration. Another parameter that can be adjusted towards higher efficiencies is the aspect ratio a for the tube-in-tube configuration of HEX2. However, the sensitivity analysis shows that a positive effect is obtained when its value tends to unity, and thus to a condition where the cross flow area and the mass flow are nearly zero, resulting in a negligible heat transfer rate.

HEX3 is the solution that provides the greatest performance per unit of active tube length; modestly distributed pressure drops can be achieved for a tube diameter around 20 mm in the optimum velocity range.

The combination of the performance and heat demand analyses provides a valuable tool to decide whether a certain heat exchanger layout is suitable for a MHHP application and aid in the selection of practical designs.
Both HEX2 and HEX3 configurations lead to non-practical designs when relevant reaction times are targeted. HEX1 is found to be the only layout that can provide realistically-sized designs that fulfill the requirements and respect the constraints defined in this study. Longer tubes positively affect both the temperature increase of the coolant and the reaction times. Also, the possibility of augmenting the reaction times by enlarging the bed thickness around the cooling tubes is an interesting feature of this layout for a heat pump application.

The design that can satisfy the performance requirements with respect of all the design criteria was found to be HEX1 with the following parameters: 2 mm diameter tubes surrounded by a 10 mm bed thickness with a total active length of 3 m, operating at a HTF velocity of 0.8 m/s. Such a system provides an effectiveness of 85% (i.e. $T_{f-m,out}$

= 88°C for T_{MH} =100°C and $T_{f-m,in}$ = 20°C), an overall pressure loss of 0.2 bar, and achieves a reaction time of 40 min.

At the end, it is worth pointing out that the thermal model can easily be tailored to include information on the hydride thermal properties, providing a more specific design for any application of interest.

C Phase change material: computational model

Only the working principle of the model that describes the phase change and the heat transfer within the PCM layer is described here, as the thermodynamic and heat transfer models employed in the tank are described in detail in Refs. [103, 104].

C.1 Phase change and heat transfer models

The energy balances and heat transfer equations are solved for the hydrogen gas and the wall, which has been discretized by means of the finite volume method in Dymola^{TM} environment. In Fig. C.1 the discretization concept and the heat transfer flows are presented with attention to the PCM and along with the boundary conditions.

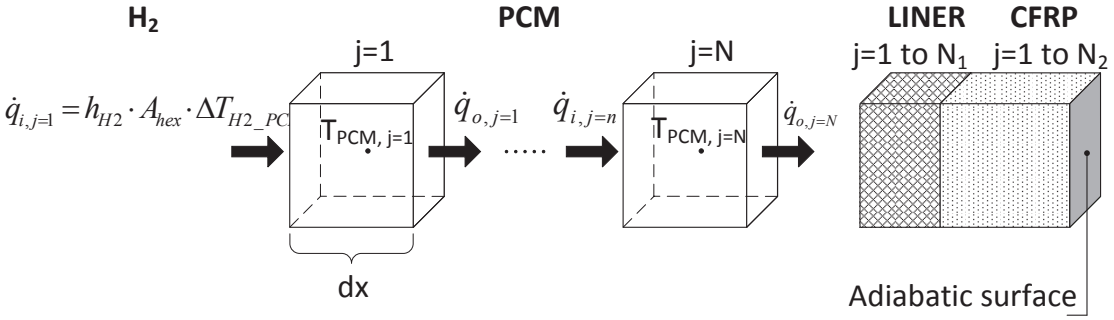

Figure C.1: Discretization scheme for the PCM thickness and tank walls. Adiabatic external wall case

As the physical and thermal properties of the PCM have only been measured in the liquid and solid phases, in the model they have been linearly interpolated during phase change with respect to the instantaneous temperature value.

Appendix C. Phase change material: computational model

The convection coefficient in the boundary condition at the hydrogen-PCM interface varies between 150-500 $W \cdot m^{-2} \cdot K^{-1}$, as discussed in Ref. [103].
The transient one-dimensional energy balance for each PCM volume reads:

$$\rho_{PCM} \cdot c_{PCM} \cdot \frac{\partial T_{PCM}}{\partial t} \cdot (dx \cdot A_{hex}) = \dot{q} \tag{C.1}$$

where ρ_{PCM} is the PCM density, T_{PCM} is the temperature calculated at the volume center point, dx is the discretization step (defined on a path parallel to the heat flow), A_{hex} is the heat transfer area and c_{PCM} is the effective specific heat capacity.
For the cases where the measured values of the thermo-physical properties (e.g. ρ_{PCM}) are only available for the solid and liquid phases, as for the paraffin wax used in Chapter 5, an interpolation procedure can be used to estimate their value during phase change with respect to the PCM instantaneous temperature. Such an interpolation is shown in the next section for the thermal conductivity of the PCM.
The specific heat capacity is computed by means of the effective capacity method for the melting range, representative of the asymmetrical triangular function that provided the highest agreement between computational and experimental data as described in Ref. [190]. The method incorporates the latent heat λ, in the phase-change region, inside an effective specific heat capacity, which ranges from the minimum values assumed in the solid and liquid phases to the maximum value at the melting temperature T_m. Any function can be selected such that:

$$\int_{T_m-\omega_1}^{T_m+\omega_2} c_{PCM} dT = \lambda \tag{C.2}$$

An explicit form for the c_{PCM} function in the solid, liquid and phase-change regions can be written as

$$\begin{aligned}
&if\ T_{PCM} < T_m - \omega_1 \\
&c_{PCM} = c_{PCM,s} \\
&if\ T_m - \omega_1 \leq T_{PCM} \leq T_m \\
&c_{PCM} = \gamma_1 + \gamma_2 \cdot (T_{PCM} - (T_m - \omega_1)) \\
&if\ T_m < T_{PCM} < T_m + \omega_2 \\
&c_{PCM} = \gamma_3 - \gamma_4 \cdot (T_{PCM} - T_m) \\
&if\ T_{PCM} \geq T_m + \omega_2 \\
&c_{PCM} = c_{PCM,l}
\end{aligned}$$

with

$$\gamma_1 = c_{PCM,s}; \gamma_2 = \frac{c_{PCM,m} - c_{PCM,s}}{\omega_1};\ \gamma_3 = c_{PCM,m};\ \gamma_4 = \frac{c_{PCM,m} - c_{PCM,l}}{\omega_2} \tag{C.3}$$

and

$$c_{PCM,m} = \frac{2\lambda - 2\omega_2 \cdot (c_{PCM,l} - c_{PCM,s}) + \omega_1 \cdot c_{PCM,s} + \omega_2 \cdot c_{PCM,l}}{\omega_1 + \omega_2} \tag{C.4}$$

C.2 Heat transfer model

The overall heat transfer rate $\dot{q}$ for each control volume accounts for both the heat that flows in, $\dot{q}_i$, and out, $\dot{q}_o$, which are function of the thermal resistance R_{th}, calculated along x-axis, and the temperature difference between the center points of the PCM volumes, as presented in Eqs. C.8a to C.8d:

$$\dot{q} = \dot{q}_i + \dot{q}_o \tag{C.5}$$

$$\dot{q}_i = \frac{T_i - T_{PCM}}{R_{th}} \tag{C.6}$$

$$\dot{q}_o = \frac{T_o - T_{PCM}}{R_{th}} \tag{C.7}$$

$$R_{th} = \frac{dx}{A_{hex} \cdot k_{PCM}} \tag{C.8}$$

The heat transfer model accounts for the conduction in the solid phase, natural convection in the liquid phase and their combination during melting. This is done via the definition of an effective thermal conductivity k_{PCM} that varies accordingly to the procedure reported below:

$$\begin{aligned}
&if\ T_{PCM} < T_m - \omega_1 \\
&k_{PCM} = k_s \\
&if\ T_m - \omega_1 \leq T_{PCM} \leq T_m \\
&k_{PCM} = k_s + (k_m - k_s) \cdot \tfrac{T_{PCM} - (T_m - \omega_1)}{\omega_1} \\
&if\ T_m < T_{PCM} < T_m + \omega_2 \\
&k_{PCM} = k_m + (k_1 \cdot k_{r,2} - k_m) \cdot \tfrac{T_{PCM} - T_m}{\omega_2} \\
&if\ if\ T_{PCM} \geq T_m + \omega_2 \\
&k_{PCM} = k_l \cdot k_{r,1}
\end{aligned}$$

where

$$k_m = k_s + (k_1 \cdot k_{r,2} - k_s) \cdot \frac{\omega_1}{\omega_1 + \omega_2} \tag{C.9}$$

For the paraffin wax considered in Chapter 5 the ω values of the an asymmetric phase change function are [190]

$\omega_1 = 3$ K or °C
$\omega_2 = 1$ K or °C

where ω_1 and ω_2 represent the values assumed by the asymmetrical phase-change function during melting/solidification, k_m is the linearly interpolated thermal conductivity calculated at T_m, whereas $k_{r,1}$ and $k_{r,1}$ are the ratio between the effective conductivity that accounts for natural convection and the thermal conductivity of the liquid defined accordingly to Ref. [203]. For the geometry of interest (i.e. annular region between long horizontal concentric cylinders with heated inner surface), the general expression of such a ratio reads:

$$k_r = \frac{k_{PCM}}{k_l} = 0.386 \cdot \frac{Pr}{(0.861 + Pr)^{1/4}} \cdot Ra^{1/4} \tag{C.10}$$

Eq. C.10 is valid for $0.7 \leq \text{Pr} \leq 6000$ and $\text{Ra} \leq 10^7$. As the minimum heat transfer cannot fall below the conduction limit, the effective thermal conductivity is imposed equal to k_l when the value predicted by Eq. C.10 is less than unity. The Rayleigh number in Eq. C.10 is computed with respect to the relevant temperature difference for k_{r1} and k_{r2}. For the former, this difference considers the time-dependent temperatures of the volumes at the two extremities of the PCM layer (i.e. at j=1 and j=n, see Fig. C.1), whereas for the latter it refers to the inner volume's central-point temperature (i.e. at j=1, see Fig. C.1) and the upper temperature in the melting range, $T_m + \omega_2$, as a reasonable approximation.

C.3 Prediction of phase change

The model presented above can be used to predict both the melting and solidification of the PCM. This means that it describes entirely the thermal cycle of the PCM layer during hydrogen charging and discharging.
In Fig. C.2 the model is applied to a a 10 mm PCM layer inserted at the wall/hydrogen interface of a non-adiabatic Type IV tank to prove the stability of the model during melting and solidification with respect to three locations within the PCM thickness.

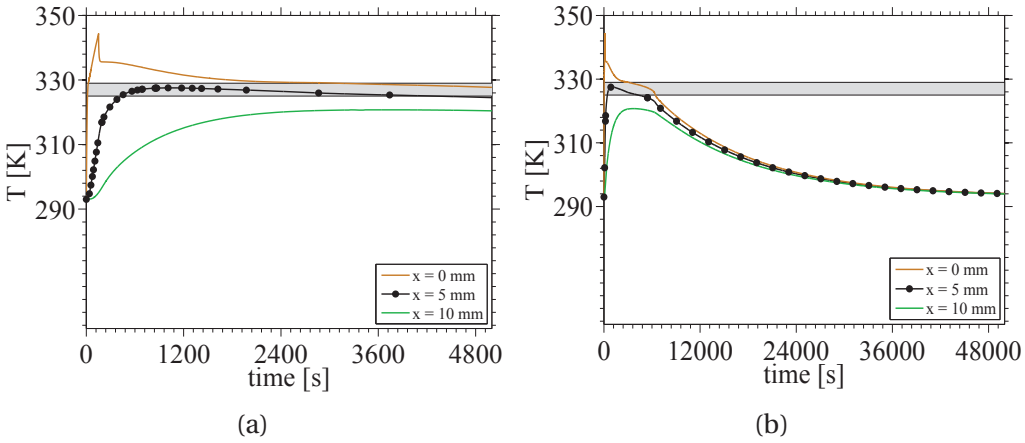

Figure C.2: Temperature profile at different PCM locations (non-adiabatic case). Simulation time limited to 5000 s (a); simulation time extended to 50000 s (b).

In Fig. C.2a the simulation time is limited to 5000 s to better appreciate the temperature profile of the PCM with respect to the phase-change region. The PCM that is at a location in direct contact with the high temperature gas (i.e. at 0 mm) starts melting at 12 s and in approximately 8 s is fully melted. It is possible to notice a reduction in the temperature increase rate when the PCM enters the liquid phase. This occurs because the natural convection reduces the thermal resistance of the first layer portion and therefore, enhances the heat transfer rates to the neighbor PCM. The PCM experiences a sharp temperature increase until the end of pressurization after which the compression heat drops and so does the temperature. The heat transferred through the PCM and the walls to the external air at 293 K causes further reduction in the PCM temperature, which enters the two-phase region and then becomes entirely solid at approximately 6000 s from the beginning of the refueling process.
At the location that corresponds to the mid-thickness (i.e. 5 mm) the PCM enters the phase-change region at approximately 30 s. The heat absorbed is not enough to completely melt the PCM that, unlike what was observed in Fig. 5.5, starts cooling due to the heat removed from the ambient air through the tank walls. Solidification occurs at approximately 4800 s. On the other hand, for the PCM in contact with the tank wall (i.e. 10 mm) the temperature never reaches the melting point. At this location the phase change material behaves as a thermal insulator and its capacity to absorb large amounts of heat during melting remains unused, see Subsection 5.3.1.
Fig. C.2b shows the results for an extended simulation time. More than 13 hr are required for the entire PCM thickness to reach the thermal equilibrium with the ambient temperature at 20 °C (or approximately 293 K).

D HySdeP: user libraries

The record structure in Modelica® language is used in HySDeP to create databases for material properties, geometric parameters and to select among different boundary conditions and kinetics equations. Each database is defined by a name (e.g. *MH_properties*, *Tube _properties*) and a variable number of fields that characterize data using types such as *Real* or *Integer* for numbers and *Boolean* for logic parameters. The underlined text, that appears in the tables of this appendix, corresponds to the default entries that the platform selects unless a selection is made by the user. As an example, if no hydrogen-absorbing alloy is chosen, the model uses the properties of $Ti_{1.1}CrMn$, which is the nominal composition.
The current appendix presents the status of the implemented libraries at the moment of the submission of the thesis.

D.1 Databases for the MHSS

D.1.1 MH composition database

The results presented in this thesis for the MH tank refer to the nominal composition presented in Section 3.4 for $Ti_{1.1}CrMn$.
As it was mentioned in Chapter 6 other hydrogen-absorbing alloys can be selected from the user. The current status of the implemented materials are listed in Tables D.1-D.3 along with the relevant thermo-physical and kinetic properties for hydriding and dehydriding processes. These materials represent the first effort of building a comprehensive library for those alloys for which kinetic and thermal properties are available in literature. All the listed materials can only be used in the constant parameter model, with the exclusion of $Ti_{1.1}CrMn$, for which, measured data has been implemented for thermal conductivity and specific heat capacity.

Table D.1: Metal hydride compositions and thermal properties included in HySDeP.

Composition	k_{MH} [W·m^{-1}·K^{-1}]	c_{MH} [J·kg^{-1}·K^{-1}]	ρ_s [kg·m^{-3}]
$Ti_{1.1}CrMn$ [55]	1	500	6200
$Ti_{1.1}CrMn$* [170]	10	500	6200
$TiFe_{0.8}Ni_{0.15}V_{0.05}$ [145, 217]	1	500	6600
$Ti_{0.95}Zr_{0.05}CrMn$ [145, 217–219]	1	500	6600
$LaNi_5$ [220, 221]	1.2	419	8200
$LaNi_{4.95}Sn_{0.05}$ [145, 217]	1	500	7200
$LaNi_{4.7}Al_{0.3}$ [76, 222]	5	419	8000

*compacted with Al powder.

D.1.2 Heat exchanger database

Table D.2 presents the configurations implemented in the heat exchanger library. These designs refer to the geometric layouts presented Chapter 4 and studied in Chapter 6 with respect to the charging and discharging analyses. In Chapter 6 a list of the main geometric parameters is given with their nominal values.

Table D.2: Configurations implemented in the heat exchanger library.

Type	Name	Description
Tube-in-tube	HEX2	Bank of coaxial cylindrical tubes. Metal hydride inside the inner tube. HTF in the annular region.
Shell-and-tube	HEX3	Bank of bear tubes. Metal hydride inside the tube. HTF in the shell.

D.1.3 Kinetic model database

Charging and discharging kinetic models other than the nominal equations presented in Appendix A can be selected from the user according to the chosen MH composition. The kinetic equation can be considered as a combination of three separate functions: the Arrhenius constant which is only function of the MH temperature, a pressure limiting function a composition function which depends on reaction order. This is

Table D.3: MH compositions and kinetic properties included in HySDep.

Composition	ΔH_abs [J·mol$^{-1}_{H2}$]	ΔS_abs [J·mol$^{-1}_{H2}$·K^{-1}]	$E_{a,abs}$ [J·mol$^{-1}_{H2}$]	$C_{a,abs}$ [s^{-1}]	ΔH_des [J·mol$^{-1}_{H2}$]	ΔS_des [J·mol$^{-1}_{H2}$·K^{-1}]	$E_{a,des}$ [J·mol$^{-1}_{H2}$]	$C_{a,des}$ [s^{-1}]	w_{max} %
$Ti_{1.1}CrMn$ [55, 61]	-14390	-91.3	20700	150	-24500	-122	16500	300	1.5
$Ti_{1.1}CrMn$* [55, 61, 170]	-14390	-91.3	20700	150	-24500	-122	16500	300	1.5
$TiFe_{0.8}Ni_{0.15}V_{0.05}$ [145, 223]	-36902	-113	20000	57	-36902	-105.4	16420	9.57	1.75
$Ti_{0.95}Zr_{0.05}CrMn$ [145, 224]	-15100	-93	20000	57	-20800	-105	16420	9.57	1.79
$LaNi_5$ [145, 224, 225]	-31168	-111.4	20000	59.187	-32151	-112.8	16420	9.57	1.49
$LaNi_{4.95}Sn_{0.05}$ [226, 227]	-30400	-106.2	20000	57	-32000	-108.4	16420	9.57	1.3
$LaNi_{4.7}Al_{0.3}$ [145, 228, 229]	-24799	-88.4	30000	1000	-28511	-90.1	-30000	1000	1.35

*compacted with Al powder.

shown in Eq. D.1.

$$\frac{\partial w}{\partial t} = C_a e^{E_a/(RT_{MH})} \cdot f_p\left(p, p^{eq}\right) \cdot f_w\left(w, w_{max}, p, p^{eq}\right) \tag{D.1}$$

Specifying the kinetic model means providing the properties of the hydrogen-absorbing alloy and selecting the pressure and composition functions. Table D.4 presents some typical expressions of f_p and f_w, used for modeling, that are implemented in the database.

Table D.4: Pressure and composition functions included in HySDeP [145, 230].

Type	f_w	f_p	Type
0^{th} order abs.	w_{max}	$(p - p^{eq})/p^{eq}$	Normalized linear
0^{th} order des.	w_{max}	$\ln(p/p^{eq})$	Logarithmic
1^{st} order abs.	$(w_{max} - w)$ or $(1 - F_{rc})$		
1^{st} order des.	w or F_{rc}		

Finally it is worth pointing out that the composition function can be written for w or F_{rc}, depending on the variable that appears in the partial derivative on the left hand side of the equation (see for example Eqs. A.19 and A.20).

D.1.4 Heat transfer media database

With the only exception of the nominal heat transfer medium, Dexcool®, the properties for the other media are retrieved from Coolprop at a fixed pressure of 1 bar and at the calculated average temperature between inlet and outlet.
The list of the available compositions is given in Ref. [231].
The properties of Dexcool® are given in Section 3.6 for the temperature of interest in this study.

D.1.5 Tube material database

Table D.5 presents the list of materials available in the *Tube_properties* library.
Considerations on the operative pressure, rather than on the thermal properties, should be done when selecting these materials. Therefore, the library also includes the relevant mechanical properties (i.e. ultimate tensile strength and tensile yield strength) that are needed to calculate the minimum thickness that can bear the operative pressure of choice (see Ref. [194] and Subsection 6.3.1 for examples).

Table D.5: Tube materials properties included in the HySDeP [194, 196].

Material	**Type**	k [W·m^{-1}·K^{-1}]	c [J·kg^{-1}·K^{-1}]	ρ [kg·m^{-3}]	σ_y [MPa]	σ_u [MPa]
Aluminum 6061 T-6	Aluminum alloy	167	896	2700	276	310
Aluminum 6351 T-6	Aluminum alloy	176	890	2710	283	310
Aluminum 6063 T-6	Aluminum alloy	200	900	2700	214	241
Aisi 304	Austenitic Cr-Ni stainless steel	16.2	500	8000	215	505
Aisi 302	Austenitic Cr-Ni stainless steel	16.2	500	7860	275	620
Aisi 316	Austenitic Mo stainless steel	16.3	500	8000	290	580
Copper	Copper	398	385	8930	33.3	210

D.2 Databases for the CHG system

D.2.1 PCM database

Only the paraffins that have a melting temperature/range between 50-65 °C have been implemented in the database (see Section 2.4.2). They are all reported in Table D.6 according to the form C_nH_{2n+2}, with the only exception of the nominal (i.e. *paraffin wax*) and commercial materials. If for lack of information available, a property value is only known for one phase, then such a value is used for both solid and liquid phases.

Table D.6: PCM compositions and thermal properties included in HySDep. Properties measured close to the melting point [116, 190, 232–235].

Composition	T_m [°C]	k [W·m^{-1}·K^{-1}]		c [J·kg^{-1}·K^{-1}]		ρ [kg·m^{-3}]		λ [J · kg^{-1}]
		Solid	Liquid	Solid	Liquid	Solid	Liquid	
n - Tetracosane	51	0.21	n.a.	1919	n.a.	912	769	255000
PCM_a	52-54	0.19	0.19	1970	2100	866	774	220000
Paraffin wax	52-55	0.24	0.18	2.905	2.905	785.3	769.2	224360
Paraffin wax_1	53	0.15	0.15	2384	n.a.	n.a.	775	184480
n - Pentacosane	54	0.21	n.a.	1919	n.a.	912	769	238000
n - Hexacosane	56	0.21	n.a.	1848.3	1848.3	770	n.a.	257000
PCM_b	58-62	0.21	0.21	2100	2490	893	782	206000
n - Heptacosane	59	0.21	n.a.	2175	n.a.	763	n.a.	236000
n - Octacosane	61	0.21	n.a.	2374	n.a.	910	765	255000
n - Triacontane	65	0.21	n.a.	1919	n.a.	910	765	252000

D.2.2 Boundary condition database

Three boundary conditions can be selected. These are reported in Table D.7 with a description of the physical explanation.

Table D.7: List of boundary conditions.

Boundary condition	Description
Adiabatic refueling	Heat transfer is not enabled between the hydrogen gas and the tank walls
Adiabatic tank	Heat transfer is enabled between the hydrogen gas and the tank walls
Non-adiabatic tank	Heat transfer is enabled between the hydrogen gas and the ambient through the tank walls

“Maybe…you’ll fall in love with me all over again.”
”Hell,” I said, ”I love you enough now. What do you want to do? Ruin me?”
”Yes. I want to ruin you.”
”Good,” I said. That’s what I want too.”

— E. Hemingway, *A farewell to arms*

DTU Mechanical Engineering
Section of Thermal Energy
Technical University of Denmark

Nils Koppels Allé, Bld. 403
DK-2800 Kgs. Lyngby
Denmark
Phone (+45) 4525 4131
Fax (+45) 4588 4325
www.mek.dtu.dk
ISBN: 978-87-7475-443-5

DCAMM
Danish Center for Applied Mathematics and Mechanics

Nils Koppels Allé, Bld. 404
DK-2800 Kgs. Lyngby
Denmark
Phone (+45) 4525 4250
Fax (+45) 4593 1475
www.dcamm.dk
ISSN: 0903-1685